The Investigation into Magnetic Skyrmion Dynamics Under the Influence of the Interfacial Spin-Transfer Torque

Callum Robert Uwe MacKinnon

A thesis submitted in partial fulfilment of the requirements for the degree of Doctor of Philosophy at the University of Central Lancashire

March 2023

RESEARCH STUDENT DECLARATION FORM

Type of Award Doctor of Philosophy

School School of Natural Sciences

1. Concurrent registration for two or more academic awards

I declare that while registered as a candidate for the research degree, I have not been a registered candidate or enrolled student for another award of the University or other academic or professional institution.

2. Material submitted for another award

I declare that no material contained in the thesis has been used in any other submission for an award and is solely my own work.

3. Collaboration

Where a candidate's research programme is part of a collaborative project, the thesis must indicate in addition clearly the candidate's individual contribution and the extent of the collaboration. Please state below:

_____

4. Use of a Proof-reader

No proof-reading service was used in the compilation of this thesis.

Signature of Candidate _____

Print name: _____

Abstract

Skyrmions are topologically protected magnetic textures that are predicted to be excellent candidates for future spintronic devices. Skyrmion dynamics under the influence of the interfacial spin-transfer torque (ISTT) and the well-established spin-orbit torque (SOT) are investigated in terms of the skyrmion Hall angle (SkHA), which is the angle at which a skyrmion deviates from the applied current direction, and the skyrmion velocity. The ISTT arises in thin magnetic layers due to a spin accumulation generated at magnetisation gradients resulting in a diffusive vertical spin current, whereas the SOT originates from the spin Hall effect in non-magnetic layers resulting in a torque on the local magnetisation.

Currently, micromagnetic studies typically involve modelling only the SOT as the main driving force in skyrmion motion which leads to a reasonable agreement with experimental results at large skyrmion diameters, however, when smaller skyrmions are considered (< 100 nm) the agreement reduces significantly unless unreasonable damping parameters ($\alpha > 0.5$) are used. Furthermore, the SOT-only Thiele model is used to compare results which correspond well to SOT-only results but do not accurately describe experimental findings.

When the ISTT is taken into account, skyrmion motion is considerably altered for skyrmion diameters < 100 nm. This is observed for skyrmion motion in which, for a skyrmion diameter of ~ 75 nm, the SkHA is reduced by ~ 25°, and the velocity is reduced by ~ 40 ms^{-1} with the inclusion of the ISTT resulting in a very good comparison to experimental observations. Furthermore, this trend is shown in ideal systems, systems with surface roughness, systems with thermal fields included, as well as in synthetic antiferromagnetic and ferrimagnetic systems. The Thiele model is also altered to include the ISTT, as well as the SOT, resulting in much better alignment with simulated and experimental results. Further work is also proposed to experimentally verify the existence of the ISTT utilising SAF structures to eliminate the SOT.

The findings in this thesis provide valuable insight into the significance of the role of the ISTT in terms of the SkHA and skyrmion velocity as well as the importance of including the ISTT in micromagnetic modelling for a complete model of current-driven magnetisation dynamics.

Table of Contents

Acknowledgements

First and foremost, I give thanks to my supervisor, Serban, for his incredible patience, encouragement, knowledge and most of all guidance throughout my time at UCLan. You have been the best supervisor and mentor to me, and I hope I have been a good student. Thank you for everything: for bearing with me when I couldn't quite grasp a concept and helping me understand the problems at hand, the great chats, rants, laughs, and without a shadow of a doubt, the best coffee in the department (cite me)! Thanks also to my second supervisor, Tim, who always had great perspectives to give. I could listen to a 'Tim monologue' every day, in particular about the best city in the land, Preston! Thank you as well to my third supervisor, Phil, your experience and wisdom were invaluable throughout this PhD. I couldn't have asked for a better supervisory team!

I also want to say thank you to my fellow basement dweller and desk neighbour, the one and only Jordan Cole, as well as the honorary basement dweller (even though he's a spaceman), the big man himself, Adam Hutchinson. You're my best buds and I couldn't have done this without you both. The countless stupid stuff we did, the rants we had, the takeaways we scronched and gaming nights will be remembered for a lifetime. I will always carry you both in any game we play and smash you in a 1vs1. I hope I have given to you what you have both given to me! Also, to Rob and Maria, it's been amazing to reconnect, take a break and spend time with you throughout writing this thesis and your support has not gone unnoticed! Also, Pete, I've known you for a minute, but our dance moves at Rob and Maria's wedding will go down in history (you still owe me a pint for golf).

An honourable mention to Lynn, Steve and Jo[2]. You allowed me and Eleanor to move into your home when times were very tough.

Last, but absolutely not least, I thank my loved ones (here comes the mush): Eleanor, you've been by my side every step of the way and carried me through even when I wanted to quit. I can't wait for our next adventure. I love you 3,000. Mum, Dad, Ella and Mr Chezzles you have supported me through everything, including this PhD. You've all always known what was best, whether it be a Kowloon and a games night, a phone call chatting crap about the world, or just a good old Chester snug. I could not have done this without any of you. I love you all very much.

I dedicate this thesis to you all

I now require a Nando’s

List of Figures

List of Tables

List of Abbreviations

ISTT	Interfacial spin-transfer torque
SOT	Spin-orbit torque
STT	Spin-transfer torque
DMI	Dzyaloshinskii-Moriya interaction
HM	Non-magnetic heavy metal
FM	Ferromagnetic
SkHA	Skyrmion Hall angle
SHE	Spin Hall effect
THE	Topological Hall effect
DW	Domain wall
STXM	Scanning transmission X-ray microscopy
XMCD	X-ray magnetic circular dichroism
BLS	Brillouin light scattering
EBL	Electron beam lithography
XRR	X-ray reflectivity
SAF	Synthetic antiferromagnet
SYF	Synthetic ferrimagnet
RKKY	Ruderman-Kittel-Kasuya-Yosida
GMR	Giant magnetoresistance
CPP	Current perpendicular-to-plane
RM	Racetrack memory
MTJ	Magnetic tunnel junction
LLG	Landau-Lifshitz-Gilbert
LLB	Landau-Lifshitz-Bloch
RK	Runge-Kutta
RKF	Runge-Kutta-Fehlberg
bbc	Body-centred cubic
fcc	Face-centred cubic

List of Symbols

$\boldsymbol{m}$	Normalised magnetisation	$\boldsymbol{J_c}$	Charge current vector
$\boldsymbol{M}$	Magnetisation	T_c	Curie temperature
$\boldsymbol{H}_{eff}$	Effective field term	$\boldsymbol{E}$	Electric field
α	Damping parameter	θ_{SHA}	Spin Hall angle
J_c	Charge current density	e	Electron charge
$\boldsymbol{T_S}$	Additional spin torques	λ_{sf}	Spin-flip length
M_S	Saturation magnetisation	$\boldsymbol{J}_s$	Spin current vector
μ_0	Vacuum magnetic permeability constant	$G^{\uparrow\downarrow}$	Complex spin-mixing conductance
g_r	Relative gyromagnetic factor	T	Temperature
γ_e	Electron gyromagnetic ratio	θ_{SkHA}	Skyrmion Hall angle
D_e	Election diffusion constant	$\theta_{SHA,eff}$	Effective spin Hall angle
λ_J	Exchange rotation length	r_G	Field-like spin-orbit torque coefficient
λ_ϕ	Spin dephasing length	D_{sk}	Skyrmion diameter
$\boldsymbol{S}$	Spin vector	G_r	Spin-mixing conductance ratio
β	Non-adiabaticity parameter	μ_B	Bohr magneton constant
$\boldsymbol{u}$	Spin-drift velocity	P	Polarisation
v	Skyrmion velocity	H	Applied magnetic field

*List of commonly use mathematical symbols

Publications by Author

MacKinnon, C. R., Lepadatu, S., Mercer, T., and Bissell, P. R. "Role of an additional interfacial spin-transfer torque for current-driven skyrmion dynamics in chiral magnetic layers" *Phys. Rev. B* **102**, 214408 (2020). DOI: https://doi.org/10.1103/PhysRevB.102.214408

MacKinnon, C. R., Zeissler, K., Finizio, S., Raabe, J., Marrows, C. H., Mercer, T., Bissell, P. R and Lepadatu, S. " Collective skyrmion motion under the influence of an additional interfacial spin-transfer torque". *Sci. Rep.* **12**, 10786 (2022). DOI: https://doi.org/10.1038/s41598-022-14969-2

Lepadatu, S., Mckenzie, G., Mercer, T., MacKinnon, C. R., and Bissell, P. R. "Computation of magnetization, exchange stiffness, anisotropy, and susceptibilities in large-scale systems using GPU-accelerated atomistic parallel Monte Carlo algorithms". J. Magn. Magn, Mater 540, 168460 (2021). DOI: https://doi.org/10.1016/j.jmmm.2021.168460

Presentations by Author

Oral Presentations

- Jeremiah Horrocks Institute Annual CARD Presentations (University of Central Lancashire, September 2020), title: “The interfacial spin-transfer torque in driving magnetic skyrmions”
- Jeremiah Horrocks Institute Annual CARD Presentations (University of Central Lancashire, September 2021), title: “The interfacial spin-transfer torque in driving a collection of skyrmions”
- IOP CRIM: Skyrmions (Online, 2021) (Micro-presentation), title: “Role of an additional interfacial spin-transfer torque for current-driven skyrmion dynamics in chiral magnetic layers”
- Jeremiah Horrocks Institute Annual CARD Presentations (University of Central Lancashire, September 2022), title: “The interfacial spin-transfer torque in driving magnetic skyrmions in SYF/SAF structures”
- Joint MMM-Intermag Conference (INTERMAG) (New Orleans, January 2022) (Online due to Covid), title: “Collective skyrmion motion under the influence of an additional interfacial spin-transfer torque”

Poster Presentations

- IOP Magnetism (University of York, 2022), title: “Collective skyrmion motion under the influence of an additional interfacial spin-transfer torque”
- IOP CRIM: Skyrmions (Online, 2021), title: “Role of an additional interfacial spin-transfer torque for current-driven skyrmion dynamics in chiral magnetic layers”
- Current Research In Magnetic Skyrmions (UKMag Soc, University of Central Lancashire 2022), title: “Collective skyrmion motion under the influence of the interfacial spin-transfer torque”

1 Introduction

1.1 Introduction and motivation

Magnetic skyrmions are topologically protected non-trivial spin textures with quasi-particle-like properties. Although skyrmions were predicted a long time ago, it is only in the recent decade that skyrmions have gained significant traction in the scientific community. This is not surprising when looking at the number of published articles containing the keyword *skyrmion*: up until 1990, there were only 116 publications, which rose to approximately 4,000 as of 2023 (according to the Web of Science database). This surge in the number of publications is not surprising however: not only are they very interesting from an industrial perspective due to their wide range of possibilities in applications for numerous technologies, but they also provide an interesting avenue from an academic perspective as they are still a relatively fresh scientific area.

The global demand for faster and larger information devices, such as data transfer and storage, respectively, as well as discovering more energy-efficient ways of moving information – in terms of computer bits – are important for the technological age we currently live in and also for the near future. The increased demand for technology devices such as home computers has surged from 13% in the mid-1980s up to a plateau of 88% in 2018. This does not include other devices such as phones and cameras to name just two. For example, to paraphrase, *the first moon landing was achieved with less computing power than a modern-day calculator*. Furthermore, devices are becoming smaller and faster with the number of transistors in devices following Moore's law which predicts the number of transistors doubles in devices every two years.

Magnetic skyrmions have a variety of potential applications in data transfer and storage devices; devices such as skyrmion racetrack memory (RM)[1–4] in which skyrmions are generally written by a write-head and then driven across a magnetic surface through a reading-head mechanism. They are based on a simple abacus. The devices typically vary by driving and reading method. Skyrmions also have applications based on logic devices[5,6], magnetic tunnel junctions (MTJs)[7–9] and neuromorphic computing[10,11].

This thesis presents a variety of skyrmion-based studies to advance the computational modelling of skyrmion motion by modelling a new torque: the interfacial spin-transfer torque (ISTT). Presented first is an investigation into isolated skyrmion motion, with the

inclusion of the ISTT alongside the spin-orbit torque (SOT), in a Co/Pt bilayer structure with cases of no roughness and included surface roughness. Furthermore, the spin-mixing conduction ratio between the real and imaginary components in ideal structures is investigated and determined. All skyrmion motion is then compared to literature and the Thiele model. These results allow some insight into the skyrmion mechanics as small skyrmion diameters at which the ISTT has a large effect.

The second study follows from the first study by investigating the skyrmion motion for a skyrmion collection – defined as a group of interacting skyrmions – in Pt/Co/Ir multilayers with landscape disorder in the form of surface roughness. The modelling results are then compared to experimental results obtained in collaboration with *The University of Leeds*, *Bragg Centre for Materials Research* and *Paul Scherrer Institut*. These results again allowed insight into the effect the ISTT has on skyrmion motion, especially at small diameters, but also experimentally validated the ISTT as a strong candidate as a skyrmion driver.

The third study progresses the thesis into the effect of a finite temperature, below the Curie temperature, on skyrmion motion in magnetic systems, in which the Monte Carlo algorithm is applied to obtain the Curie temperature of the systems. This study transitions from micromagnetic modelling to atomistic modelling. Furthermore, a new algorithm for tracking skyrmion motion is developed, as methods used in micromagnetic modelling were no longer applicable.

The final study involves the preliminary investigation into skyrmion motion in synthetic antiferromagnetic (SAF) and ferrimagnetic structures (SYF) under the influence of the SOT and ISTT. The structure modelled is Pt/Co/Ir/Co/Pt in which the upper layer of Co is varied in thickness, causing the balancing of the SAF into an SYF. Thus, the effect of the ISTT and varying the Co thickness are explored. Furthermore, an experimental system is proposed to isolate the ISTT to experimentally verify its existence.

To introduce this work, a research context is provided, beginning with a short history of magnetic skyrmions. A discussion of the methods for creation, stabilisation and annihilation which moves into the mechanism of driving skyrmions then follows. Finally, moving into the detection methods of skyrmions and their applications.

1.2 A brief history

Skyrmions were originally proposed by Skyrme[12,13] initially as a topological soliton in a pion field as a model of high-energy physics, however, unbeknownst to Skyrme this would affect and have many uses in other branches of physics, one of which is condensed matter. To that extent, even though skyrmions, as they are known now, were predicted by Skyrme in 1962, the field of skyrmionics – the study of skyrmions – did not gain much attention, as shown in the number of publications, until much later. The topologically non-trivial structure of a skyrmion can be distinguished by the characterising of the field. For magnetic systems, the topology quantifies how many times the local spins wrap a unit sphere given as, $\mathcal{W} = \frac{1}{4\pi}\int dxdy\, \boldsymbol{m} \cdot \left(\partial_x \boldsymbol{m} \times \partial_y \boldsymbol{m}\right)$. The topological nature of skyrmions is captured by the above equation and is deemed the winding number where $\boldsymbol{m}$ is the unit vector in the direction of the local magnetisation for a skyrmion occupying the *xy*-plane. For $\mathcal{W}$ = 1 an object exists with a skyrmion topology, whereas $\mathcal{W}$ = 0 results in uniform magnetisation. Interestingly, systems with a skyrmion topology are observed in systems including liquid crystals[14], quantum Hall systems[15] and Bose-Einstein condensates[16]. It wasn't until 1989, many years after Skyrme's publication, that skyrmions were predicted to exist in magnetic materials with competing interactions by Bogdanov and Yablonskii (1989)[17,18]. Up to this point, skyrmions were solely a theoretical postulate which had no experimental evidence or material-specific prediction that they could exist, and it was assumed that skyrmions could not form spontaneous ground states in magnetic materials. That was until a prediction of skyrmion stabilisation was made in 2006 in a helical magnetic MnSi[19]. It was shown within a phenomenological continuum model with few experimentally determined parameters that a spontaneous ground state skyrmion lattice not only existed in a large range of materials, including surfaces and thin films, but also bulk compounds where there was a lack of inversion symmetry such as B20 MnSi. Following this exceptional discovery, Mühlbauer *et al*. (2009)[20] conducted an experimental study on MnSi. Based on pressure-dependent MnSi parameter studies[21–23], an additional phase was discovered, namely the *A phase*, in which Bragg spots are located perpendicular to the applied magnetic field and displayed a six-fold symmetry. Further development was carried out, resulting in the conclusion that the Bragg spots observed in the *A phase* of MnSi was a chiral spin crystal. Finally, the skyrmion density was determined by the winding number, remembering that $\mathcal{W}$ = ±1 indicated a skyrmion topology. It was found that the winding number oscillated between $\mathcal{W}$ = -2 and $\mathcal{W}$ = 0.5,

however, when a unit cell was determined, the winding number summed to $\mathcal{W}$ = -1, thus the first experimental skyrmion was observed. This was quickly followed by further observation in the helical magnet $Fe_{0.5}Co_{0.5}Si$[24] and a change in nomenclature from the *A phase* to the *Skyrmion lattice phase*. What followed was a surge of skyrmion observations and development.

1.3 Skyrmions

When considering localised spin texture with forms like those shown in Figure 1-1, a clarification of these spin structures can be based on their topology, given by the winding number. A magnetic skyrmion is a localised spin texture with a form like that shown in Figure 1-1(b-d), since there is a variety of skyrmion-like spin textures, a stricter description is defined for this work which follows consensus[25,26]. Therefore, a skyrmion is defined as any spin structure with a central magnetic core which opposes the boundary magnetic moment direction and can be mapped to a unit sphere such that $\mathcal{W}$ = 1.

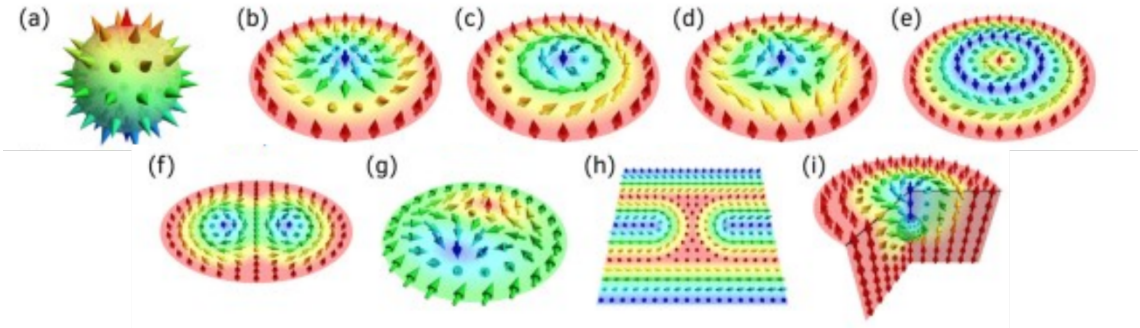

Figure 1-1 An array of topological spin textures with varying winding numbers. (a) Hedgehog, (b) Néel-skyrmion ($|\mathcal{W}|$ = 1), (c) Bloch-skyrmion ($|\mathcal{W}|$ = 1), (d) anti-skyrmion ($|\mathcal{W}|$ = 1), (e) skyrmionium (trivial), (f) biskyrmion ($|\mathcal{W}|$ = 2), (g) example of in-plane skyrmion ($|\mathcal{W}|$ = 1), (h) skyrmion in the helical background ($|\mathcal{W}||$ = 1), (i) chiral bobber. (a), (i) are 3D and thus determining the winding number does not apply. Image accreditation – Ref.[26].

Focused in this work are Néel-skyrmions realised in magnetic thin-film systems in which for an out-of-plane magnetised thin film the central core of a skyrmion opposes the bulk magnetisation of the thin film. At the circular boundary of the skyrmion, all spins point opposite the core and in the direction of the thin-film magnetisation. Traversing the diameter of the skyrmion through the central core, there is a continual rotation of the spins about 360º, the chirality of which is dependent on the Dzyaloshinskii-Moriya interaction (DMI)[27,28]. Beyond the standard spin structures such as skyrmion-type spin textures, a

range of other spin textures have been discussed: skyrmionium, in Figure 1-1(e), consisting of a large base skyrmion with a much smaller skyrmion of opposite chirality[29–31]; biskyrmions, in Figure 1-1(f), which can be considered as a bound pair of skyrmions with a winding number, $\mathcal{W} = 2$, each with oppositely non-central core spiralling spins[32–34]; in-plane skyrmion, in Figure 1-1(g), in which there is a mirror symmetry in the x-axis but not in the y-axis. A simple description is a vortex and anti-vortex pair[35–37]; Skyrmion in a helical background, in Figure 1-1(h), in which a helical background provides a natural channel along which a skyrmion can traverse rapidly[38–40]; Chiral bobber, in Figure 1-1(i), which is a localised 3D magnetisation configuration, terminated by a Bloch-point[41–43]. They can be considered skyrmion tubes with a finite length. Note for any twisting magnetic spin texture there is always at least one interaction that favours alignment of neighbouring spins, such as the exchange interaction or anisotropy, and one that favours a continual rotation of neighbouring spins such as the DMI. The topic of skyrmions does not simply open up to study a skyrmion's characteristics in magnetic materials; as discussed above, there can be many types of skyrmion-type spin textures but also non-trivial spin textures.

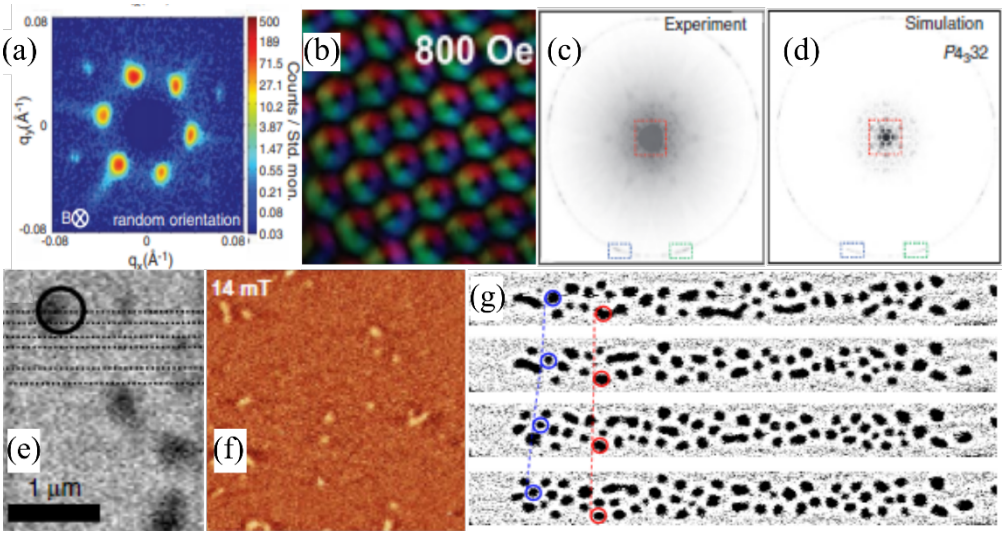

Figure 1-2 Images of skyrmion spin structures using different bulk and thin film materials. Scale is not consistent for all images. Bloch-skyrmions are shown in (a)-(d) and Néel-skyrmions in (e)-(g). Bloch-skyrmions present in bulk (a) MnSi, (b) Cu_2OSeO_3, (c) $Co_8Zn_9Mn_4$ and (d) simulation of $P4_332$ space group. Néel-skyrmions are shown in (e) Ta/Pt/$[Pt/CoB/Ir]_x$Pt, (f) Ni/Co/Ni, symmetric stacks and (g) a series of skyrmion images in Pt/Co/Ir progressing in time down each image. Current direction towards the left. Images are adapted for (a) from Ref. [20], (b) from Ref. [51], (c, d) from Ref. [57], (e) from Ref. [69], (f) from Ref. [74] and (g) from Ref. [75].

1.4 Verification of skyrmions

Material science has also developed significantly with the evolution of skyrmions due to the dependence on several interactions and conditions. Much effort has been put into material research that allows for the stabilisation of skyrmions, such as the DMI and anisotropy, as well as the thickness of magnetic systems, as Bloch-skyrmions and Néel-skyrmions are realised in bulk and thin film structures, respectively, some of which are shown in Figure 1-2. The former is mainly found in bulk (> 15 nm) materials favoured by the lack of inversion symmetry which breaks the standard bulk DMI and has been observed in bulk MnSi[20,44–46], Cu_2OSeO_3[47–52], FeGe[53] and $Co_8Zn_9Mn_3$[54] where for thin films observations of MnSi (~ 50 nm)[55], Cu_2OSeO_3 (~ 150 nm)[51,56], $Co_8Zn_9Mn_4$ (~ 150 nm)[57] and $FeCo_{0.5}Rh_{0.5}Mo_3N$ (110 nm)[58] have also shown Bloch-skyrmions. The latter is characteristic of interfacial DMI. The interfacial effect can also play a significant role in spin-texture development, for example, a magnetic layer interfaced with a heavy metal layer of sufficient thickness and strong spin-orbit coupling, such as Pt, can cause a strong interfacial DMI, as shown in Figure 1-4(c). Néel-skyrmions have been observed in thin films such as PdFe/Ir[59–64], $[Pt/Co/Ta]_x$ [65–67] and Pt/Co/Ir[68–71] with more complex structures such as Pt/GdFeCo/MgO[72], Ta/CoFeB/TaO_x[73] and Ta/Pt/$[Pt/CoB/Ir]_xPt$[74] as well as symmetric stacks[75,76]. A very common structure that is used involves a Co/Pt interface which exhibits strong DMI and spin-orbit coupling through the interface[77,78], due to this Co/Pt interface is exclusively investigated in this work.

1.5 Skyrmion temperature dependence

On the other hand, with the increased research into material and structure composition, as discussed above, there has also been a significant drive into skyrmion stabilisation at larger temperatures more akin to room temperature. It is well documented that skyrmions are to be the next large innovation in storage devices, however, this will never be released if skyrmions can not be stabilised at ambient temperatures. We know from the Curie law that for temperatures far below the Curie temperature, a magnetic material holds magnetisation well, however, when close to the Curie temperature, the material loses its permanent magnetic properties. Herein lies an issue: due to thermal fluctuations, skyrmions have the potential to spontaneously generate and annihilate. A generic phase diagram for skyrmion hosting materials is shown in Figure 1-3(b), which is akin to the *A*

phase found in MnSi. Much of the early skyrmion study occurred for temperatures far below room temperature (< 300 K), especially in bulk materials resulting in Bloch-skyrmions[20,44–52], however, Bloch-skyrmions have been observed at larger temperatures [53,54]. Conversely, Néel-skyrmions have a much larger range of stabilisation temperatures (50 K – 300 K)[65,68,79–82] due to the DMI inverse dependence on thickness in bilayer structures when interfaced with heavy metal (HM). Quessab *et al.* (2020)[83] show that as thickness decreases, in a Pt/CoGd system, the interfacial effects become more important and the DMI increases. Over the entire range of thickness studied, the interfacial effects were significant. This is partly why skyrmions in ferromagnetic (FM)/HM systems can be stabilised at these larger temperatures, however, this is usually accompanied by an applied magnetic field opposing the core of the skyrmion. Woo *et al.* (2016)[65] observed a wide range of spin textures including skyrmions in 400 nm Pt/Co/Ta disks. Furthermore, an excellent description of the importance of DMI in skyrmion stability was devised, shown in Figure 1-3(a), which shows a phase diagram of DMI strength as a relationship of magnetisation and predicts the type of spin structure as set values.

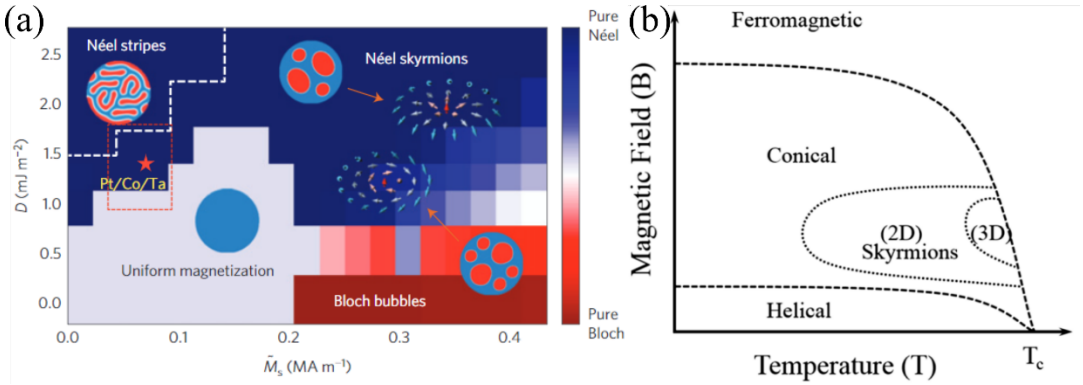

Figure 1-3 Magnetic equilibrium states. (a) DMI strength as a function of the magnetisation saturation for Pt/Co/Ta thin-film disks. The colour scale represents the spin-structure type from Bloch to Néel. (b) A generic magnetic phase diagram for materials hosting skyrmions up to the Curie temperature. Images adapted from (a) Ref.[65] and (b) Ref.[84].

1.6 Nucleation of skyrmions

A material's ability to host magnetic skyrmions is a very important characteristic of a skyrmionic system, however, skyrmions typically need a *helping hand* to be generated. There have been many methods of generating and annihilation skyrmions purposed both voluntarily, through magnetic fields and spin torques, and involuntarily, such as nucleation at a strong pinning site under a driving force.

Generating skyrmions by utilising a magnetic field is a common method of creating and stabilising skyrmions. By appropriately tuning the applied magnetic field, the spin textures in a material can reach its lowest energy for that system. This can be seen in Figure 1-3(b) where spin textures are dependent on the applied magnetic field allowing skyrmions to be dialled into. Thus, skyrmions can spontaneously form directly due to the material parameters and applied magnetic being in the perfect balance, or, form as a result of a phase change in the system from a stripe domain or Bloch bubble. Localised fields have also been shown to nucleate skyrmions using magnetic force microscopy tips which can be accomplished as the probe stray field interacts with existing domain structures resulting in a contraction into a skyrmion without an increase in external field strength[85].

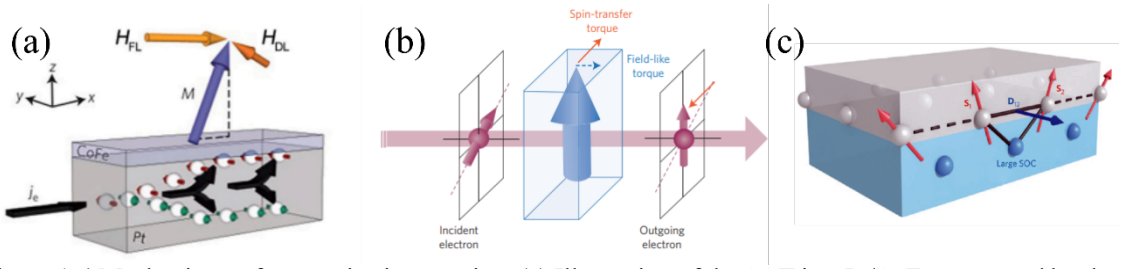

Figure 1-4 Mechanisms of magnetisation rotation. (a) Illustration of the SOT in a Pt/CoFe, governed by the SHE in the Pt layer creating a pure spin current. (b) A spin-polarised current is injected into an FM layer. The incident electron interacts with the magnetisation causing an alignment of the spin to the magnetisation resulting in a field-like torque and a rotation for the magnetisation. The red and blue arrows represent spin and magnetisation, respectively. (c) Sketch of the interfacial DMI at an HM/FM interface with strong spin-orbit coupling in the HM layer. Ref.[105] for (a) Ref.[106] for (b) and Ref.[107] for (c).

Spin torques are another method of generating skyrmions mainly due to being an effective manipulator of skyrmion motion, such as the SOT, therefore methods for nucleation of skyrmions have been devised[19,63,86–89]. Spin torques utilise spin currents which can accumulate causing local rotation of the magnetisation in an FM material due to the conservation of total angular momentum. Similar to generating skyrmions via a phase change utilising a magnetic field, Liu *et al.* (2020)[90] demonstrated that the SOT resulted in a local rotation of the magnetisation. For a Pt/Co/Ir system with a stripe domain equilibrium state, injection of spin current results in a dissection of the stripe domain into a skyrmion lattice state. To date, using spin torques through current pulse is a very common method and used widely[74,75,91–94].

There are other methods for skyrmion creation, but for brevity, not all will be discussed. To name a few, further methods include: using temperature[95,96], joule heating[97], laser

pulse[98,99] and surface acoustic waves[100]. Furthermore, electric fields[101–104] inducing strain in a material resulting in altered DMI and anisotropy parameter can also be incorporated to generate skyrmions.

1.7 Moving skyrmions

As will be discussed in detail in later chapters, driving skyrmions is fundamental if they are deemed for future spintronics devices. Following is a discussion on the method of driving Néel-skyrmions in ultra-thin magnetic films using spin torques such as the spin-orbit and spin-transfer torques. Other methods of driving skyrmions and other spin-textures exist but are not discussed due to their relevance to this work which includes driving via electric fields, magnetic field gradients, spin-waves, temperature gradients and thermal fluctuations.

Spin torques are the most widely used method for driving skyrmions in thin films which are induced by a polarised spin current which has the effect of rotating the magnetisation and thus moving magnetic textures such as domain walls, vortex domains and skyrmions. Interestingly, from both a dynamic and application point of view, spin torque-driven skyrmions experience a transverse motion resulting in a deviation from the required path, parallel to the applied current direction. This motion is due to the topological Magnus effect, similar to the macroscopic Magnus effect on a ball. The reaction of the skyrmion to this Magnus force results in a trajectory towards the boundary of the material, which is well documented by both experimental and computation observation, and is deemed the skyrmion Hall effect. Regardless, the transverse motion that skyrmions obtain is not ideal for future applications as it leads to the inevitability of annihilating skyrmions at the boundary of materials, thus skyrmion motion with an eliminated Magus effect is a necessity. Therefore, the angle of deviation between an applied current and transfer skyrmion motion, otherwise known as the skyrmion Hall angle (SkHA), should be negligible.

An approach to eliminating the SkHA is with the use of coupled skyrmions in SAF and SYF structures consisting of two ferromagnetic layers, or opposite magnetisation, coupled through a spacer layer via the Ruderman-Kittel-Kasuya-Yosida (RKKY) interaction, resulting in an effective antiferromagnet when both FM layers are balanced and ferrimagnet when unbalanced. The benefit of an SAF structure is the net elimination

of the Magnus force effect as the coupled skyrmions in the FM layers have equal and opposite transverse motion, thus eliminating the SkHA. However, experimental observation of skyrmions in SAF structures is difficult due to the lack of a net magnetic moment to measure, so it is typical to unbalance the SAF into an SYF, resulting in a net moment and slight skyrmion Hall angle.

Even though the spin-transfer torques were predicted to move domain walls[108,109] and then observed experimentally[110,111], spin-transfer torques (STTs) did not gain significant traction due to the massive applied currents required. A visualisation of the STT is shown in Figure 1-4(b), in which a spin-polarised current is injected into an FM layer. The electron spin interacts with the local magnetisation and aligns with the direction of magnetisation, resulting in a slight change in direction of the magnetisation and thus an STT. The study was then advanced by the discovery of giant magnetoresistance (GMR)[112,113] by Grünberg and Fert groups in particular with current flow perpendicular to the plane (CPP) of magnetic multilayers, however, arguably the most significant studies came from Slonczewksi[114,115] and Berger[116,117] who discovered that CPP in multilayers generated significant STT to rotate the magnetisation in a layer. For STT-driven skyrmions in magnetic multilayers, the FM layers are thin, resulting in small bulk STT contribution. Compared to the SOT rising from the HM/FM interface in materials with strong spin-orbit coupling, the bulk STT is typically overpowered by the SOT. However, there have been studies suggesting that STT could theoretically drive skyrmions solely[118–122]. There have been vigorous mathematical studies into modelling the STT contribution which has been achieved through the use of adiabaticity and non-adiabaticity parameters, the most notable being by Zhang-Li STT[123,124].

This thesis studies the effect of an interfacial STT[94,125,126] which is mathematically similar to the Zhang-Li bulk STT, this being small in thin layers, however, due to an inverse relationship on FM thickness, the ISTT can have a significant contribution to skyrmion movement given there is a sharp enough magnetisation gradient.

The SOT is widely accepted to be the most significant contribution to skyrmion motion when driven by an applied current. It is governed by the spin Hall effect (SHE) which results in a spin accumulation, at lateral boundaries of a current-carrying material due to both extrinsic effects such as spin-dependent Mott – spin diffusion in opposite direction due to a collision with impurities – and intrinsic effects due to the spin-orbit interaction

as a consequence of asymmetry in the material. The SHE is prominent in Pt, Ta and W[127,128]. The asymmetry leads to a deflection of spin-up and -down electrons in opposite directions leading to the transverse spin current. The spin current produced by the SHE is orthogonal to the charge current and spin polarisation with the transverse components being absorbed in the interface of an HM/FM layer resulting in the SOT, thus a transfer of angular momentum to the magnetisation of the FM layer; this is shown as an illustration in Figure 1-4(a). Therefore, this effect can be significant in the dynamics of skyrmion and other spin texture. Reversal of the magnetisation due to SOTs has been observed[129,130] in CoFeB[131,132] and Pt/Co/AlO_x[133,134] as well as domain wall motion in Ta/CoFeB/MgO[130,135] and Ta/CoFe[136].

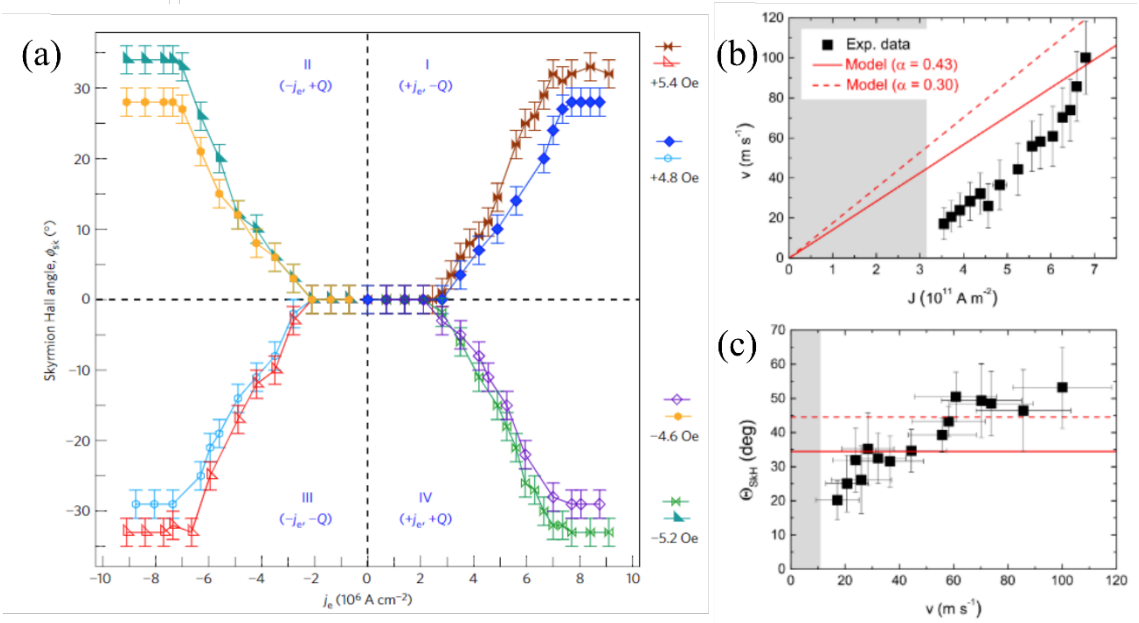

Figure 1-5 (a) Phase diagram of the skyrmion Hall angle as a function of applied current density (sign signifies direction). Several tens of skyrmions were tracking in as a subset of a larger sample. Skyrmion diameters ranged from D_{sk} = 800 nm to 1,100 nm. (b) The velocity as a function of applied current in Pt/Co/MgO. (c) The SkHA as a function of velocity. The black point shows experimental data with red lines showing the predicted Thiele motion with different damping parameters. Images adapted from Ref.[143] for (a) and Ref.[144] for (b,c).

Skyrmion motion under the influence of SOTs was first observed, at room temperature, in Pt/Co/Ta and Pt/CoFeB/MgO by Woo *et al.* (2016)[65] with an applied field for stabilisation. Velocity is dependent on applied current strength, however, velocities < 1 ms^{-1} and > 50 ms^{-1} have been shown which resulted in skyrmion motion regimes being defined based on velocity and motion characteristics, namely, pinned, creep and flow

regimes. The pinned regime describes skyrmion that does not have the required driving force to overcome the local energy landscape; the creep regime describes a skyrmion in motion with a heavily distorted path as it sporadically *jumps* between local pinning sites; and the flow regime, in which a skyrmion has a significant driving force so it is minimal effect by the local energy landscape. The regimes are evident in Figure 1-5(a) which shows how the SkHA varies with applied current strength. For driving current, there is no SkHA as the skyrmions are pinned, then with increasing current, the SkHA linearly increases, which indicates the flow regime. In this case, the creep regime range is small. These regimes have been well documented experimentally as well as through vigorous theoretical predictions[137–142]. To this extent, the driving force, or applied current density, has been observed to vary the SkHA significantly[74,143,144] which is not reproduced by any analytical models in ideal structures as seen in Figure 1-5(b, c).

While material imperfections play a very important role, there are many gaps in the literature, and a full understanding of how the SkHA varies with driving strength, skyrmion diameter, skyrmion chirality, and varying levels of magnetic and non-magnetic imperfections is required. In recent experimental work, a SkHA largely independent of skyrmion diameter has been observed[74]; however, analytical results based on the Thiele equation predict a significant increase in SkHA with decreasing skyrmion diameter, and this discrepancy is significantly pronounced for small diameters below 100 nm. In another study[73], experimental results were also compared to modelling based on SOT for very large skyrmions with diameters above 800 nm. Experimental results and SOT simulations show good agreement for large skyrmion diameters, which showed slightly larger SkHA value for the SOT model; however, the SOT model predictions deviate significantly from the experimental results at small skyrmion diameters[74] even when very large damping values are assumed.

1.8 Damping inconsistencies

In recent work, the SkHA was investigated in Pt(3 nm)/Co(1.2 nm)/MgO(1.5 nm) multilayered tracks, also as a function of skyrmion diameter, and using skyrmion collections[145]. The experimental results are remarkably similar to those shown here, also showing small SkHA values, nearly independent of skyrmion diameter and small velocities under 10 ms^{-1}. Previous works on multilayers incorporating HM/FM layers, e.g. Pt(3 nm)/Co(0.9 nm)[144] and Pt(3.2 nm)/CoFeB(0.7 nm)[79], have also shown small

SkHA values at skyrmion diameters ~ 100 nm to 150 nm. Similarly in Ref.[146], low SkHA values were obtained (average ~ 15.2°) in Pt(2.7 nm)/CoFeB(0.86 nm)/MgO(1.5 nm) multilayers, with skyrmion diameters ~ 150 nm. These values could be reproduced by SOT-only modelling, only by assuming very large damping values, up to $\alpha = 0.5$. This results[94] in the SOT-only SkHA values closer to those found in experiments, however, a monotonic increase in SkHA with decreasing diameter persists, with discrepancies remaining for sub-100 nm diameter skyrmions. Moreover, a large body of work with measurements of damping in ultra-thin Co, CoB and CoFe films interfaced with Pt, reveal values of $\alpha \cong 0.1$ and lower[74,145,147–157], for typical FM layer thicknesses used for skyrmion studies. With an emerging consensus pointing to damping values $\alpha < 0.1$, large quantitative discrepancies would arise between experimental SkHA values[79,144,146] and SOT-only modelling, particularly for small skyrmion diameters. The large values of damping used in these works are derived from domain wall mobility measurements, for example, as shown in Ref.[158], although some experimental evidence for large damping values was also obtained for Pt/Co/Pt trilayers in Ref.[159]. These damping values, however, stand in sharp contrast with those obtained from other measurement techniques. For example, in Ref.[145], FMR measurements have shown $\alpha = 0.05$, for Co(1.2 nm) on Pt(3 nm). Other FMR measurements were obtained α in the range of 0.02 to 0.1 for stacks containing Co with thickness in the range of 1.1 nm down to 0.6 nm respectively, on Pt(3 nm)[157], $\alpha = 0.03$ for $[\text{Pt(1.5 nm)/Co(1 nm)/W(1.5 nm)}]_N$[147], $\alpha = 0.02$ for $[\text{Co(0.5 nm)/Pt(0.3 nm)}]_{\times 6}$[156], $\alpha < 0.1$ for $[\text{Co(1.4 nm)/Pt(1 nm)}]_8$[148].

Spin-torque FMR measurements on stacks incorporating Co(1 nm)/Pt(4 nm) and CoFe(1 nm)/Pt(4 nm) have obtained $\alpha < 0.1$[151]. Brillouin light scattering (BLS) measurements on Pt(2 nm)/Co(0.6 nm – 3.6 nm)/Ir(2 nm), have shown $\alpha < 0.1$[150]. Time-resolved magneto-optical Kerr effect measurements have shown α between 0.1 and 0.13 for $[\text{Co(0.4 nm)/Pt(0.8 nm)}]_N$[149], whilst values in the range 0.03 to 0.06 were obtained for Pt(3 nm)/Co(0.8 nm)/HM trilayers (HM = W, Ta, Pd)[153]. In stacks containing Pt(2.7 nm)/CoB(0.8 nm)/Ir(0.4 nm), as in the current work, we've also previously determined $\alpha = 0.07$ by analysing larger diameter skyrmions[74]. A review of experimental results on damping in ferromagnetic thin films and multilayers is found in Ref.[160].

At large skyrmion diameters, the SOT-only model is close to the full spin torque model in terms of SkHA, and SOT-only modelling can reproduce experimental values in this

diameter range with realistic damping values. Thus, in Ref.[143], skyrmion diameters were ~ 800 nm and larger, and experimental SkHA values were close to those obtained from SOT-only modelling with $\alpha = 0.02$, in Ta(5 nm)/CoFeB(1.1 nm).

1.9 Skyrmion applications

Up to this point, magnetic textures such as skyrmions have been explored. More specifically, the method of generating skyrmions and driving skyrmions has led to the development of skyrmion-based applications from theoretical predictions. Following is a summary of skyrmionic devices suitable for the industry. Early device prediction will be explored, as well as current technologies, furthermore, future theoretical devices will be discussed. Skyrmions possess improved features compared to domain walls with the most exciting being the significant reduction in the energy required to move them in thin films, as well as their ability to traverse material defects which have led to a large push in applied research.

The most renowned technology is skyrmions in racetrack technology which has already been realised and involves the alignment of skyrmions in a long wire, however, this technology was originally developed for domain walls (DWs), but the advancement of STT and SOT has proven very beneficial from skyrmions development. Domain wall RM was theorised by Parkin *et al.* (2008)[161] by using an array of magnetic nano-wires arranged on a silicon chip. Each wire would hold individual reading and writing devices which are used to modify or read a line of DWs representing '0' and '1' bits. Figure 1-6(a) shows the theorised racetrack device in vertical construction. A current is applied to the wire which causes all DWs to traverse along the wire through a read or write phase depending on what is required.

However, DWs pose certain issues, such as: constant connection with the boundary of a carrying medium leading to significant effects due to defects at the edges and requiring a significant driving force to traverse along the wire. Skyrmions can overcome these issues of RM with skyrmion RM, as shown in Figure 1-6(f), as they are free objects within a magnetic media – stable with no boundary connections. Skyrmion RM consisted of an ordered line of skyrmions separated by fixed distances. The present skyrmions can then act as information carriers. Skyrmions overcome the issues of DWs as they possess the ability to transverse around pinning sites as well as require a significantly reduced driving

strength. This was shown by Zhang *et al.* (2016)[2] experimentally however it was also shown that skyrmions can annihilate at regions with surface defects or severe surface roughness. The main issue with skyrmion RM is due to the effect of the SOT and STT, namely, the SkHA where skyrmions deviate from the applied current direction as discussed earlier, which not only leads to interaction with the boundaries of the material, but can result in a non-uniformity of skyrmion-skyrmion separation resulting in a large read error rate.

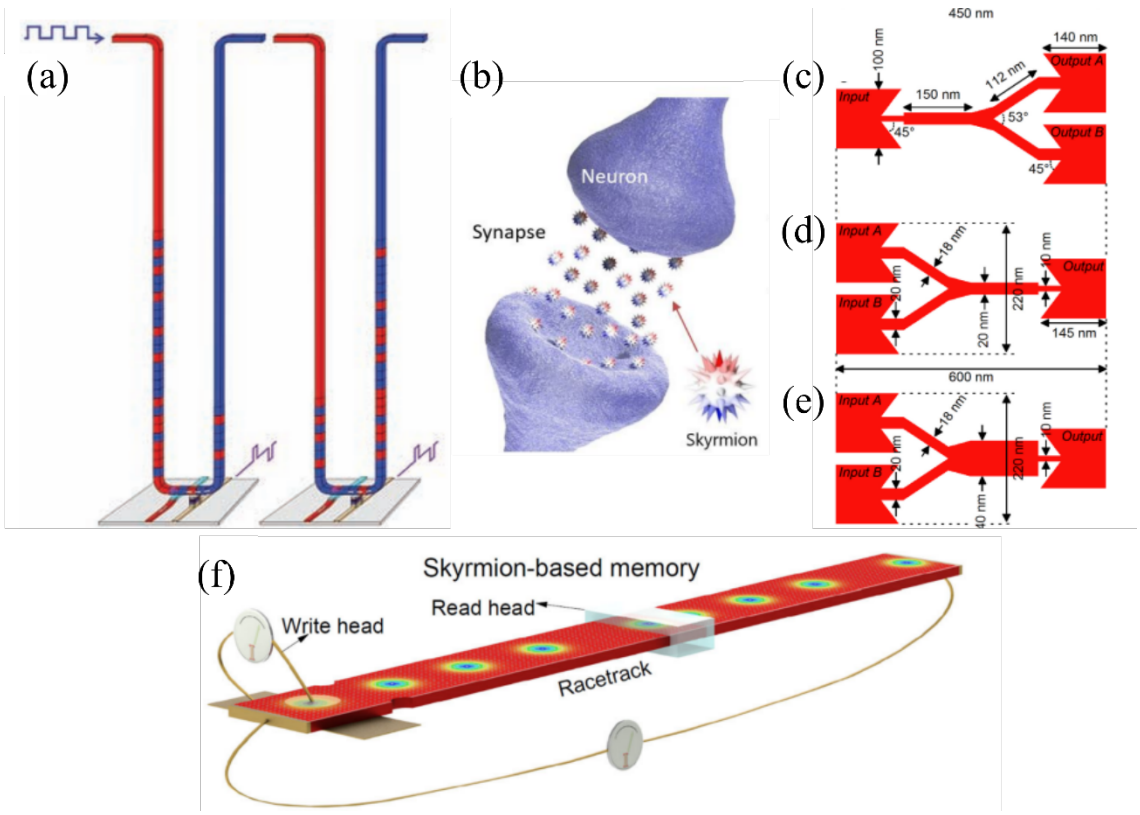

Figure 1-6 Applications for current and future skyrmionics devices. (a) A vertical configuration of a single node of RM. The red and blue stripes represent DWs opposite in orientation which are moved by an applied current through read and write devices at the bottom of the 'U' track. (b) Schematic of an artificial skyrmion-based synapse. (c-e) Logic gates for (c) duplication of a skyrmion, (d) logical OR gate and (e) logical AND gate. (f) A proposed skyrmion racetrack. Data is encoded by a chain of magnetic skyrmions. Images adapted from Ref.[161] for (a), Ref.[162] for (b), Ref.[5] for (c-e) and Ref.[84] for (f).

The ability to read skyrmions in RM is paramount with multiple methods devised. A promising method is electrical reading by harnessing the topological Hall effect (THE)[46,53,163,164] arising from a charge carrier interacting with an emergent magnetic field, through a skyrmion. The transverse deflection of charge carriers with the emergent magnetic fields results in the THE. The THE was shown to have a large electrical signal

for skyrmion lattices, however, isolated skyrmions were also demonstrated to have a signal through electrical Hall measurement[84,91,165]. Furthermore, Hall conductance measurements[166] have shown peaks and reductions when a skyrmion is present and vacant, respectively. Another method utilises MTJs by measuring the magnetoresistance[166–169] with signals representing present skyrmions at the MTJ. This was proposed by Tomasselo *et al.* (2017)[169] by measuring the tunnel magnetoresistance in an MTJ.

Table 1-1 Logic gate operations on a skyrmion. For a skyrmion representing a '1' bit and the lack of a skyrmion representing a '0' bit, i.e. for a set of inputs with a skyrmion in input 1 and a blank in input 2. The result of an *AND* operation is 0 and *OR* is 1.

Input 1	Input 2	*AND* result	*OR* result
0	0	0	0
0	1	0	1
1	0	0	1
1	1	1	1

Many other applications have been suggested and demonstrated using skyrmions by utilising their stability, low energy requirements and small size. A field that has a lot of attention at the moment is neuromorphic computing[170] which is inspired by the brain's natural ability to compute massive workloads to a high degree of accuracy with minimal energy required. Artificial skyrmionics synapses[11] were shown micromagnetically by Grollier *et al.* (2016)[170] and later it was shown skyrmions could mimic the potentiation and depression behaviour of biological synapses experimentally by Song *et al.* (2020)[162]. A visualisation of a skyrmionics synapse is shown in Figure 1-6(b). This has logical progression in the skyrmion neural networks[171,172]. Further advancement into information carrying via skyrmion motion has resulted in logical gate operations. Logic operators such as *AND* and *OR*, Figure 1-6(c-e), allow a skyrmion representing a '1' bit to be manipulated which is shown in Table 1-1.

1.10 Modelling skyrmions

In the study of magnetism the development of tools such as micromagnetic software rapidly progressed the field. Micromagnetic software has aided research massively post-1998 as before this the Landau-Lifshitz-Gilbert (LLG) had to be solved numerically which was difficult to achieve for complex systems. Micromagnetic and atomistic modelling allows for quantum- to macro-scale magnetisation studies to occur without the absolute requirement of expensive and time-consuming experimental methods to synthesise magnetic systems and then validation of the structure and also to proceed with the intended experimental process for a given hypothesis. The experimental process can take upwards of months to fully complete, whereas modelling can take a matter of hours.

Modelling spintronic devices, like those in this thesis, the phenomenological LLG equation, or some slight variation, see Chapter 2, is solved using methods such as the Runge-Kutta (RK) methods in the picoseconds timescale range. The diversity of the LLG is quite astonishing due to the additions that can be incorporated to model different effects. For example, additional torques describing the effect of spin current on magnetisation can be incorporated, namely the SOT, or the inclusion of thermal fluctuations to model the effect of temperature with the use of the stochastic LLG or Landau-Lifshitz-Bloch (LLB) equation. Furthermore, simplification can be made to ease resource use for simple problems such as finding an equilibrium state of a system. In Chapter 2 & 3, different variations on the LLG are discussed, as well as different methods of solving the magnetisation equations of motion. Another benefit of micromagnetic modelling is the number of magnetic interactions that can be included, such as the exchange interaction, dipole-dipole interaction, magnetocrystalline anisotropy and DMI, to name a few. This allows a unique perspective into these types of interactions as each can be individually tuned as well as completely negated which, although physically impossible, allows for a great insight into magnetic mechanisms.

Micromagnetic modelling has allowed for a more accessible method of understanding magnetic system dynamics compared to solving the LLG numerically: not only for designing simulations but also for simulation total time, however, other more advanced software is now freely available. In modern micromagnetic software, alongside the backend equation of motion solvers that provide the data, is a graphical interface that visualises the magnetic system in question. The most notable are: Object Oriented

Micromagnetic Framework (OOMMF)[173] (1998), Magpar[174] (2003), Nmag[175] (2007), Mumax[176] (2014), Mumax[177] (2015) and Grace (2015). Throughout this thesis, *Boris Computational Spintronics*[178,179] (2019) is used due to its multifunctional nature as it allows for different magnetisation equations of motion including the LLG, stochastic LLG and LLB which can be solved via many methods by utilising not only the central processing unit (CPU) but also the graphics processing unit (GPU). Furthermore, it includes in-depth design capabilities for magnetic systems as well as accurate methods of tracking skyrmion motion. Alongside the graphical visualisation of magnetisation dynamics, this then allows for direct comparisons between modelling results and experimental observations. Due to this, micromagnetic modelling now goes hand in hand with experimental observations.

1.11 Summary

This thesis focuses on skyrmion dynamics under the influence of the interfacial spin-transfer torque (ISTT). In Chapter 2, the fundamental theory of modelling skyrmions including the LLG, drift-diffusion model, magnetic effects and the ISTT are discussed and implemented in *Boris Computational Spintronics*. In Chapter 3, the methods and techniques involved throughout this work are explored, including methods of solving the LLG, data acquisition, skyrmion tracking and the experimental processes used. This is followed by four results chapters. In Chapter 4, isolated skyrmion motion under the influence of the ISTT is investigated, with and without surface roughness. In Chapter 5, collective skyrmion motion is investigated. In Chapter 6, the study of isolated skyrmion motion with the inclusion of a stochastic thermal field is shown. In Chapter 7, the foundations for further development are introduced for skyrmion motion in synthetic antiferromagnetic and ferromagnetic structures. Finally, Chapter 8 concludes this thesis and discusses possible further work.

Chapter References

1. Kang, W. *et al.* Voltage controlled magnetic skyrmion motion for racetrack memory. *Sci Rep* **6**, (2016).

2. Zhang, X. *et al.* Skyrmion-skyrmion and skyrmion-edge repulsions in skyrmion-based racetrack memory. *Sci Rep* **5**, (2015).

3. Zhang, S. L. *et al.* Manipulation of skyrmion motion by magnetic field gradients. *Nat Commun* **9**, (2018).

4. Tomasello, R. *et al.* A strategy for the design of skyrmion racetrack memories. *Sci Rep* **4**, 6784 (2014).

5. Zhang, X., Ezawa, M. & Zhou, Y. Magnetic skyrmion logic gates: Conversion, duplication and merging of skyrmions. *Sci Rep* **5**, 9400 (2015).

6. Tang, C. *et al.* Effects of temperature and structural geometries on a skyrmion logic gate. *IEEE Transactions on Electron Devices*, **69**, 1706-1712 (2022)

7. Sheng, Q. *et al.* Realization of skyrmion subtracter and diverter in a voltage-gated synthetic antiferromagnetic racetrack. *J Appl Phys* **125**, 064502 (2019).

8. Li, S. *et al.* Experimental demonstration of skyrmionic magnetic tunnel junction at room temperature. *Sci Bull (Beijing)* **67**, 691–699 (2022).

9. Zhang, X. *et al.* Skyrmions in Magnetic Tunnel Junctions. *ACS Appl Mater Interfaces* **10**, 16887–16892 (2018).

10. Song, K. M. *et al.* Skyrmion-based artificial synapses for neuromorphic computing. *Nat Electron* **3**, 148–155 (2020).

11. Yokouchi, T. *et al.* Pattern recognition with neuromorphic computing using magnetic field-induced dynamics of skyrmions. *Sci Adv* **8**, 5652 (2022).

12. Skyrme, T. H. R. A unified field theory of mesons and baryons. *Nuclear Physics* **31**, 556–569 (1962).

13. Skyrme, T. H. R. A non-linear field theory. *Proc R Soc Lond A Math Phys Sci* **260**, 127–138 (1961).

14. Wright, D. C. & Mermin, N. D. Crystalline liquids: the blue phases. *Rev Mod Phys* **61**, 385 (1989).

15. Sondhi, S. L., Karlhede, A., Kivelson, S. A. & Rezayi, E. H. Skyrmions and the crossover from the integer to fractional quantum Hall effect at small Zeeman energies. *Phys Rev B* **47**, 16419 (1993).

16. Ho, T. L. Spinor Bose Condensates in Optical Traps. *Phys Rev Lett* **81**, 742 (1998).

17. Bogdanov, A. N. & Yablonskii, D. A. Contribution to the theory of inhomogeneous states of magnets in the region of magnetic-field-induced phase transitions. Mixed state of antiferromagnets. *Zh. Eskp. Teor. Fiz* **96**, 253–260 (1989).

18. Bogdanov, A. N. & Yablonskii, D. A. Thermodynamically stable vortices in magnetically ordered crystals. *Zh. Eksp. Teor. Fiz* **95**, 178–182 (1989).

19. Rößler, U. K., Bogdanov, A. N. & Pfleiderer, C. Spontaneous skyrmion ground states in magnetic metals. *Nature* **442**, 797–801 (2006).

20. Mühlbauer, S. *et al.* Skyrmion Lattice in a Chiral Magnet. *Science (1979)* **323**, 915–919 (2009).

21. Pfleiderer, C., Julian, S. R. & Lonzarich, G. G. Non-Fermi-liquid nature of the normal state of itinerant-electron ferromagnets. *Nature* **414**, 427–430 (2001).

22. Pfleiderer, C. *et al.* Partial order in the non-Fermi-liquid phase of MnSi. *Nature* **427**, 227–231 (2004).

23. Pfleiderer, C., Böni, P., Keller, T., Rößler, U. K. & Rosch, A. Non-Fermi Liquid Metal Without Quantum Criticality. *Science (1979)* **316**, 1871–1874 (2007).

24. Yu, X. Z. *et al.* Real-space observation of a two-dimensional skyrmion crystal. *Nature* **465**, 901–904 (2010).

25. Marrows, C. H. & Zeissler, K. Perspective on skyrmion spintronics. *Appl Phys Lett* **119**, 250502 (2021).

26. Everschor-Sitte, K., Masell, J., Reeve, R. M. & Kläui, M. Perspective: Magnetic skyrmions – Overview of recent progress in an active research field. *J Appl Phys* **124**, 240901 (2018).

27. Dzyaloshinsky, I. A Thermodynamic Theory of 'Weak' Ferromagnetism of Antiferromagnetics. *Journal of Physics and Chemistry of Solids* **4**, 241–255 (1958).

28. Moriya, T. Anisotropic superexchange interaction and weak ferromagnetism. *Physical Review* **120**, 91–98 (1960).

29. Kolesnikov, A. G., Stebliy, M. E., Samardak, A. S. & Ognev, A. V. Skyrmionium – high velocity without the skyrmion Hall effect. *Sci Rep* **8**, 16966 (2018).

30. Obadero, A. S. Theoretical study of current-induced dynamics of an antiferromagnetic skyrmionium. [Doctoral dissertation, African University of Science and Technology] Repository. http://repository.aust.edu.ng/xmlui/handle/123456789/4935 (2019).

31. Zhang, S., Kronast, F., van der Laan, G. & Hesjedal, T. Real-Space Observation of Skyrmionium in a Ferromagnet-Magnetic Topological Insulator Heterostructure. *Nano Lett* **18**, 1057–1063 (2018).

32. Göbel, B., Henk, J. & Mertig, I. Forming individual magnetic biskyrmions by merging two skyrmions in a centrosymmetric nanodisk. *Sci Rep* **9**, 9521 (2019).

33. Yu, X. Z. *et al.* Biskyrmion states and their current-driven motion in a layered manganite. *Nat Commun* **5**, 3198 (2014).

34. Zuo, S. *et al.* Spontaneous Biskyrmion Lattice in a Centrosymmetric Rhombohedral Rare-Earth Magnet with Easy-Plane Anisotropy. *Nano Lett* **23**, 550–557 (2023).

35. Sandhoefner, S., Raeliarijaona, A., Nepal, R., Snyder-Tinoco, D. & Kovalev, A. A. Regular and in-plane skyrmions and antiskyrmions from boundary instabilities. *Phys Rev B* **104**, 064417 (2021).

36. Baláž, P. Interaction of In-Plane Magnetic Skyrmions with 90° Magnetic Domain Walls: Micromagnetic Simulations. *Phys Rev Appl* **17**, 044031 (2022).

37. Moon, K.-W., Yoon, J., Kim, C. & Hwang, C. Existence of in-Plane Magnetic Skyrmion and its Motion under Current Flow. *Phys Rev Appl* **12**, 064054 (2019).

38. Kong, L., Chen, X., Wang, W., Song, D. & Du, H. Dynamics of interstitial skyrmions in the presence of temperature gradients. *Phys Rev B* **104**, 214407 (2021).

39. Knapman, R., Rodrigues, D. R., Masell, J. & Everschor-Sitte, K. Current-induced H-shaped-skyrmion creation and their dynamics in the helical phase. *J Phys D Appl Phys* **54**, 404003 (2021).

40. Müller, J. *et al.* Magnetic Skyrmions and Skyrmion Clusters in the Helical Phase of Cu2OSeO3. *Phys Rev Lett* **119**, 137201 (2017).

41. Bassirian, P., Hesjedal, T., Parkin, S. S. P. & Litzius, K. Breathing mode dynamics of coupled three-dimensional chiral bobbers. *APL Mater* **10**, 101107 (2022).

42. Zheng, F. *et al.* Experimental observation of chiral magnetic bobbers in B20-type FeGe. *Nat Nanotechnol* **13**, 451–455 (2018).

43. Ran, K. *et al.* Creation of a Chiral Bobber Lattice in Helimagnet-Multilayer Heterostructures. *Phys Rev Lett* **126**, 017204 (2021).

44. Mühlbauer, S. *et al.* Kinetic small angle neutron scattering of the skyrmion lattice in MnSi. *New J Phys* **18**, 075017 (2016).

45. Adams, T. *et al.* Long-Range Crystalline Nature of the Skyrmion Lattice in MnSi. *Phys Rev Lett* **107**, 217206 (2011).

46. Neubauer, A. *et al.* Topological Hall Effect in the A Phase of MnSi. *Phys Rev Lett* **102**, 186602 (2009).

47. Zhang, S. L. *et al.* Imaging and manipulation of skyrmion lattice domains in Cu2OSeO3. *Appl Phys Lett* **109**, 192406 (2016).

48. Zhang, S. L. *et al.* Multidomain Skyrmion Lattice State in Cu2OSeO3. *Nano Lett* **16**, 3285–3291 (2016).

49. Zhang, S. L. *et al.* Resonant elastic X-ray scattering from the skyrmion lattice in Cu2OSeO3. *Phys Rev B* **93**, 214420 (2016).

50. Okamura, Y., Kagawa, F., Seki, S. & Tokura, Y. Transition to and from the skyrmion lattice phase by electric fields in a magnetoelectric compound. *Nat Commun* **7**, 12669 (2016).

51. Seki, S., Yu, X. Z., Ishiwata, S. & Tokura, Y. Observation of Skyrmions in a Multiferroic Material. *Science (1979)* **336**, 198–201 (2012).

52. Adams, T. *et al.* Long-Wavelength Helimagnetic Order and Skyrmion Lattice Phase in Cu2OseO3. *Phys Rev Lett* **108**, 237204 (2012).

53. Huang, S. X. & Chien, C. L. Extended Skyrmion Phase in Epitaxial FeGe(111) Thin Films. *Phys Rev Lett* **108**, 267201 (2012).

54. Karube, K. *et al.* Robust metastable skyrmions and their triangular–square lattice structural transition in a high-temperature chiral magnet. *Nat Mater* **15**, 1237–1242 (2016).

55. Tonomura, A. *et al.* Real-Space Observation of Skyrmion Lattice in Helimagnet MnSi Thin Samples. *Nano Lett* **12**, 1673–1677 (2012).

56. Rajeswari, J. *et al.* Filming the formation and fluctuation of skyrmion domains by cryo-Lorentz transmission electron microscopy. *Proceedings of the National Academy of Sciences* **112**, 14212–14217 (2015).

57. Tokunaga, Y. *et al.* A new class of chiral materials hosting magnetic skyrmions beyond room temperature. *Nat Commun* **6**, 7638 (2015).

58. Li, W. *et al.* Emergence of skyrmions from rich parent phases in the molybdenum nitrides. *Phys Rev B* **93**, 060409 (2016).

59. Hanneken, C., Kubetzka, A., von Bergmann, K. & Wiesendanger, R. Pinning and movement of individual nanoscale magnetic skyrmions via defects. *New J Phys* **18**, 055009 (2016).

60. Schmidt, L. *et al.* Symmetry breaking in spin spirals and skyrmions by in-plane and canted magnetic fields. *New J Phys* **18**, 075007 (2016).

61. Romming, N., Kubetzka, A., Hanneken, C., von Bergmann, K. & Wiesendanger, R. Field-Dependent Size and Shape of Single Magnetic Skyrmions. *Phys Rev Lett* **114**, 177203 (2015).

62. Bergmann, K. von, Kubetzka, A., Pietzsch, O. & Wiesendanger, R. Interface-induced chiral domain walls, spin spirals and skyrmions revealed by spin-polarized scanning tunneling microscopy. *Journal of Physics: Condensed Matter* **26**, 394002 (2014).

63. Romming, N. *et al.* Writing and Deleting Single Magnetic Skyrmions. *Science (1979)* **341**, 636–639 (2013).

64. Wiesendanger, R. Nanoscale magnetic skyrmions in metallic films and multilayers: a new twist for spintronics. *Nat Rev Mater* **1**, 16044 (2016).

65. Woo, S. *et al.* Observation of room-temperature magnetic skyrmions and their current-driven dynamics in ultrathin metallic ferromagnets. *Nat Mater* **15**, 501–506 (2016).

66. Park, J. *et al.* Compositional gradient induced enhancement of Dzyaloshinskii–Moriya interaction in Pt/Co/Ta heterostructures modulated by Pt–Co alloy intralayers. *Acta Mater* **241**, 118383 (2022).

67. Chen, Z.-D. *et al.* Experimental observation of interlayer perpendicular standing spin wave mode with low damping in skyrmion-hosting $[Pt/Co/Ta]_{10}$ multilayer. *Chinese Physics B* **31**, 117501 (2022).

68. Moreau-Luchaire, C. *et al.* Additive interfacial chiral interaction in multilayers for stabilization of small individual skyrmions at room temperature. *Nat Nanotechnol* **11**, 444–448 (2016).

69. Legrand, W. *et al.* Room-Temperature Current-Induced Generation and Motion of sub-100 nm Skyrmions. *Nano Lett* **17**, 2703–2712 (2017).

70. Ye, C. *et al.* Generation and manipulation of skyrmions and other topological spin structures with rare metals. *Rare Metals* **41**, 2200–2216 (2022).

71. Liu, J. *et al.* The 20-nm Skyrmion Generated at Room Temperature by Spin-Orbit Torques. *Chinese Physics Letters* **39**, 017501 (2022).

72. Woo, S. *et al.* Current-driven dynamics and inhibition of the skyrmion Hall effect of ferrimagnetic skyrmions in GdFeCo films. *Nat Commun* **9**, 959 (2018).

73. Jiang, W. *et al.* Skyrmions in magnetic multilayers. *Phys Rep* **704**, 1–49 (2017).

74. Zeissler, K. *et al.* Diameter-independent skyrmion Hall angle observed in chiral magnetic multilayers. *Nat Commun* **11**, 428 (2020).

75. Hrabec, A. *et al.* Current-induced skyrmion generation and dynamics in symmetric bilayers. *Nat Commun* **8**, 15765 (2017).

76. He, M. *et al.* Room temperature skyrmions in symmetric multilayers. *Appl Phys Lett* **121**, 192403 (2022).

77. Yang, H., Thiaville, A., Rohart, S., Fert, A. & Chshiev, M. Anatomy of Dzyaloshinskii-Moriya Interaction at Co/Pt Interfaces. *Phys Rev Lett* **115**, 267210 (2015).

78. Yang, H., Boulle, O., Cros, V., Fert, A. & Chshiev, M. Controlling Dzyaloshinskii-Moriya Interaction via Chirality Dependent Atomic-Layer Stacking, Insulator Capping and Electric Field. *Sci Rep* **8**, 12356 (2018).

79. Litzius, K. *et al.* Skyrmion Hall effect revealed by direct time-resolved X-ray microscopy. *Nat Phys* **13**, 170–175 (2017).

80. Zázvorka, J. *et al.* Thermal skyrmion diffusion used in a reshuffler device. *Nat Nanotechnol* **14**, 658–661 (2019).

81. Jaiswal, S. *et al.* Investigation of the Dzyaloshinskii-Moriya interaction and room temperature skyrmions in W/CoFeB/MgO thin films and microwires. *Appl Phys Lett* **111**, 022409 (2017).

82. Boulle, O. *et al.* Room-temperature chiral magnetic skyrmions in ultrathin magnetic nanostructures. *Nat Nanotechnol* **11**, 449–454 (2016).

83. Quessab, Y. *et al.* Tuning interfacial Dzyaloshinskii-Moriya interactions in thin amorphous ferrimagnetic alloys. *Sci Rep* **10**, 7447 (2020).

84. Wang, S. *et al.* Electrical Detection of Magnetic Skyrmions. *J Low Temp Phys* **197**, 321–336 (2019).

85. Casiraghi, A. *et al.* Individual skyrmion manipulation by local magnetic field gradients. *Commun Phys* **2**, 145 (2019).

86. Li, J. *et al.* Tailoring the topology of an artificial magnetic skyrmion. *Nat Commun* **5**, 4704 (2014).

87. Zhou, Y. & Ezawa, M. A reversible conversion between a skyrmion and a domain-wall pair in a junction geometry. *Nat Commun* **5**, 4652 (2014).

88. Mohseni, S. M. *et al.* Spin torque-generated magnetic droplet solitons. *Science (1979)* **339**, 1295–1298 (2013).

89. Heinze, S. *et al.* Spontaneous atomic-scale magnetic skyrmion lattice in two dimensions. *Nat Phys* **7**, 713–718 (2011).

90. Liu, J. *et al.* The 20-nm Skyrmion Generated at Room Temperature by Spin-Orbit Torques. *Chinese Physics Letters* **39**, 17501–017501 (2021).

91. Zeissler, K. *et al.* Discrete Hall resistivity contribution from Néel skyrmions in multilayer nanodiscs. *Nat Nanotechnol* **13**, 1161–1166 (2018).

92. Ahrens, V. *et al.* Skyrmions Under Control—FIB Irradiation as a Versatile Tool for Skyrmion Circuits. *Advanced Materials* **35**, 2207321 (2023).

93. Paikaray, B., Kuchibhotla, M., Haldar, A. & Murapaka, C. Skyrmion based majority logic gate by voltage controlled magnetic anisotropy in a nanomagnetic device. *Nanotechnology* (2023) doi:10.1088/1361-6528/acbeb3.

94. MacKinnon, C. R. *et al.* Collective skyrmion motion under the influence of an additional interfacial spin-transfer torque. *Sci Rep* **12**, (2022).

95. Wang, J. *et al.* Spontaneous creation and annihilation dynamics of magnetic skyrmions at elevated temperature. *Phys Rev B* **104**, 054420 (2021).

96. Garanin, D. A., Chudnovsky, E. M., Zhang, S. & Zhang, X. Thermal creation of skyrmions in ferromagnetic films with perpendicular anisotropy and Dzyaloshinskii-Moriya interaction. *J Magn Magn Mater* **493**, 165724 (2020).

97. Je, S.-G. *et al.* Targeted Writing and Deleting of Magnetic Skyrmions in Two-Terminal Nanowire Devices. *Nano Lett* **21**, 1253–1259 (2021).

98. Zhang, W. *et al.* Optical Creation of Skyrmions by Spin Reorientation Transition in Ferrimagnetic CoHo Alloys. *ACS Appl Mater Interfaces* **15**, 5608–5619 (2023).

99. Gerlinger, K. *et al.* Application concepts for ultrafast laser-induced skyrmion creation and annihilation. *Appl Phys Lett* **118**, 192403 (2021).

100. Yokouchi, T. *et al.* Creation of magnetic skyrmions by surface acoustic waves. *Nat Nanotechnol* **15**, 361–366 (2020).

101. Feng, D. *et al.* Strain-induced magnetic phase transition, magnetic anisotropy switching and bilayer antiferromagnetic skyrmions in van der Waals magnet $CrTe_2$. *Nanoscale* **15**, 1561–1567 (2023).

102. Hsu, P.-J. *et al.* Electric-field-driven switching of individual magnetic skyrmions. *Nat Nanotechnol* **12**, 123–126 (2017).

103. Bhattacharya, D., Al-Rashid, M. M. & Atulasimha, J. Voltage controlled core reversal of fixed magnetic skyrmions without a magnetic field. *Sci Rep* **6**, 31272 (2016).

104. Zhou, Y. *et al.* Dynamically stabilized magnetic skyrmions. *Nat Commun* **6**, 8193 (2015).

105. Emori, S., Bauer, U., Ahn, S. M., Martinez, E. & Beach, G. S. D. Current-driven dynamics of chiral ferromagnetic domain walls. *Nat Mater* **12**, 611–616 (2013).

106. Brataas, A., Kent, A. D. & Ohno, H. Current-induced torques in magnetic materials. *Nat Mater* **11**, 372–381 (2012).

107. Fert, A., Cros, V. & Sampaio, J. Skyrmions on the track. *Nat Nanotechnol* **8**, 152–156 (2013).

108. Berger, L. Domain drag effect in the presence of variable magnetic field or variable transport current. *J Appl Phys* **50**, 2137–2139 (1979).

109. Berger, L. Low-field magnetoresistance and domain drag in ferromagnets. *J Appl Phys* **49**, 2156 (2008).

110. Hung, C. -Y. & Berger, L. Exchange forces between domain wall and electric current in permalloy films of variable thickness. *J Appl Phys* **63**, 4276–4278 (1988).

111. Freitas, P. P. & Berger, L. Observation of s-d exchange force between domain walls and electric current in very thin Permalloy films. *J Appl Phys* **57**, 1266–1269 (1985).

112. Binasch, G., Grünberg, P., Saurenbach, F. & Zinn, W. Enhanced magnetoresistance in layered magnetic structures with antiferromagnetic interlayer exchange. *Phys Rev B* **39**, 4828–4830 (1989).

113. Baibich, M. N. *et al.* Giant Magnetoresistance of (001)Fe/(001)Cr Magnetic Superlattices. *Phys Rev Lett* **61**, 2472–2475 (1988).

114. Slonczewski, J. C. Excitation of spin waves by an electric current. *J Magn Magn Mater* **195**, L261–L268 (1999).

115. Slonczewski, J. C. Current-driven excitation of magnetic multilayers. *J Magn Magn Mater* **159**, L1–L7 (1996).

116. Berger, L. Emission of spin waves by a magnetic multilayer traversed by a current. *Phys Rev B* **54**, 9353–9358 (1996).

117. Berger, L. Effect of interfaces on Gilbert damping and ferromagnetic resonance linewidth in magnetic multilayers. *J Appl Phys* **90**, 4632–4638 (2001).

118. Yamane, Y. & Sinova, J. Skyrmion-number dependence of spin-transfer torque on magnetic bubbles. *J Appl Phys* **120**, 233901 (2016).

119. Iwasaki, J., Koshibae, W. & Nagaosa, N. Colossal Spin Transfer Torque Effect on Skyrmion along the Edge. *Nano Lett* **14**, 4432–4437 (2014).

120. Iwasaki, J., Mochizuki, M. & Nagaosa, N. Universal current-velocity relation of skyrmion motion in chiral magnets. *Nat Commun* **4**, 1463 (2013).

121. Kim, K.-W., Moon, K.-W., Kerber, N., Nothhelfer, J. & Everschor-Sitte, K. Asymmetric skyrmion Hall effect in systems with a hybrid Dzyaloshinskii-Moriya interaction. *Phys Rev B* **97**, 224427 (2018).

122. Komineas, S. & Papanicolaou, N. Skyrmion dynamics in chiral ferromagnets. *Phys Rev B* **92**, 064412 (2015).

123. Zhang, S. & Li, Z. Roles of nonequilibrium conduction electrons on the magnetization dynamics of ferromagnets. *Phys Rev Lett* **93**, 127204 (2004).

124. Li, Z. & Zhang, S. Domain-wall dynamics driven by adiabatic spin-transfer torques. *Phys Rev B* **70**, 024417 (2004).

125. MacKinnon, C. R., Lepadatu, S., Mercer, T. & Bissell, P. R. Role of an additional interfacial spin-transfer torque for current-driven skyrmion dynamics in chiral magnetic layers. *Phys Rev B* **102**, 214408 (2020).

126. Lepadatu, S. Effect of inter-layer spin diffusion on skyrmion motion in magnetic multilayers. *Sci Rep* **9**, 9592 (2019).

127. Sinova, J., Valenzuela, S. O., Wunderlich, J., Back, C. H. & Jungwirth, T. Spin Hall effects. *Rev Mod Phys* **87**, 1213–1260 (2015).

128. Dyakonov, M. I. & Perel, V. I. Current-induced spin orientation of electrons in semiconductors. *Phys Lett A* **35**, 459–460 (1971).

129. Heide, C., Zilberman, P. E. & Elliott, R. J. Current-driven switching of magnetic layers. *Phys Rev B* **63**, 064424 (2001).

130. Lo Conte, R. *et al.* Role of B diffusion in the interfacial Dzyaloshinskii-Moriya interaction in Ta/Co20/Fe60B20/MgO nanowires. *Phys Rev B* **91**, 014433 (2015).

131. Wang, K., Qian, L., Ying, S. C. & Xiao, G. Spin-orbit torque switching of chiral magnetization across a synthetic antiferromagnet. *Commun Phys* **4**, 10 (2021).

132. Murray, N. *et al.* Field-free spin-orbit torque switching through domain wall motion. *Phys Rev B* **100**, 104441 (2019).

133. Miron, I. M. *et al.* Perpendicular switching of a single ferromagnetic layer induced by in-plane current injection. *Nature* **476**, 189–193 (2011).

134. Liu, L., Lee, O. J., Gudmundsen, T. J., Ralph, D. C. & Buhrman, R. A. Current-induced switching of perpendicularly magnetized magnetic layers using spin torque from the spin hall effect. *Phys Rev Lett* **109**, 096602 (2012).

135. Cao, J. *et al.* Spin orbit torques induced magnetization reversal through asymmetric domain wall propagation in Ta/CoFeB/MgO structures. *Sci Rep* **8**, 1355 (2018).

136. Zhang, Y., Luo, S., Yang, X. & Yang, C. Spin-orbit-torque-induced magnetic domain wall motion in Ta/CoFe nanowires with sloped perpendicular magnetic anisotropy. *Sci Rep* **7**, 2047 (2017).

137. Reichhardt, C. & Reichhardt, C. J. O. Thermal creep and the skyrmion Hall angle in driven skyrmion crystals. *Journal of Physics Condensed Matter* **31**, 07LT01 (2019).

138. Reichhardt, C. & Reichhardt, C. J. O. Dynamics of Magnus-dominated particle clusters, collisions, pinning, and ratchets. *Phys Rev E* **101**, 062602 (2020).

139. Reichhardt, C. & Reichhardt, C. J. O. Plastic flow and the skyrmion Hall effect. *Nat Commun* **11**, 738 (2020).

140. Reichhardt, C., Ray, D. & Reichhardt, C. J. Collective transport properties of driven skyrmions with random disorder. *Phys Rev Lett* **114**, 217202 (2015).

141. Reichhardt, C., Reichhardt, C. J. O. & Milosevic, M. V. Statics and Dynamics of Skyrmions Interacting with Pinning: A Review. *ArXiv* (2021) doi:10.1103/RevModPhys.94.035005.

142. Lin, S.-Z., Reichhardt, C., Batista, C. D. & Saxena, A. Particle model for skyrmions in metallic chiral magnets: Dynamics, pinning, and creep. *Phys Rev B* **87**, 214419 (2013).

143. Jiang, W. *et al.* Direct observation of the skyrmion Hall effect. *Nat Phys* **13**, 162–169 (2017).

144. Juge, R. *et al.* Current-Driven Skyrmion Dynamics and Drive-Dependent Skyrmion Hall Effect in an Ultrathin Film. *Phys Rev Appl* **12**, 044007 (2019).

145. Tan, A. K. C. *et al.* Visualizing the strongly reshaped skyrmion Hall effect in multilayer wire devices. *Nat Commun* **12**, 4252 (2021).

146. Litzius, K. *et al.* The role of temperature and drive current in skyrmion dynamics. *Nat Electron* **3**, 30–36 (2020).

147. Benguettat-El Mokhtari, I. *et al.* Interfacial Dzyaloshinskii-Moriya interaction, interface-induced damping and perpendicular magnetic anisotropy in Pt/Co/W based multilayers. *J Appl Phys* **126**, 133902 (2019).

148. Yuan, J., Sun, L., Sang, H., Du, J. & Zhou, M. Interfacial effects on magnetic relaxation in Co/Pt multilayers. *Phys Rev B* **68**, 134443 (2003).

149. Barman, A. *et al.* Ultrafast magnetization dynamics in high perpendicular anisotropy [CoPt]n multilayers. *J Appl Phys* **101**, 09D102 (2007).

150. Dhiman, A. K. *et al.* Thickness dependence of interfacial Dzyaloshinskii-Moriya interaction, magnetic anisotropy and spin waves damping in Pt/Co/Ir and Ir/Co/Pt trilayers. *J Magn Magn Mater* **519**, 167485 (2021).

151. Pai, C.-F., Ou, Y., Vilela-Leão, L. H., Ralph, D. C. & Buhrman, R. A. Dependence of the efficiency of spin Hall torque on the transparency of Pt/ferromagnetic layer interfaces. *Phys Rev B* **92**, 064426 (2015).

152. Azzawi, S. *et al.* Evolution of damping in ferromagnetic/nonmagnetic thin film bilayers as a function of nonmagnetic layer thickness. *Phys Rev B* **93**, 054402 (2016).

153. Zhang, B. *et al.* Influence of heavy metal materials on magnetic properties of Pt/Co/heavy metal tri-layered structures. *Appl Phys Lett* **110**, 012405 (2017).

154. Caprile, A. *et al.* Microwave Properties and Damping in [Pt/Co] Multilayers with Perpendicular Anisotropy. *IEEE Magn Lett* **5**, 3000304 (2014).

155. Di, K. *et al.* Direct Observation of the Dzyaloshinskii-Moriya Interaction in a Pt/Co/Ni Film. *Phys Rev Lett* **114**, 047201 (2015).

156. Devolder, T., Couet, S., Swerts, J. & Kar, G. S. Gilbert damping of high anisotropy Co/Pt multilayers. *J Phys D Appl Phys* **51**, 135002 (2018).

157. Nguyen, T. V. A. *et al.* Magnetic properties of Co film in Pt/Co/Cr2O3/Pt structure. *AIP Adv* **10**, 015152 (2020).

158. Metaxas, P. J. *et al.* Creep and flow regimes of magnetic domain-wall motion in ultrathin Pt/Co/Pt films with perpendicular anisotropy. *Phys Rev Lett* **99**, 217208 (2007).

159. Mizukami, S. *et al.* Gilbert damping in perpendicularly magnetized Pt/Co/Pt films investigated by all-optical pump-probe technique. *Appl Phys Lett* **96**, 152502 (2010).

160. Azzawi, S., Hindmarch, A. T. & Atkinson, D. Magnetic damping phenomena in ferromagnetic thin-films and multilayers. *J Phys D Appl Phys* **50**, 473001 (2017).

161. Parkin, S. S. P., Hayashi, M. & Thomas, L. Magnetic Domain-Wall Racetrack Memory. *Science (1979)* **320**, 190–194 (2008).

162. Song, K. M. *et al.* Skyrmion-based artificial synapses for neuromorphic computing. *Nat Electron* **3**, 148–155 (2020).

163. Lee, M., Kang, W., Onose, Y., Tokura, Y. & Ong, N. P. Unusual Hall Effect Anomaly in MnSi under Pressure. *Phys Rev Lett* **102**, 186601 (2009).

164. Kanazawa, N. *et al.* Large Topological Hall Effect in a Short-Period Helimagnet MnGe. *Phys Rev Lett* **106**, 156603 (2011).

165. Maccariello, D. *et al.* Electrical detection of single magnetic skyrmions in metallic multilayers at room temperature. *Nat Nanotechnol* **13**, 233–237 (2018).

166. Hamamoto, K., Ezawa, M. & Nagaosa, N. Purely electrical detection of a skyrmion in constricted geometry. *Appl Phys Lett* **108**, 112401 (2016).

167. Kubetzka, A., Hanneken, C., Wiesendanger, R. & von Bergmann, K. Impact of the skyrmion spin texture on magnetoresistance. *Phys Rev B* **95**, 104433 (2017).

168. Hanneken, C. *et al.* Electrical detection of magnetic skyrmions by tunnelling non-collinear magnetoresistance. *Nat Nanotechnol* **10**, 1039–1042 (2015).

169. Tomasello, R. *et al.* Electrical detection of single magnetic skyrmion at room temperature. *AIP Adv* **7**, 056022 (2017).

170. Grollier, J., Querlioz, D. & Stiles, M. D. Spintronic Nanodevices for Bioinspired Computing. *Proceedings of the IEEE* **104**, 2024–2039 (2016).

171. Chen, R. *et al.* Nanoscale Room-Temperature Multilayer Skyrmionic Synapse for Deep Spiking Neural Networks. *Phys Rev Appl* **14**, 014096 (2020).

172. Liu, S. *et al.* Magnetic Skyrmion-Based Spiking Neural Network for Pattern Recognition. *Applied Sciences* **12**, 9698 (2022).

173. Donahue, M. J. OOMMF User's Guide, Version 1.0, National Institute of Standards and Technology, Gaithersburg, MD. Preprint at https://doi.org/10.6028/NIST.IR.6376 (1999).

174. Scholz, W. *et al.* Scalable parallel micromagnetic solvers for magnetic nanostructures. *Comput Mater Sci* **28**, 366–383 (2003).

175. Fischbacher, T., Franchin, M., Bordignon, G. & Fangohr, H. A Systematic Approach to Multiphysics Extensions of Finite-Element-Based Micromagnetic Simulations: Nmag. *IEEE Trans Magn* **43**, 2896–2898 (2007).

176. Vansteenkiste, A. *et al.* The design and verification of MuMax3. *AIP Adv* **4**, 107133 (2014).

177. Zhu, R. Grace: A cross-platform micromagnetic simulator on graphics processing units. *SoftwareX* **3–4**, 27–31 (2015).

178. Lepadatu, S. Boris Computational Spintronics User Manual. Preprint at https://doi.org/10.13140/RG.2.2.31496.88322/1.

179. Lepadatu, S. Boris computational spintronics – High performance multi-mesh magnetic and spin transport modeling software. *J Appl Phys* **128**, 243902 (2020).

2 Theory

In the previous chapter, the topic of skyrmions was introduced with a brief history and background literature discussed. In the chapter that follows, the magnetic equations of motion used in the thesis are explored, followed by a brief description of the drift-diffusion model. Furthermore, the modules used in *Boris Computational Spintronics* are explained in both physical and mathematical terms. Finally, the interfacial spin-transfer torque (ISTT) and spin-orbit torque (SOT) used to drive skyrmion throughout this work are discussed and shown mathematically.

2.1 Introduction

Micromagnetism is the basis used to understand magnetisation phenomena on lengths scales including nano- to micro- to macro-scale. The most relevant length scales for understanding magnetic mechanics are down to the nano-scale for applications including memory devices, magnetic sensors, multilayer compositions, tunnel junctions, logic gates and skyrmionics devices.

To model spintronic devices, the Landau-Lifshitz-Gilbert (LLG) equation is almost always used with the inclusion of various contributions such as additional torques to model the interactions of spin currents on magnetisation. These torques can be due to an in-plane injected polarised charge current in a thin magnetic layer, namely the spin-transfer torques (STTs), or alongside the SOTs which utilise the spin-orbit interactions in heavy metal (HM) metals, in HM/ferromagnetic (FM) interfaces.

Before micromagnetic software was developed, the LLG needed to be solved numerically which is difficult to accomplish due to the effective magnetic field containing multiple contributing energies. Despite the rapidly advancing computational technology in terms of central processing unit (CPU) and graphics processing unit (GPU) resources, in a given workstation, it was still very challenging to obtain a significant amount of information in a reasonable time. Today, however, there has been significant development not only of both computational hardware but also software and programming languages which has given rise to much more user-friendly interactive software. One of the original free software to take advantage of the advances was OOMMF[1], which appeared in 1998, and Mumax[3] [2] in 2014, allowed for a more accessible method of micromagnetic modelling:

not only for designing simulations but also for simulation total time, however, other more advanced software is now freely available.

Boris Computational Spintronics[3–6], from here onwards *Boris*, is one such software. *Boris* is a multiphysics software designed to solve simple and complex three-dimensional magnetic dynamics problems. It is coupled with a self-consistent charge and spin transport solver and heat flow solver for temperature-dependent materials. A major strength of *Boris* is the computational routines that are designed to run efficiently on CPUs but moreover GPUs using Nvidia CUDA cores. Furthermore, *Boris* uses a seamless integration with *Python* that allows for full simulation scripts and control of the software, allowing scripts to be created and run easier, and allowing for more advanced procedures and methods to be created. A simple script to create, relax and drive a skyrmion is shown in Appendix A: Skyrmion Motion Script.

Boris is used throughout this work to model skyrmion motion in ultra-thin magnetic devices under the influence of an applied charge current. Various conditions are also considered including zero-temperature, temperatures above the Curie temperature, systems with multilayers and stacks repetitions, synthetic magnetic systems and much more.

2.2 Ordinary differential equation

Modelling magnetisation dynamics is based solely on solving magnetisation equations of motion such as the LLG equation. Following are the most used equations in this work and also the magnetism communities[7,8]. All the functions used in this work are based on the Landau-Lifshitz[9,10] equations with adaptations from Gilbert[11] and Bloch[12] and also include mathematical assumptions to achieve simplistic, yet effective solutions.

2.2.1 Landau-Lifshitz-Gilbert

The effect of spin torques on skyrmion motion is modelled using the LLG[9,11,13] equation:

$$\frac{\partial \boldsymbol{m}}{\partial t} = -\gamma \boldsymbol{m} \times \boldsymbol{H}_{eff} + \alpha \boldsymbol{m} \times \frac{\partial \boldsymbol{m}}{\partial t} + \frac{1}{M_S} \boldsymbol{T_S} \qquad \text{Eq. 2-1}$$

Here, $\gamma = \mu_0 g_r |\gamma_e|$, where γ_e is the electron gyromagnetic ratio, g_r is a relative gyromagnetic factor, α is the Gilbert damping and M_s is the saturation magnetisation. $\boldsymbol{H}_{eff}$ is the effective field term consisting of several additive terms, namely the demagnetisation field, exchange interaction including the interfacial Dzyaloshinskii-Moriya exchange interaction in the *xy*-plane, applied magnetic field and uniaxial magnetocrystalline anisotropy. $\boldsymbol{T}_s$ is the total spin-torque term[14], which includes contributions from SOT, STT and ISTT, and can be computed self-consistently using the drift-diffusion model[5].

2.2.2 Landau-Lifshitz-Gilbert static assumption

The static LLG, *LLGstatic* [3], is an equation used for static problems only when the relaxed magnetisation state is required. It is the explicit LLG equation without the processional term, as well as zero damping and no additional torques. The derivation is given below beginning with Eq. 2-1 with a cross-product of the existing LLG.

$$\boldsymbol{m} \times \frac{\partial \boldsymbol{m}}{\partial t} = -\gamma \boldsymbol{m} \times \boldsymbol{m} \times \boldsymbol{H}_{eff} + \alpha \boldsymbol{m} \times \boldsymbol{m} \times \frac{\partial \boldsymbol{m}}{\partial t} \qquad \text{Eq. 2-2}$$

Using the triple cross-product identity $\boldsymbol{A} \times \boldsymbol{B} \times \boldsymbol{C} = \boldsymbol{B}(\boldsymbol{A}.\boldsymbol{C}) - \boldsymbol{C}(\boldsymbol{A}.\boldsymbol{B})$ on the damping-like term, $\alpha \boldsymbol{m} \times \boldsymbol{m} \times \frac{\partial \boldsymbol{m}}{\partial t}$, noting also that $\boldsymbol{m}.\frac{\partial \boldsymbol{m}}{\partial t} = 0$, the following is obtained:

$$\boldsymbol{m} \times \boldsymbol{m} \times \frac{\partial \boldsymbol{m}}{\partial t} = \boldsymbol{m}\left(\boldsymbol{m}.\frac{\partial \boldsymbol{m}}{\partial t}\right) - \frac{\partial \boldsymbol{m}}{\partial t}(\boldsymbol{m}.\boldsymbol{m}) = -\frac{\partial \boldsymbol{m}}{\partial t} \qquad \text{Eq. 2-3}$$

Then equation Eq. 2-2 becomes:

$$\boldsymbol{m} \times \frac{\partial \boldsymbol{m}}{\partial t} = -\gamma \boldsymbol{m} \times \boldsymbol{m} \times \boldsymbol{H}_{eff} - \alpha \frac{\partial \boldsymbol{m}}{\partial t} \qquad \text{Eq. 2-4}$$

Finally substituting Eq. 2-4 into Eq. 2-1.

$$\frac{\partial \boldsymbol{m}}{\partial t} = -\gamma \boldsymbol{m} \times \boldsymbol{H}_{eff} + \alpha\left[-\gamma \boldsymbol{m} \times \boldsymbol{m} \times \boldsymbol{H}_{eff} - \alpha \frac{\partial \boldsymbol{m}}{\partial t}\right] + \frac{1}{M_S}\boldsymbol{T_S} \qquad \text{Eq. 2-5}$$

As this is a stationary problem $\alpha = 1$ and $\boldsymbol{T}_s = 0$, as well as the assumption that the processional motion does not exist, thus the field-like term $-\gamma \boldsymbol{m} \times \boldsymbol{H}_{eff} = 0$. Hence,

$$2\frac{\partial \boldsymbol{m}}{\partial t} = -\gamma \boldsymbol{m} \times \boldsymbol{m} \times \boldsymbol{H}_{eff} \qquad \text{Eq. 2-6}$$

Finally, the LLG with static assumptions is realised:

$$\frac{\partial \boldsymbol{m}}{\partial t} = -\frac{\gamma}{2} \boldsymbol{m} \times \boldsymbol{m} \times \boldsymbol{H}_{eff} \qquad \text{Eq. 2-7}$$

This is the final form describing the static LLG equation, which is a very powerful adaptation as, even though the LLG is significantly simplified due to the assumptions discussed above, it allows for complex systems to be relaxed to their lowest energy state or equilibrium state quickly. This method cannot be used to gain any magnetisation dynamics information but would be used to create a system with the correct starting conditions.

2.2.3 Landau-Lifshitz-Gilbert with spin accumulation

The LLG can also include a spin accumulation term which can be included in an additional term $\boldsymbol{T}_s$ given below. What arises from a calculated spin accumulation are bulk and interfacial torques which are included additively in Eq. 2-1. The bulk spin torque is given by[3,5,14,15]

$$\boldsymbol{T}_s = -\frac{D_e}{\lambda_J^2}\boldsymbol{m}\times\boldsymbol{S} - \frac{D_e}{\lambda_\varphi^2}\boldsymbol{m}\times\boldsymbol{m}\times\boldsymbol{S} \qquad \text{Eq. 2-8}$$

Here, D_e is the electron diffusion constant, $\boldsymbol{S}$ is the spin vector, λ_J is the exchange rotation length and λ_φ is the spin dephasing length. This is included into a $\boldsymbol{H}_{eff}$ term in the explicit form of the equation, given below:

$$\boldsymbol{H}_s = \frac{D_e}{\gamma|\boldsymbol{M}|}\left(\frac{\boldsymbol{S}}{\lambda_J^2} + \frac{\boldsymbol{m}\times\boldsymbol{S}}{\lambda_\varphi^2}\right) \qquad \text{Eq. 2-9}$$

This leads to the final equation including the effective field term, $\boldsymbol{H}_{eff}$, and the bulk spin torque $\boldsymbol{H}_s$.

$$\frac{\partial\boldsymbol{m}}{\partial t} = -\gamma\boldsymbol{m}\times(\boldsymbol{H}_{eff}+\boldsymbol{H}_s) + \alpha\boldsymbol{m}\times\frac{\partial\boldsymbol{m}}{\partial t} \qquad \text{Eq. 2-10}$$

2.2.4 Landau-Lifshitz-Gilbert with STT

When considering spin current effects on magnetisation, the LLG can also include the STT, more specifically the Zhang-Li STT[16–19]. The STT in this case requires a spin accumulation to be calculated which is accomplished following the method in the previous section (see Section 2.2.3). The Zhang-Li STT can be expressed as:

$$\boldsymbol{T}_s = (\boldsymbol{u}\cdot\nabla)\boldsymbol{m} - \beta\boldsymbol{m}\times[(\boldsymbol{u}\cdot\nabla)\boldsymbol{m}] \qquad \text{Eq. 2-11}$$

Here, β is the non-adiabaticity parameter obtained via a fitting procedure, and $\boldsymbol{u}$ is the spin-drift velocity given by[20]:

$$\boldsymbol{u} = \boldsymbol{J_c}\frac{P}{M_s}\frac{\mu_B}{e}\frac{1}{1+\beta^2} \qquad \text{Eq. 2-12}$$

Here, $\boldsymbol{J}_c$ is the charge current in vector form and P is the polarisation fitting constant. Finally, the LLG can be complemented by the Zhang-Li STT in implicit form as:

$$\frac{\partial\boldsymbol{m}}{\partial t} = -\gamma\boldsymbol{m}\times\boldsymbol{H}_{eff} + \alpha\boldsymbol{m}\times\frac{\partial\boldsymbol{m}}{\partial t} + (\boldsymbol{u}\cdot\nabla)\boldsymbol{m} - \beta\boldsymbol{m}\times[(\boldsymbol{u}\cdot\nabla)\boldsymbol{m}] \qquad \text{Eq. 2-13}$$

Note here the factor of M_s that precedes $\boldsymbol{T}_s$ in Eq. 2-1 is absorbed into $\boldsymbol{u}$. The application of Eq. 2-13 is shown in Chapter 4 to Chapter 7.

2.2.5 Stochastic Landau-Lifshitz-Gilbert

It is well documented that temperature can have a significant effect on magnetisation dynamics such as the damping[21,22], magnetisation saturation[23,24] and exchange stiffness[25–27] to name a few. Therefore, including a form of temperature in micromagnetic modelling

is imperative and can be achieved by including an additive thermal field term, $\boldsymbol{H}_{thermal}$, which follows a gaussian distribution with zero mean and standard deviation given by[3]:

$$H_\sigma = \left(\frac{2\alpha k_B T}{\gamma \mu_0 M_s V \Delta t}\right)^{0.5} \quad \text{Eq. 2-14}$$

Here, k_B is the Boltzmann constant, T is the temperature, V is the volume of the stochastic computation cell and Δt is the time step used to update the stochastic fields. By default, V is the mesh cell size and Δt is the evaluation method time step. Therefore, the $\boldsymbol{H}_{thermal}$ can be included in the explicit LLG according to Eq. 2-14 as:

$$\frac{\partial \boldsymbol{m}}{\partial t} = -\gamma \boldsymbol{m} \times \left(\boldsymbol{H}_{eff} + \boldsymbol{H}_{thermal}\right) + \boldsymbol{m} \times \left(\boldsymbol{m} \times \left(\boldsymbol{H}_{eff} + \boldsymbol{H}_{thermal}\right)\right) + \frac{1}{M_s}\boldsymbol{T}_s \quad \text{Eq. 2-15}$$

2.2.6 Landau-Lifshitz-Bloch equation

The Landau-Lifshitz-Bloch (LLB)[12,28,29] equation of motion for macroscopic magnetisation dynamics has become a well-used approach in temperature-dependent systems, especially when T approached the Curie temperature, T_c. For non-zero temperature simulations, the LLB equation is given by, in implicit form, as:

$$\frac{\partial \boldsymbol{m}}{\partial t} = -\gamma \boldsymbol{m} \times \boldsymbol{H} + \frac{\tilde{\alpha}_{\perp}}{|\boldsymbol{M}|} \boldsymbol{m} \times \frac{\partial \boldsymbol{m}}{\partial t} + \frac{\gamma \tilde{\alpha}_{\parallel}}{|\boldsymbol{M}|} (\boldsymbol{m} \cdot \boldsymbol{H}) \boldsymbol{m} \qquad \text{Eq. 2-16}$$

Here, the terms $\tilde{\alpha}_{\perp}$ and $\tilde{\alpha}_{\parallel}$ are the normalised transverse and longitudinal damping terms given by $\tilde{\alpha}_{\perp} = \frac{\alpha_{\perp}}{m}$ and $\tilde{\alpha}_{\parallel} = \frac{\alpha_{\parallel}}{m}$, respectively, where $m = \frac{|\boldsymbol{M}|}{M_S^0}$. The transverse and longitudinal terms are temperature specific depending on if T is larger or smaller than T_c, which are given below.

$$\alpha_{\parallel} = \begin{cases} \alpha \dfrac{2T}{3T_c}, & T < T_c \\ \dfrac{2T}{3T_c}, & T > T_c \end{cases}$$

$$\alpha_{\perp} = \begin{cases} \alpha \left(1 - \dfrac{T}{3T_c}\right), & T < T_c \\ \dfrac{2T}{3T_c}, & T > T_c \end{cases} \qquad \text{Eq. 2-17}$$

Note that for $T > T_c$, $\alpha_{\perp} = \alpha_{\parallel} = \frac{2T}{3T_c}$. Finally, considering longitudinal susceptibility and temperature-dependent equilibrium magnetisation, the explicit form of the LLB can be expressed as:

$$\frac{\partial \boldsymbol{M}}{\partial t} = -\frac{\gamma}{1 + \tilde{\alpha}_{\perp}^2} \boldsymbol{M} \times \boldsymbol{H} + \frac{\tilde{\alpha}_{\perp} \gamma}{(1 + \tilde{\alpha}_{\perp}^2)|\boldsymbol{M}|} \boldsymbol{M} \times (\boldsymbol{M} \times \boldsymbol{H}) + \frac{\gamma \tilde{\alpha}_{\parallel}^2}{|M|} (\boldsymbol{M} \cdot \boldsymbol{H}) \boldsymbol{M} \qquad \text{Eq. 2-18}$$

2.3 Drift-diffusion model

The drift-diffusion model[5,30–33] is a powerful method used to understand the important physics behind the phenomena of spin current and spin accumulation in magnetic systems. In this chapter, the spin current and spin accumulation as well as transport parameters such as spin polarisation, the spin-flip, exchange rotation and spin dephasing length scales are introduced.

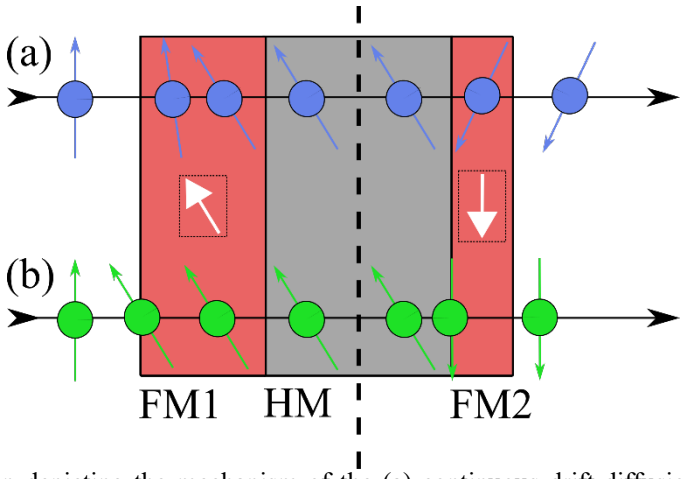

Figure 2-1 Illustration depicting the mechanism of the (a) continuous drift-diffusion model and (b) the interfacial drift-diffusion model. FM1 and FM2 are FM layers with different thicknesses and HM is a non-magnetic layer. The white arrows state the magnetisation orientation of the corresponding FM layer. The black arrow signifies the direction of propagation and the coloured points and arrows show the orientation of the spin as passing through the system.

In particular, two approaches of the drift-diffusion model are defined: the continuous and interfacial approach, both of which are shown in Figure 2-1. The continuous approach, as shown in Figure 2-1(a), utilised an unpolarised charge current, which when passed into a magnetic layer, FM1, aligns to the local magnetisation over a displacement according to the material parameters such as the spin-flip, exchange rotation and spin dephasing length. In general, the transverse components of spin are absorbed by the local magnetisation thus applying a torque, and yielding a polarised charge current exiting FM1. However, if the charge current was to pass into an insufficiently thick FM layer such as FM2, the transverse spin component of spin cannot be fully absorbed by the local magnetisation which can cause an issue in terms of torque parameters fitting. On the other hand, the interfacial effect, as shown in Figure 2-1(b), takes into account the interface between the HM/FM layer. When an unpolarised charge current is injected, all of the transverse spin components are absorbed in the interface instantaneously, resulting in an

instantaneous spin torque and rotation of the spin moment. This is an advantage over the continuous method as layer thickness will not affect the transverse spin absorption due to the instantaneous nature of the absorption in this method.

From this point onwards, the simple derivation of the drift-diffusion model is completed and discussed. To begin, the charge current model is defined as[5,30,34]:

$$\boldsymbol{J}_c = \sigma \boldsymbol{E} + \beta_D D_e \frac{e}{\mu_B} (\nabla \boldsymbol{S}) \boldsymbol{m} + \theta_{SHA} D_e \frac{e}{\mu_B} (\nabla \times \boldsymbol{S}) \qquad \text{Eq. 2-19}$$

The charge current is given by Eq. 2-19. Here, $\boldsymbol{J}_C$ is the charge current density which includes four distinct contributions: the first term is the usual Ohm's law, where $\boldsymbol{E}$ and σ are the electric field and the electrical conductivity, respectively, the second term is the giant magnetoresistance (GMR) term arising in current perpendicular to the plane[30,31], where D_e is the election diffusion constant, β_D is the diffusion polarisation, $\boldsymbol{m}$ is the magnetisation direction and $\boldsymbol{S}$ is the spin accumulation. The third term is the contribution due to the inverse spin Hall angle where θ_{SHA} is the spin Hall angle which describes the ratio of deflected current and injected spin current[35]. The spin current density is also required as it is a consequence of in-plane charge current injection and is given by[5,36]:

$$\boldsymbol{J}_S = -\frac{\mu_B}{e} \beta_\sigma \sigma (\boldsymbol{E} \otimes \boldsymbol{m}) - D_e \nabla \boldsymbol{S} + \theta_{SHA} \frac{\mu_B}{e} \varepsilon \sigma \boldsymbol{E} \qquad \text{Eq. 2-20}$$

Here, $\boldsymbol{J}_S$ is a rank-2 tensor such that J_{Sij} regards the direction *i* of the *j* component of spin polarisation following the convention used by Dyakonov[36]. Eq. 2-20 includes three spin current contributions; the first term is the flow of spins carried by a spin-polarised charge current in a magnetic layer due to an external field $\boldsymbol{E}$, where β_σ is the diffusion of spin polarisation. The second term is the diffusion of spins caused by the local spin accumulation gradient. The final term is the spin current generated by the spin Hall effect (SHE) in which a pure spin current is generated perpendicular to the plane of an injected current density, where ε is the rank-3 antisymmetric tensor.

Next, the effect of the exchange interaction between the spin accumulation and the local magnetisation is considered. When a spin interacts with local magnetisation a torque is generated between the two components only if there is a difference of direction between them, therefore, only the transverse spin accumulation to the magnetisation creates a torque. Thus, to upkeep the conservation of spin angular momentum, the transverse spin components are absorbed, but are dictated by the length scales, namely: the spin-flip length, λ_{sf} which describes the diffusive decay of the longitudinal spin accumulation process, the exchange rotation length, λ_J, which describes the relaxation of the transverse spin accumulation given by $\lambda_J = \sqrt{\frac{\hbar D_e}{J}}$ where J is the exchange interaction energy strength[30,31] and the spin dephasing length, $\lambda_\varphi = \lambda_J \sqrt{\frac{l_\perp}{l_L}}$, where $l_\perp$ and l_L are the spin coherence and spin precession lengths[5,32] respectively. The spin accumulation equation of motion is given by:

$$\frac{\partial \boldsymbol{S}}{\partial t} = -\nabla \cdot \boldsymbol{J}_s - D_e \left(\frac{\boldsymbol{S}}{\lambda_{sf}^2} + \frac{\boldsymbol{S} \times \boldsymbol{m}}{\lambda_J^2} + \frac{\boldsymbol{m} \times (\boldsymbol{S} \times \boldsymbol{m})}{\lambda_\varphi^2} \right) \qquad \text{Eq. 2-21}$$

The torque on the magnetisation is obtained from the divergence of the spin currents by considering the conservation of total spin angular moments[31]. This is achieved via a steady state where $\frac{\partial \boldsymbol{S}}{\partial t} = 0$ and results in:

$$\boldsymbol{T}_S = -\frac{D_e}{\lambda_J^2} \boldsymbol{m} \times \boldsymbol{S} - \frac{D_e}{\lambda_\varphi^2} \boldsymbol{m} \times (\boldsymbol{m} \times \boldsymbol{S}) \qquad \text{Eq. 2-22}$$

The equation of motion for magnetisation is now an altered LLG equation, including Eq. 2-22, given by Eq. 2-1.

Using the relations $\nabla \cdot J_c = 0$ and $\boldsymbol{E} = -\nabla V$, the following Poisson equation[37,38] for the electric potential is obtained from Eq. 2-19. It should be noted that the timescales of $\boldsymbol{m}$ and $\boldsymbol{S}$ have vastly different timescales, ps and fs, respectively.

$$\nabla^2 V = -\frac{(\nabla V)\cdot(\nabla\sigma)}{\sigma} + \frac{\beta_D D_e e}{\sigma\mu_B}\nabla\cdot(\nabla \boldsymbol{S})\boldsymbol{m} \qquad \text{Eq. 2-23}$$

Eq. 2-23 is evaluated for a set spin accumulation and potential boundary conditions on a set of electrodes and thus using the calculated electric potential, the spin current density is obtained as:

$$\begin{aligned}\boldsymbol{J}_S = &-\beta_\sigma \frac{\mu_B}{e}\sigma(\boldsymbol{E}\otimes\boldsymbol{m}) - \beta_\sigma\beta_D D_e\big((\nabla\boldsymbol{S})\boldsymbol{m}\big)\otimes\boldsymbol{m} - D_e\nabla\boldsymbol{S} \\ &+ \theta_{SHA}\frac{\mu_B}{e}\boldsymbol{\varepsilon}\sigma\boldsymbol{E}\end{aligned} \qquad \text{Eq. 2-24}$$

And finally, from Eq. 2-1 and Eq. 2-24, the spin accumulation equation of motions becomes:

$$\begin{aligned}\frac{\partial\boldsymbol{S}}{\partial t} = &-\beta_\sigma\frac{\mu_B}{e}\sigma(\boldsymbol{E}\nabla)\boldsymbol{m} - \beta_\sigma\beta_D D_e\big[\big((\nabla\boldsymbol{S})\boldsymbol{m}\nabla\big)\boldsymbol{m} + \boldsymbol{m}\nabla\cdot(\nabla\boldsymbol{S})\boldsymbol{m}\big] \\ &- \theta_{SHA}\frac{\mu_B}{e}\sigma\nabla\cdot(\epsilon\boldsymbol{E}) + D_e\nabla^2\boldsymbol{S} \\ &- D_e\left(\frac{\boldsymbol{S}}{\lambda_{sf}^2} + \frac{\boldsymbol{S}\times\boldsymbol{m}}{\lambda_J^2} + \frac{\boldsymbol{m}\times(\boldsymbol{S}\times\boldsymbol{m})}{\lambda_\varphi^2}\right)\end{aligned} \qquad \text{Eq. 2-25}$$

Here, the equation is solved to obtain a steady state spin accumulation, $\frac{\partial\boldsymbol{S}}{\partial t} = 0$.

For a multilayered geometry, it is important to consider the mesh and interface boundary conditions. Boundary conditions are derived from the physical concept that both charge and spin currents perpendicular to a boundary not containing electrodes are zero such that $\mathbf{J}_\mathrm{C}\cdot\boldsymbol{n} = 0$ and $\mathbf{J}_\mathrm{S}\cdot\boldsymbol{n} = 0$, where $\boldsymbol{n}$ is normal to the boundary[39]. Applying these physical properties to Eq. 2-19 and Eq. 2-20 the following non-homogeneous Neumann boundary conditions are obtained, respectively, where $\nabla V\cdot\boldsymbol{n}$ is a boundary with an electrode.

$$\nabla V \cdot \boldsymbol{n} = \frac{\theta_{SHA} D_e e}{\sigma \mu_B} (\nabla \times \boldsymbol{S}) \cdot \boldsymbol{n}$$

$$(\nabla \mathrm{S}) \cdot \boldsymbol{n} = \frac{\theta_{SHA} \sigma \mu_B}{D_e e} (\varepsilon \mathbf{E}) \cdot \boldsymbol{n} \qquad \text{Eq. 2-26}$$

For cases without interfacial spin-orbit coupling, values of V and $\boldsymbol{S}$ at the interface can be derived by strictly applying both $\mathbf{J}_\mathrm{C} \cdot \boldsymbol{n}$ and $\mathbf{J}_\mathrm{S} \cdot \boldsymbol{n}$ [30,40]. For this case, the length scales λ_J and λ_φ govern the absorptions of the transverse components of a spin accumulation. However, another method utilises the complex spin-mixing conductance, $G^{\uparrow\downarrow}$, when the absorptions of transverse spin are confined to the interface, this follows the magnetoelectronic circuit theory[41]. The boundary conditions at an NM/FM interface for charge and spin currents are given as:

$$\mathbf{J}_\mathrm{C} \cdot \boldsymbol{n}|_N = \mathrm{J}_\mathrm{C} \cdot \boldsymbol{n}|_F = -\left(G^\uparrow + G^\downarrow\right)\Delta V + \left(G^\uparrow - G^\downarrow\right) \Delta V_S \cdot \boldsymbol{m}$$

$$\mathbf{J}_S \cdot \boldsymbol{n}|_N - \boldsymbol{J}_S \cdot \boldsymbol{n}|_F = \frac{2\mu_B}{e}\left[\mathrm{Re}\{G^{\uparrow\downarrow}\}\boldsymbol{m} \times (\boldsymbol{m} \times \Delta V_S) + \mathrm{Im}\{G^{\uparrow\downarrow}\}\boldsymbol{m} \times \Delta V_S\right] \qquad \text{Eq. 2-27}$$

$$\mathbf{J}_S \cdot \boldsymbol{n}|_F = \frac{\mu_B}{e}\left[-\left(G^\uparrow + G^\downarrow\right)(\Delta V_S \cdot \boldsymbol{m})\boldsymbol{m} + \left(G^\uparrow - G^\downarrow\right)\Delta V \boldsymbol{m}\right]$$

Here, ΔV is the potential drop across the NM/FM interface where $\Delta V = V_F - V_N$ and $\Delta \boldsymbol{V}_s$ is the chemical spin potential drop, where $\Delta \boldsymbol{V}_s = \left(\frac{D_e e}{\sigma \mu_B}\right) \boldsymbol{S}$. $G^\uparrow$and $G^\downarrow$ are the interface conductances for the majority and minority spin carriers, respectively. Using Eq. 2-27 alongside Eq. 2-19 and Eq. 2-24, the potential and spin accumulation on both sides of the boundary can be calculated. The transverse spin current absorbed at the boundary gives rise to a torque in addition to any other resulting torques due to the transverse spin accumulation in Eq. 2-22, to give:

$$\boldsymbol{T}_s^{\text{interface}} = \frac{g\mu_B}{e d_F}\left[\mathrm{Re}\{G^{\uparrow\downarrow}\}\boldsymbol{m} \times (\boldsymbol{m} \times \Delta V_S) + \mathrm{Im}\{G^{\uparrow\downarrow}\}\boldsymbol{m} \times \Delta V_S\right] \qquad \text{Eq. 2-28}$$

2.4 Thiele equation

A very common model used when considering skyrmion motion is the Thiele model[42] and the set of equations obtained for a skyrmion's velocity and angle of deviation from the applied current direction, namely the skyrmion Hall angle (SkHA). As skyrmions are considered stable quasi-particle objects it is commonly assumed that a rigid-body description is sufficient so the dynamics can be analysed using the Thiele equations[20,42–47]. This has been relatively successful in driving current-induced skyrmion motion, yielding good agreements at large skyrmion diameters at zero temperature. The Thiele equation is used throughout this work with contributions from the SOT and ISTT[20,44], as discussed later. The Thiele equation[47] is given below:

$$\boldsymbol{G} \times \boldsymbol{v} + \alpha \boldsymbol{\mathcal{D}} \cdot \boldsymbol{v} + 4\pi \boldsymbol{\mathcal{B}} \cdot \boldsymbol{J_c} = 0 \qquad \text{Eq. 2-29}$$

Here, the skyrmion velocity is $\boldsymbol{v} = (v_x, v_y)$. The first term in the above equation is known as the Magnus force term in which $\boldsymbol{G} = (0,0,4\pi\mathcal{W})$ is the gyromagnetic coupling vector. This term is akin to the macroscopic Magnus effect (like that of a spinning ball in the air) which tends to cause an object to deviate from the path of a driving force. The skyrmion topological charge is given as[47,48]:

$$\mathcal{W} = \frac{1}{4\pi} \int \boldsymbol{m} \cdot \left(\frac{\partial \boldsymbol{m}}{\partial x} \times \frac{\partial \boldsymbol{m}}{\partial y}\right) dx dy \qquad \text{Eq. 2-30}$$

The second term in Eq. 2-29 is the dissipative force term which includes the dissipative tensor that describes the effect of the force on a moving skyrmion given as:

$$\boldsymbol{\mathcal{D}} = 4\pi \begin{pmatrix} \mathcal{D}_{xx} & \mathcal{D}_{xy} \\ \mathcal{D}_{yx} & \mathcal{D}_{yy} \end{pmatrix} \qquad \text{Eq. 2-31}$$

Where $\mathcal{D}_{ij}$ are determined via an integral of the region containing the skyrmion. When considering rigid body skyrmions $\mathcal{D}_{xx} = \mathcal{D}_{yy} = \mathcal{D}$ and $\mathcal{D}_{xy} = \mathcal{D}_{yx} = 0$.

The final term in Eq. 2-29 is the driving force term where $\boldsymbol{J_c} = (j_x, j_y)$ is the charge current in a HM substrate layer and $\boldsymbol{\mathcal{D}}$ is a dissipative tensor. Through an extensive mathematical process which has been completed by numerous authors, the Thiele equation outputs under the assumptions above the velocity and SkHA as given below, respectively[20,44,49,50].

$$v = \left(v_x^2 + v_y^2\right)^{\frac{1}{2}} = \left(\frac{(u_{SOT} - \beta_{STT} D u_{STT})^2 + u_{STT}^2}{1 + (\alpha D)^2}\right)^{\frac{1}{2}}$$

$$\tan(\theta_{SKHA}) = \frac{v_y}{v_x} = \frac{u_{SOT} + (\alpha - \beta_{STT}) D u_{STT}}{\alpha D u_{SOT} - (1 + \alpha\beta_{STT} D^2) u_{STT}} \qquad \text{Eq. 2-32}$$

Here, $u_{SOT} = \frac{J_{HM}\mu_B \theta_{SHA,eff} \pi R}{4\pi e M_s d_F}$ is the SOT spin drift velocity and $u_{STT} = \frac{J_{FM} P g \mu_B}{2e M_s (1+\beta^2)}$ is the STT spin drift velocity. Furthermore, $D = \frac{R}{2\Delta}$, where R is the skyrmion radius as Δ, is the domain wall width. Each velocity component, $v_{(x,y)}$ has SOT and ISTT components included such that $v_{(x,y)} = v_{(x,y)}^{SOT} + v_{(x,y)}^{ISTT}$.

2.5 Modules

Modules in *Boris* are vitally important to the success of simulations. Various modules can be included in the system, by a simple command, that allows for a large amount of customisability for simulations. Listed below are the modules that have been used either singularly or in some combination throughout this work. In micromagnetic modelling, all modules are included via an effective field such that they are captured within the $\boldsymbol{H}_{eff}$ term in the LLG. In this section, italicised phrases are directly related to *Boris* – for example, *demag* is the demagnetising module in *Boris*.

2.5.1 Demagnetisation field

Magnetic dipoles interact via the dipole-dipole interaction, which tends to align magnetic dipoles anti-parallel to each other, causing a magnetic field to oppose the magnetisation internally, avoiding free poles. In magnetic materials, the dipole-dipole interaction results in the demagnetising field which opposes the magnetisation in a magnetic media as shown in Figure 2-2(a). The demagnetising field is highly dependent on the shape of the material which can be described by a demagnetising factor.

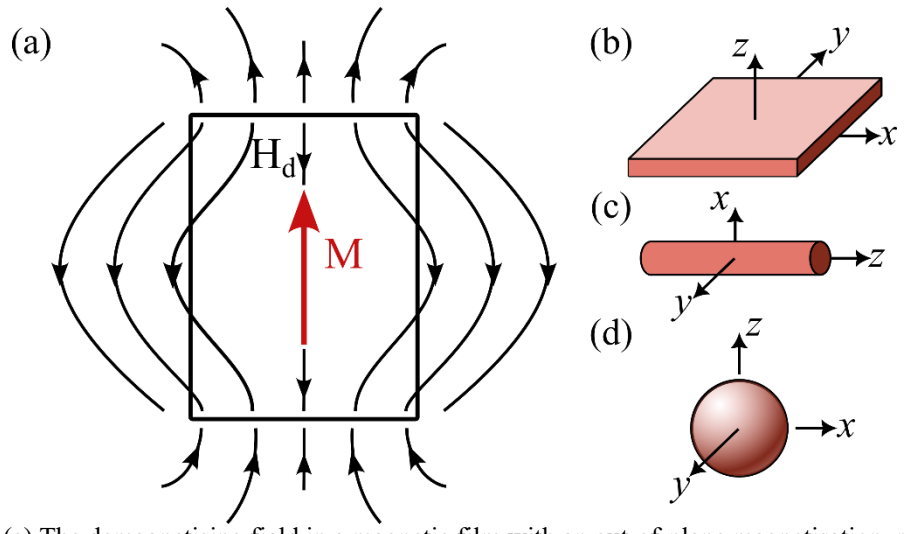

Figure 2-2 (a) The demagnetising field in a magnetic film with an out-of-plane magnetisation, represented by the red arrow. For uniform magnetisation, the demagnetisation component factors are for (b) a thin film, $N_x = N_y = 0, N_Z = 1$, (c) a thin rod, $N_x = N_y = 1/2\,, N_Z = 0$ and (d) a sphere $N_x = N_y = N_Z = 1/3$.

More importantly, for flat planes such as magnetic thin films, which are exclusively investigated in this work, the in-plane demagnetisation factors are zero and solely out-of-plane as shown in Figure 2-2(b). Therefore, for uniform magnetisation in-plane the

demagnetisation factor is zero but equal to the magnetisation strength for magnetisation out-of-plane, but in the opposite direction. The demagnetisation factors for uniform magnetisation in a thin rod and sphere are shown in Figure 2-2(c,d).

The demagnetisation term[51,52], *demag*, is a standard term that is included in all simulations and allows for the determination of the demagnetisation or stray field. It can be shown that for a magnetic body, the magnetostatic energy is given by:

$$E_d = -\frac{\mu_0}{2}\iiint \boldsymbol{M} \cdot \boldsymbol{H}_d dV \qquad \text{Eq. 2-33}$$

Here, $\boldsymbol{M}$ is the magnetisation vector, $\boldsymbol{H}_d$ is the demagnetisation field and V is the integration region which is the volume of the magnetic body. Thus, $\boldsymbol{H}_d$ is dependent on the shape of the material, for example, for simple ellipsoids $H_d = -NM$, however, a more general form is given below[53].

$$\boldsymbol{H}_d(\boldsymbol{r}_0) = -\int_{\boldsymbol{r}\epsilon V} \boldsymbol{N}(\boldsymbol{r}-\boldsymbol{r}_0)\boldsymbol{M}(\boldsymbol{r})\, d\boldsymbol{r} \qquad \text{Eq. 2-34}$$

Here, $\boldsymbol{r}_0$ is the position for the current demagnetising field and $\boldsymbol{r}$ are position vectors in the mesh and $\boldsymbol{N}$ is the symmetric demagnetisation tensor, given as[54]:

$$\boldsymbol{N} = \begin{pmatrix} N_{xx} & N_{xy} & N_{xz} \\ N_{xy} & N_{yy} & N_{yz} \\ N_{xz} & N_{yz} & N_{zz} \end{pmatrix} \qquad \text{Eq. 2-35}$$

Thus, for the demagnetisation field in the cell $\boldsymbol{r}_0$ the sum in Eq. 2-34 runs over all cells $\boldsymbol{r}$ in the discretisation mesh. This is a convolution sum evaluated using a fast Fourier

transform, based on the convolution theorem, as it requires a significant amount of computation resources for each iteration[51,52].

The demagnetisation field is also included in atomistic modelling, however, now a sum of all spins in a microcell of size h is incorporated such that $\boldsymbol{M} = (\mu_B/h^3)\sum_i \boldsymbol{S}_i$ which leads to the adapted version of Eq. 2-34 given as:

$$\boldsymbol{H}_d(\boldsymbol{r}_0) = -\frac{\mu_B}{h^3}\int_{\boldsymbol{r}\epsilon V} \boldsymbol{N}(\boldsymbol{r}-\boldsymbol{r}_0)\sum_i \boldsymbol{S}_i \; d\boldsymbol{r} \qquad \text{Eq. 2-36}$$

2.5.2 Dipole-dipole interaction

The dipole-dipole interaction is an effect that occurs between all spins within a magnetic body and as such can only be considered in atomistic modelling, given as[55]:

$$\boldsymbol{H} = \frac{\mu_B}{4\pi}\sum_{i\neq j}\frac{3(\boldsymbol{S}_j\cdot\hat{\boldsymbol{r}}_{ij})\hat{\boldsymbol{r}}_{ij}-\boldsymbol{S_j}}{r_{ij}^3} \qquad \text{Eq. 2-37}$$

Where $\boldsymbol{r}_{ij} = r_{ij}\hat{\boldsymbol{r}}_{ij}$ is the distance vector from spin i to spin j. However, the dipole-dipole interaction may also be calculated using macrocells where $\boldsymbol{M}_i = \sum_j \boldsymbol{S}_j$ is the total moment of the microcell in units of μ_B and the sum runs over all spins in a microcell i with size h. Therefore, the macrocell adaptation of the dipole-dipole interaction is given by:

$$\boldsymbol{H} = \frac{\mu_B}{4\pi}\sum_{i\neq j}\frac{3(\boldsymbol{M}_j\cdot\hat{\boldsymbol{r}}_{ij})\hat{\boldsymbol{r}}_{ij}-\boldsymbol{M_j}}{r_{ij}^3} - \frac{\mu_B}{3}\frac{\boldsymbol{M}_i}{h^3} \qquad \text{Eq. 2-38}$$

2.5.3 Exchange interaction

The exchange interaction between electrons is fundamental in ferromagnetism. In contrast to the magnetostatic term, the exchange interaction acts to align neighbouring

electron spins and the competition between these two terms gives rise to many domain structures.

When considering electrons intra-atomically – electrons in the same atom – the exchange interaction is described by Hund's rule[56], where electrons sharing the same orbital fill the orbital with the same spin quantum number taking into account Pauli's exclusion principle[57], in which no two fermions can occupy the same quantum state. Furthermore, the interatomic exchange interaction tends to align electron spins located in neighbouring atoms, macroscopically resulting in a net magnetic moment.

The exchange interaction, *exchange*, is the term considered for interaction between neighbouring magnetic moments. In general, the exchange energy between spins is given by the Heisenberg exchange Hamiltonian[55,58].

$$\mathcal{H}_{ij} = -2J\boldsymbol{S}_i \cdot \boldsymbol{S}_j \qquad \text{Eq. 2-39}$$

Here, J is the direction exchange integral in Joules, $\boldsymbol{S}_i$ and $\boldsymbol{S}_j$ are the spin operators in vector form. Thus, the exchange energy is given in terms of the energy between the neighbouring spins such that,

$$E_{ij} = -2JS^2\cos(\theta) \qquad \text{Eq. 2-40}$$

Where E is the energy in units of Joules, S and θ are the magnitude and the angle between $\boldsymbol{S}_i \cdot \boldsymbol{S}_j$, respectively. Note for $J > 0$ ferromagnetism results. Finally, the field term[6] that is included in $\boldsymbol{H}_{eff}$ is given as:

$$\boldsymbol{H}_{ex} = \frac{2A}{\mu_0 M_s^2}\left(\nabla^2\boldsymbol{M} - \frac{\boldsymbol{M}}{2|M|^2}\nabla^2(|M|^2)\right) \qquad \text{Eq. 2-41}$$

Here, ∇^2 is the Laplacian operator which requires homogenous Neumann boundary conditions to evaluate. The exchange interaction term can also be determined atomistically by considering all spins such that,

$$\boldsymbol{H}_{ex} = \frac{J}{\mu_0 \mu_B \mu_S} \sum_{j \epsilon N} \widehat{\boldsymbol{S}}_j \qquad \text{Eq. 2-42}$$

Here, $S = \mu_s \widehat{\boldsymbol{S}}$ in units of μ_B and the summation runs over all neighbouring spins *j*. J is the atomistic exchange energy which is a conversion from A in energy density units (J/m) such that $J = 2Aa\ (J)$ and μ_s is the atomistic magnetic moment in units of Bohr magneton such that $\mu_s = \frac{M_s a^3}{\mu_B}$, where a is the lattice discretisation.

2.5.4 Interfacial Dzyaloshinskii-Moriya exchange interaction

The Dzyaloshinskii-Moriya interaction (DMI)[59,60], or asymmetric exchange, is similar to the Heisenberg exchange interaction, however, instead of aligning neighbouring magnetic moment parallel or antiparallel, the DMI tends to align magnetic moments perpendicular or canted spins. It was originally proposed to explain weak ferromagnetism in antiferromagnetic systems, however, it is not a general interaction that exists in many systems as it requires specific conditions. The existence of DMI has prompted many studies and is now vitally important for manipulating magnetic structures and dynamics, such as magnetic skyrmions. There are two main situations in which DMI may arise: at an interfacial boundary and in bulk magnetic materials.

Interfacial DMI arises in FM/HM bilayers at the interface between which an interfacial asymmetry combined with a strong spin-orbit coupling exists and results in a canting of neighbouring spins as shown in Figure 2-3(a). Figure 2-3(a) shows an HM/FM bilayer in which the direction DMI factor is shown with spins becoming unaligned from one another. It should be noted that this effect is in constant competition with the exchange interaction. The bulk DMI arise in thicker magnetic media with a strong spin-orbit

coupling and non-centrosymmetric crystal structures which lack an inversion centre, as shown in Figure 2-3(c), for example, the B20 compound MnSi[61].

The DMI is crucial for chiral magnetic structures such as magnetic skyrmions as the continual rotation of neighbouring moments causes a full rotation over a given length dependent on the strength of the DMI. An example is shown in Figure 2-3(b) in which there is a continual rotation of the spins due to the interfacial DMI resulting in a skyrmion-like configuration, thus making skyrmion stability highly dependent on the DMI.

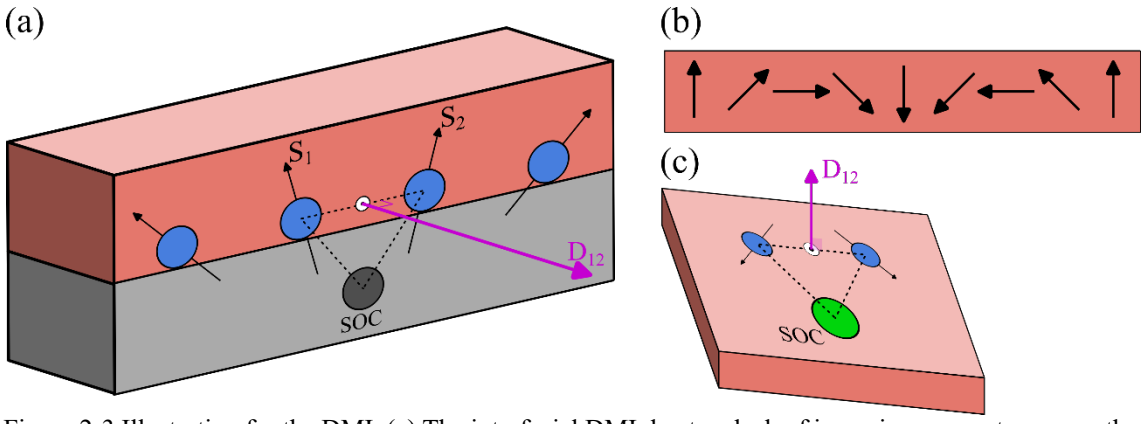

Figure 2-3 Illustration for the DMI. (a) The interfacial DMI due to a lack of inversion symmetry across the HM/FM interface, (b) the resultant effect of the interfacial DMI at an HM/FM boundary which resembles a Néel-skyrmion and (c) the bulk DMI, resulting from an internal asymmetry. D_{12} represents the DMI constant and directions between spins S_1 and S_2. The blue and green circles represent magnetic moments in FM media. The purple arrows display the direction of the DMI constant. The grey circles show strong spin-orbit coupling sites in HM media.

The effect of DMI[59,60] interactions between the surfaces, *iDMexchange*, of connected HM and FM layers is vital in this work as Pt/Co layers are predominantly considered. Similar to the Heisenberg exchange Hamiltonian[62] the DMI can be expressed as a Hamiltonian given as:

$$\mathcal{H}_{ij}^{DMI} = \boldsymbol{D}_{ij} \cdot \left(\boldsymbol{S}_i \times \boldsymbol{S}_j\right) \qquad \text{Eq. 2-43}$$

Here, $\boldsymbol{D}_{ij}$ is the Dzyaloshinskii-Moriya vector. The energy is thus given by $E_{DMI} = \sum_{i \neq j} \boldsymbol{D}_{ij} \cdot \left(\boldsymbol{S}_i \times \boldsymbol{S}_j\right)$. Finally, the field term can be expressed as[3]:

$$\boldsymbol{H}_{DMI} = -\frac{2D_{at}}{\mu_0 M_s^2}\left((\nabla \cdot \mathbf{M})\hat{\mathbf{z}} - \nabla M_z\right) \quad \text{Eq. 2-44}$$

Where D is the DMI constant and M_z is the out-of-plane magnetisation. Furthermore, for atomistic modelling $\boldsymbol{H}_{DMI}$ becomes $\hat{\boldsymbol{r}}_{ij}$ is the unit vector from the current spin i to the neighbouring spin j. D_{at} is the atomistic DM energy which is a conversion from D in energy density units (Jm^{-2}) such that $D_{at} = Da^2$ where a is the lattice discretisation.

2.5.5 Roughness

It is well-known that surface roughness in magnetic structures has a significant effect on magnetic textures, for instance, the pinning of skyrmions and domain walls, due to the changes in the physical behaviour of the magnetic system. For finite difference modelling, roughness is typically mapped on to the rectangular mesh, however, this leads to the staircase approximation which can become problematic for small roughness levels as very small cell sizes are required to represent the roughness. A 3D simulation with a cell-size reduction from 5 nm to 1 nm can increase the simulation complexity by two orders of magnitude, resulting in massive simulation periods even for modern-day processing power, however, there is a fine equilibrium to be found between cell size and simulation time. Figure 2-4(a) shows a large cell size for a roughened body resulting in a fast simulation time but neglects the roughness due to the resolution, conversely Figure 2-4(b) shows the same roughened body with a small cell resulting in a higher resolution simulation but a significant increase in time, the reciprocal effect of Figure 2-4(a). Finally, Figure 2-4(c) combines the latter two methods by increasing the resolution in the roughened region but using a much lower resolution in the bulk of the body where the changes in the magnetisation are minimal.

The method in Figure 2-4(c) can be implemented by introducing a new energy term which will accommodate the roughness without the requirement of mesh refinement. For a magnetic body with a uniform magnetisation direction, the magnetostatic energy can be obtained from the magnetostatic field, given as:

$$\boldsymbol{H}_d(\boldsymbol{r}_0) = -\int_{\boldsymbol{r}\epsilon V} \boldsymbol{N}(\boldsymbol{r}-\boldsymbol{r}_0) \times \boldsymbol{M}(\boldsymbol{r})\, d\boldsymbol{r} \qquad \text{Eq. 2-45}$$

$$\varepsilon_{(SL,\ ST,\ SP)} = \frac{\mu_0 M_s^2}{2} \sum_{\boldsymbol{r}\epsilon V} N_{xx}(\boldsymbol{r}-\boldsymbol{r}_0)\ \ (\boldsymbol{r}_0 \epsilon V) \qquad \text{Eq. 2-46}$$

Where M_s is the saturation magnetisation, $\mathbf{r}$ and $\mathbf{r}_0$ are the cell position vectors inside the magnetic body V, $\boldsymbol{M}$ is the magnetisation vector function and $\boldsymbol{N}$ is the demagnetising vector. The demagnetising vector contains three diagonal elements, N_{xx}, N_{yy} and N_{zz}, where the off-diagonal elements are $N_{xy} = N_{yx}$, $N_{xz} = N_{zx}$ and $N_{yz} = N_{zy}$.

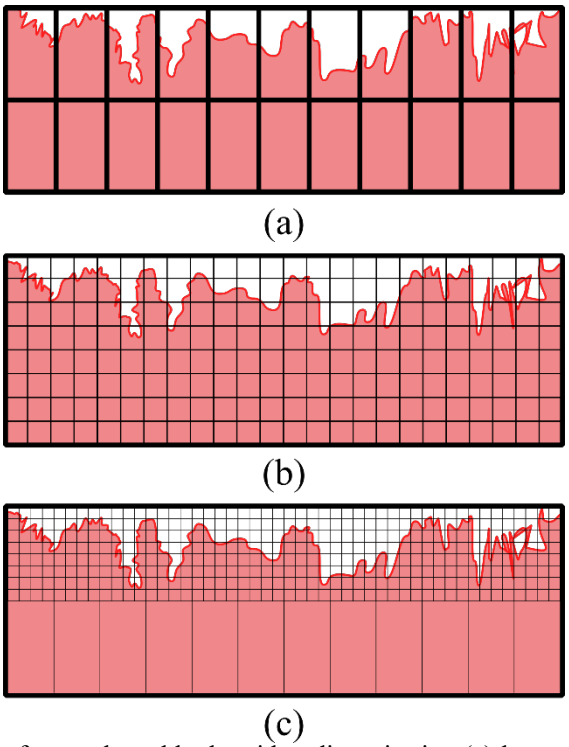

Figure 2-4 Representation of a roughened body with a discretisation (a) larger than the roughness depth, (b) sufficiently small to capture the resolution of the roughness and (c) a combination of the methods (a) and (b).

The equations above only describe *smooth* surfaces and do not include the added roughness energy terms, $\varepsilon_{RL,RT,RP}$, which are obtained in all magnetisation directions for the roughened body from Eq. 2-46 with V replaced with V_r [63]. These terms are then superimposed on to the smooth body, the full expansion and validation are not shown for

brevity but can be found in Ref.[37], which leads to a final field-like equation for a roughened body, given by:

$$\boldsymbol{H}_R(\boldsymbol{r}_0) = -\left[\sum_{r\in V} \boldsymbol{N}(\boldsymbol{r}-\boldsymbol{r}_0)G(\boldsymbol{r},\boldsymbol{r}_0)\right]\boldsymbol{M}(\boldsymbol{r}_0) \quad (\boldsymbol{r}_0 \epsilon V) \qquad \text{Eq. 2-47}$$

Here, $G(\boldsymbol{r},\boldsymbol{r}_0)$ is used as a simplification given by:

$$G(\boldsymbol{r},\boldsymbol{r}_0) = \begin{cases} \frac{N_V}{N_{Vr}} - 1 & \boldsymbol{r} \wedge \boldsymbol{r}_0 \in V_r \\ -1 & \boldsymbol{r} \vee \boldsymbol{r}_0 \in V - V_r \end{cases} \qquad \text{Eq. 2-48}$$

Here, N_V and N_{Vr} are the number of cells containing magnetic moments, counted in the same finite difference mesh. Note, $N_{Vr} < N_V$ as the roughened magnetic body will always be smaller than the smooth body.

2.5.6 Uniaxial magnetocrystalline anisotropy

Many magnetic materials have well-defined crystal structures, for example, hexagonal close-packed and body-centred cubic for Co and Ir, respectively, resulting in periodic lattice potential which electron spins can couple to through the spin-orbit interaction. As such, there is an additional energy term which varies locally with the orientation of the magnetic moments. As a result, a preferential direction for magnetic moments arises, which is known as magnetocrystalline anisotropy (MCA), and is dependent on the crystal structure.

The simplest form of MCA is uniaxial MCA which is characterised as having one rotational symmetry axis. As such, the standard nomenclature describing the direction of the rotational symmetry axis, which also happens to be the direction of lowest anisotropy energy, is deemed the easy axis with the largest anisotropy energy deemed the hard axis. Typically, the hard axis is perpendicular to the easy axis. MCA is essential in permanent

magnets as it dictates magnetic characteristics. For example, magnetic moments in materials with weak MCA break in domain structures due to the demagnetising field on the macro-scale, resulting in a significantly reduced magnetic moment at remanence. Furthermore, due to the reduced coercivity, the material is easy to demagnetise. On the other hand, materials that show a strong anisotropy typically have a large coercivity and remanence, allowing the magnetic media to have a strong net magnetic moment which is typically showcased by the strongest magnetic media.

The uniaxial MCA, *aniuni*, is present in all magnetic bodies. Uniaxial anisotropy is the simplest type of MCA as it is characterised as having a single rotational symmetry axis[64].

$$\boldsymbol{H}_{uni} = \frac{2K_1}{\mu_0 M_s}(\boldsymbol{m}\cdot\boldsymbol{e}_A)\boldsymbol{e}_A + \frac{4K_2}{\mu_0 M_s}[1-(\boldsymbol{m}\cdot\boldsymbol{e}_A)^2](\boldsymbol{m}\cdot\boldsymbol{e}_A)\boldsymbol{e}_A \qquad \text{Eq. 2-49}$$

Where $\boldsymbol{m} = \frac{\boldsymbol{M}}{|Ms|}$, K_1 and K_2 are uniaxial constants, and $\boldsymbol{e}_A$ is the easy axis direction. Which can be expressed atomistically as:

$$\boldsymbol{H}_{uni} = \frac{2K_{1,at}}{\mu_0\mu_B\mu_S}[\boldsymbol{e}_1\alpha(\beta^2+\gamma^2)+\boldsymbol{e}_2\beta(\alpha^2+\gamma^2)+\boldsymbol{e}_3\gamma(\alpha^2+\beta^2)] \qquad \text{Eq. 2-50}$$
$$-\frac{2K_{2,at}}{\mu_0\mu_B\mu_S}[e_1\alpha\beta^2\gamma^2+\boldsymbol{e}_2\alpha^2\beta\gamma^2+\boldsymbol{e}_3\alpha^2\beta^2\gamma]$$

Here, $\alpha = \widehat{\boldsymbol{S}}\cdot\boldsymbol{e}_1, \beta = \widehat{\boldsymbol{S}}\cdot\boldsymbol{e}_2, \gamma = \widehat{\boldsymbol{S}}\cdot\boldsymbol{e}_3$. Also $\boldsymbol{S} = \mu_s\widehat{\boldsymbol{S}}$. $K_{n,at}$ is the atomistic anisotropy in units of Joules and is given by $K_{n,at} = K_n a^3$.

2.5.7 Spin-orbit torque field

The SOT is given by[3]:

$$\boldsymbol{T}_{SOT} = \theta_{SHA,eff}\frac{\mu_B}{e}\frac{|J_c|}{d_F}(\boldsymbol{m}\times(\boldsymbol{m}\times\boldsymbol{p}) + r_G\boldsymbol{m}\times\boldsymbol{p}) \quad \text{Eq. 2-51}$$

Here, $\boldsymbol{p} = \boldsymbol{d}\times\boldsymbol{e}_{Jc}$, where $\boldsymbol{d}$ is the spin current direction incident on the interface, and $\boldsymbol{e}_{Jc}$ is the current density direction, d_F is the thickness of the FM layer. The additive field-like term is given by:

$$\boldsymbol{H}_{SOT} = -\frac{1}{\gamma M_s}\,\theta_{SHA,eff}\,\frac{\mu_B}{e}\,\frac{|J_c|}{d_F}\,(\boldsymbol{m}\times\boldsymbol{p} + r_G\,\boldsymbol{p}) \quad \text{Eq. 2-52}$$

Here, $\gamma = \mu_0|\gamma_e|g_r$ where γ_e is the electron gyromagnetic ratio and g_r is a relative gyromagnetic factor. The quantity $\theta_{SHA,eff}$ is the effect SHA, proportional to the real or intrinsic SHA and r_G being the FL-SOT coefficient. Both are given by:

$$\theta_{SHAeff} = \theta_{SHA}\left(1 - \frac{1}{\cosh\left(d_N/\lambda_{sf}^N\right)}\right)\times\frac{Re\{\tilde{G}\}^2 - Im\{\tilde{G}\}^2 + N_\lambda Re\{\tilde{G}\}}{\left(N_\lambda + Re\{\tilde{G}\}^2\right) + Im\{\tilde{G}\}^2} \quad \text{Eq. 2-53}$$

$$r_G = \frac{N_\lambda Im\{\tilde{G}\}^2 + 2Re\{\tilde{G}\}Im\{\tilde{G}\}^2}{N_\lambda Re\{\tilde{G}\}^2 + Re\{\tilde{G}\} - Im\{\tilde{G}\}^2}$$

Here, $N_\lambda = \frac{\tanh\left(d_N/\lambda_{sf}^N\right)}{\lambda_{sf}^N}$ and $\tilde{G} = \frac{2G^{\uparrow\downarrow}}{\sigma_N}$.

2.5.8 Zeeman interaction

An externally applied magnetic field on magnetic material will exert a torque on the magnetic poles within the media. The Zeeman effect describes the displacement of energy levels resulting in the uniformly spaced multiplet splitting of spectral lines. An example

of this is shown in Figure 2-5 which describes the splitting of energy levels of an electron in an externally applied magnetic field. The electron separated into two possible energy states: spin-up or spin-down. As expected, the electron spin-down (opposite direction to the field in this case) has much larger energy than an electron aligned parallel to the field. In micromagnetism, the Zeeman effect is simply the inclusion of an applied magnetic field which tends to align magnetic moments in the same direction as the field.

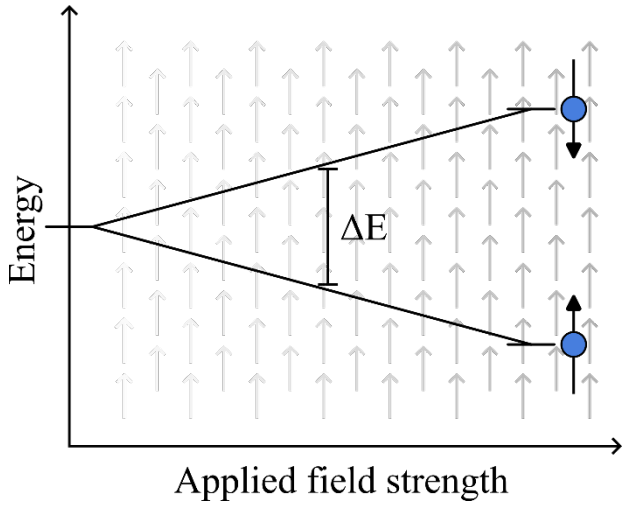

Figure 2-5 An arbitrary energy relationship on applied field strength on spin alignment. Increasing the applied magnetic field, represented by the gradient-shaded arrows, causes the splitting of spectral lines into two components – spin-up and spin-down – with a resulting change of energies between these states increasing with field strength.

2.5.9 Ruderman-Kittel-Kasuya-Yoshida interaction

The Ruderman-Kittel-Kasuya-Yoshida[65–67] (RKKY) interaction occurs in metals with localised magnetic moments, however, unlike the Heisenberg and DMI exchange interaction, it is not a direct interaction as it is mediated across valence electrons. The effect is an exchange coupling over a long range and is also anisotropic which can lead to complex domain structures. Interestingly, the RKKY interaction has an oscillatory behaviour which is dependent on the thickness of a non-magnetic spacer layer in multiple structures, as shown in Figure 2-6. When the exchange constant is positive, ferromagnetic couple occurs across the boundary, however, when it is negative, antiferromagnetic coupling exists, with the behaviour oscillating between the two states with increasing thickness. Note that this sign's dependence on the exchange constant is akin to that of the exchange interaction.

The RKKY interaction is thus extremely tuneable and allows for complex but elegant magnetic structures to be realised. A highly studied topic utilising this is synthetic antiferromagnets and ferrimagnets which allow for the stabilisation of skyrmions and zero SkHA in theory.

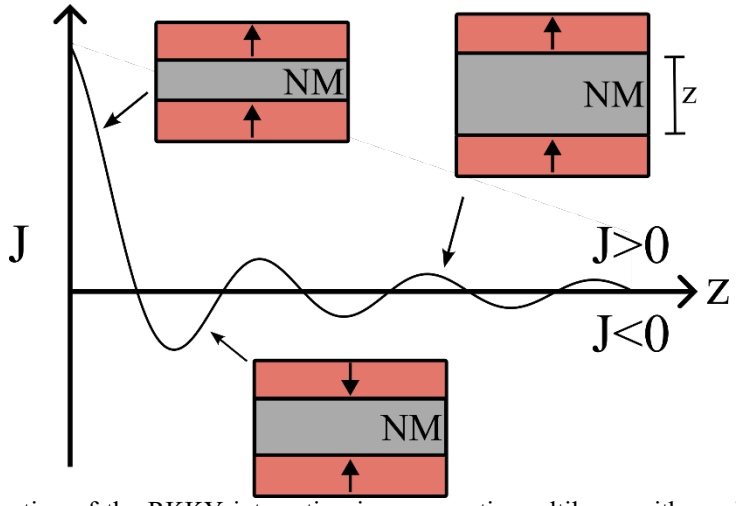

Figure 2-6 Visualisation of the RKKY interaction in a magnetic multilayer with a middle spacer layer, FM/HM/HM. Shown is the exchange constant, J, as a function of NM layer thickness. When $J > 0$ and $J < 0$, ferromagnetic and antiferromagnetism results, respectively.

2.6 Interfacial spin-transfer torque

The ISTT is the main focus of this work and, as the later results suggest, is a significant contribution to skyrmion motion. The ISTT is an unrecognised spin-torque contribution with no in-depth research conducted, however, it works alongside the SOT and in conjunction with the bulk STT, namely the Zhang-Li STT[17,19,68].

The ISTT arise due to an imbalance in the spin accumulation on either side of the HM/FM interface, which is shown in Figure 2-7. The spin imbalance arises due to the spin accumulation generated at magnetisation gradients and is due to the non-zero divergence of the in-plane spin current in the FM layer, as well as the spin mistracking effect due to the exchange rotation and spin dephasing processes. The imbalance gives rise to vertical spin current acting towards the HM layer, which contains both longitudinal and transverse spin components. However, it is the transverse spin currents that are absorbed in the interface due to the conservation of angular momentum resulting in the interfacial spin-torque. It is therefore similar to the SOT, however, instead of originating in the HM layer, this interfacial spin-torque originates in the FM layer.

The generated transverse components of the vertical spin current are the same transverse components from the spin accumulation which give rise to the Zhang-Li adiabatic and non-adiabatic STTs, however, the ISTT has a strength inversely proportional to the FM layer thickness. The ISTT is given below in the same form as the Zhang-Li STT.

$$\frac{\boldsymbol{T_{ISTT}}}{M_s} = -[(\boldsymbol{u}_{ISTT} \cdot \nabla)\boldsymbol{m} - \beta_{ISTT}\boldsymbol{m} \times (\boldsymbol{u}_{ISTT} \cdot \nabla)\boldsymbol{m}] \quad \text{Eq. 2-54}$$

Here, $\boldsymbol{u}_{ISTT} = P_{ISTT} g \mu_B \boldsymbol{J}_{FM} / 2eM_S(1 + \beta_{ISTT}^2)$ where the non-adiabaticity parameter β_{ISTT} are effective interfacial terms that can differ significantly from their bulk counterparts given in Eq. 2-11.

Figure 2-7 shows a representation of the ISTT effect. For an in-plane current injection into an HM/FM bilayer, yellow circles and electron spins accumulate at a magnetisation gradient such as a skyrmion, or other domain wall structure, shown in blue, which then diffuses into the HM layer. A sharper magnetisation gradient results in a larger spin accumulation and thus a stronger spin diffusion across the interface, and *vice versa* for shallower magnetisation gradients. Given that the FM layer is sufficiently thin enough to overcome the bulk STT, for magnetic textures (magnetisation gradients) such as skyrmions and domain walls, the ISTT will have a significant effect given that the magnetic textures are also small (and magnetisation gradients sharp). As shown in Ref.[20,44] when the skyrmion diameters are less than 100 nm, the ISTT has a significant effect which causes a deviation from the expected Thiele model but also aligns simulations closer to experimental results. The effect of the ISTT then is pronounced for skyrmions under 100 nm due to the magnetisation gradients being sharp enough for the ISTT to be significant enough to overcome the Zhang-Li STT.

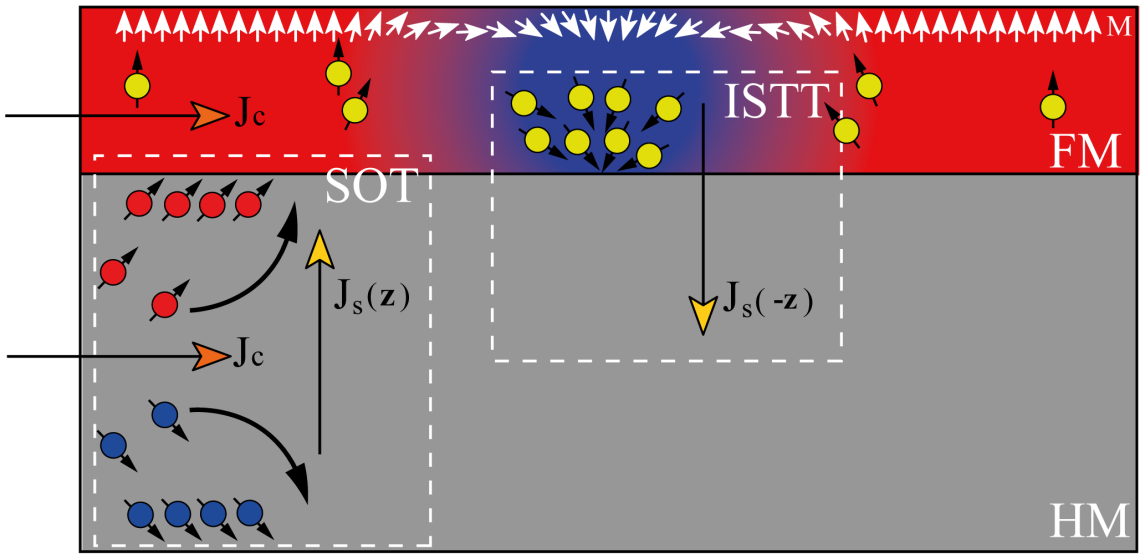

Figure 2-7 Illustration visualising the ISTT and the SOT in a magnetic multilayer consisting of HM and FM layers. A current is applied in-plane, from left to right of the figure. The white arrows represent the orientation of the local magnetisation in the FM layer and the coloured circles represent electron spins in a different configuration. The ISTT arises in the FM layer and diffuses into the HM layer due to spin-mistracking effects. The SOT arises in the HM layer due the SHE resulting in a vertical spin-current incident on the FM layer. Both effects result in a torque on the local magnetisation in the FM layer.

2.7 Spin-orbit torque

Another spin torque that is significant in current-driven magnetics is the well-understood SOT, which is typically the main contribution to skyrmion motion. The SOT is governed by the spin Hall effect (SHE) which is a phenomenon analogous to the classic Hall effect. However, the SHE considers electron spin accumulation at the lateral edges of a material and not electrons solely due to Lorentz force. The SOT is given by Eq. 2-51 with the field-like given by Eq. 2-52.

The physical origin of the SHE arises from two possible mechanisms, in which an electric current is converted into a spin current. The first is the extrinsic effect which consists of spin-dependent Mott scattering[69], where carriers with opposite spin diffuse in opposite directions when colliding with impurities in the material. The second is due to the intrinsic properties of the material, where the carrier's trajectories are distorted due to the spin-orbit interaction as a consequence of the asymmetries in the materials.

The SHE governs SOT via the accumulation of spins at the boundaries, as shown in a current-carrying sample due to the generation of a spin current. The spin current produced by the SHE is orthogonal to both charge current and spin polarisation, which results in

SOT, as the transverse components of the spin current are absorbed in the HM/FM interface. Figure 2-7 shows an illustration of SHE resulting in the SOT. SHE exploits the spin-orbit coupling (SOC) in an HM to convert the unpolarised charge into a pure spin current, which arises from both intrinsic and extrinsic effects, and gives rise to asymmetric scattering of conduction electrons. The asymmetry leads to deflections of spin-up and spin-down electrons in opposing directions leading to the transverse spin current. Due to the conservation of angular momentum, a resultant spin torque on the magnetisation in the FM occurs from absorbed itinerant electron spins which are converted to lattice and localised electron spins, and thus resulting in the SOT.

2.8 Conclusion

Presented in this chapter is the fundamental backend and theory of micromagnetic modelling in *Boris*. Starting with the LLG equation various adaptations including the spin accumulation, STT, stochasticity and temperature were shown, as well as an LLG with static assumption, all of which are crucial magnetisation equations of motion for work discussed later in Chapter 4 up to Chapter 7.

The drift-diffusion model was derived in brief to illustrate the methods of describing the interaction of a spin current with local magnetisation, namely the continuous and interfacial methods, both of which had advantages and disadvantages due to interface boundary assumptions.

With the LLG and solving method explained, the modules that *Boris* allows to be incorporated into the LLG could now be explained. Due to the nature of micromagnetics, all terms are included in an effective field term that can be simply added to the existing field term in the LLG.

Chapter References

1. Donahue, M. J. OOMMF User's Guide, Version 1.0, National Institute of Standards and Technology, Gaithersburg, MD. Preprint at https://doi.org/10.6028/NIST.IR.6376 (1999).

2. Vansteenkiste, A. *et al.* The design and verification of MuMax3. *AIP Adv* **4**, 107133 (2014).

3. Lepadatu, S. Boris Computational Spintronics User Manual. Preprint at https://doi.org/10.13140/RG.2.2.31496.88322/1.

4. Lepadatu, S., Mckenzie, G., Mercer, T., MacKinnon, C. R. & Bissell, P. R. Computation of magnetization, exchange stiffness, anisotropy, and susceptibilities in large-scale systems using GPU-accelerated atomistic parallel Monte Carlo algorithms. *J Magn Magn Mater* **540**, 168460 (2021).

5. Lepadatu, S. Unified treatment of spin torques using a coupled magnetisation dynamics and three-dimensional spin current solver. *Sci Rep* **7**, 12937 (2017).

6. Lepadatu, S. Boris computational spintronics - High performance multi-mesh magnetic and spin transport modeling software. *J Appl Phys* **128**, 243902 (2020).

7. Kittel, C. Introduction to Solid State Physics Charles Kittel. (John Wiley & Sons, Inc, 2005).

8. Hillebrands, B. & Ounadjela, K. *Spin dynamics in confined magnetic structures I*. (Springer, 2002).

9. Landau, L. & Lifshitz, E. On The Theory Of The Dispersion Of Magnetic Permeability In Ferromagnetic Bodies. *Phys. Zeitsch. der Sow* **8**, 153–169 (1935).

10. Landau, L. D. & Lifshitz, E. M. *Statistical Physics*. (Pergamon Press Ltd, 1980).

11. Gilbert, T. L. A phenomenological theory of damping in ferromagnetic materials. *IEEE Trans Magn* **40**, 3443–3449 (2004).

12. Garanin, D. Fokker-Planck and Landau-Lifshitz-Bloch equations for classical ferromagnets. *Phys Rev B* **55**, 3050 (1997).

13. Lakshmanan, M. The fascinating world of the Landau-Lifshitz-Gilbert equation: an overview. *Philosophical Transactions: Mathematical, Physical and Engineering Sciences* **369**, 1280–1300 (2011).

14. Lepadatu, S. Effect of inter-layer spin diffusion on skyrmion motion in magnetic multilayers. *Sci Rep* **9**, 9592 (2019).

15. di Fratta, G., Jüngel, A., Praetorius, D. & Slastikov, V. Spin-diffusion model for micromagnetics in the limit of long times. *J Differ Equ* **343**, 467–494 (2023).

16. Zhang, S. & Li, Z. Roles of nonequilibrium conduction electrons on the magnetization dynamics of ferromagnets. *Phys Rev Lett* **93**, 127204 (2004).

17. Li, Z. & Zhang, S. Magnetization dynamics with a spin-transfer torque. *Phys Rev B* **68**, 024404 (2003).

18. Albert, J., Macià, F. & Hernàndez, J. M. Effect of the Zhang-Li torque on spin-torque nano-oscillators. *Phys Rev B* **102**, 184421 (2020).

19. Li, Z. & Zhang, S. Domain-Wall Dynamics and Spin-Wave Excitations with Spin-Transfer Torques. *Phys Rev Lett* **92**, 207203 (2004).

20. MacKinnon, C. R. *et al.* Collective skyrmion motion under the influence of an additional interfacial spin-transfer torque. *Sci Rep* **12**, (2022).

21. Verhagen, T. G. A. *et al.* Temperature dependence of spin pumping and Gilbert damping in thin Co/Pt bilayers. *Journal of Physics: Condensed Matter* **28**, 056004 (2016).

22. Zhao, Y. *et al.* Experimental Investigation of Temperature-Dependent Gilbert Damping in Permalloy Thin Films. *Sci Rep* **6**, 22890 (2016).

23. Grenet, L. *et al.* Spin injection in silicon at zero magnetic field. *Appl Phys Lett* **94**, 032502 (2009).

24. Gozdur, R. & Najgebauer, M. Scaling analysis of phase transitions in magnetocaloric alloys. *J Magn Magn Mater* **499**, 166239 (2020).

25. Moreno, R. *et al.* Temperature-dependent exchange stiffness and domain wall width in Co. *Phys Rev B* **94**, 104433 (2016).

26. Atxitia, U. *et al.* Multiscale modeling of magnetic materials: Temperature dependence of the exchange stiffness. *Phys Rev B* **82**, 134440 (2010).

27. Vértesy, G. & Tomáš, I. Temperature dependence of the exchange parameter and domain-wall properties. *J Appl Phys* **93**, 4040 (2003).

28. Atxitia, U., Hinzke, D. & Nowak, U. Fundamentals and applications of the Landau–Lifshitz–Bloch equation. *J Phys D Appl Phys* **50**, 033003 (2016).

29. Evans, R. F. L. *et al.* Stochastic form of the Landau-Lifshitz-Bloch equation. *Phys Rev B* **85**, 014433 (2012).

30. Zhang, S., Levy, P. M. & Fert, A. Mechanisms of spin-polarized current-driven magnetization switching. *Phys Rev Lett* **88**, 236601 (2002).

31. Shpiro, A., Levy, P. M. & Zhang, S. Self-consistent treatment of nonequilibrium spin torques in magnetic multilayers. *Phys Rev B* **67**, 104430 (2003).

32. Petitjean, C., Luc, D. & Waintal, X. Unified drift-diffusion theory for transverse spin currents in spin valves, domain walls, and other textured magnets. *Phys Rev Lett* **109**, 117204 (2012).

33. Haney, P. M., Lee, H. W., Lee, K. J., Manchon, A. & Stiles, M. D. Current induced torques and interfacial spin-orbit coupling: Semiclassical modeling. *Phys Rev B* **87**, 174411 (2013).

34. Heide, C., Zilberman, P. E. & Elliott, R. J. Current-driven switching of magnetic layers. *Phys Rev B* **63**, 064424 (2001).

35. Keller, S. *et al.* Determination of the spin Hall angle in single-crystalline Pt films from spin pumping experiments. *New J. Phys.* **20**, 053002 (2018).

36. Dyakonov, M. I. Magnetoresistance due to Edge Spin Accumulation. *Phys Rev Lett* **99**, 126601 (2007).

37. Lepadatu, S. Effective field model of roughness in magnetic nano-structures. *J Appl Phys* **118**, 243908 (2015).

38. Lepadatu, S. Interaction of magnetization and heat dynamics for pulsed domain wall movement with Joule heating. *J Appl Phys* **120**, (2016).

39. Zhang, S. Spin Hall Effect in the Presence of Spin Diffusion. *Phys Rev Lett* **85**, 393 (2000).

40. Zhang, J., Levy, P. M., Zhang, S. & Antropov, V. Identification of Transverse Spin Currents in Noncollinear Magnetic Structures. *Phys Rev Lett* **93**, 256602 (2004).

41. Brataas, A., Nazarov, Y. U. V. & Bauer, G. E. W. Finite-element theory of transport in ferromagnet-normal metal systems. *Phys Rev Lett* **84**, 2481 (2000).

42. Thiele, A. A. Steady-state motion of magnetic domains. *Phys Rev Lett* **30**, 230–233 (1973).

43. Weißenhofer, M., Rózsa, L. & Nowak, U. Skyrmion Dynamics at Finite Temperatures: Beyond Thiele's Equation. *Phys Rev Lett* **127**, 047203 (2021).

44. MacKinnon, C. R., Lepadatu, S., Mercer, T. & Bissell, P. R. Role of an additional interfacial spin-transfer torque for current-driven skyrmion dynamics in chiral magnetic layers. *Phys Rev B* **102**, 214408 (2020).

45. Zeissler, K. *et al.* Diameter-independent skyrmion Hall angle observed in chiral magnetic multilayers. *Nat Commun* **11**, 428 (2020).

46. Koshibae, W. & Nagaosa, N. Theory of skyrmions in bilayer systems. *Sci Rep* **7**, 42645 (2017).

47. Büttner, F., Lemesh, I. & Beach, G. S. D. Theory of isolated magnetic skyrmions: From fundamentals to room temperature applications. *Sci Rep* **8**, 4464 (2018).

48. Everschor-Sitte, K., Masell, J., Reeve, R. M. & Kläui, M. Perspective: Magnetic skyrmions - Overview of recent progress in an active research field. *J Appl Phys* **124**, 240901 (2018).

49. Zhang, X., Zhou, Y. & Ezawa, M. Magnetic bilayer-skyrmions without skyrmion Hall effect. *Nat Commun* **7**, 1–7 (2016).

50. Jiang, W. *et al.* Direct observation of the skyrmion Hall effect. *Nat Phys* **13**, 162–169 (2017).

51. Miltat, J. & Donahue, M. Numerical Micromagnetics : Finite Difference Methods. In *Handbook of Magnetism and Advanced Magnetic Materials* (Wiley & Sons, Ltd, 2007).

52. Hayashi, N., Saito, K. & Nakatani, Y. Calculation of demagnetizing field distribution based on fast Fourier transform of convolution. *Japanese Journal of Applied Physics, Part 1: Regular Papers and Short Notes and Review Papers* **35**, (1996).

53. Lepadatu, S. Efficient computation of demagnetizing fields for magnetic multilayers using multilayered convolution. *J Appl Phys* **126**, 103903 (2019).

54. Newell, A. J., Williams, W. & Dunlop, D. J. A generalization of the demagnetizing tensor for nonuniform magnetization. *J Geophys Res Solid Earth* **98**, 9551–9555 (1993).

55. Evans, R. F. L. *et al.* Atomistic spin model simulations of magnetic nanomaterials. *Journal of Physics: Condensed Matter* **26**, 103202 (2014).

56. Hund, F. Zur Deutung verwickelter Spektren, insbesondere der Elemente Scandium bis Nickel. *Zeitschrift für Physik* **33**, 345–371 (1925).

57. Pauli, W. Über den Zusammenhang des Abschlusses der Elektronengruppen im Atom mit der Komplexstruktur der Spektren. *Zeitschrift für Physik* **31**, 765–783 (1925).

58. Mankovsky, S., Polesya, S. & Ebert, H. Extension of the standard Heisenberg Hamiltonian to multispin exchange interactions. *Phys Rev B* **101**, 174401 (2020).

59. Dzyaloshinsky, I. A Thermodynamic Theory of 'Weak' Ferromagnetism of Antiferromagnetics. *Journal of Physics and Chemistry of Solids* **4**, 241–255 (1958).

60. Moriya, T. Anisotropic superexchange interaction and weak ferromagnetism. *Physical Review* **120**, 91–98 (1960).

61. Mühlbauer, S. *et al.* Skyrmion Lattice in a Chiral Magnet. *Science (1979)* **323**, 915–919 (2009).

62. Cortés-Ortuño, D. *et al.* Proposal for a micromagnetic standard problem for materials with Dzyaloshinskii–Moriya interaction. *New J Phys* **20**, 113015 (2018).

63. Belusky, M., Lepadatu, S., Naylor, J. & Vopson, M. M. Evidence of substrate roughness surface induced magnetic anisotropy in Ni80Fe20 flexible thin films. *J Magn Magn Mater* **478**, 77–83 (2019).

64. Stoner, E. C. & Wohlfarth, E. P. A mechanism of magnetic hysteresis in heterogeneous alloys. *Philosophical Transactions of the Royal Society of London. Series A, Mathematical and Physical Sciences* **240**, 599–642 (1948).

65. Ruderman, M. A. & Kittel, C. Indirect Exchange Coupling of Nuclear Magnetic Moments by Conduction Electrons. *Physical Review* **96**, 99–102 (1954).

66. Kasuya, T. A Theory of Metallic Ferro- and Antiferromagnetism on Zener's Model. *Progress of Theoretical Physics* **16**, 45–57 (1956).

67. Yosida, K. Magnetic Properties of Cu-Mn Alloys. *Physical Review* **106**, 893–898 (1957).

68. Li, Z. & Zhang, S. Domain-wall dynamics driven by adiabatic spin-transfer torques. *Phys Rev B* **70**, 024417 (2004).

69. Farago, P. S. Spin-dependent features of electron scattering from optically active molecules. *Journal of Physics B: Atomic and Molecular Physics* **13**, L567 (1980).

3 Methods and Techniques

In the previous chapter, the magnetic equations of motion were explored alongside the drift-diffusion model and magnetic interactions used in *Boris*. In this chapter, the methods used to solve the magnetic equations of motion are outlined and explained. Following this, the algorithms used to track skyrmion motion in simulations as well as experiments are discussed. The experimental techniques used to create and analyse $(Ta(3.2)/Pt(2.7)/[Co_{68}B_{32}(0.8)/Ir(0.4))/Pt(0.6)]_{\times 8}/Pt(2.2)$ are then outlined. Finally, a discussion on the damping parameter discrepancies of similar structures is carried out.

3.1 Introduction

By its very nature, skyrmionics is an interdisciplinary field. The techniques for obtaining skyrmion information span over a large range of experiential methods such as scanning tunnel X-ray microscopy and time-resolved magneto-optical Kerr effect, to name two, but also computation methods with the use of a wide range of software packages. Some packages have been in development since micromagnetic modelling has been possible, namely, OOMMF[1], however, in recent years software has taken a massive innovative and technological leap forward, such as *Boris*[2].

All computational data in this project has been obtained using *Boris* with the use of its self-consistent spin transport solver, graphical processing unit (GPU) capabilities and seamless *Python* integration allowing for complex simulation to be designed. Furthermore, some experimental work has been completed in collaboration with the *University of Leeds, Bragg Centre for Material Research* and *Paul Scherrer Institut*. This work involves the creation of a magnetic system capable of sustaining magnetic skyrmions using direct-current magnetron sputtering, with material and skyrmion measurements conducted via electron beam lithography, scanning tunnel X-ray microscopy, X-ray reflectivity and the TrackMate algorithm.

These methods are outlined below alongside methods of solving the magnetic equations of motion, required for micromagnetic modelling.

3.2 Ordinary differential equation solver

There are many methods of solving ordinary differential equations (ODE), such as the Landau-Lifshitz-Gilbert (LLG) equation or in more general forms, Eq. 3-1. Following is a set of methods which can be used to find a numerical solution to the above equation. All are available in *Boris*.

$$\frac{dy(t)}{dt} = y'(t) = f(t, y), \qquad y(t_0) = y_0 \qquad \text{Eq. 3-1}$$

3.2.1 Steepest descent method

Most micromagnetic software solves the LLG, over some time frame, typically with additions such as additional torques, for example, the spin-orbit torque (SOT), interfacial spin-transfer torque (ISTT) and Zang-Li bulk spin-transfer torque (STT). There have been many successful attempts at optimising the solvers in terms of energy minimisation, however, numerical optimisation has taken the solving of the LLG to a heightened step, for static cases only (see Chapter 3.2.1).

For systems that require an initial ground state or energy equilibrium, the *steepest descent method*[3,4] can be used to obtain these states by only considering the static system at hand. The *steepest descent* or *gradient descent* is an iterative algorithm for finding the local minimum of an ODE which is accomplished by taking repeated steps in the opposite direction of the gradient of the function at the current point. Hence why this method is called the steepest descent as it is opposite to the steepest ascent which favours the direction of the gradient.

The process of determining the minima of a function, $f(t, y)$, can be achieved iteratively using the following procedure. Firstly, a point given by the initial conditions is located, as shown by the purple point in Figure 3-1, then the direction of the sharpest slope is required, and given that the function is differentiable this is given by $\nabla f(t, y)$, however, as we required the direction towards the minima, the opposite direction of this is taken, therefore, $-\nabla f(t, y)$, the direction is shown in Figure 3-1 by a black arrow for each new point. A step is then taken in the direction of the steepest slope given by h which is predefined. A second point is then obtained, and this process is then repeated until the rate of change of slope has converged. Therefore, for some initial point $f(t_0, y_0)$, as

shown by the purple point in Figure 3-1, the next point at which the procedure is repeated is given as $f(t_1, y_1) = f(t_0, y_0) - h\nabla f(t_0\,, y_0)$, shown as a red spot.

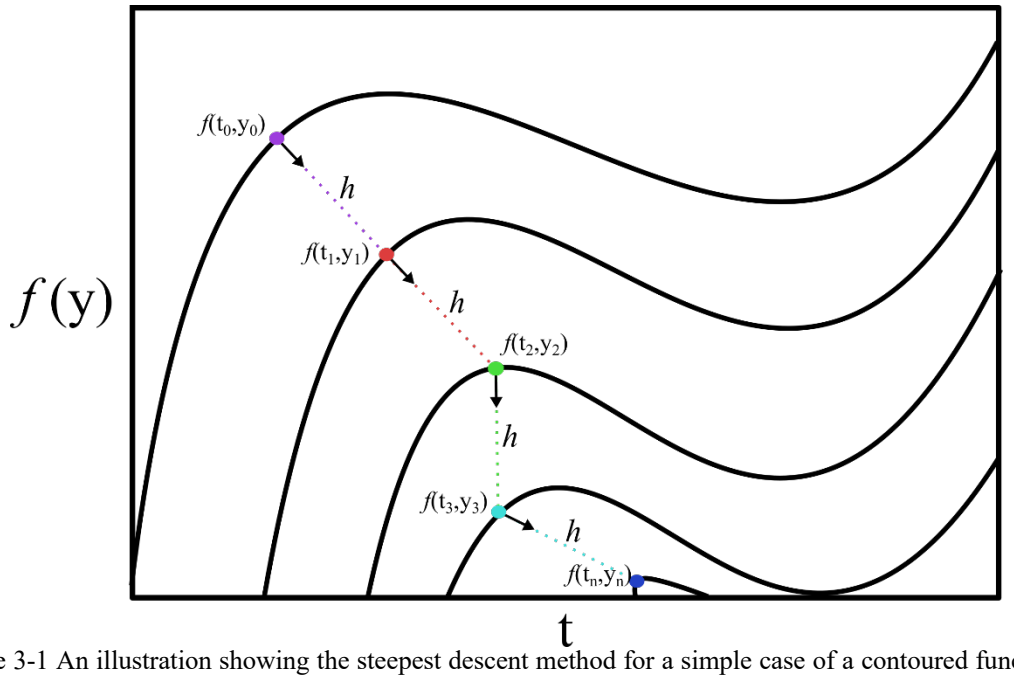

Figure 3-1 An illustration showing the steepest descent method for a simple case of a contoured function, akin to the contour lines on an ordnance survey map. The coloured points represent the points at which a new slope is determined for the next iteration. The arrows show the direction of the slope, and the dotted lines show the paths of length *h*.

Therefore, the *steepest descent method* can be generalised for *n* number of iterations as

$$f(t, y)_{n+1} = f(t, y)_n - h\nabla f(t, y)_n \qquad \text{Eq. 3-2}$$

The *steepest descent algorithm* would then follow the above rule, where for each iteration, the direction $\nabla f(t, y)_n$ always has the steepest slope. That is, the method continues to search in the direction which tends to minimise the value of the function at the given point.

3.2.2 Euler's method

Euler's method is a simple first-order numerical procedure for solving first-order differential equations with given initial conditions, also known as the Runge-Kutta 1st-order method. The method can be used to obtain a solution to an unknown function, given the initial conditions, by determining the slope from the differential equation and the tangent line. A small step h is taken along the tangent line and the process is repeated. Furthermore, it is assumed that the unknown curve does not change over a small step size, thus the estimated point, determined from the initial conditions, is assumed to lie on the unknown function. Therefore, the accuracy of the process is dependent on the step size Δt. The step size Δt is the difference between the successive steps h such that $\Delta t = h_i - h_{i-1}$ where i is the current step.

In essence, Euler's method, the approximation of the curve and subsequent curves can be determined by a sequence of short line segments expressed as

$$y_{i+1} = y_i + f(t_i, y_i)\Delta t \qquad \text{Eq. 3-3}$$

Here, y_{i+1} is the next estimated solution, y_i is the current value, h is the constant interval between steps and $f(t_i, y_i)$ is the value of the derivative at the current point. Thus, with initial conditions the starting point is y_0 and the slope $f(t, y_0)$ is evaluated. After deciding on a step size Δt, y_1 this is expressed as $y_1 = y_0 + f(t, y_0)\Delta t$.

3.2.3 Heun's method

Heun's method is very similar to Euler's method above, however, in this procedure, a predictor and a corrector are included. The predictor step is identical to Euler's method and, as the name suggests, gives a prediction to the next point, given by Eq. 3-3. Therefore, the point (t_{i+1}, y_{i+1}) is the new value from Euler's method where $t_{i+1} = t_i + \Delta t$ and the slope of the new point can be evaluated. This is where the similarities stop, and the corrector step is introduced. The corrector step involves returning to the original slope $f(t_i, y_i)$ with the predictor slope from the first step $f(t_{i+1}, y_{i+1})$ and taking the average. This is called the corrector, given below.

$$\Phi = \left[f(t_i, y_i) + f(t_{i+1}, y_{i+1})\right]\Big/_2 \qquad \text{Eq. 3-4}$$

Therefore, the general formula for Heun's method is

$$y_{i+1} = y_i + \frac{\left[f(t_i, y_i) + f(t_{i+1}, y_{i+1})\right]}{2}\ \Delta t = y_i + \Phi \Delta t \qquad \text{Eq. 3-5}$$

3.2.4 Runge-Kutta 4th order

The Runge-Kutta (RK) are a family of methods deemed some of the most effective and widely used methods for solving first-order differential equations given some set of initial conditions, for example. In the previous section, it was shown that using one estimate of the slope can give a reasonable prediction, namely Euler's method, otherwise known as the Runge-Kutta 1st-order method. It would be logical to assume that more estimates for the slope would result in a more accurate prediction, which is true in general and results in the higher-order Runge-Kutta method. Note that there is a Runge-Kutta 2nd-order method which is commonly used, however, here the Runge-Kutta 4th-order method (RK4)[5,6] will be discussed as it is an extension of the RK2 method with more steps of estimation. In essence, the RK4 method used four approximations to the slope. RK methods are all of the forms.

$$y(t_0 + \Delta t) = y(t_0) + \phi \Delta t, \qquad \phi = (1/6)[\mathrm{k}_1 + 2k_2 + 2k_3 + k_4] \qquad \text{Eq. 3-6}$$

Where t_0 is the current t, Δt is the interval step and ϕ is the weighted average of predicted slopes of the function $f(t, y)$ and k_n is the prediction of each step. It is clear now from this that the term fourth order originates from the four slope estimates of the function. The method also takes the average of the estimated slope and determines a weighted average which is shown by the integer values preceding k_n as well as the factor of 1/6

from the sum of these integers (1+2+2+1).The expression for the slope predictions k_n is shown below, as represented in Figure 3-2.

$$k_1 = f(t_0, y_0) \quad \text{Eq. 3-7}$$

$$k_2 = f\left(t_0 + {\Delta t}/{2}, y_0 + {k_1 \Delta t}/{2}\right) \quad \text{Eq. 3-8}$$

$$k_3 = f\left(t_0 + {\Delta t}/{2}, y_0 + {k_2 \Delta t}/{2}\right) \quad \text{Eq. 3-9}$$

$$k_4 = f(t_0 + \Delta t, y_0 + k_3 \Delta t) \quad \text{Eq. 3-10}$$

The method is as follows, with reference to Figure 3-2. To begin, an initial point is selected, determined from the given initial conditions $y(t_0) = y_0$, and the slope is determined, in this case k_1 given by Eq. 3-7. The slope at this point is known, due to $y(t_0)$, as it is an approximation to the derivative $y'(t)$ of the function over the next period.

Next, as an assumption is made over a small step the unknown function can be considered linear over that step. Thus, a forward half step is complete $t_0 + {\Delta t}/{2}$. This process isn't perfect, however, the results are very accurate. Now the derivative of the function at the new point, a half step forward along the slope of k_1, is required, therefore, the new point is dependent on k_1 and can be expressed as k_2 by Eq. 3-8. The second prediction should be better than the previous estimate at the midpoint, rather than the value of the slope, at the first point.

For the third prediction a similar approach is in use, however, another step forward is not taken, instead another prediction is made at the midpoint $t_0 + {\Delta t}/{2}$ using the slope of k_2 from the initial point determined. This is shown in Figure 3-2 by the blue dashed line which is the same slope as the predicted blue solid line for k_2. The estimate is then made at $t = t_0 + {\Delta t}/{2}$ for k_3, which is dependent on k_2, given by Eq. 3-9. This now gives a new estimate for the midpoint. Finally, a full step at $t = \Delta t$ from the original point is taken along the slope k_3. The point at $t = \Delta t$ can then be estimated for k_4 via Eq. 3-10.

Four estimates have now been determined for $t = t_0 \rightarrow \Delta t$ which can now be weighted and averaged for ϕ in Eq. 3-6 and hence a solution for $f(t_0 + \Delta t)$ is found with a reasonable accuracy. An example *Python* script for $dy/dt = t^2, y(1) = 1, \Delta t = 0.4$ is shown in Appendix B: RK4 simple python, which compares the Euler's and the RK4 method.

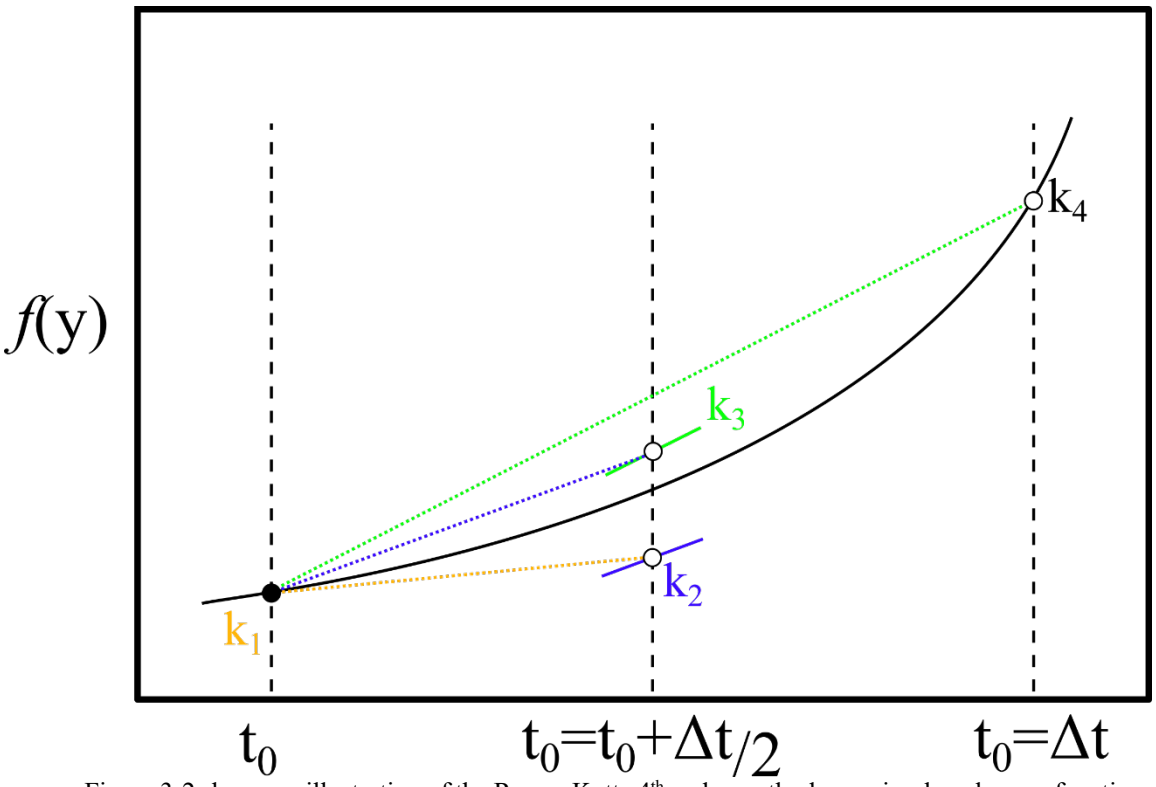

Figure 3-2 shows an illustration of the Runge-Kutta 4th-order method on a simple unknown function shown as the solid black line; the specifics of the function are, however, not important. The coloured dashed lines represent the prediction of the slope corresponding to the colour text indicating the order of the predictions. The black point is a point in the unknown function given by a set of initial conditions and the uncoloured points are the point at which the slope is predicted for k_{n+1}.

3.2.5 Runge-Kutta-Fehlberg of orders four and five

The Runge-Kutta-Fehlberg[5–7] method (RKF45) is a self-consistent method of solving ODEs based on the RK4 method. Both methods are of the fourth order, however, the RKF45 also includes an error estimate of the fifth order, hence the term RKF45.

Referring to the RK4 method, one major issue with this method is determining the best step size – too large results in reduced accuracy and too small results in a significant amount of computation. The RKF45 method can overcome this issue by introducing an extra procedure into the RK4 method. This procedure is used to determine the most

suitable step size at each step by comparing two estimates made for the solution. If the comparison lies within a certain tolerance, then the estimate is excepted with that step size, however, if the result is above the tolerance, then the step size is reduced. This loop is repeated until an estimate is accepted. Furthermore, if an estimate is accepted but to an unreasonably large accuracy or significant figures then the step size is increased. Herein lies the brilliance of this method as it internally self-adjusts the step size. For example, in a 1 ns simulation, the RK4 and RKF45 can be used to evaluate the LLG. The RK4 requires a set time step, which is in essence a guess unless multiple repeats of the system are completed, which is a waste of resources[8]. Whereas the RKF45 can be simply initialised with no set initial time step. A comparison of each method per iteration can result in a faster interaction, with a reasonable estimate for the time step, but using the RKF45 over the time of a simulation will result in a typically faster and more accurate evaluation.

Using a similar method to the RK4 the RKF45 method can be expressed as

$$y_{n+1} = y_n + \sum_{i=1}^{6} c_i k_1 \qquad \text{Eq. 3-11}$$

$$k_i = \Delta t f\left(t_n + a_i \Delta t, y_n + \sum_{j=1}^{i-1} \beta_{ij} k_i\right), \qquad i = 1,..,6 \qquad \text{Eq. 3-12}$$

Here, c_i are found by expanding y_{n+1} in powers of Δt. The coefficients k_n are determined by Fehlberg[9] and are given in Table 3-1 The Butcher tableau proposed by Fehlberg for the coefficient in Eq. 3-11 and Eq. 3-12, β_{ij} and c_i are weighting coefficients. In this case, as the time step may differ between interactions such that $\Delta t = t_{n+1} - t_n$. The values of k can be thought of as the change in slope, as in the RK4, as Δt varies. As shown above, $i = 1, \ldots, 6$ requires that this method has six function evaluations per step. The first four functions relate to the evaluation of the function such that this method becomes $O(\Delta t^4)$, however, due to six function evaluations the accuracy $O(\Delta t^5)$ as the expansion in the sixth order does not match. Fehlberg's addition does still allow for the exploitation of the sixth function.

Table 3-1 The Butcher tableau proposed by Fehlberg for the coefficients in Eq. 3-11 and Eq. 3-12

α_i	β_{ij}					c_i
0						16/135
1/4	1/4					0
3/8	3/32	9/32				6656/12825
12/13	1932/2197	-7200/2197	7296/2197			28561/56420
1	439/216	-8	3690/513	-845/4104		-9/50
1/2	-8/27	2	-3544/2565	1859/1404	-11/40	2/55

3.3 Data acquisition

Obtaining information from simulations is vitally important for obvious reasons, with *Boris* allowing for multiple methods of recording for a given system. Specific and detailed data, such as the iteration step, time step, magnetisation solver step, relaxations step and more can be obtained. Furthermore, magnetisation, charge and spin current, spin accumulation, temperature and contribution energy-specific data can be acquired. By far the most important for this work is the *skypos* and *skyshift* algorithms that allow tracking of skyrmions using different methods.

3.3.1 Skyshift algorithm

A simple yet resource-effective method of tracking skyrmions is the *skyshift* algorithm which allows the skyrmion position to be tracked to the accuracy of the discretisation. Figure 3-3 shows an illustration of the *skyshift* procedure which works by averaging the out-of-plane component of magnetisation in four quadrants of a tracking box.

Initially, the position of a skyrmion is determined so that a tracking box can be placed around the centre of the skyrmion, as shown in Figure 3-3(a), which is split into four quadrants M_I, M_{II}, M_{III} and M_{IV} which are the average magnetisation inside the quadrants. M_I, M_{II}, M_{III} and M_{IV} are all equal at initialisation (signified by the green colour). If a skyrmion shifts over the next time step, it moves relative to and thus becomes off-centre to the tracking box, as shown in Figure 3-3(b). The average magnetisation in each quadrant becomes uneven such that in this case $M_I > M_{IV} > M_{II} > M_{III}$. The tracking

algorithm will then shift the tracking box such that each quadrant is again equal, which is repeated every iteration. This then outputs the skyrmion position in terms of an *x* and *y* coordinate which doesn't necessarily start at (0,0) as the coordinate system is relative to the position in the mesh, therefore, the offset is typically removed. Although this algorithm is easy on computational resources, the output information is lacking as only the position is obtained, furthermore, the resulting skyrmion path possesses an algorithm artefact in the form of a staircase path. If more information is required, the *skypos* algorithm is better suited.

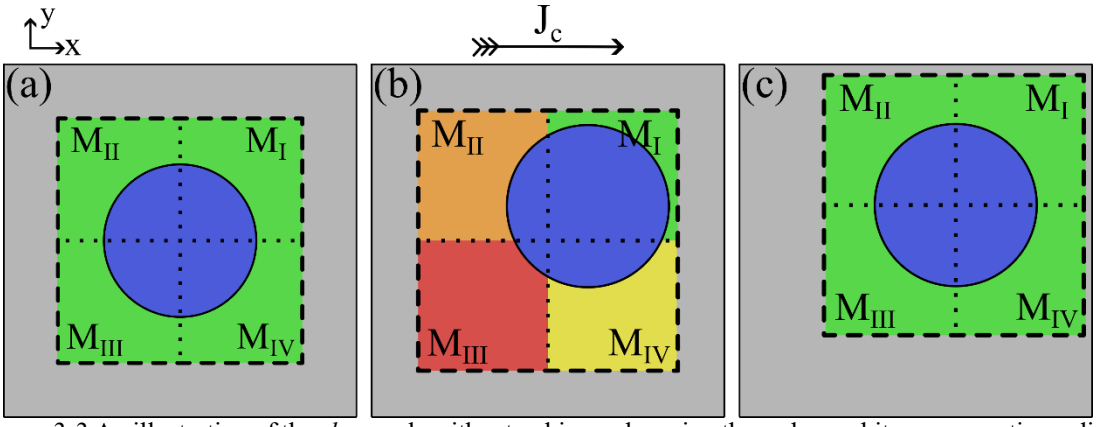

Figure 3-3 An illustration of the *skypos* algorithm tracking a skyrmion through an arbitrary magnetic media. (a) An initialisation of the skyrmion and tracking box, (b) the end of an iteration in which the skyrmion has moved in the *xy*-plane and (c) the tracking box centred on the skyrmion. The blue circle shape surrounded by a black dashed box signifies a skyrmion inside a tracking box, respectively. The tracking box is split into four quadrants M_I, M_{II}, M_{III} and M_{IV} with the colour of the quadrant representing the total area of the skyrmion in the corresponding quadrant (red and green meaning lowest and largest area as a comparison between all quadrants – yellow and orange are intermediate colours). When all quadrants are equal then all are coloured green.

3.3.2 Skypos algorithm

The *skypos* algorithm is more involved than the *skyshift* algorithm as more intensive steps are carried out and there is no averaging of magnetisation quadrants, however, instead of obtaining the position solely, *skypos* outputs the *xy*-position, *xy*-diameters, the domain wall width and the magnetisation saturation alongside the corresponding fitting errors, therefore eight output parameters compared to the previous two. The procedure is shown in Figure 3-4.

The initialisation of this system is the same as the *skyshift* algorithm in which a skyrmion is located and a tracking box is defined around the skyrmion, the size and centre positions are not as crucial as *skyshift* for reasons that will become clear. The skyrmion, when driven, will then shift relative to the tracking box as shown in Figure 3-4(b). From this point on, the algorithms are different in the procedure.

$$M_Z(x) = M_s \cos\left(2\, arctan\left(sinh\frac{\frac{R}{w}}{sinh\left(\frac{x - x_0}{w}\right)}\right)\right) \qquad \text{Eq. 3-13}$$

Next, a magnetisation line profile – a one-dimensional strip of magnetic moments – is taken in the *x*-direction along the black dashed line of the tracking box in Figure 3-4(b). An out-of-plane magnetisation vs *x*-position curve is obtained which allows a numerical solution to be obtained from Eq. 3-13. Where *R* is the skyrmion radius, *w* is the domain wall width, *x* is the dependent variable of *x*-position and x_0 is the skyrmion centre, are all fitting parameters to be obtained from the magnetisation line profile.

Given this information, the tracking box is shifted along the *x*-plane by the difference in the original position and x_0. This results in a tracking box centred on the skyrmion in only the *x*-plane, as shown in Figure 3-4(c). Note at this point the skyrmion diameter is not taken as *R* does not give an accurate representation. This is then repeated *y*-plane so that the tracking box can be adjusted in the *y*-direction, shown in Figure 3-4(d). However, the skyrmion diameter $D_{sk} = 2R$ is saved to be returned to the user.

The final step involves taking another line profile in the *x*-plane with the sole purpose of obtaining the skyrmion information in the *x*-plane, namely, the now accurate representation of the diameter. Now, the algorithm has the *x*-*y* position, relative to the starting position and not relative to the mesh coordinates, and the *x*-*y* diameters which are then output to the user directly or saved to a file. To finish, the tracking box is adjusted to fit the skyrmion, so the algorithm runs more efficiently, as shown in Figure 3-4(e). This algorithm provides the majority of the data obtained in the work.

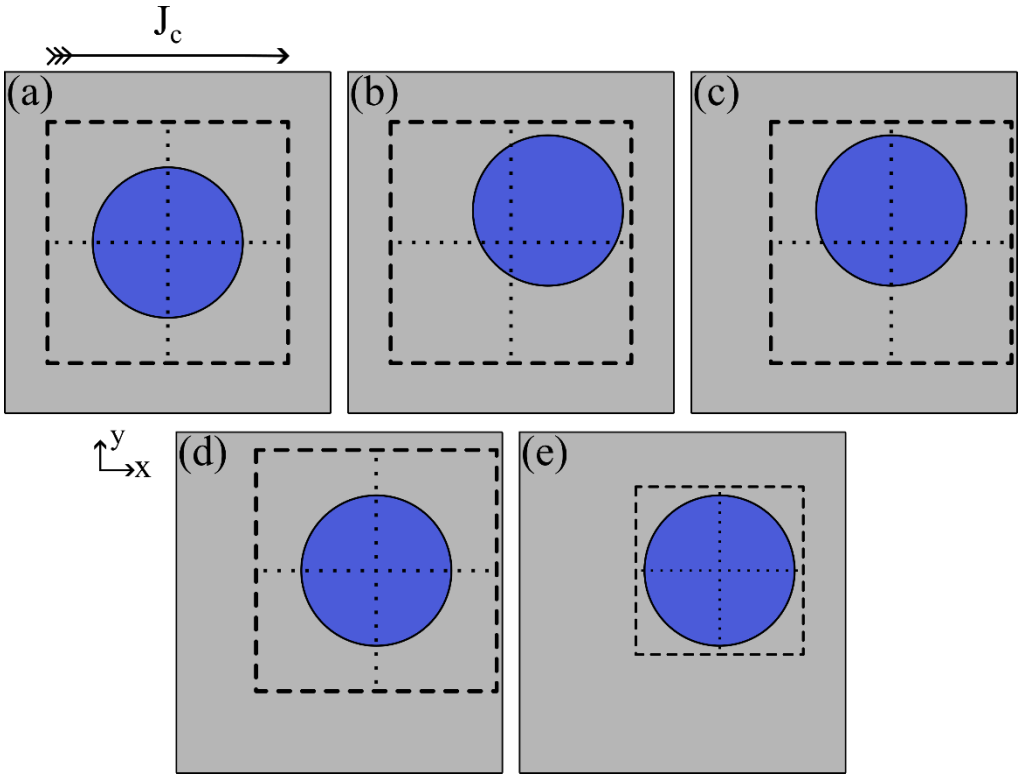

Figure 3-4 A representation of the *skypos* algorithm. (a) The skyrmion tracking initialisation in which the tracking box is set about the skyrmion centred. (b) Skyrmion transition through the magnetic media. (c) A line profile is taken in the *x*-direction to align the tracking box to the centre of the skyrmion with a step in the *x*-plane. (d) A line profile is taken in the *y*-direction to align the tracking box to the centre of the skyrmion with a step in the *y*-plane. (e) A final *x*-line profile is taken as a check and the excess space between the edges of the skyrmion and tracking box is reduced. The blue circle shape surrounded by a black dashed box signifies a skyrmion inside a tracking box, respectively. The black dotted line aims to give a guide to the centre of the tracking box.

3.3.3 TrackMate algorithm

The TrackMate package[10,11] is software that goes hand in hand with experimental observations and is used as a post-experimental method of analysis. It is perfectly adapted for skyrmion observations given that the images taken are of high enough resolution. Simply, the TrackMate package takes time-resolved images gathered from techniques such as scanning transmission X-ray microscopy (STXM) to highlight all circular objects within a single static image with a unique identifier. The specificity of the circular object tracked is highly tunable and will be unique for each set of images. This is then completed for the following image with the tracked objects.

Each image is then compared for object locations with the assumption that like-positioned objects are the same. This is completed for all images such that each object is tracked through multiple images. Thus, giving post-experiment tracking capabilities.

3.4 Experimental methods

Although a small portion of this work, various experimental techniques have been used to create magnetic systems capable of sustaining skyrmion stabilisation and skyrmion motion. Furthermore, methods of imaging skyrmions in real time, such as scanning tunnel X-ray microscopy, are required to capture skyrmion motion for extrapolation using tracking software.

Experimental methods in this work were used by the *University of Leeds* and *Bragg Centre for Material Research* whom obtained the silicon nitride membranes, fabricated the magnetic multilayer and used the TrackMate algorithm to obtain positional data of skyrmions from experimental imaging. The *Paul Scherrer Institut* conducted the skyrmion manipulation and imaging. The data analysis on the TrackMate algorithm data was conducted by *MacKinnon., C.* The methods used by the aforementioned groups is discussed below.

3.4.1 Direct-current sputtering

Direct-current (DC) sputtering[12–14] is a deposition technique used for creating thin-film structures, such as magnetic multilayers. It utilises a target material, the material required for deposition, which is liberated and attracted to a substrate; an illustration of DC sputtering apparatus is shown in Figure 3-5.

A basic DC sputtering set-up consists of a vacuum chamber that encases the entire system, a substrate to be coated and a target sample to liberate the material. Figure 3-5 shows a simple illustration of DC sputtering in effect. Initially, the vacuum chamber is evacuated to a base pressure which is then backfilled with high-purity Ar gas, as shown by the purple points; other gases can be used as long as they are inert. A DC electrical current is then applied to create an anode on the substrate and a cathode on the target material resulting in a potential gradient in the system. Violent collisions between the target material surface and the neutral argon atoms occur, resulting in the liberation of negatively charged target atoms which conglomerate into localised plasma. The positive anode, or charge bias,

attracts the ionised argon, free electrons and vaporised target atoms, and condenses on the substrate forming a thin film of the target.

Magnets can also be included behind the cathode which is used to reduce electron collisions with the substrate coated in the target materials, which allows for fast deposition rates.

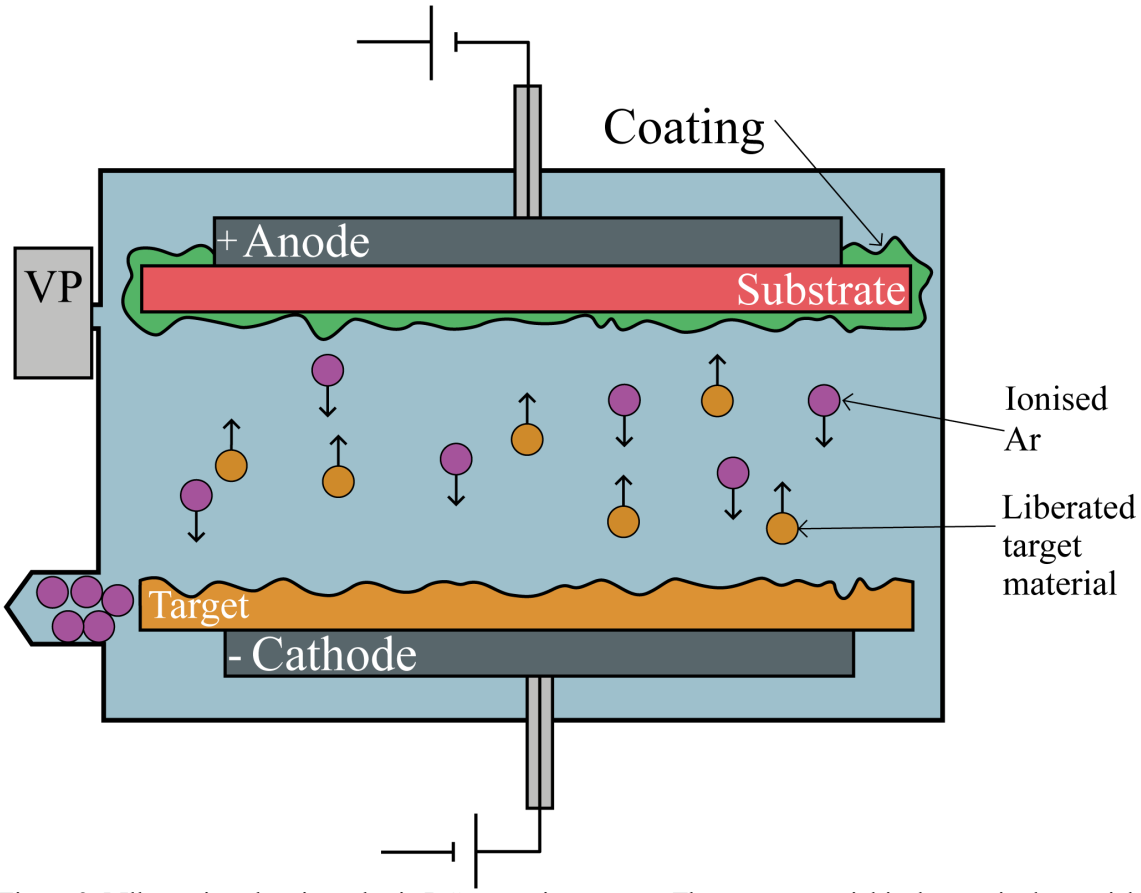

Figure 3-5 Illustration showing a basic DC sputtering system. The target material is the required material for a thin-layer adhesion to the substrate. The system itself is encased in a vacuum which is flooded with Ar which is ionised by a potential gradient.

3.4.2 Electron beam lithography

It is very common when designing nano-scale structures for more complex and intricate systems to be created, such as electrical contacts, which require a very accurate method for creation. Electron beam lithography[15–17] (EBL) is one such method which involves transferring a pattern on to a substrate by scanning the surface of a layer of resist by an accurate electron beam. The choice is then made to remove the exposed or non-exposed regions of the resist in a solvent. The benefit of using this method is that it allows for very

precise actions to be made, resulting in very small distinct features in the range of μm to nm. As with all methods, there are advantages and disadvantages compared to other methods. In essence, EBL uses a very small wavelength of electrons compared to higher wavelength optical methods, allowing for greater precisions but leading to significantly larger development times.

3.4.3 X-ray reflectivity

X-ray reflectivity (XRR)[18–20] is a method of measuring the thickness, density and roughness of both crystalline and amorphous multilayer structures. Furthermore, XRR can be used for single layers as well as multilayers.

XRR utilises X-rays which are applied to systems, ideally, flat surfaces at a very low incident angle such that total external reflection occurs at or below the critical angle. That critical angle itself is highly dependent on the material parameters, namely, the electronic density.

For XRR in single layers, the reflection on a substrate can be described as the interference of the reflection at two interfaces and requires the Fresnel equations of transmission and reflection. In essence, the principle of XRR is to reflect an X-ray beam from a flat surface and then measure the intensity of the reflected X-rays. This can become difficult if there is significant roughness on the surface such that the intensity profile will deviate from the predicted Fresnel law. The resulting intensity profile can be used to determine the density profile of the interface normal to the surface. For multilayers, the same process is followed for single layers, however, there is now a significantly different intensity profile as the reflections show many oscillations, namely Kiesseg fringes, akin to the Fabry-Pérot effect. The periodicity of these oscillations is then used to obtain the layer thickness, interlayer roughness and more.

3.4.4 Scanning transmission X-ray microscopy

The ability to image ever smaller objects in equally small structures is always increasingly important in research, not only in magnetism but in chemistry and biology. There are several cutting-edge techniques available for different length scales, maximum resolutions and imaging capabilities such as time-resolved and static methods. These included electron, soft-X-ray and light microscopy.

STXM[21–23] is one relatively simple method. An X-ray beam is incident on a zoning plate that focuses the X-ray beam into a small point source, then a sample is scanned in the plane of the zoning plane and then transmitted X-ray intensity is measured as a function of position on the sample. The use of soft X-rays[24] gives a high resolution of the surface of the sample, however, this then only takes into account the static systems. To take images of dynamic magnetic systems, the STXM must be converted to a time-resolved STXM system by using a stroboscopic scheme in which the magnetic circular dichroism (XMCD) effect is utilised as a contrast mechanism.

Skyrmion dynamics were imaged using STXM at the PolLux beamline of the Swiss Light Source. The X-ray magnetic circular dichroism (XMCD) effect was utilised as a contrast mechanism. The X-ray incident angle was chosen to be perpendicular to the sample, resulting in out-of-plane magnetisation sensitivity. This is discussed more in Section 5.2 in which the details of fabrication, imaging and tracking are detailed.

3.5 Conclusion

In this chapter the methods by which *Boris* solves magnetic equations of motions were discussed. An important method, the *steepest descent method*, which allows for complex and large simulations to be relaxed to a minimum or equilibrium energy state quickly, was discussed. Although this would never be used for dynamic magnetisation simulations, such as skyrmion prorogation, it does provide a very quick and effective method for relaxation to ensure correct initial conditions, thus saving computational resources albeit very situational.

Following this, the development of the main methods of solving the equations of motion was explored. Beginning with Euler's method, which involves making a prediction at a half step forward and then using this prediction to determine the result at the next full interaction point. Although this method is simple in execution it lacks accuracy. This was then developed into Heun's method which is markedly similar to Euler's, however, a corrector step is included for the final result which takes the average of previous predictions. Again, this is a quick method but lacks accuracy. Up to this point, the methods had been quick but lacked accuracy, however, the RK4 method was developed which is a commonly used method of solving differential equations. It involves following a similar procedure as Euler's method, however, four predictions for the function slope

are determined, weighted and averaged, resulting in a significant advancement in the accuracy. Up to this point, all the methods discussed were highly dependent on the step size selected before solving equations. This caveat was eliminated by using the RKF45 method which follows the RK4 method but uses a comparative step in which the slopes determined are compared to a set tolerance. The result is a highly efficient method which always determines the most efficient step size for the iteration at hand.

Data acquisition was then discussed, namely, the *skyshift* and *skypos* algorithms which allow for skyrmion information to be tracked during simulations. Whilst the *skyshift* algorithm was simple and resource-kind, it did not allow for detailed descriptions of a skyrmion with only the positions available. On the other hand, the more resource-intensive *skypos* algorithm allows for serval parameters to be probed at any time, and as a result is the method used to track skyrmions motion in the project herein out.

The experimental techniques used in this project were then outlined from the creation of the samples using direct-current magnetron sputtering and electron beam lithography. XRR was also used to determine the thickness of the individual layers in a multilayer system. Finally, time-resolved scanning tunnel X-ray microscopy was used to take images of the magnetic system containing skyrmions by utilising circular dichroism which was then fed into the TrackMate algorithm to track the position and size of multiple skyrmions.

Chapter References

1. Donahue, M. J. OOMMF User's Guide, Version 1.0, National Institute of Standards and Technology, Gaithersburg, MD. Preprint at https://doi.org/10.6028/NIST.IR.6376 (1999).

2. Lepadatu, S. Boris Computational Spintronics User Manual. Preprint at https://doi.org/10.13140/RG.2.2.31496.88322/1.

3. Curry, H. B. The method of steepest descent for non-linear minimization problems. *Q Appl Math* **2**, 258–261 (1944).

4. Cauchy, M. A. Méthode générale pour la résolution des systèmes ` d'équations simultanées. *Comptes rendus, Ac. Sci. Paris* **25**, 536–538 (1847).

5. Kutta, W. Beitrag zur näherungsweisen Integration totaler Differentialgleichungen. In *Zeitschrift für Mathematik und Physik* 435–453 (1901).

6. Runge, C. Ueber die numerische Auflösung von Differentialgleichungen. *Math Ann* **46**, 167–178 (1895).

7. Fehlberg, E. Eine Methode zur Fehlerverkleinerung beim Runge-Kutta-Verfahren. *Zeitschrift für angewandte Mathematik und Physik* **38**, 421–426 (1958).

8. Lepadatu, S. Speeding Up Explicit Numerical Evaluation Methods for Micromagnetic Simulations Using Demagnetizing Field Polynomial Extrapolation. *IEEE Trans Magn* **58**, 1–6 (2022).

9. Fehlberg, E. New High-Order Runge-Kutta Formulas with Step Size Control for Systems of First- and Second-Order Differential Equations. *Z Angew Math Mech* **44**, T17–T29 (1964).

10. Tinevez, J. Y. *et al.* TrackMate: An open and extensible platform for single-particle tracking. *Methods* **115**, 80–90 (2017).

11. Ershov, D. *et al.* TrackMate 7: integrating state-of-the-art segmentation algorithms into tracking pipelines. *Nat Methods* **19**, 829–832 (2022).

12. Wasa, K. & Hayakawa, S. Some features of magnetron sputtering. *Thin Solid Films* **52**, 31–43 (1978).

13. Gill, W. D. & Kay, E. Efficient Low Pressure Sputtering in a Large Inverted Magnetron Suitable for Film Synthesis. *Review of Scientific Instruments* **36**, 277 (2004).

14. Wu, Z.-Z. & Xiao, S. Physics and technology of magnetron sputtering discharges. *Plasma Sources Sci Technol* **29**, 113001 (2020).

15. Chen, Y. Nanofabrication by electron beam lithography and its applications: A review. *Microelectron Eng* **135**, 57–72 (2015).

16. Pease, R. F. W. Electron beam lithography. *Contemp Phys* **22**, 265–290 (1981).

17. Vieu, C. *et al.* Electron beam lithography: resolution limits and applications. *Appl Surf Sci* **164**, 111–117 (2000).

18. Toney, M. F. & Brennan, S. Measurements of carbon thin films using X-ray reflectivity. *J Appl Phys* **66**, 1861 (1998).

19. Gibaud, A. & Hazra, S. X-ray Reflectivity and diffuse Scattering. *Curr Sci* **78**, 1467–77 (2000).

20. Chason, E. & Mayer, T. M. Thin film and surface characterization by specular X-ray reflectivity. *Critical Reviews in Solid State and Materials Sciences* **22**, 1–67 (1997).

21. Prabu, V. *et al.* Instrumentation for in situ flow electrochemical Scanning Transmission X-ray Microscopy (STXM). *Review of Scientific Instruments* **89**, 063702 (2018).

22. Warwick, T. *et al.* A scanning transmission X-ray microscope for materials science spectromicroscopy at the advanced light source. *Review of Scientific Instruments* **69**, 2964 (1998).

23. Morrison, G. R. & Browne, M. T. Dark-field imaging with the scanning transmission X-ray microscope. *Review of Scientific Instruments* **63**, 611 (1998).

24. Kim, S. K., Kortright, J. B. & Shin, S. C. Vector magnetization imaging in ferromagnetic thin films using soft X-rays. *Appl Phys Lett* **78**, 2742 (2001).

4 Varying Surface Roughness Coherence Length for Isolated Skyrmion Motion

Skyrmions have emerged in recent years as potential information carriers for future spintronic devices, such as in random access and racetrack memory (RM), due to their topological stability and reduced energy requirements compared to traditional domain wall devices. Studying the behaviour of current-driven isolated skyrmion motion is important for a variety of information storage, transport and stability applications. Current-driven skyrmion motion is currently hindered by the skyrmion Hall angle (SkHA), in which the skyrmion path deviates from the direction of the applied charge current[1], which poses problems for these spintronics applications. Very recently, it has been proposed that interfacial spin-transfer torques (ISTTs)[2] may also be important, and thus a more complete model based on both spin-orbit torque (SOT) and ISTT can be formed.

Presented in this chapter is the study of the effect of including an additional ISTT term on skyrmion motion in a Co(1 nm)/Pt(3 nm) bilayer with and without surface disorder in the form of surface roughness as a function of skyrmion diameter.

4.1 Introduction

Skyrmions are topologically protected quasi-particle-like magnetic structures[3], which are of great interest as they can be efficiently manipulated using spin torques due to applied currents in ultra-thin magnetic multilayers, thus opening the possibility of a new class of spintronics devices[4–6]. Skyrmions have been observed at room temperature in systems with broken inversion symmetry[7–11], stabilised by the interfacial Dzyaloshinskii-Moriya interaction (DMI)[12,13], and more recently current-induced skyrmion motion has been demonstrated in ultra-thin magnetic multilayers[1,14–20] by utilising spin currents due to the spin Hall effect (SHE) which gives rise to SOT[21–25]. The SHE governs SOT via the accumulation of spins at the boundaries of a current-carrying non-magnetic (NM) metal/ferromagnetic (FM) bilayer due to the generation of transverse spin currents. The SHE exploits the spin-orbit coupling in an NM to convert the unpolarised charge into a pure spin current which arises from both intrinsic and extrinsic effects, and gives rise to an asymmetric scattering of conduction electrons. Irrespective of the underlying origins of the SHE, and thus spin accumulation at the NM/FM interface, the SOT exerted on the

FM magnetisation can be broken down into two components, namely the damping-like (DL) SOT and the field-like (FL) SOT. The two terms are shown in Eq. 2-51 in which the first term is ascribed as the DL-SOT which tends to eliminate the processional motion to align the spin towards the effective field. The seconds term in Eq. 2-51 is the FL-SOT which drives processional motion of magnetisation. Both FL- and DL-SOT are competing processes.

Current-driven skyrmion motion is currently hindered by the SkHA, θ_{SkHA}, in which the skyrmion path deviates from the direction of the applied charge current[1], which poses problems for spintronics applications. Furthermore, the SkHA has been shown to vary with the applied current strength[1,17–20], and this effect is not reproduced by analytical or numerical models in ideal structures. Whilst material imperfections play a very important role[26], there are many gaps in the literature, and a full understanding of how the SkHA varies with driving strength, skyrmion diameter, skyrmion chirality, and varying levels of magnetic and non-magnetic imperfections are required.

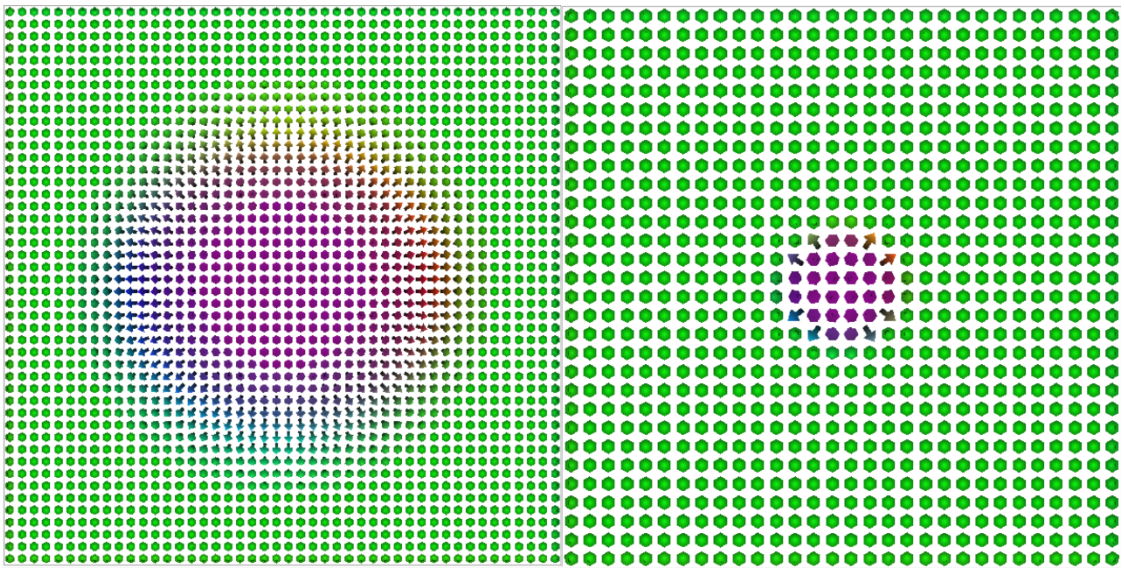

(a) (b)

Figure 4-1 A simulated comparison between (a) a 600 nm skyrmion that has not been relaxed in the current system, thus has not reached the equilibrium state, and (b) the same skyrmion as (a) but has reached an equilibrium state during relaxation and a diameter of 165 nm skyrmion. An out-of-plane field, H_z = 3 kAm^{-1}, was applied. Relaxation was achieved using the steepest descent method. The cell size for (a) and (b) is $(2 \times 2 \times 1)$ nm in a $(1000 \times 1000 \times 1)$ nm mesh size, however, (a) and (b) have different visual resolutions.

In recent experimental work, a largely independent SkHA on skyrmion diameter has been observed[16], however, analytical results based on the Thiele equation predict a significant increase in SkHA with decreasing skyrmion diameter, and this discrepancy is significantly pronounced for small diameters below 100 nm. In another study[1], experimental results are also compared to modelling based on SOT for very large skyrmions with diameters above 800 nm. Experimental and SOT simulations show good agreement for large skyrmion diameters, which showed slightly larger SkHA values for the SOT model, however, the SOT model predictions deviate significantly from the experimental results at small skyrmion diameters[16], even when very large damping values are assumed. Reducing the SkHA is paramount, and it has been theoretically shown that the spin-orbit coupling in an FM/FM bilayer can be used to tune the skyrmion Hall effect by controlling gate voltages to steer skyrmions[27], furthermore, changing the strength of the Rashba spin-orbit coupling has been shown to result in a negligible SkHA[28]. Here it is shown, using micromagnetics modelling coupled with a self-consistent spin transport solver in multilayers, the addition of ISTT results in a significantly reduced discrepancy between experimental and modelling results, and a good agreement is obtained with recent experimental results which have demonstrated a nearly diameter-independent SkHA[16].

4.2 Method

4.2.1 Initialisation

To begin, a system is designed so that the effect of the ISTT can be studied. The first step is to create a 1,000 x 1,000 nm mesh with two layers of 3 nm and 1 nm which correspond to Pt and Co, respectively, after the corresponding parameters are set as shown in Table 4-1. The magnetisation of the Co layer is aligned out-of-plane – the expected direction of magnetisation for ultrathin Co[29] – then a Néel-type skyrmion with a given core direction, chirality and diameter is generated in the centre of the FM mesh. Dirichlet boundary conditions are also implemented in the x-y direction to provide a wraparound effect for the demagnetisation field. If the boundary conditions were not included then skyrmions would interact with the boundaries of the mesh, however, with the wraparound effect of the included boundary conditions the system can effectively model a much larger and longer system. The system is then set to relax to equilibrium by minimising the steady

state precession, using the steepest descent method (see Chapter 3.2.1). Relaxing using this method is completed for a number of out-of-plane applied magnetic field values, allowing for skyrmions of varying diameters in an equilibrium state as shown in Figure 4-1.

Computations are completed using cell-centred finite difference discretisation. For magnetisation dynamics, the computational cell size used is (2 nm, 2 nm, 1 nm). For spin transport calculations the computation cell size is (2 nm, 2 nm, 0.5 nm) for both the Co and Pt layers. The Landau-Lifshitz Gilbert (LLG) equation is evaluated using the RKF45 evaluation which is an adaptive time step method. All computations are completed on the graphical processing unit (GPU) using the CUDA C framework. Roughness profiles are generated using a jagged granular generator algorithm. Equally spaced coefficients at 20, 40 and 60 nm spacings in the x-y plane are randomly generated. The remaining coefficients are obtained using bi-linear interpolation from the randomly generated points. These values are selected as they represent surface roughness profiles seen experimentally. Whilst it is important to study the effect of the ISTT on ideal structures, it is also paramount that surface roughness is considered as this can alter skyrmion motion significantly[45].

Finally, a skyrmion is placed in the centre of the Co layer and the system is relaxed to equilibrium using the steepest descent method after which the simulation is saved for electrical manipulation.

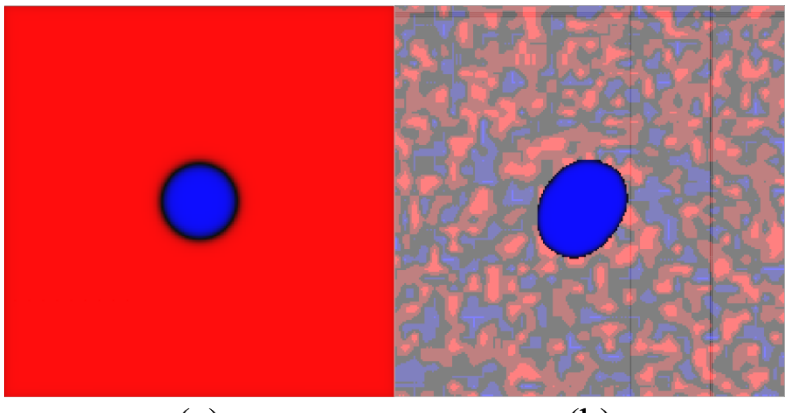

Figure 4-2 A Néel-skyrmion with minimised steady-state precession in a Co/Pt bilayer (a) with no surface roughness and (b) with an applied surface roughness with a maximum penetration depth of 1Å and coherence length of 40 nm. Both skyrmions are stabilised with an out-of-plane field of 1,600 Am^{-1}.

Table 4-1 Material parameters used to model the Pt/Co bilayer. $|D|$ is the DMI constant; M_S, the saturation magnetisation; A, the exchange stiffness; K_u, the magneto-crystalline energy; α, the gilbert damping; g_r, the relative gyromagnetic ratio; σ, the electical conductivity; D_e, the electron diffusion constant;$\lambda_{sf,J,\varphi}$, the spin flip, spin exchange rotation and dephasing lengths, respectively; $Re\left(G^{\uparrow\downarrow}\right)$ and $Im\left(G^{\uparrow\downarrow}\right)$, the real and imaginary components of the spin-mixing conductance, respectively; θ_{SHA}, the spin Hall angle and l_{ex} the exchange length.

Parameter	Value	References
$\|D\|$ (Co)	1.5 mJm^{-2}	14
M_S (Co)	600 kAm^{-1}	14
A (Co)	10 pJm^{-1}	14
K_u (Co)	380 kJm^{-3}	14
α (Co)	0.03, 0.1	30–36
g_r (Co)	1.3	37
σ (Co)	5 MSm^{-1}	38
D_e (Co)	0.0012 m^{2}s^{-1}	39
D_e(Pt)	0.004 m^{2}s^{-1}	40
λ_{sf} (Co)	42 nm	37–39,41
λ_J (Co)	2 nm	42
λ_φ (Co)	3.2 nm	43
λ_{sf} (Pt)	1.4 nm	44
σ (Pt)	7 MSm^{-1}	44
Re(G$^{\uparrow\downarrow}$) (Pt/Co)	1.5 +i0.45	20,44,45
Im(G$^{\uparrow\downarrow}$) (Pt/Co)	0.45 PSm^{-2}	*
θ_{SHA} (Pt)	0.19	44
l_{ex}	6.8 nm	**

* Value is obtained using Ref.[20] in conjunction with Eq. 4-1 (given later in this section) which can be solved for Im(G$^{\uparrow\downarrow}$).

** Value obtained using $l_{ex} = \sqrt{\frac{2A}{\mu_0 M_S^2}}$

4.2.2 Driving isolated skyrmion

After the completion of the initialisation phase, the manipulation of the skyrmions through a range of out-of-plane applied magnetic fields, current densities and, as discussed above, roughness coherence lengths, can begin. All permutations of these variables are handled within a *Python* script connected to *Boris*.

To begin, electrodes are attached to the lateral edges of the bilayer (y-z direction) so a chosen current density may be applied, as shown in Figure 4-3, thus the transport module must be enabled in both the Co and Pt layers.

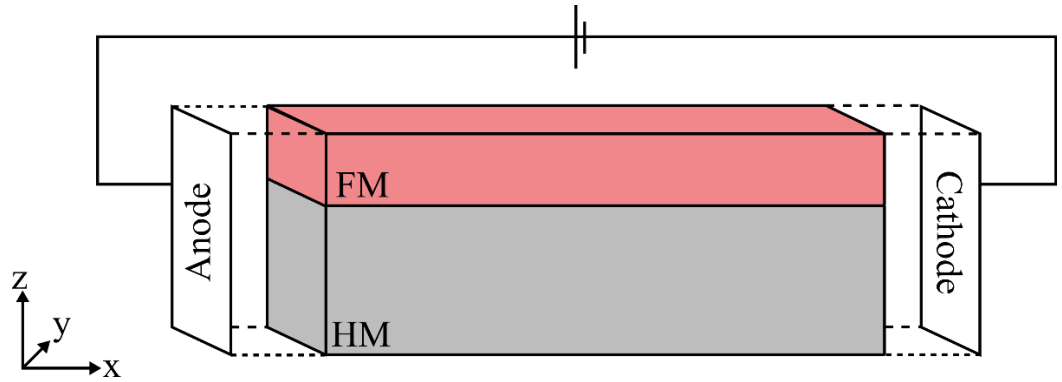

Figure 4-3 Diagram illustrating the attachment of the electrodes to the bilayer via an anode and cathode. The electrodes span the entirety of the y-z lateral boundaries of the bilayer.

The selection of the ordinary differential equation is a crucial step and is dependent on the spin torque combination chosen to drive the skyrmion, namely the SOT, ISTT, the bulk spin-transfer torque (STT) and all permutations of the torques. When the sole driving force is the SOT (using $P = 0$, $\beta = 0$, $\theta_{SHA,eff} \neq 0$, $r_G \neq 0$) the LLG equation is used, solved via the RKF45 method[46,47]. Note that the SOTField module is enabled when considering the SOT. When the ISTT and/or the STT is used, the LLG-STT (using $P \neq 0$, $\beta \neq 0$, $\theta_{SHA,eff} = 0$, $r_G = 0$) is set with the RKF45 method. Finally, if all the torques are considered, the LLG-STT (using $P \neq 0$, $\beta \neq 0$, $\theta_{SHA,eff} \neq 0$, $r_G \neq 0$) is set with the RKF45 method with the SOTField module.

4.2.3 Skyrmion field sweep

The skyrmion diameter is controlled using an out-of-plane magnetic field in the $+z$ direction ranging from $|H_z| = 0.875$ kAm^{-1} to $|H_z| = 54$ kAm^{-1}, which yielded diameters ranging from 396 nm to 21 nm, respectively, which is shown in Figure 4-4.

An isolated skyrmion is set in the centre of a disorder-free Co(1 nm)/Pt(3 nm) bilayer and allowed to relax. Relaxation is achieved by evaluating the LLG equation with the steepest descent method to the order of $|\mathbf{m}\times\mathbf{H}|=1\times10^{-6}$. The value selected for $|\mathbf{m}\times\mathbf{H}|$ will finish the stage/simulation when the normalized maximum torque, calculated as $|\mathbf{m}\times\mathbf{H}|/M_s^2$, falls below that value. After this initial relaxation phase, a small out-of-plane applied magnetic field is applied (+z direction) and the skyrmion is allowed to relax under the new field. Once the equilibrium state is achieved, the diameter of the skyrmion is obtained by taking the mean of a one-dimensional magnetisation profile through the centre of the skyrmion in the x and y directions. The skyrmion diameter dependence on the applied magnetic field is shown in Figure 4-4. There are two characteristics shown; at small field values there is a large change in the diameter with a constant field step, thus a strong dependence is shown. Also, at larger field values, a plateau in the skyrmion diameter begins and the field dependence vanishes.

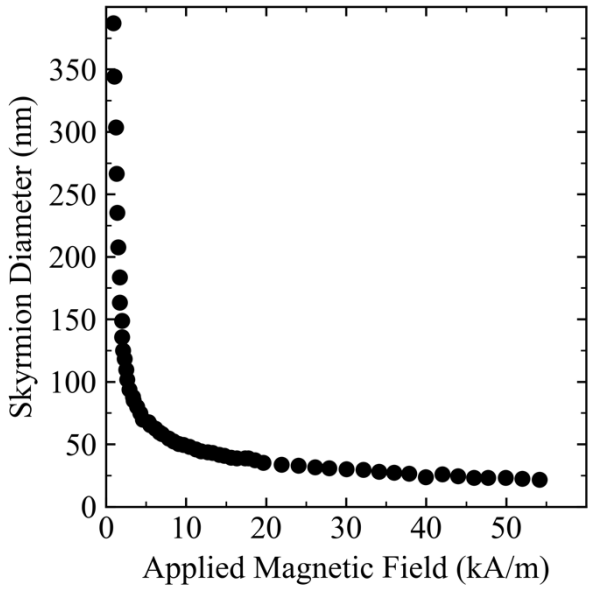

Figure 4-4 Skyrmion diameter dependence on the out-of-plane magnetic field, computed for the a system with no surface roughness and with not thermal fields.

4.2.4 Obtaining fitting parameters

For the spin torques obtained with the self-consistent spin transport solver, there are two distinct contributions and the combined torque effect. The contributions observed are the SOT due to SHE, as well as another important contribution obtained due to the interlayer diffusion of spin currents, namely the ISTT. To obtain solutions for these contributions,

spin carrier polarisation, P, non-adiabaticity parameter, β, field-like spin torque, r_G and effective spin Hall angle, $\theta_{SHA,eff}$, are obtained numerically. Thus, the spin accumulation is computed using the spin transport solver, and the total spin torque is obtained from Eq. 2-28. Then, Eq. 2-51 and Eq. 2-54 for the SOT and ISTT respectively, are used to obtain the above constants as fitting parameters to the total spin torque. Whilst $\theta_{SHA,eff}$ and r_G do not depend on the skyrmion diameter, P and β are not constant, and show a small dependence on skyrmion diameter due to spin diffusion, similar to the enhancement of Zhang-Li non-adiabaticity obtained for vortex cores[48,49]. Sharp magnetisation gradients cause a spin mistracking effect in which spin cannot track to the local magnetisation which results in a enhancement of P and β, even more so for sharper gradients. The dependence of these parameters on skyrmion diameter is shown in Figure 4-5.

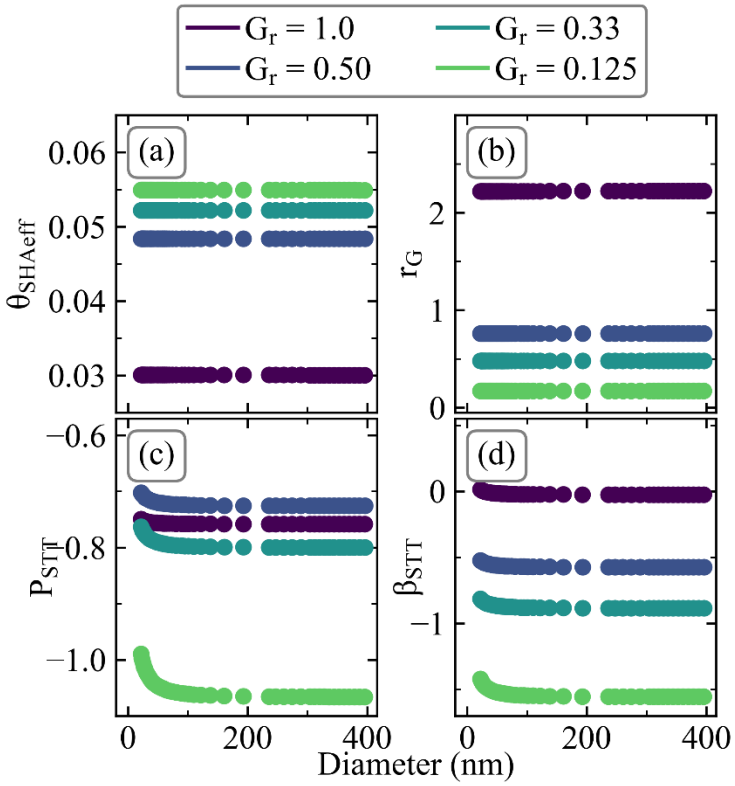

Figure 4-5 The dependence of modelling (a) effective spin Hall angle, (b) field-like spin coefficient, (c) effective spin polarisation and (d) effective non-adiabaticity parameters respectively, on skyrmion diameter in a disorder-free Co/Pt bilayer for a range of imaginary to real spin-mixing conductance ratios, $G_r = Im(G^{\uparrow\downarrow})/Re(G^{\uparrow\downarrow})$.

4.3 Driving skyrmion through a disorder-free system

Figure 4-6(a) shows three clear distinct curves which are identified by the dashed, solid and dash-dot lines which represent the SOT, the full spin torque and ISTT, respectively. There is a clear difference in each line, suggesting each component has a significant contribution to the skyrmion motion. The ISTT has a significant effect on the SkHA for small skyrmion diameters which is only applicable for ultra-thin films due to the inverse thickness dependence.

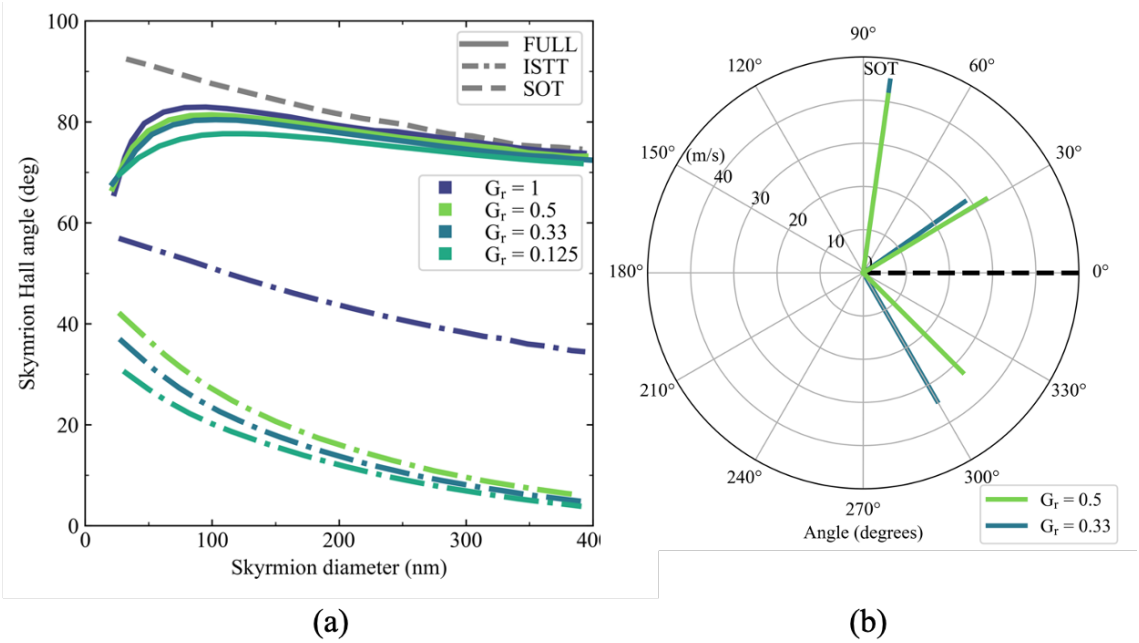

Figure 4-6 Relationship between the skyrmion Hall angle and skyrmion diameter for different imaginary to real spin-mixing conductance ratios, G_r. (a) Individual SOT and ISTT contributions for each ratio represented by a dashed and dash-dot line, respectively, as well as the full spin transport solver solution including both SOT and ISTT shown by the solid lines. (b) Skyrmion paths for G_r = 0.33 and 0.5. The individual SOT and ISTT contributions are shown alongside the full spin transport solver path. The current is applied along the x-direction, 0°. To obtain these results a damping value of α = 0.1 is used. The black dashed line represents the applied current direction.

Figure 4-6(b) shows the skyrmion path for each component, which shows that the SOT has the largest effect on the skyrmion motion compared to the ISTT component, as can be deduced from the SOT and ISTT skyrmion displacements. For large diameters, the SOT and full torque dependencies tend towards each other and become nearly identical. This is an important result as it shows the SOT-modelled results for the skyrmion motion to be a good assumption for large diameters. However, for small skyrmion diameters, the

two trends deviate rapidly, which would explain discrepancies between experimental and theoretical results. The combined torque results correspond well with results obtained experimentally both for small skyrmion diameters[16] as well as for large diameters[1,16,17].

The ISTT is not confined to Néel-type skyrmions alone as the ISTT arises from spin accumulation at magnetisation gradients and is therefore applicable for any magnetic texture including antiskyrmions, skyrmionium[4] and domain walls. In the case of the different magnetic textures, Figure 4-6 may display different ISTT characteristics, which is not in the scope of this work, but this investigation would be insightful.

The imaginary part of the spin-mixing conductance, $Im\left(G^{\uparrow\downarrow}\right)$, is commonly neglected with an effective spin-mixing conductance used instead. The imaginary component is usually assumed to be much smaller than the real component, however imaginary to real spin-mixing conductance ratios, $G_r = Im\left(G^{\uparrow\downarrow}\right)/Re\left(G^{\uparrow\downarrow}\right)$, larger than one has been measured recently[50]. Figure 4-6(a) shows the dependence of SkHA on the spin-mixing conductance ratio with a clear influence from the ratio apparent. The SOT is not affected by G_r in terms of the SkHA, but skyrmion velocity is affected by the G_r ratio, as is apparent in Figure 4-6(b) in which the velocity is larger for G_r = 0.33. The velocity is inferred as the length of each line as the simulation time is constant. Furthermore, the G_r ratio affects the ISTT contribution of both velocity and SkHA. The peaks of the combined torque curves range from 44° to 57.3° for G_r = 1 and G_r = 0.125, respectively. Figure 4-6(b) shows the skyrmion paths for each component for G_r = 0.33 and 0.5, illustrating further the velocity dependence on G_r. The ratio used in all subsequent modelling throughout this paper is determined using both DL- and FL-SOTs components, values of which are given in Ref.[20] for a Pt/Co(0.9 nm) bilayer, which are used to obtain the field-like torque coefficient. The imaginary component of the spin-mixing conductance can then be determined numerically, given below.

$$\mathrm{Im}\{\tilde{G}\} = \frac{-\left(N_\lambda + 2\mathrm{Re}\{\tilde{G}\}\right) \pm \sqrt{\left(N_\lambda + 2\mathrm{Re}\{\tilde{G}\}\right)^2 + 4 * r_g^2 \mathrm{Re}\{\tilde{G}\}\left(N_\lambda + \mathrm{Re}\{\tilde{G}\}\right)}}{2r_g} \quad \text{Eq. 4-1}$$

From Eq. 4-1, $Im\left(G^{\uparrow\downarrow}\right)$ = 4.49×10^{14} Sm^{-2} and hence G_r = 0.3 is obtained. It should be noted that there is a possibility for another reverse, back reflection, effect due to the transmitted spin-mixing conductance[50,51]. This has been theoretically investigated in ultra-thin heavy metal (HM)/FM/HM layer in which the drift-diffusion model is modified to describe the spin transport in systems with comparable FM layer thickness and spin dephasing length. For a spin dephasing length smaller than the FM thickness, the spin transmittance from the HM to the FM layer is absorbed entirely, however, when the spin dephasing length is larger than the FM layer thickness, the spin transmittance is not entirely absorbed. The unabsorbed spin caused the rise of a SOT, as well as the inverse SHE in the current direction, in the second HM layer causing a back reflection into the FM layer. The exact quantitative dependence of the SkHA on skyrmion diameter is expected to change, qualitatively the conclusions are unaffected, namely, the ISTT generated at magnetisation gradients in multilayers needs to be taken into consideration in addition to the SOT.

4.4 Skyrmion characteristics on disordered surfaces

4.4.1 Skyrmion roughness

In-depth theoretical investigations of skyrmions interacting with defects have shown significant changes to the skyrmion path[1,26,27,52–56] with further investigations showing disorder to have a large effect on the SkHA and skyrmion velocity[2,16,18,20,57]. There is also an inherent problem when using the Thiele equation for comparison due to the inability to incorporate skyrmion malleability. Furthermore, the effect surface disorder has on the SkHA with the ISTT component included in the simulations is investigated. Figure 4-7(a) illustrates the SOT and ISTT components acting on a current-driven skyrmion with the combined effect displayed, which is a vector addition of the two torques. This is accomplished by using a similar method to that used for the disorder-free results, however, in this case, a surface disorder is applied which is accomplished using a jagged surface roughness profile[27]. To investigate the effect of disorder on skyrmion motion, three surface roughness variation periods are applied, with 20 nm, 40 nm and 60 nm average spacing respectively between peaks and troughs. Figure 4-7(b) shows a disorder variation period of 60 nm. Furthermore, in the ideal case, a single applied current is used as the SkHA values are independent of the applied current density, but in the disordered

case a range of applied current densities are used, ranging from J_c = 6 GAm^{-2} up to J_c = 625 GAm^{-2}.

To incorporate roughness, the roughness module is enabled which allows a roughness to be applied to a mesh and then refined (see Chapter 2.5.5). In this instance, the inbuilt roughness generator is used to generate a roughness on to the surface of the Co layer by varying the algorithm parameters, namely the roughness depth, roughness coherence length, a seed for the pseudo-random number generator and mesh surface. The roughness depth controls the maximum penetration depth for the roughness, the coherence length controls the spacing between roughness nodes, the seed allows different roughness profiles to be generated, but more importantly allows for replication of a disordered landscape, and the mesh surface selects which surface of the layer has roughness applied. The roughness is controlled by using the *surfroughenjagged* command with the above-discussed parameters. A set of uniform random values between 0 and the roughness depth are generated on the specified body surface with the given roughness coherence length. The roughness is then generated via a bi-linear interpolation of the pseudo-generated points.

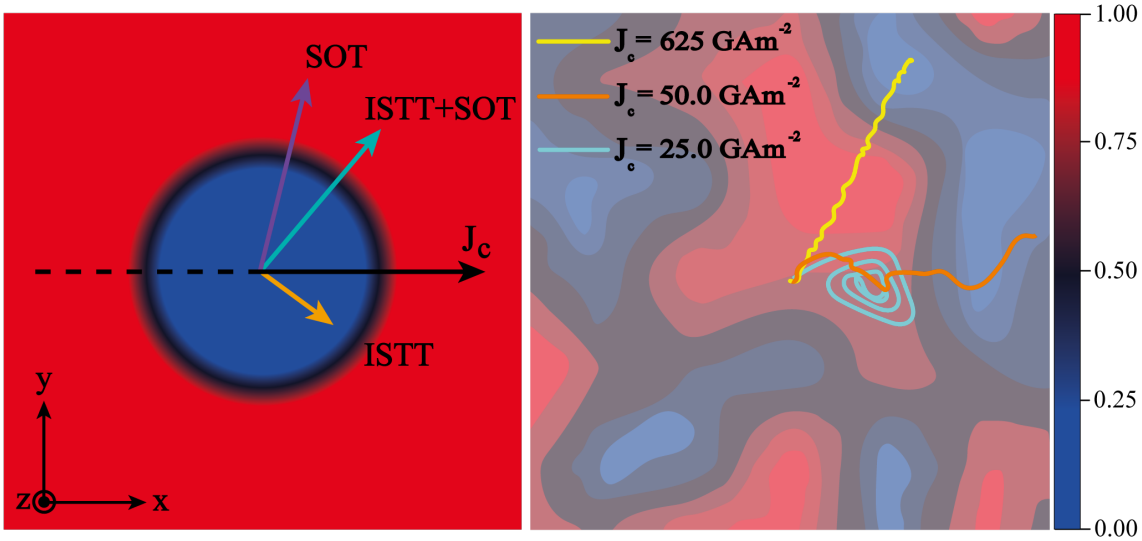

(a) (b)

Figure 4-7 (a) A snapshot of a 400 nm diameter Néel-skyrmion, showing the z magnetisation component. The magenta, orange and cyan arrows represent the direction in which the SOT, ISTT and the combination of these two torques in the spin transport solver act on the skyrmion when a current is applied, respectively. The black arrow indicates the conventional current direction, J_c. (b) Skyrmion motion in a bilayer system displaying pinned, creep and flow regimes in cyan, orange and yellow, respectively. The contoured effect outlines the disordered pattern on the surface of the sample with depth displayed by the heatmap. All paths are obtained using a damping constant α = 0.03 and a disorder variation period of 60 nm.

It is clear then there is a large amount of tunability for surface roughness which is utilised by using roughness coherence lengths of 20, 40 and 60 nm. Figure 4-2 shows a comparison between a perfectly smooth surface and a surface with a 40 nm coherence length. Figure 4-7(b) shows three simulated skyrmion paths which display three regimes: pinned, creep and flow regime. These have been defined when being driven by current as: (i) the pinned regime in which the skyrmion is confined within a potential well due to the energy landscape surrounding the skyrmion, and displays an orbiting path inside the pinning potential. (ii) The creep regime, in which the skyrmion has a large enough driving force to overcome the energy barrier and unpin itself, however, the skyrmion is heavily affected by the local energy landscape resulting in a significantly distorted path via sporadic jumps between pinning sites. (iii) The flow regime, in which the skyrmion displays a near-linear path across the disorder landscape, close to that obtained in the ideal case.

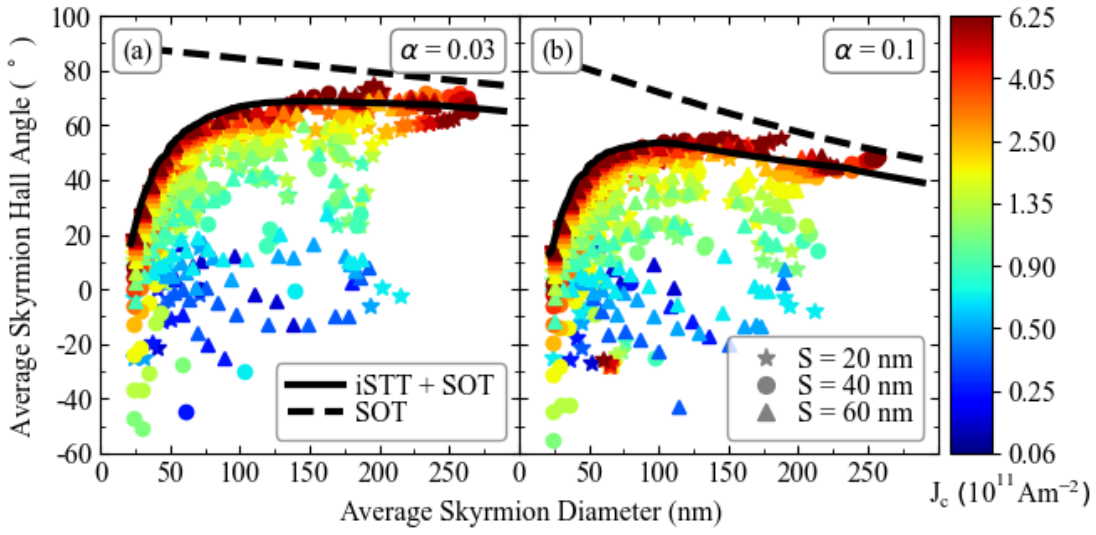

Figure 4-8 Skyrmion Hall angle dependence on skyrmion diameter for damping values of (a) α = 0.03 and (b) α = 0.1, with varying surface disorder periodicity in a Co(1 nm)/Pt(3 nm) bilayer. Star, circle and triangle correspond to 20, 40 and 60 nm disorder periods, respectively. The colour map corresponds to the applied current density in the +x direction of the Co/Pt system. The solid black lines display the full spin transport solver results in the ideal case. The dashed black lines show the SOT dependence obtained from the Thiele equation solution.

4.4.2 Skyrmion diameter dependence

Figure 4-8 shows the relationship between the SkHA and skyrmion diameter for α = 0.03 and α = 0.1. The solid black line is the trend obtained in the ideal (no surface roughness and at absolute zero) case for the full spin torque, and the dashed black line shows the expected behaviour under SOT using the rigid skyrmion model. The SkHA increases rapidly with skyrmion diameter up to 100 nm, after which a flattening of the trend occurs. The maximum SkHA obtained is θ_{SkHA} = 75° for α = 0.03, and θ_{SkHA} = 55° for α = 0.1. At small driving currents, skyrmions experience high deflection due to the local energy landscape, which is typical for the creep regime[58] where skyrmion motion occurs via sporadic jumps between pinning sites. In this regime, the SkHA is nearly independent of the skyrmion diameter, in agreement with experimental observations[16]. At larger driving currents, a more defined SkHA behaviour becomes apparent, tending towards the ideal case and entering the flow regime. There are two distinct regions at larger driving currents: (i) skyrmions with diameters of 100 nm and less which show a rapid SkHA increase with increasing diameters due to the combined action of the SOT and ISTT, and (ii) skyrmions with diameters greater than 100 nm that show a saturation of the SkHA, which becomes near-constant. Thus the effect of the combined SOT and ISTT model is in sharp contrast to the Thiele equation solution in Eq. 2-32 which predicts a monotonic increase in the SkHA with decreasing skyrmion diameter.

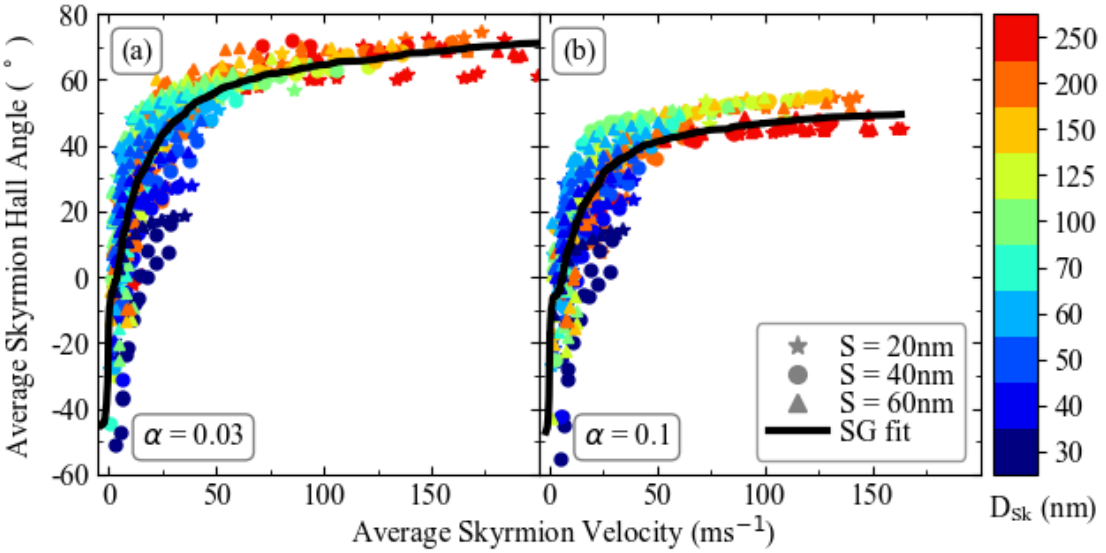

Figure 4-9 Skyrmion Hall angle-dependence on the skyrmion velocity for three disorder variation periods. Two damping values in (a) α = 0.03 and (b) α = 0.1 are used to obtain the dependence. The colour map details the diameter bin ranges from the minimum range of less than 30 nm up to a maximum of 250 nm. The points labelled in (a) and (b) correspond to the disorder variation periods on the Co(1 nm)/Pt(3 nm) bilayer. Star, circle and triangle correspond to 20, 40 and 60 nm spacings, respectively. The solid black line shows the Savitzky-Golay trend line.

4.4.3 Skyrmion Hall angle

Figure 4-9 shows the SkHA as a function of the skyrmion velocity, with the skyrmion diameter colour-coded as shown in the legend, for the three different disorder variation periods. The black line shows the Savitzky-Golay fit to the data to illustrate the average trend of the SkHA. There are two distinct velocity behaviours apparent in Figure 4-9. Initially, there is a steep increase in the SkHA with an increasing velocity at mainly small skyrmion diameters, indicative of the creep regime, which agrees well with established defect theory[1] and experimental works[16,18,20]. Following this initial steep increase in SkHA, a flattening of the behaviour occurs at which a much more gradual increase is observed over a much larger velocity range. These results for a range of skyrmion diameters suggest a collapse on to a universal SkHA versus skyrmion velocity dependence which is nearly independent of the surface roughness characteristics, similar to experimental results obtained in similar systems[1,16,18,20].

4.4.4 Skyrmion velocity

Figure 4-10 shows the velocity dependence on the applied current. The relationship for the ideal case is shown by the colour-coded dashed lines. A current-velocity relationship is subsequently established for both α = 0.03 and 0.1, indicating a monotonic increase of the average skyrmion velocity, dependent on the applied current density. The disordered simulations correspond very well to simulations of no disorder in which the effect of surface roughness mainly affects the SkHA by deflecting skyrmions and does not have an appreciable influence on the skyrmion velocity. Furthermore, the damping values have a significant effect on the skyrmion velocity which is predicted by the Thiele equation and is most evident in the 250 nm bin at the largest applied current, where for α = 0.03 and α = 0.1, the skyrmion velocities are v = 191 ms^{-1} and v = 163 ms^{-1} respectively. As pinned skyrmions are not shown, the skyrmion velocity at low driving current displays slight stochasticity for $J_c < 1\times10^{11}$ Am^{-2}, after which the skyrmions have a well-defined velocity with respect to the applied current. Furthermore, for $J_c > 2.5\times10^{11}$ Am^{-2} the skyrmion velocity tends to the linear profile of the disorder-free case. This behaviour corresponds well with experimental behaviour[1,20,54]. A more detailed depiction of the velocity-current-density relationship at small current densities is shown in Figure 4-11 which shows a more stochastic behaviour due to skyrmions being in a week creep regime thus resulting in large fluctuations in the average skyrmion velocity. Furthermore, for larger current densities there is little variation in the average skyrmion velocity for all three disorder periods due to skyrmions traversing in the flow regime. However, for smaller current densities this variation increases between the disorder periods. Although, the velocities for each period are quite sporadic, it can be seen that S = 60 nm typically yields larger velocities than that of S = 20 nm which is most likely due to the sharpness of the local energy landscape with S = 20 nm having larger roughness gradients than that of S = 60 nm.

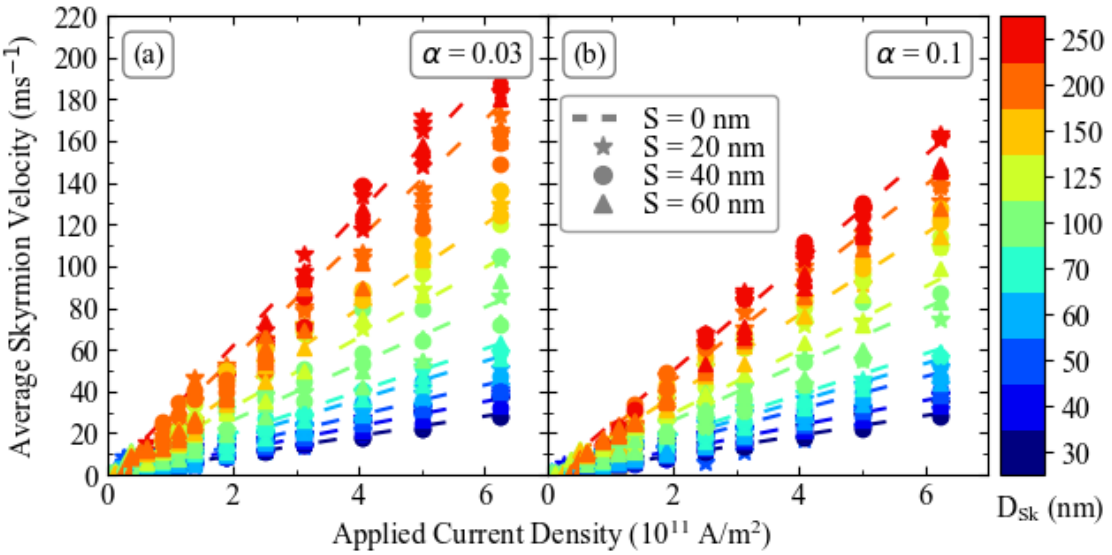

Figure 4-10. Relationship between skyrmion velocity and applied current density for damping values of (a) $\alpha = 0.03$ and (b) $\alpha = 0.1$, with surface disorder periodicity in a Co(1 nm)/Pt(3 nm) bilayer. Star, circle and triangle correspond to 20, 40 and 60 nm disorder periods respectively. Each skyrmion is assigned to a bin with assigned diameter ranges. The colour key details the diameter bin ranges from 30 nm up to a maximum of 250 nm. The dashed lines correspond to the relationship for the ideal (S = 0 nm) case at each diameter range.

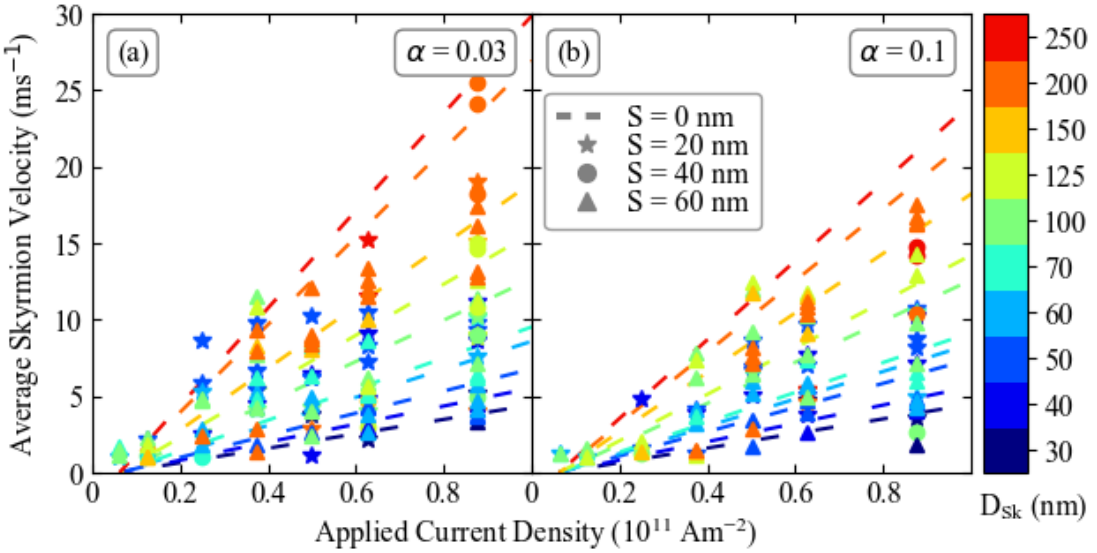

Figure 4-11 The velocity dependence on applied current density for (a) $\alpha = 0.03$ and (b) $\alpha = 0.01$. This is a truncated version of Figure 4-10 so the stochastic behaviour at lower applied current densities can be seen. The colour key details the skyrmion diameter bin ranges from a minimum of less than 30 nm up to a maximum of 250 nm. The dashed lines in (a) and (b) correspond to the relationship for the ideal case (S = 0 nm) at each diameter range.

4.4.5 Threshold current density

Figure 4-12 shows the relationship between the skyrmion threshold current and skyrmion diameter for α = 0.03 and α = 0.1. In this work, the threshold current is defined as the current required to change the skyrmion from the pinned regime to the creep regime which has been referred to as the depinning current. For α = 0.1, the required current to unpin the skyrmions is larger than for α = 0.03 at small skyrmion diameters, however, for larger diameters the threshold currents for both α = 0.1 and α = 0.03 tend towards each other. Typically for small skyrmions, the threshold current density is significantly greater than for larger skyrmions, which is most likely due to greater skyrmion rigidity at smaller diameters. Thus, as the diameter increases, the skyrmions become more malleable and start to deform as diametrically opposite points on the skyrmion border experience different pinning energies. This helps to reduce the threshold current, as the exchange energy built up through skyrmion deformations assists in depinning the skyrmion border for skyrmions much larger than the disorder variation period. It should be noted that the method for obtaining the threshold current is a combination of data and image analysis techniques. The threshold current is defined when a skyrmion unpins from the local energy landscape, however, as already discussed, smaller skyrmions pin to the local energy landscape much easily than larger skyrmions, resulting in a possible behaviour shown in Figure 4-12 for a skyrmion diameter ~50 nm and a disorder period of S = 40 nm where there is a jump. This jump maybe due to the skyrmion being in a stronger pinning site compared to other simulated skyrmions resulting in a larger calculated threshold current.

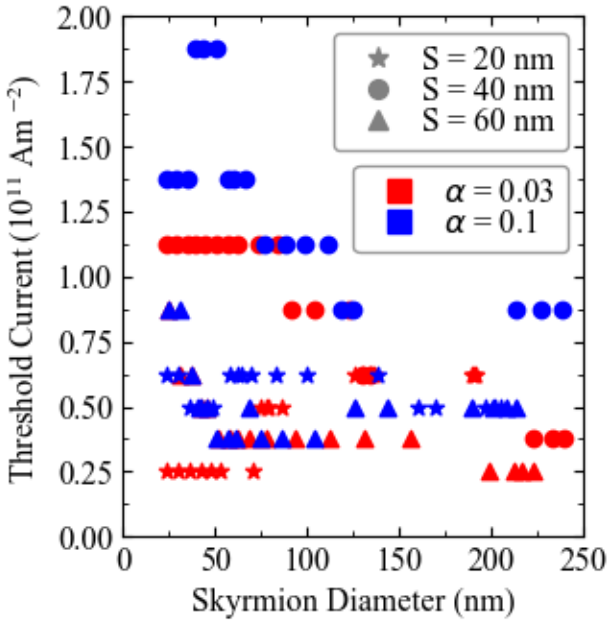

Figure 4-12 Skyrmion threshold current for damping values α = 0.03 and α = 0.1 represented by the solid and dashed lines, respectively. Varying applied disorder variation periods of 20, 40 and 60 nm are also used which are represented in red, green and blue, respectively.

4.5 Discussion

Current-induced Néel-skyrmion movement has been observed in asymmetric stacks including $[Pt/Co/Ta]_x$[14], Pt/GdFeCo/MgO[15], Ta/CoFeB/TaO_x[59], Pt/Co/Ir[19] as well as more complex stacks such as Ta/Pt/$[Pt/CoB/Ir]_x$Pt[16] and symmetric stacks[57]. To study the effect of the SOT and ISTT on skyrmion motion, a Pt(3 nm)/Co(1 nm) bilayer thin-film[60,61] structure is chosen for this work, using periodic boundary conditions for the demagnetising field. Ref.[20] reported on the current-driven motion of Néel-skyrmions with diameters of the order 100 nm in a Pt/Co/MgO trilayer, with and without disorder. Micromagnetics simulations are carried out to validate experimental results and the drive dependence of the skyrmion Hall effect is not observed to be accounted for by the FL-SOT. An analytical model is shown for damping coefficients α = 0.43, 0.30 and shows a relatively good agreement with the experimental results. It was suggested that a recreation of the SkHA could be achieved using the description of SOT only with the use of large damping factors, whereas if a smaller damping factor was used the result would be significantly different due to model relation given by Eq. 2-32.

Ref.[16] observed skyrmion characteristics experimentally and analysed using a range of damping factors. Using the Thiele equation, significant discrepancies are observed

between modelling and experimental results. In particular, the experimental results show a SkHA largely independent of skyrmion diameter, whereas the model based on the Thiele equation predicts a significant increase in SkHA with decreasing skyrmion diameter, and this discrepancy is significantly pronounced below a diameter of 100 nm and has not been reproduced using micromagnetics simulations to date. The results obtained here show the ISTT contribution is particularly important for small skyrmion diameters, which can lead to a near-diameter independent SkHA as observed experimentally, particularly when defect energy landscapes are taken into consideration.

Ref.[18] shows interesting skyrmion temperature characteristics in which skyrmion velocity is strongly dependent on temperature due to the increase in the temperature-dependent DL-SOT. However, the temperature is shown to have little effect on the SkHA, based on a model of spin structure deformations due to the FL-SOT, as the relationship between velocity and SkHA collapses on to a universal trend line. This behaviour has also been simulated[2] in which the skyrmion path and SkHA deviate insignificantly at T = 0 K and T = 297 K in a Pt/Co/Ta stack. When considering both ISTT and SOT components in our model, the SkHA and skyrmion velocity show similar characteristics to the experimental results, as shown in Figure 4-9.

The results shown in this investigation so far could explain the additional unidentified driving torque suggested in Ref.[73] which was found to oppose the STT resulting in domain wall motion along the current direction. Eq. 2-54, which is similar to the Zhang-Li STT and opposite, could explain the additional driving torque.

4.6 Conclusion

Isolated skyrmion motion in ultra-thin Pt/Co bilayers with and without disorder for a large range of skyrmion diameters has been studied utilising micromagnetics simulations coupled with a self-consistent spin transport solver. As well as SOT acting on the Co layer arising from the SHE, the ISTT is also shown to have a significant contribution to skyrmion motion. The included ISTT term is shown to significantly reduce the discrepancy for the SkHA between experimental results in the literature and SOT-only modelling for skyrmion diameters less than 100 nm. The SOT-only model is shown to agree with large skyrmions, whilst for smaller skyrmions, the inclusion of the additional ISTT term results in decreasing SkHA with decreasing skyrmion diameter. The results

obtained for a range of skyrmion diameters are shown to collapse on to a universal SkHA-velocity dependence, nearly independent of the surface roughness characteristics. Surface roughness was also included with the ISTT again showing to have a significant effect on the SkHA and velocity with results markedly similar, qualitatively, to published experimental works by other authors. The SOT-only model resulted in a SkHA of ~ 88° for a skyrmion diameter of ~ 65 nm, whereas, with the ISTT included resulted in a SkHA of ~ 60°. In addition to this, the spin mixing conductance ratio for Co/Pt was determined numerically, using literature-obtained values resulting in a G_r= 0.3. When considering a skyrmion of ~ 65 nm, the ratio of the spin-mixing conductance resulted in SkHAs of ~ 38° and ~ 60° for G_r= 1 and G_r= 0.125, respectively, when including the ISTT.

These results shed light on the current-induced skyrmion dynamics for a large range of diameters and highlight the current shortfalls of using a purely SOT-based model in micromagnetics modelling.

Chapter References

1. Jiang, W. *et al.* Direct observation of the skyrmion Hall effect. *Nat Phys* **13**, 162–169 (2017).

2. Lepadatu, S. Effect of inter-layer spin diffusion on skyrmion motion in magnetic multilayers. *Sci Rep* **9**, 9592 (2019).

3. Bogdanov, A. N. & Yablonskii, D. A. Thermodynamically stable vortices in magnetically ordered crystals. *Zh. Eksp. Teor. Fiz* **95**, 178–182 (1989).

4. Everschor-Sitte, K., Masell, J., Reeve, R. M. & Kläui, M. Perspective: Magnetic skyrmions - Overview of recent progress in an active research field. *J Appl Phys* **124**, 240901 (2018).

5. Fert, A., Reyren, N. & Cros, V. Advances in the Physics of Magnetic Skyrmions and Perspective for Technology. *Nat Mater* **2**, (2017).

6. Ramaswamy, R., Lee, J. M., Cai, K. & Yang, H. Recent advances in spin-orbit torques: Moving towards device applications. *Appl Phys Rev* **5**, 031107 (2018).

7. Soumyanarayanan, A. *et al.* Tunable room-temperature magnetic skyrmions in Ir/Fe/Co/Pt multilayers. *Nat Mater* **16**, 898–904 (2017).

8. Maccariello, D. *et al.* Electrical detection of single magnetic skyrmions in metallic multilayers at room temperature. *Nat Nanotechnol* **13**, 233–237 (2018).

9. Yu, X. Z. *et al.* Near room-temperature formation of a skyrmion crystal in thin-films of the helimagnet FeGe. *Nat Mater* **10**, 106–109 (2011).

10. Yu, G. *et al.* Room-Temperature Skyrmions in an Antiferromagnet-Based Heterostructure. *Nano Lett* **18**, 980–986 (2018).

11. Moreau-Luchaire, C. *et al.* Additive interfacial chiral interaction in multilayers for stabilization of small individual skyrmions at room temperature. *Nat Nanotechnol* **11**, 444–448 (2016).

12. Dzyaloshinsky, I. A Thermodynamic Theory of 'Weak' Ferromagnetism of Antiferromagnetics. *Journal of Physics and Chemistry of Solids* **4**, 241–255 (1958).

13. Moriya, T. Anisotropic superexchange interaction and weak ferromagnetism. *Physical Review* **120**, 91–98 (1960).

14. Woo, S. *et al.* Observation of room-temperature magnetic skyrmions and their current-driven dynamics in ultrathin metallic ferromagnets. *Nat Mater* **15**, 501–506 (2016).

15. Woo, S. *et al.* Current-driven dynamics and inhibition of the skyrmion Hall effect of ferrimagnetic skyrmions in GdFeCo films. *Nat Commun* **9**, 959 (2018).

16. Zeissler, K. *et al.* Diameter-independent skyrmion Hall angle observed in chiral magnetic multilayers. *Nat Commun* **11**, 428 (2020).

17. Litzius, K. *et al.* Skyrmion Hall effect revealed by direct time-resolved X-ray microscopy. *Nat Phys* **13**, 170–175 (2017).

18. Litzius, K. *et al.* The role of temperature and drive current in skyrmion dynamics. *Nat Electron* **3**, 30–36 (2020).

19. Legrand, W. *et al.* Room-Temperature Current-Induced Generation and Motion of sub-100 nm Skyrmions. *Nano Lett* **17**, 2703–2712 (2017).

20. Juge, R. *et al.* Current-Driven Skyrmion Dynamics and Drive-Dependent Skyrmion Hall Effect in an Ultrathin Film. *Phys Rev Appl* **12**, 044007 (2019).

21. Haazen, P. P. J. *et al.* Domain wall depinning governed by the spin Hall effect. *Nat Mater* **12**, 299–303 (2013).

22. Emori, S., Bauer, U., Ahn, S. M., Martinez, E. & Beach, G. S. D. Current-driven dynamics of chiral ferromagnetic domain walls. *Nat Mater* **12**, 611–616 (2013).

23. Pai, C. F. *et al.* Spin transfer torque devices utilizing the giant spin Hall effect of tungsten. *Appl Phys Lett* **101**, 122404 (2012).

24. Liu, L. *et al.* Spin-torque switching with the giant spin Hall effect of tantalum. *Science (1979)* **336**, 555 (2012).

25. Liu, L., Lee, O. J., Gudmundsen, T. J., Ralph, D. C. & Buhrman, R. A. Current-induced switching of perpendicularly magnetized magnetic layers using spin torque from the spin Hall effect. *Phys Rev Lett* **109**, 096602 (2012).

26. Reichhardt, C., Ray, D. & Reichhardt, C. J. Collective transport properties of driven skyrmions with random disorder. *Phys Rev Lett* **114**, 217202 (2015).

27. Plettenberg, J., Stier, M. & Thorwart, M. Steering of the Skyrmion Hall Angle by Gate Voltages. *Phys Rev Lett* **124**, 207202 (2020).

28. Akosa, C. A., Li, H., Tatara, G. & Tretiakov, O. A. Tuning the Skyrmion Hall Effect via Engineering of Spin-Orbit Interaction. *Phys Rev Appl* **12**, 054032 (2019).

29. Stupakiewicz, A. *et al.* Magnetization processes in ultrathin Au/Co/Au films grown on a bifacial Mo(110)/Mo(540) single crystal. *J Appl Phys* **103**, 07B520 (2008).

30. Yuan, J., Sun, L., Sang, H., Du, J. & Zhou, M. Interfacial effects on magnetic relaxation in Co/Pt multilayers. *Phys Rev B* **68**, 134443 (2003).

31. Benguettat-El Mokhtari, I. *et al.* Interfacial Dzyaloshinskii-Moriya interaction, interface-induced damping and perpendicular magnetic anisotropy in Pt/Co/W based multilayers. *J Appl Phys* **126**, 133902 (2019).

32. Beaujour, J. M. L. *et al.* Ferromagnetic resonance study of sputtered Co|Ni multilayers. *European Physical Journal B* **59**, 475–483 (2007).

33. Barati, E., Cinal, M., Edwards, D. M. & Umerski, A. Gilbert damping in magnetic layered systems. *Phys Rev B* **90**, 014420 (2014).

34. Schellekens, A. J. *et al.* Determining the Gilbert damping in perpendicularly magnetized Pt/Co/AlOx films. *Appl Phys Lett* **102**, 082405 (2013).

35. Barman, A. *et al.* Ultrafast magnetization dynamics in high perpendicular anisotropy [CoPt]n multilayers. *J Appl Phys* **101**, 09D102 (2007).

36. Mizukami, S. *et al.* Gilbert damping in perpendicularly magnetized Pt/Co/Pt films investigated by all-optical pump-probe technique. *Appl Phys Lett* **96**, 152502 (2010).

37. Beaujour, J. M. L., Lee, J. H., Kent, A. D., Krycka, K. & Kao, C.-C. Magnetization damping in ultrathin polycrystalline Co films: Evidence for nonlocal effects. *Phys Rev B* **74**, 214405 (2006).

38. Bass, J. & Pratt, W. P. Spin-diffusion lengths in metals and alloys, and spin-flipping at metal/metal interfaces: An experimentalist's critical review. *Journal of Physics Condensed Matter* **19**, 183201 (2007).

39. Lepadatu, S. Boris computational spintronics - High performance multi-mesh magnetic and spin transport modeling software. *J Appl Phys* **128**, 243902 (2020).

40. Halas, S. & Durakiewicz, T. Work functions of elements expressed in terms of the Fermi energy and the density of free electrons. *Journal of Physics Condensed Matter* **10**, 10815 (1998).

41. Piraux, L., Dubois, S., Fert, A. & Belliard, L. The temperature dependence of the perpendicular giant magnetoresistance in Co/Cu multilayered nanowires. *European Physical Journal B* **4**, 413–420 (1998).

42. Zhang, S., Levy, P. M. & Fert, A. Mechanisms of spin-polarized current-driven magnetization switching. *Phys Rev Lett* **88**, 236601 (2002).

43. Petitjean, C., Luc, D. & Waintal, X. Unified drift-diffusion theory for transverse spin currents in spin valves, domain walls, and other textured magnets. *Phys Rev Lett* **109**, 117204 (2012).

44. Zhang, W., Han, W., Jiang, X., Yang, S. H. & Parkin, S. S. P. Role of transparency of platinum-ferromagnet interfaces in determining the intrinsic magnitude of the spin Hall effect. *Nat Phys* **11**, 496–502 (2015).

45. MacKinnon, C. R., Lepadatu, S., Mercer, T. & Bissell, P. R. Role of an additional interfacial spin-transfer torque for current-driven skyrmion dynamics in chiral magnetic layers. *Phys Rev B* **102**, 214408 (2020).

46. Fehlberg, E. Low-order classical Runge-Kutta formulas with stepsize control and their application to some heat transfer problems. *NASA Technical Report* **R-315**, 1–49 (1969).

47. Lepadatu, S. Speeding Up Explicit Numerical Evaluation Methods for Micromagnetic Simulations Using Demagnetizing Field Polynomial Extrapolation. *IEEE Trans Magn* **58**, 1–6 (2022).

48. Claudio-Gonzalez, D., Thiaville, A. & Miltat, J. Domain wall dynamics under nonlocal spin-transfer torque. *Phys Rev Lett* **108**, 227208 (2012).

49. Bisig, A. *et al.* Enhanced Nonadiabaticity in Vortex Cores due to the Emergent Hall Effect. *Phys Rev Lett* **117**, 277203 (2016).

50. Dubowik, J. *et al.* Non-Negligible Imaginary Part of the Spin-Mixing Conductance and its Impact on Magnetization Dynamics in Heavy-Metal – Ferromagnet Bilayers. *Phys Rev Appl* **13**, 054011 (2020).

51. Carva, K. & Turek, I. Spin-mixing conductances of thin magnetic films from first principles. *Phys Rev B* **76**, 104409 (2007).

52. Reichhardt, C. & Olson Reichhardt, C. J. Noise fluctuations and drive dependence of the skyrmion Hall effect in disordered systems. *New J Phys* **18**, 095005 (2016).

53. Reichhardt, C., Ray, D. & Reichhardt, C. J. O. Quantized transport for a skyrmion moving on a two-dimensional periodic substrate. *Phys Rev B* **91**, 104426 (2015).

54. Müller, J. & Rosch, A. Capturing of a magnetic skyrmion with a hole. *Phys Rev B* **91**, 054410 (2015).

55. Kim, J.-V. & Yoo, M.-W. Current-driven skyrmion dynamics in disordered films. *Appl Phys Lett* **110**, 132404 (2017).

56. Díaz, S. A., Reichhardt, C. J. O., Arovas, D. P., Saxena, A. & Reichhardt, C. Fluctuations and noise signatures of driven magnetic skyrmions. *Phys Rev B* **96**, 085106 (2017).

57. Hrabec, A. *et al.* Current-induced skyrmion generation and dynamics in symmetric bilayers. *Nat Commun* **8**, 15765 (2017).

58. Reichhardt, C. & Reichhardt, C. J. O. Thermal creep and the skyrmion Hall angle in driven skyrmion crystals. *Journal of Physics Condensed Matter* **31**, 07LT01 (2019).

59. Jiang, W. *et al.* Skyrmions in magnetic multilayers. *Phys Rep* **704**, 1–49 (2017).

60. Yang, H., Thiaville, A., Rohart, S., Fert, A. & Chshiev, M. Anatomy of Dzyaloshinskii-Moriya Interaction at Co/Pt Interfaces. *Phys Rev Lett* **115**, 267210 (2015).

61. Yang, H., Boulle, O., Cros, V., Fert, A. & Chshiev, M. Controlling Dzyaloshinskii-Moriya Interaction via Chirality Dependent Atomic-Layer Stacking, Insulator Capping and Electric Field. *Sci Rep* **8**, 12356 (2018).

62. Tan, A. K. C. *et al.* Visualizing the strongly reshaped skyrmion Hall effect in multilayer wire devices. *Nat Commun* **12**, 4252 (2021).

63. Dhiman, A. K. *et al.* Thickness dependence of interfacial Dzyaloshinskii-Moriya interaction, magnetic anisotropy and spin waves damping in Pt/Co/Ir and Ir/Co/Pt trilayers. *J Magn Magn Mater* **519**, 167485 (2021).

64. Pai, C.-F., Ou, Y., Vilela-Leão, L. H., Ralph, D. C. & Buhrman, R. A. Dependence of the efficiency of spin Hall torque on the transparency of Pt/ferromagnetic layer interfaces. *Phys Rev B* **92**, 064426 (2015).

65. Azzawi, S. *et al.* Evolution of damping in ferromagnetic/nonmagnetic thin film bilayers as a function of nonmagnetic layer thickness. *Phys Rev B* **93**, 054402 (2016).

66. Zhang, B. *et al.* Influence of heavy metal materials on magnetic properties of Pt/Co/heavy metal tri-layered structures. *Appl Phys Lett* **110**, 012405 (2017).

67. Caprile, A. *et al.* Microwave Properties and Damping in [Pt/Co] Multilayers with Perpendicular Anisotropy. *IEEE Magn Lett* **5**, 3000304 (2014).

68. Di, K. *et al.* Direct Observation of the Dzyaloshinskii-Moriya Interaction in a Pt/Co/Ni Film. *Phys Rev Lett* **114**, 047201 (2015).

69. Devolder, T., Couet, S., Swerts, J. & Kar, G. S. Gilbert damping of high anisotropy Co/Pt multilayers. *J Phys D Appl Phys* **51**, 135002 (2018).

70. Nguyen, T. V. A. *et al.* Magnetic properties of Co film in Pt/Co/Cr2O3/Pt structure. *AIP Adv* **10**, 015152 (2020).

71. Metaxas, P. J. *et al.* Creep and flow regimes of magnetic domain-wall motion in ultrathin Pt/Co/Pt films with perpendicular anisotropy. *Phys Rev Lett* **99**, 217208 (2007).

72. Azzawi, S., Hindmarch, A. T. & Atkinson, D. Magnetic damping phenomena in ferromagnetic thin-films and multilayers. *J Phys D Appl Phys* **50**, 473001 (2017).

73. Je, S.-G. *et al.* Emergence of Huge Negative Spin-Transfer Torque in Atomically Thin Co layers. *Phys Rev Lett* **118**, 167205 (2017).

5 Skyrmion-Rich Arrays Under the Influence of the Interfacial Spin-Transfer Torque

In the previous chapter, the interfacial spin-transfer torque (ISTT) was investigated, in addition to the spin-orbit torque (SOT), on isolated skyrmions – a singular skyrmion in a magnetic body. Experimentally this can be rather difficult to achieve, with skyrmions typically being created in clusters with varying diameters due to geometrical constraints and neighbouring skyrmion interactions, all leading to possible changes in the skyrmion motion.

5.1 Introduction

It is well-known that the movement of isolated skyrmions, as well as skyrmion collections – a group of skyrmions dense enough to undergo collective dynamics – is strongly influenced by disorder, pinning sites and boundaries[1]. Skyrmions moving near the boundary of a magnetic multilayer have also been shown to be repelled away from the boundary[2]. Furthermore, skyrmions interacting with neighbouring skyrmions have also been shown to repel each other due to the dipole-dipole and exchange interactions, thus leading to the possibility of skyrmion-skyrmion interaction[3,4] and constraint of skyrmion diameter when a layer is saturated by skyrmions[5]; the extreme case being a skyrmion crystal. Moreover, the interaction of a skyrmion collection with the boundaries of a multilayered track was recently shown to result in a reshaped skyrmion Hall effect[6]. Driving individual skyrmions through a disordered landscape has been extensively studied under the effects of SOT from a heavy metal (HM) layer[7,8], spin transfer torque (STT) in the ferromagnetic (FM) layer[9], and as shown previously, the ISTT[10,11]

In this work, the effect of the additional ISTT term is investigated, alongside the STT and SOT, on skyrmion collections – defined as a group of interacting skyrmions – in HM/FM multilayers with landscape disorder in the form of surface roughness. Modelling results are compared to experimental results on skyrmion Hall angle (SkHA) and velocities, for skyrmion collections with a range of diameters. Through micromagnetic simulations coupled to a self-consistent drift-diffusion spin transport solver, it is shown that the SkHA-diameter dependence is in quantitative agreement with experimental results, contrary to modelling results which consider the SOT as the sole driving spin torque, particularly for small skyrmion diameters. Moreover, skyrmion collections are shown to

move approximately at an average group velocity, independent of diameter, and the experimental velocities are close to those obtained from modelling when the ISTT is included, whilst SOT-only modelling again shows discrepancies with experimental data.

5.2 Method

To begin, the geometrical constraints on skyrmions in a collection, whilst relaxing the system to an equilibrium state is discussed. A selected number of skyrmions were placed randomly within the FM mesh and relaxed using the steepest descent method, as shown in Figure 5-1(a) for a skyrmion density of $N = 12.5$ Sk/μm^2. Periodic boundary conditions along the x-axis are incorporated into our model. This allows us to simulate over a much larger effective length, which is useful in the case of many skyrmions, but also allows for y-boundary interactions as in the experimental samples. Therefore, as the skyrmions are not interacting with the x-boundaries of the FM layer, the skyrmions can traverse large distances and can interact with the y-boundary. The skyrmion diameters are strongly influenced by adjacent skyrmions, in addition to y-boundary interactions, such that there is confinement of diameter as the sample becomes saturated with skyrmions[12]. The simulation space also incorporates landscape disorder, in the form of surface roughness, with 1 Å maximum depth and a 40 nm in-plane coherence length, as detailed previously obtained results, as shown in Chapter 4[11]. A 40 nm in-plane coherence length is chosen to coincide with results obtained in Chapter 4 as well as being a mid-range value between previous values for the coherence length (S = 20, 40 and 60 nm). During the relaxation phase, skyrmions collectively adjust to the most energetically favourable diameter, which is strongly influenced not only by interactions with neighbours but crucially by landscape disorder which results in a variation of the effective out-of-plane anisotropy, as explained in Chapter 2.5.5. The skyrmion-skyrmion interaction has been studied in great detail and is known to result in a repulsive force between neighbouring skyrmions[13–15], dependent on the distance between them, the exchange interaction and the Dzyaloshinskii-Moriya interaction (DMI)[3]. Without disorder, the skyrmions relax to a regular hexagonal lattice. This is not the case when disorder is introduced, and a skyrmion collection will typically contain a range of diameters as indicated in Figure 5-2(a,b), for example in Figure 5-2(a) the diameters range from 70 nm to 180 nm, with a median of 110 nm. Here, the smallest diameter skyrmions tend to arrange into local hexagonal lattice clusters, with the larger diameter skyrmions showing significant distortions. This is in agreement with

experimental images of skyrmion collections in the studied samples – for example, Figure 5-2(b) shows a scanning transmission X-ray microscopy (STXM) image, obtained by the *University of Leeds*, of a skyrmion collection in a Ta(3.2)/Pt(2.7)/[$Co_{68}B_{32}$(0.8)/Ir(0.4)/Pt(0.6)]$_{\times 8}$/Pt(2.2) which is 2 µm wide wire. Here the diameters range from 72 nm to over 475 nm, with a median of 164 nm, and as for the simulated skyrmion collection the smaller skyrmions arrange into approximately hexagonal clusters, whilst the largest skyrmions appear significantly distorted and elongated.

It should be noted that in the experimental set-up, over 4,500 skyrmions are analysed of which over 3,500 are not pinned, and 75% of skyrmions are in the diameter range 70–180 nm, as shown in Figure 5-1(c), which span the entirety of the skyrmion diameter range achieved via modelling. This is discussed more in the next section.

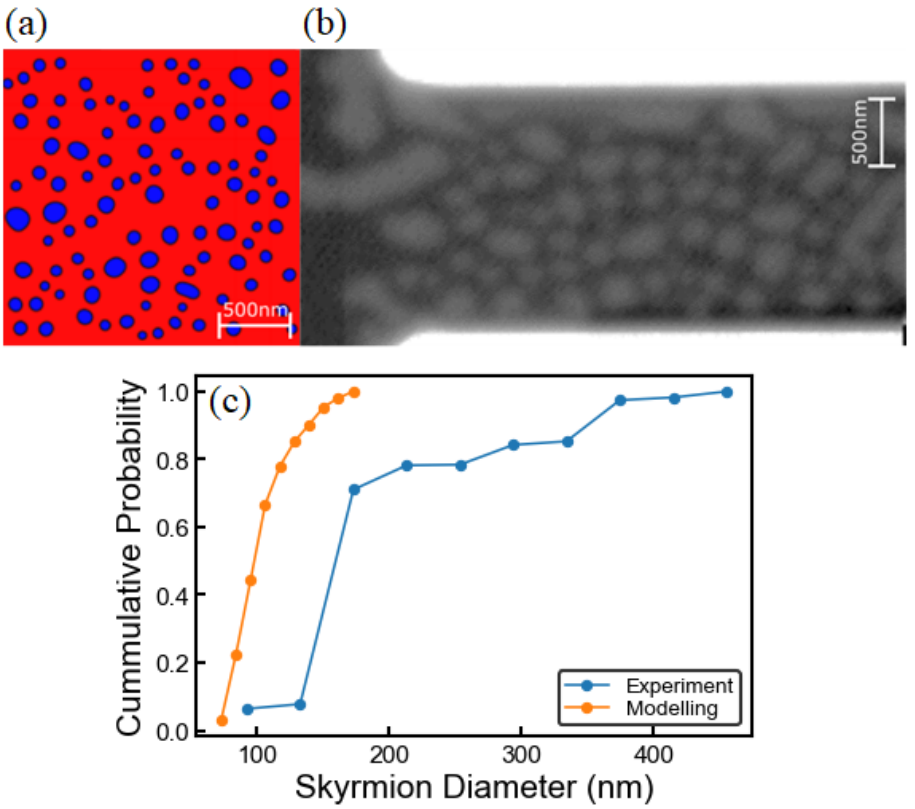

Figure 5-1 Skyrmion collections. (a) A simulated system with skyrmion density N = 12.5 Sk/µm^2, with a range of diameters stabilised by an out-of-plane field of H = 1.2 kAm^{-1}. Blue indicates in-plane magnetisation and red is out-of-plane. (b) STXM image of a skyrmion collection after a current pulse, J_c = 4.5×10^{11} Am^{-2}, in a 2 µm wide wire. The system composition is Ta(3.2)/Pt(2.7)/[$Co_{68}B_{32}$(0.8)/Ir(0.4)/Pt(0.6)]$_{\times 8}$/Pt(2.2). Bright contrast indicates skyrmions. Images are shown at zero field. (c) Cumulative probability as a function of diameter, where around 75% of skyrmions in experiments are in the diameter range 70 – 180 nm.

5.2.1 System parameters

Direct current (DC) magnetron sputtering at a base pressure of 2×10^{-8} mbar and a target-substrate separation of ~ 7 cm was used to deposit the thin-film heterostructure with typical growth rates of around 0.1 nms^{-1}. During the growth, the argon pressure was 3.2 mbar. The heterostructure studied consists of Ta(3.2)/Pt(2.7)/$[Co_{68}B_{32}$(0.8)/Ir(0.4)/Pt(0.6)$]_{\times8}$/Pt(2.2) (thicknesses are in nm). The patterned samples, 2-µm-wide wires, fabricated using electron beam lithography, were grown on X-ray transparent, highly resistive 200 nm thick silicon nitride membranes. An identical thin film was simultaneously sputtered on to a thermally oxidised Si substrate with a 100 nm thick oxide layer to enable the characterisation of the materials properties using standard techniques. X-ray reflectivity was used to measure the layer thicknesses.

The 2-µm-wide wires were fabricated using a bilayer electron-beam-sensitive resist process with a bottom layer of methyl-methacrylate (MMA) and a top layer of polymethylmethacrylate (PMMA). The spun and baked resist bilayer was exposed using a 100 kV Vistec EBPG 5000Plus electron beam writer with a writing dose of 1,650 µC cm^{-2}. The pattern was developed for 90 s in a 1:3 methyl-isobutyl-ketone and isopropyl alcohol solution (by volume), and rinsed for 60 s in isopropyl alcohol. The unpatterned regions were lifted off in acetone following the heterostructure growth procedure described above. Thermally evaporated 200-nm-thick Cu electrodes were fabricated using lift-off electron beam lithography (EBL) with the same exposure procedure as for the magnetic wires. The electrodes were designed to achieve an electrical impedance close to 50 Ω, minimising unwanted reflections of the injected current pulses.

The magnetic configuration of the wires was imaged using STXM at the PolLux beamline of the Swiss Light Source[16]. The X-ray magnetic circular dichroism (XMCD) effect[17] was utilised as a contrast mechanism. The X-ray incident angle was chosen to be perpendicular to the sample, resulting in out-of-plane magnetisation sensitivity. Skyrmions in the wire were nucleated after initial saturation at 80 kAm^{-1}, by two current pulses with a width of 22 ns and a peak current density of 4×10^{11} Am^{-2} at -8 kAm^{-1}, using a combination of thermal, spin torques and field effects to randomly nucleate skyrmions in the nanostructure[18,19]. An example of the experimental skyrmion path measurement is shown in Figure 5-2. After the nucleation pulse, the initial magnetic state was imaged, as shown in Figure 5-2(b), with analysed skyrmions identified using circles. Then, the

motion image sequence was taken by applying three 22-ns-long current pulses, shown in Figure 5-2(a), separated by a delay of 2 μs, with a maximum current density of 4.6×10^{11} Am^{-2} and an average value of 2.0×10^{11} Am^{-2}. Subsequently, static single helicity STXM images of the magnetisation state of the wire were taken. This sequence was repeated 19 times. The TrackMate algorithm[20] was used to identify the skyrmions' centre coordinates and the best-fit diameter. Using the change in the centre position of each skyrmion, its velocity and SkHA were evaluated. Brillouin light scattering (BLS) measurements, performed on samples grown in identical conditions and with the same layer thicknesses (but with five stack repetitions), have obtained a DMI constant[21] of D = -1.1 mJ/m^2. This exceeds the critical value to enforce homochiral Néel walls around spin textures. Moreover, the generated structures move with a finite SkHA when driven, which is dependent on skyrmion diameter, as discussed extensively in Chapter 4. This shows that they cannot be trivial bubbles but must possess topological charge and hence a gyrovector. Micromagnetic simulations were also performed using the same stack with eight repetitions as used in experiments and have confirmed the stabilisation of homochiral Néel-skyrmions in the multilayered stack as well.

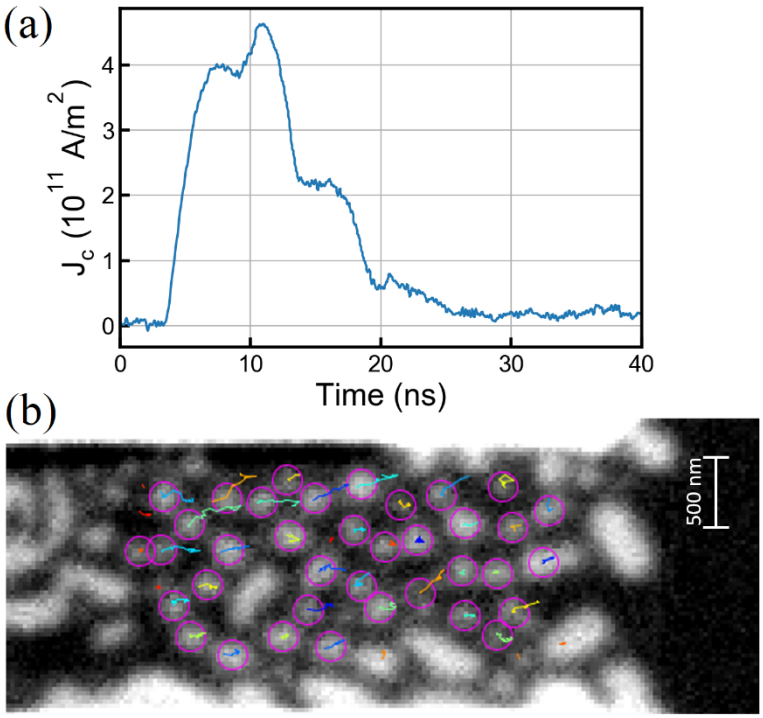

Figure 5-2 Experimental measurements of skyrmion movement. (a) Current pulse used to drive skyrmions, (b) STXM image of skyrmions, identified using circles, with skyrmion paths identified using different colours, extracted using the TrackMate algorithm from multiple STXM images. An out-of-plane field of H = 1.2 kAm^{-1} was used here.

5.3 Predicted skyrmion behaviour

Skyrmion behaviour can be predicted reasonably well using the Thiele equation as previously discussed, furthermore, the spin torque contributions can be individualised and subsequently, the skyrmion behaviour can be explored in more depth. To begin, the predicted skyrmion behaviour with multiple FM layer thicknesses is explored with the spin torques taken into account, namely, the ISTT, SOT and STT. To achieve this, the numerical spin torques are obtained for each torque contribution, as discussed earlier, for a predetermined FM layer thickness. The numerical torque values and layer thickness are then used in conjunction with the Thiele equation to determine the skyrmion behaviour.

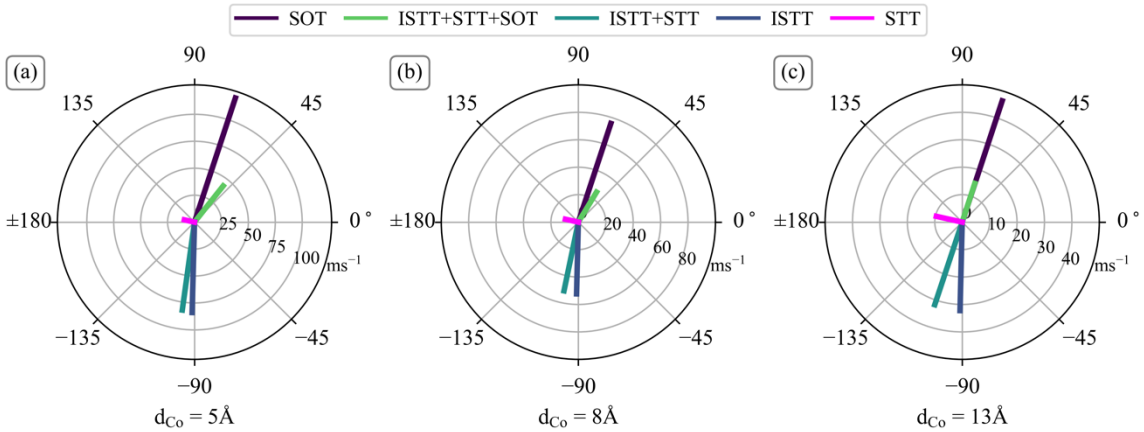

Figure 5-3 Effect of individual torques on a 100 nm diameter skyrmion, and combined effect, for Co layer of different thickness, (a) 5 Å, (b) 8 Å and (c) 13 Å. A damping value of $\alpha = 0.1$ was used here, with a driving current density of $J_c = 2.5\times10^{11}$ Am^{-2}. The polar plots show the skyrmion velocity, obtained using the Thiele model.

The effects of different spin torques acting on a single skyrmion, in a Pt(2.7 nm)/Co(d_{Co})/Ir(0.4 nm) multilayer with d_{Co} ranging from 5 Å to 13 Å, are shown in Figure 5-3 for a skyrmion with 100 nm diameter. The different spin torques are computed self-consistently using the spin transport solver for each value of d_{Co}, and skyrmion velocities and SkHA at $J_c = 2.5\times10^{11}$ Am^{-2} are shown as polar plots, for the individual spin torques and combinations. As expected, the paths under the combined spin torques are exactly those obtained by vector addition of the paths taken under the individual spin torques. The effect of the bulk STT is independent of Co layer thickness and significantly smaller than those of SOT and ISTT. However, SOT and ISTT are strongly dependent on the Co layer thickness and rapidly decrease in strength with increasing Co layer thickness, as expected from the interfacial spin torque in Eq. 2-28. For $d_{Co} = 8$ Å, as used for the results

that follow, both SOT and ISTT are significantly stronger than bulk STT, and it may be seen from Figure 5-3(b) how both the SkHA and skyrmion velocity are affected for the full spin torque model when compared to the SOT-only model.

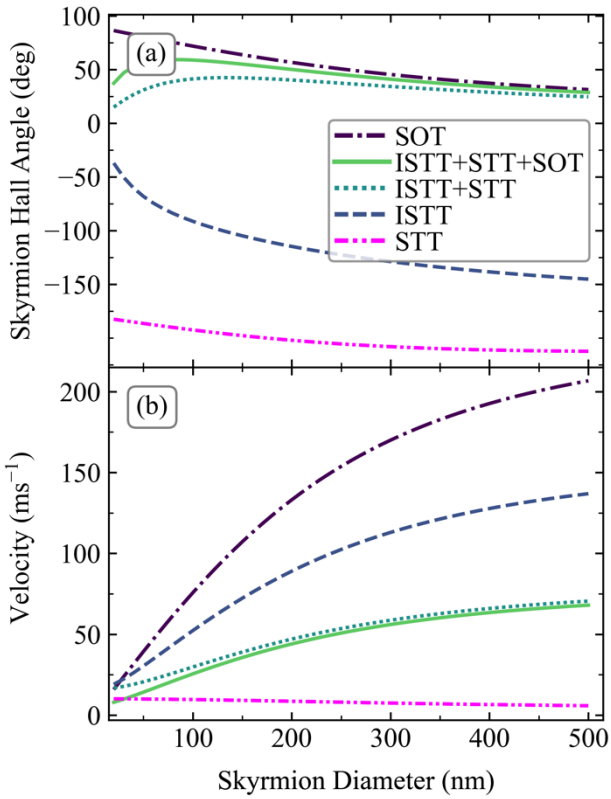

Figure 5-4 Variation of (a) SkHA and (b) skyrmion velocity, with skyrmion diameter for the individual spin torques and combinations, obtained using the Thiele model for Co layer thickness of 8 Å. A damping value of $\alpha = 0.1$ was used here, with a driving current density of $J_c = 2.5\times10^{11}$ Am^{-2}. SkHA and velocity as a function of diameter are obtained using the Thiele model.

The effect of the different spin torques is also strongly dependent on the skyrmion diameter. The SkHA and skyrmion velocities are shown in Figure 5-4 as a function of diameter, obtained using the Thiele model of Eq. 2-32. As expected, the SOT-only model shows a monotonic increase in SkHA with decreasing diameter. On the other hand, the full spin torque model shows a much flatter SkHA-diameter dependence, and for diameters below 100 nm shows a decrease in SkHA with decreasing diameter. Moreover, skyrmion velocities under the full spin torque are much smaller than those of the SOT-only model and closely align with experimental results.

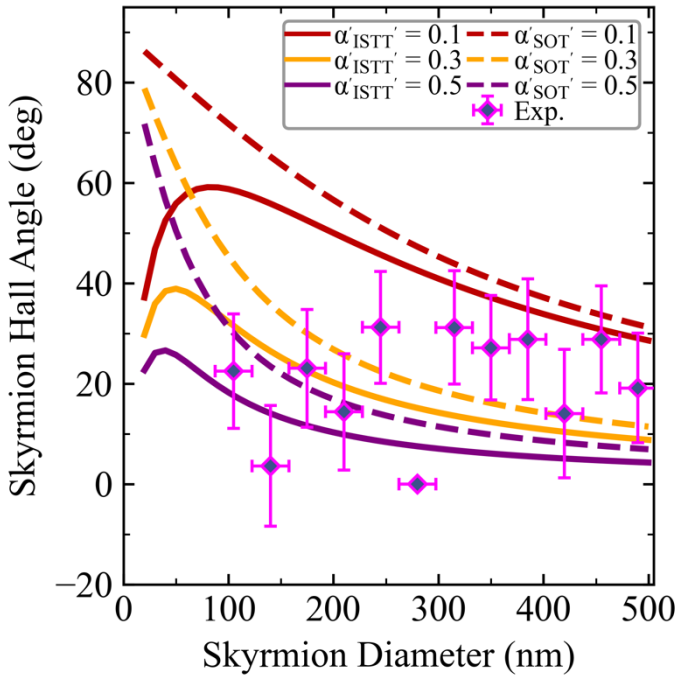

Figure 5-5 Variation of SkHA as a function of skyrmion diameter for FM layer thickness of 8 Å, where the dashed lines are the SOT-only contribution, whilst the solid lines are the full SOT+ISTT+STT results. The damping value is varied from 0.1 up to 0.5, with Thiele model results compared with the experimental data.

Furthermore, isolated skyrmion velocities obtained in other experiments align closely with the full spin torque model, whilst the SOT-only model predicts much larger velocities at damping values of $\alpha = 0.1$ and lower, although disorder also plays a part in reducing velocities. For example, Litzius *et al*. (2017) shows ~ 40 ms^{-1} at $J_c = 2.5\times10^{11}$ Am^{-2} with skyrmion diameters 100–150 nm, Litzius *et al*. (2020) shows < 30 ms^{-1} at $J_c = 5\times10^{11}$ Am^{-2} and room temperature, with skyrmion diameters 100–150 nm, Juge *et al.* (2019) shows ~ 30 ms^{-1} at $J_c = 5\times10^{11}$ Am^{-2} with skyrmion diameters 100–150 nm, and Woo *et al.* (2016) with stacks containing Pt(3 nm)/Co(0.9 nm)/Ta(4 nm), and also for Pt(4.5 nm)/CoFeB(0.7 nm)/MgO(1.4 nm), shows ~ 20 ms^{-1} at $J_c = 2.5\times10^{11}$ Am^{-2} with skyrmion diameters 100 – 150 nm.

Finally, the effect of damping on the SkHA is shown in Figure 5-5. As shown previously[11], increasing damping results in smaller SkHA values as expected, both for the SOT-only as well as the full spin torque models. However, even for large values of $\alpha = 0.3$, the SOT-only model cannot explain the small SkHA values obtained for small-diameter skyrmions, showing instead a rapidly increasing SkHA as the diameter decreases. The full spin torque reproduces experimental results with a realistic damping

value (α = 0.1) when comparing modelling results in the elastic depinning regime to experimental results at the same current density, whilst the SOT-only model results in ~ 50° discrepancy.

5.4 Effect of multiple stacks

It is known that stacks with multiple FM layer repetitions can result in a hybrid skyrmion, where the chirality changes between the bottom and top layers[22]. With the DMI constant of -1.1 mJm^{-2}, a skyrmion is stabilised in a stack with eight Co layers, each 0.8 nm thick, and with 1 nm spacing, as for the measured stack. The dipolar field between the layers was computed exactly using the multilayered convolution algorithm previously developed[23]. The magnetisation profile through the centre of the skyrmion is plotted in Figure 5-6, showing the m_x component for different layers. These results confirm the homochiral Néel-skyrmion structure expected for samples with a high DMI constant.

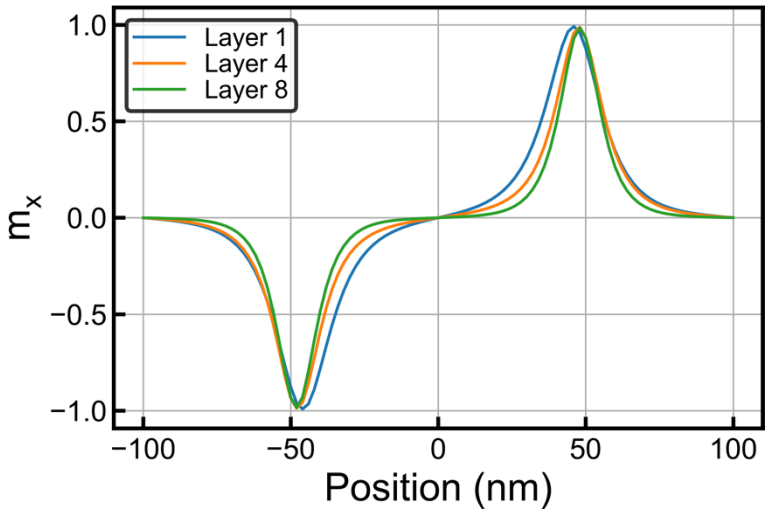

Figure 5-6 Normalised *x* component of magnetisation profile through the centre of the skyrmion along the same direction. A stack with eight repetitions of Co layer is used here, and the profile is plotted for different layers (numbered 1 through 8).

As the number of stack repetitions increases, another expected effect is an increase in the skyrmion diameter for the same external field, due to the decrease in the effective anisotropy[24]. When a skyrmion collection is considered, however, this effect is not as pronounced, due to a confinement effect from repulsive interactions with neighbouring skyrmions. To analyse this, the average skyrmion diameter was calculated, as well as spread, for skyrmion collections as a function of the number of stack repetitions in a Pt(2.7)/[Co(0.8)/Ir(0.4)/Pt(0.6)]$_{\times n}$/Pt(2.2) stack. Results are shown in Figure 5-7. As may

be seen, the average skyrmion diameter increases as the number of stack repetitions is increased, reaching a constant value after five repetitions. This effect is relatively small, however, with an increase in the average skyrmion diameter of ~ 50 nm. As shown in Figure 5-1, the experimental samples have on average larger skyrmions and the inclusion of a stack repetition would more closely align the experiment and modelling data.

Finally, the effect on spin torques from stack repetition is discussed. For a multi-stack repetition, the spin torque parameters are extracted by fitting the self-consistent computed spin torque. The fitting parameters for a single stack and eight stack repetition are shown in Table 5-1.

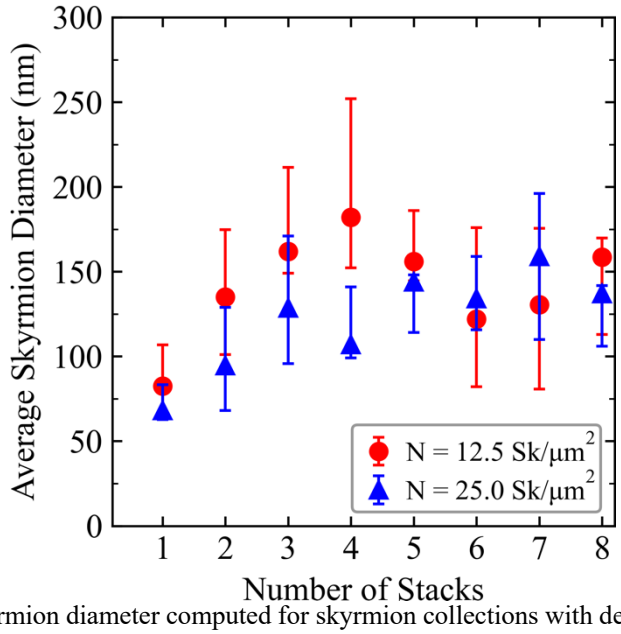

Figure 5-7 Average skyrmion diameter computed for skyrmion collections with densities N = 12.5 Sk/μm^2 and 25 Sk/μm^2 respectively, and out-of-plane field of H = 1.2 kAm^{-1}, as a function of the number of stack repetitions in Pt(2.7)/[Co(0.8)/Ir(0.4)/Pt(0.6)]$_{\times n}$/Pt(2.2). The error bars indicate the quartile 1 to quartile 3 spread.

The bulk STT values are P = 0.42 and β = 0.002 ($\tilde{P} = 0.42$) in all cases. A very small decrease in the effective spin Hall angle is obtained since the value is largely set by the thicker Pt(2.7 nm) underlayer. The effect of the thinner Pt(0.6 nm) layer from the next repetition is to reduce the SOT strength, however, this effect is negligible. With the ISTT, vertical spin currents generated at skyrmions in one Co layer, traverse the adjacent Ir and Pt layers, reaching the neighbouring Co layer from the next stack repetition. The effect on the total ISTT is small, however, as may be seen by comparing the extracted spin torque parameters above, for two reasons: (i) the spin-flip lengths of Pt and Ir are small,

which results in a rapid exponential decay of spin accumulation. Thus, whilst the diffusive spin currents originating in the Co layer are large close to the interface, they are smaller when reaching the neighbouring Co layer. (ii) Transverse components of spin accumulation are absorbed at the interface, resulting in ISTT, and thus these diffusive spin currents in Ir and Pt are largely of longitudinal polarisation. The additional ISTT contribution between interacting Co layers is negligible due to a very good approximation of like magnetisation textures within the layers themselves.

Table 5-1 Comparison of the spin torque parameters, extracted by fitting the self-consistent computed spin torque, for a singular stack and eight stack repetitions.

Spin torque Parameter	Singular Stack	8 Stack repetitions
$\theta_{SHA,eff}$	0.048	0.046
r_G	0.45	0.47
P_{ISTT}	-1.34	-1.25
β_{ISTT}	-0.96	-0.95
$\tilde{P}_{ISTT}$ **	-0.69	-0.66
P	0.42	0.42
β	0.002	0.002
$\tilde{P}$ ***	0.42	0.42

* The net change results from the singular stack minus the 8-stack repetition

**The effective ISTT polarisation is determined by $\tilde{P}_{ISTT} = \frac{P_{ISTT}}{1+\beta_{ISTT}^2}$

*** The effective bulk STT polarisation is determined by $\tilde{P} = \frac{P}{1+\beta^2}$

5.5 Contributions of the individual spin torques

The material parameters used to model spin transport in the Pt(2.7 nm)/Co(d_{Co})/Ir(0.4 nm) multilayer are shown in Table 5-2. In order to investigate the effect of various material parameters and layer thicknesses on the SkHA and skyrmion velocities, the parameters having a marked effect on skyrmion motion are explored: Pt and Co layer thicknesses, Pt spin-flip length and spin-mixing conductance at the Co/Pt interface; the effect of magnetic damping has been discussed previously. The bulk and interfacial contribution from the Ir layer is small compared to that from Pt.

A 100 nm diameter skyrmion is set, and for each combination of material parameters the spin transport solver is used to compute the various spin torques self-consistently using the equations already discussed. The SOT, STT and ISTT are then fitted to the computed spin torques in order to extract their respective spin torque parameters. Using the spin torque parameters, the Thiele model – Eq. 2-32 – is then used to compute the SkHA and skyrmion velocities. The results are shown in Figure 5-8 to Figure 5-11. It must be emphasised, the results shown below are obtained for ideal and isolated skyrmions, without landscape disorder, and are thus limiting cases. However, this analysis is useful for understanding the effect of the different spin torques and combinations, for experimentally relevant material parameters and associated uncertainty ranges.

Varying the Co layer thickness results in an inverse dependence of the spin torque strengths, as expected Eq. 2-28 which leads to an inverse dependence of the skyrmion velocity as shown in Figure 5-8(b). By comparing the velocities obtained with ISTT+STT and ISTT-only, the effect of the bulk STT on skyrmion velocities is relatively negligible. For SOT-only and ISTT-only, the SkHA value is constant – Figure 5-8(a) – however, when the full spin torque is considered, a linear dependence on the Co layer thickness results. This arises since the motion under the combined spin torques is obtained as vector addition of the motion under the separate spin torques; thus, a variation in their relative velocities results in a variation of the SkHA under the combined spin torques.

Table 5-2 Transport parameters used to model spin transport in the Pt/Co/Ir stack

Transport Parameters (Co)	Value
σ	5 M S/m [25]
D_e	0.001 m^2/s [26]
λ_{sf}	42 nm [25]
λ_J	2 nm [27]
λ_φ	3.2 nm [28]
Transport Parameters (Pt)	
σ	7 MS/m [29]
D_e	0.004 m^2/s [26]
λ_{sf}	1.4 nm [29]
θ_{SHA}	0.19 [29]
$G^{\uparrow\downarrow}$ (Pt/Co)	1.5 + i0.45 PS/m^2 [11,29,30]
Transport Parameters (Ir)	
σ	1.4 MS/m [31]
D_e	0.0002 m^2/s [26]
λ_{sf}	0.5 nm [32]
θ_{SHA}	0.02 [32]
$G^{\uparrow\downarrow}$ (Co/Ir)	0.35 + i0.045 PS/m^2 [33]

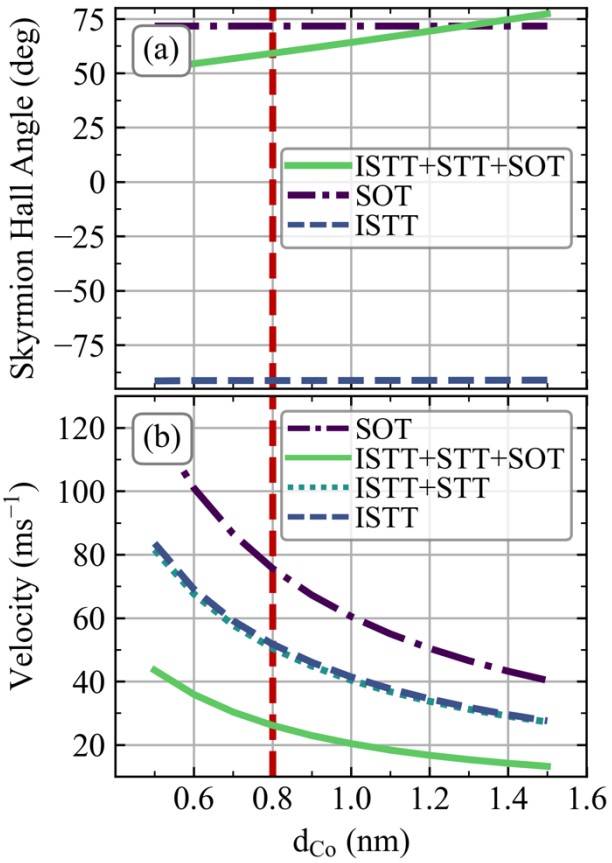

Figure 5-8 Effect of Co layer thickness, d_{Co}, on (a) SkHA and (b) velocity (at J_c = 2.5×10^{11} Am^{-2}) for various spin torques and combinations. The dashed vertical line shows the value used for the results in the main text. The ISTT+STT is not shown in (a) as there is little to no change in SkHA compared to ISTT only.

Varying the Pt layer thickness results in a change in the SOT and ISTT strength, primarily due to a change in the spin accumulation at the Pt/Co interface, which is strongly dependent on the spin-flip length to layer thickness ratio. For the SOT, the change in thickness results in a change in the effective SHA, $\theta_{SHA,eff}$, obtained by solving the drift-diffusion model as Eq. 2-53[11]. Thus, for example, with an intrinsic Pt SHA value of θ_{SHA} = 0.19, $\theta_{SHA,eff}$ = 0.048 at 2.7 nm thickness, but this decreases to $\theta_{SHA,eff}$ = 0.006 at 0.5 nm thickness. This results in a monotonic dependence of the skyrmion velocity with Pt thickness under SOT, and similarly for ISTT as shown in Figure 5-9(b). As the Pt layer thickness is decreased, eventually the velocity contribution from ISTT becomes dominant (noting that an ISTT contribution from the 0.4 nm thick Ir layer is also present). This explains the marked change in SkHA seen in Figure 5-9(a). These results show it is possible to control the SkHA by varying the relative strengths of the contributing spin torques. However, the desired zero SkHA for applications occurs close to the point when the effects of SOT and ISTT nearly cancel out and is thus accompanied by very low

skyrmion velocities. Synthetic structures such as synthetic antiferromagnets and ferrimagnets could provide structures to achieve the net cancellation of the SOT and ISTT, which is further discussed in Chapter 7.

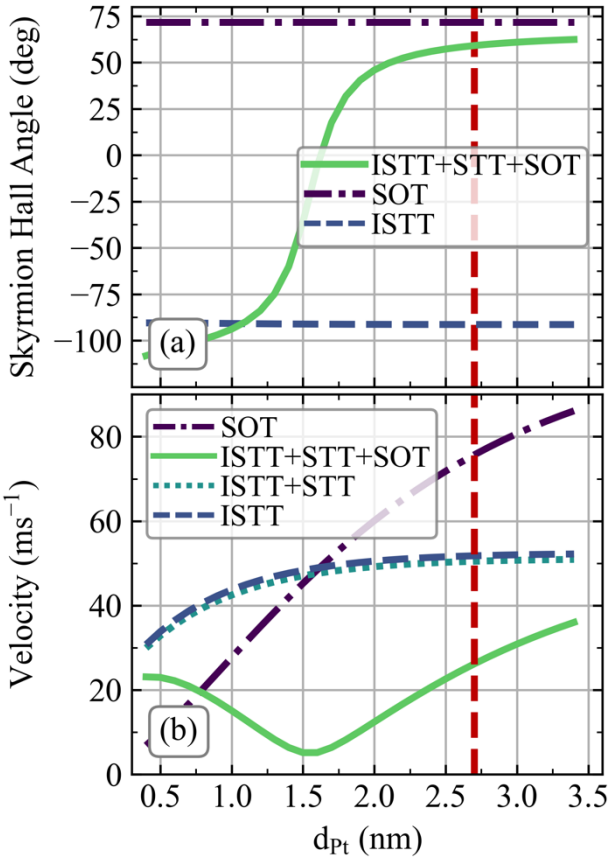

Figure 5-9 Effect of Pt layer thickness, d_{Pt}, on (a) SkHA and (b) velocity (at $J_c = 2.5\times10^{11}$ Am^{-2}) for various spin torques and combinations. The dashed vertical line shows the value used for the results in the main text. The ISTT+STT is not shown in (a) as there is little to no change in SkHA compared to ISTT only.

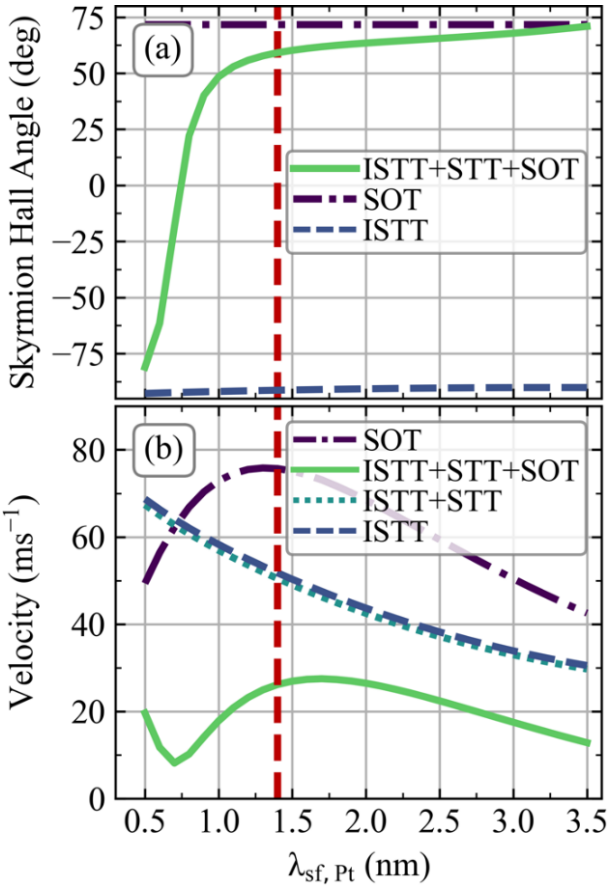

Figure 5-10 Effect of Pt spin-flip length, $\lambda_{sf,Pt}$, on (a) SkHA and (b) velocity (at J_c = 2.5×10^{11} Am^{-2}) for various spin torques and combinations. The dashed vertical line shows the value used for the results in the main text. The ISTT+STT is not shown in (a) as there is little to no change in SkHA compared to ISTT only.

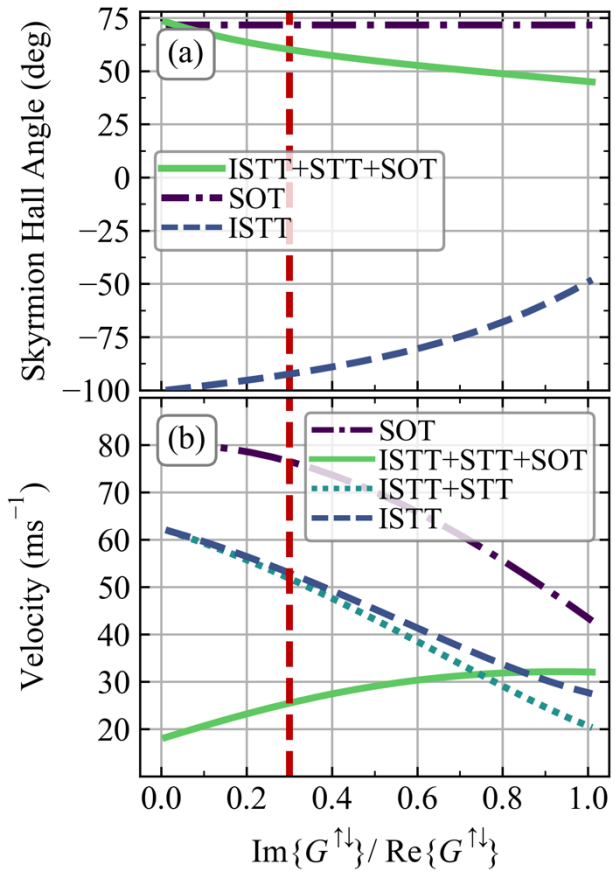

Figure 5-11 Effect of spin-mixing conductance imaginary to real part ratio on (a) SkHA and (b) velocity (at $J_c = 2.5\times10^{11}$ Am^{-2}) for various spin torques and combinations. The dashed vertical line shows the value used for the results in the main text. The ISTT+STT is not shown in (a) as there is little to no change in SkHA compared to ISTT only.

Similar remarks also apply to the dependence on Pt spin-flip length, shown in Figure 5-10. The ISTT depends inversely on the spin-flip length since smaller values result in larger spin accumulation gradients at the interface, and thus stronger diffusive vertical spin currents resulting from the shorter diffusion length scales. The SOT strength also depends on the spin-flip length, as given by Eq. 2-53, noting that $\theta_{SHA,eff}$ depends not just on the $d_{Pt}/\lambda_{sf,Pt}$ ratio, but also on $\lambda_{sf,Pt}$ separately.

The spin-mixing conductance, $G^{\uparrow\downarrow}$, also has an important effect on interfacial spin torques, Eq. 2-28. Experimental data on the real part of $G^{\uparrow\downarrow}$,are readily available in the literature, as in Zhang *et al.* (2015) for Pt/Co interfaces. On the other hand, data on the imaginary part of $G^{\uparrow\downarrow}$, are scarcer. In this work, $Im\{G^{\uparrow\downarrow},\}$ is obtained using experimental data from Juge *et al.* (2019) on the FL-SOT to DL-SOT ratio. The FL-SOT coefficient, r_G, may be obtained by solving the drift-diffusion model to give Eq. 2-53. From experimental values of r_G, this can be solved to obtain $Im\{G^{\uparrow\downarrow},\}$. The effect of the imaginary part of the spin-mixing conductance is shown in Figure 5-11, by plotting the SkHA and velocity as a function of the ratio $G_r \quad = Im\{G^{\uparrow\downarrow}\}/Re\{G^{\uparrow\downarrow}\}$. Decreasing r_G results in stronger SOT and ISTT. At the same time, the interfacial non-adiabaticity parameter, $\beta_{\perp}$, also depends on r_G[10], which results in a change of the SkHA under ISTT-only, unlike for SOT-only. For very small values of r_G, the effect of SOT and ISTT is nearly opposite, which results in skyrmion velocities tending towards zero under the combined spin torque.

5.6 Results

There are three skyrmion motion regimes for a single skyrmion: (i) the pinned regime, in which skyrmions are pinned by the local energy landscape and cannot move, (ii) the depinning regime, in which skyrmions jump intermittently between pinning sites with a net motion, and (iii) the flow regime in which the motion is not heavily impeded by the local energy landscape and appears near linear[34]. The presence of these regimes is also found in a skyrmion collection, which is discussed in relation to Figure 5-12. It should be noted that skyrmions in the pinned regime are not included, for all figures here and onwards, as they have a net zero velocity and thus an undeterminable SkHA. For a skyrmion collection, the depinning regime can be subdivided into elastic and plastic depinning[35], the former occurring for a weak disorder and is characterised by skyrmions

retaining their original neighbours throughout the motion, and the latter occurring for a strong disorder such that skyrmions continuously change their neighbours over time.

Modelling results shown in Figure 5-12 are given for a skyrmion density of (a) N = 12.5 Sk/μm^2 and (b) N = 25 Sk/μm^2. The skyrmion density in experiments is estimated to be in the range of 10–15 Sk/μm^2. At low current densities ($1.0\times10^{11} \leq J_c \leq 4.0\times10^{11}$ Am^{-2}), skyrmions are largely in the elastic depinning regime and are strongly influenced by the local landscape disorder, as well as repulsive interactions with neighbouring skyrmions, resulting in a pronounced dependence of the SkHA on driving current density. This is especially evident for results obtained using the full spin torque (ISTT+STT+SOT), and to a lesser extent for the results obtained using SOT alone. For the full spin torque, due to the combination of ISTT, STT and SOT, the net effect is a significantly smaller driving force for the same current density when compared to SOT-only, which helps to explain the more pronounced variation in SkHA under the effect of landscape disorder.

The spread of SkHA is further enhanced for the skyrmion collection with higher density, observed by comparison of Figure 5-12(a,b), expected due to the increased effect of repulsive interactions with neighbouring skyrmions. At larger current densities ($J_c >$ 4.0×10^{11} Am^{-2}) skyrmions are largely in the flow regime, with SkHA approximately described by the ideal SkHA-diameter dependence obtained using the Thiele equation. This is shown in Figure 5-12 for the full spin torque as a solid line, and for the SOT-only model as a dashed line. The experimental SkHA values, bin-averaged over skyrmions in the collection for the observed diameter range, are shown as diamonds. At the current density used in experiments (average J_c = 2.0×10^{11} Am^{-2}), the skyrmions also move largely in the elastic depinning regime. Thus a large discrepancy arises between the results obtained using the Thiele model, although it should be noted this is more pronounced for the SOT-only model.

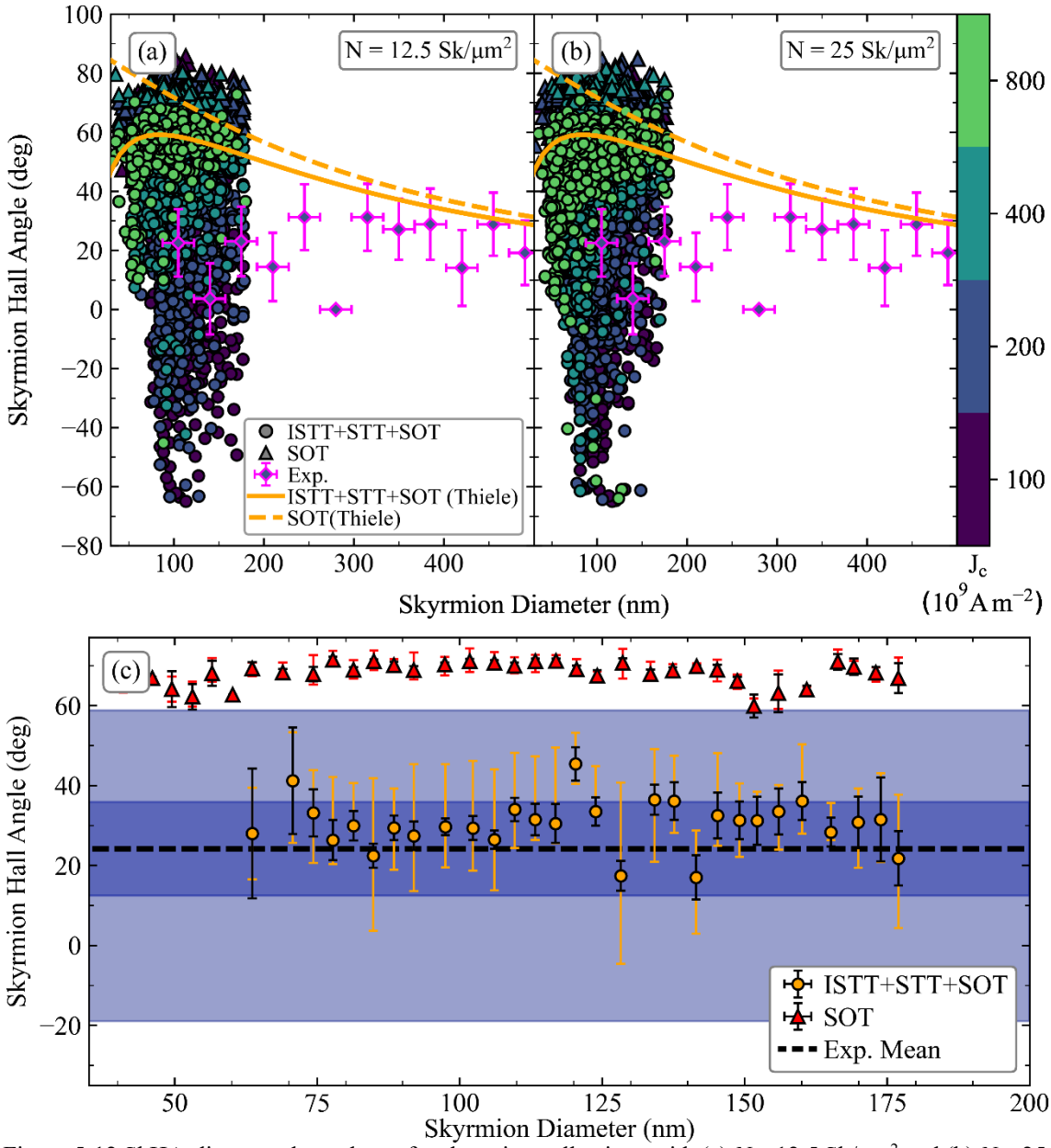

Figure 5-12 SkHA-diameter dependence for skyrmion collections with (a) $N = 12.5$ Sk/μm^2 and (b) $N = 25$ Sk/μm^2. The solid disks and triangles represent results for ISTT+STT+SOT and SOT-only respectively, for a corresponding applied current density indicated by the colour bar. Magenta-outlined diamonds with blue centre represent the experimental results. The orange solid and dashed lines represent the Thiele equation solution for spin torque contributions ISTT+STT+SOT and SOT-only respectively, with a damping value $\alpha = 0.1$. (c) Detail at the average current density used in experiments, $J_c = 2\times10^{11}$ Am^{-2}. The dashed horizontal line is the mean experimental SkHA, with the inner blue horizontal band showing standard error on the mean, and the lighter blue outer band showing the spread (quartile 1 to quartile 3). This is compared to the solid disks showing modelling results with ISTT+STT+SOT and solid triangles for SOT-only, also at $J_c = 2\times10^{11}$ Am^{-2} (smaller error bars are standard error on the mean, and larger error bars are the spread).

This discrepancy persists for the SOT-only model even at large damping values of α = 0.3, as discussed above, where the effect of varying the damping constant is also considered. Instead, to compare with experimental results, the SkHA values of skyrmions in the collection are shown in Figure 5-12(c) for J_c = 2.0×10^{11} Am^{-2}, thus in the elastic depinning regime. The experimental SkHA is largely independent of skyrmion diameter, and the overall mean is indicated as a dashed line. The inner blue band shows the standard error on the mean, whilst the outer lighter blue band shows the overall spread of experimentally measured SkHA values (defined as quartile 1 to quartile 3). As mentioned earlier, 75% of skyrmions are in the diameter range of 70–180 nm, overlapping with the range obtained in modelling. A very good overlap is seen with the modelling results for the full spin torque, whilst for the SOT-only results a large discrepancy of over 50° is observed. Thus, whilst both the full spin torque and SOT-only models reproduce the nearly diameter-independent SkHA trend qualitatively, only the full spin torque model is able to reproduce the SkHA values quantitatively. Moreover, the full spin torque model also reproduces the relatively large spread of experimental SkHA values in the skyrmion collection, as shown in Figure 5-5(c), with an excellent overlap between the two regions. Also, the negative SkHA values observed in the spread of experimental results are only reproduced when the ISTT is included, which is due to the significant reduction in average SkHA, as well as a reduction in velocities in the depinning regime. The spread of SkHA values is larger for skyrmion collections, compared to isolated skyrmion motion[11], since skyrmions interact not only with the local landscape disorder but also with neighbouring skyrmions. As noted above, the spread in SkHA is reduced for the SOT-only model, since skyrmion velocities are significantly larger at the same current density – skyrmion velocities and a comparison with experimental results are discussed later in this chapter. The measured samples consist of eight stack repetitions, thus eight FM layers, whereas the simulated geometry contains one FM layer. The results shown in this chapter would not be feasibly obtained for eight stack repetitions in terms of simulation time, due to current software parallelisation limitations. A stack repetition has the effect of further reducing the SkHA, as discussed previously[10], both for SOT and ISTT+STT+SOT models, however, this is not enough to explain the experimental SkHA values with the SOT-only model[10]. Indeed, as the stack repetition is increased, the skyrmion diameter increases due to the reduction in effective anisotropy[24]. However, this effect is much weaker for a skyrmion collection, where the skyrmion diameter is constrained by repulsive interactions with neighbouring skyrmions. The average skyrmion diameter is

calculated for a collection as a function of a number of stack repetitions, and for eight repetitions as used in the experiment, the increase in the average skyrmion diameter is ~ 50 nm as shown in Figure 5-7. Furthermore, the stack repetition does not significantly alter the spin torques, as the SOT is largely generated through the thicker Pt underlayer, and the ISTT is due to vertical spin currents flowing away from the Co layer, generated by spin-dependent scattering at skyrmions. Other factors which result in a decrease of the SkHA include damping value, with larger values resulting in lower SkHA, both for SOT and ISTT+STT+SOT models, as may be obtained in Eq. 2-32, as shown above.

It is well-known the SkHA depends on the driving force when the effect of disorder is taken into acouunt[30,34,36]. This is also reproduced for skyrmion collections, as shown in Figure 5-13, both for the SOT-only results, and the full spin torque, although the effect is more pronounced for the latter. These results show an initial increase in the SkHA with increasing velocity, indicative of the depinning regime. At larger velocities, the SkHA tends to a constant value, indicative of the flow regime, reaching the limiting SkHA values obtained using the Thiele model as expected. Whilst for the collective skyrmion motion a large spread of SkHA is obtained, as may be seen in Figure 5-12, the results in Figure 5-13 are velocity-bin-averaged. The spread in SkHA values is larger for the full spin torque model in agreement with experimental results shown in Figure 5-12(c), since the combination of the various spin torques results in lower skyrmion velocities and is, therefore, more strongly influenced by the local landscape disorder compared to the SOT-only case. In experiments containing over 4,500 skyrmion paths, just over 3,500 skyrmions are not pinned. From these, the average SkHA is ~ 24° ± 12°, with velocities ranging up to 2.5 ms^{-1} and a mean of 0.5 ms^{-1}. These values are in agreement with the trend obtained with ISTT+STT+SOT in Figure 5-13 and is again in disagreement with SOT-only modelling. To obtain larger velocities in experiments, larger current densities are required, however, these degrade the samples over repeated measurements.

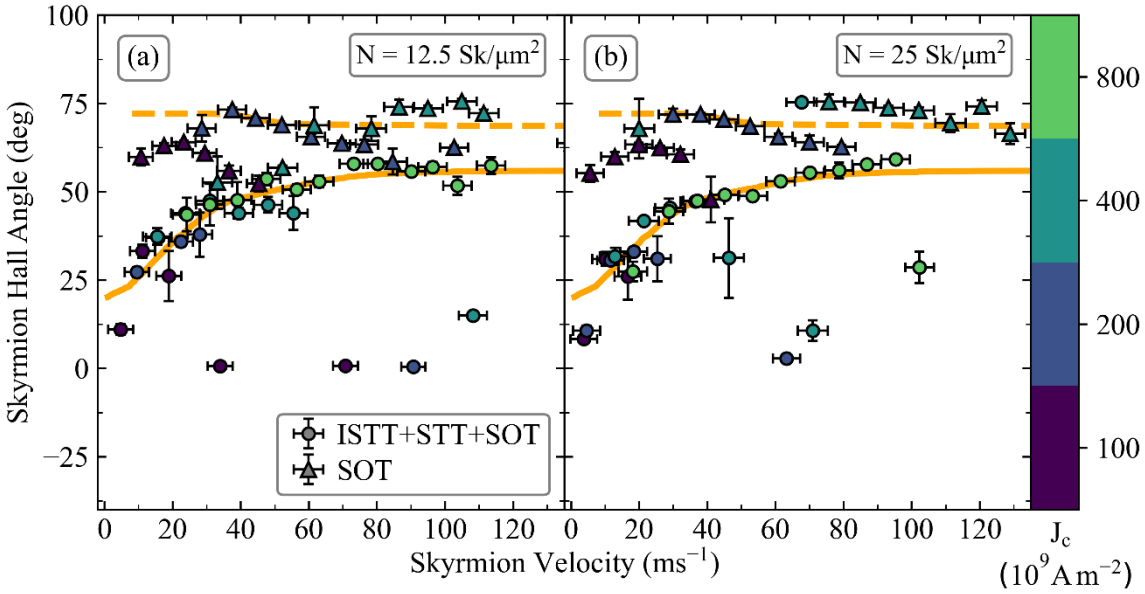

Figure 5-13 SkHA dependence on the skyrmion velocity with landscape disorder, for skyrmion collections with (a) N = 12.5 Sk/μm^2 and (b) N = 25 Sk/μm^2. The solid disks and triangles show results for ISTT+STT+SOT and SOT-only respectively, for a corresponding applied current density indicated by the colour bar. The solid and dashed lines are Savitzky-Golay-fit trend lines, for ISTT+STT+SOT and SOT respectively, acting as a guide to the eye.

The skyrmion velocity-diameter dependence is shown in Figure 5-14 for (a) ISTT+STT+SOT and (b) SOT only. The symbols show results obtained for collective motion, whilst the dashed lines are obtained from the Thiele model, thus for isolated skyrmions without landscape disorder. For the isolated skyrmion motion, the velocity increases monotonically with the diameter as expected. For the skyrmion collection, however, it is observed the velocity is nearly independent of diameter. This is to be expected since the skyrmions move elastically, and due to repulsive interactions with neighbouring skyrmions, an average group velocity is established. Thus, the larger diameter skyrmions, which in isolation move with larger velocities, are slowed down by smaller diameter skyrmions in the collection, and conversely the smaller diameter skyrmions move faster than they do in isolation, as they are pushed by the larger diameter skyrmions.

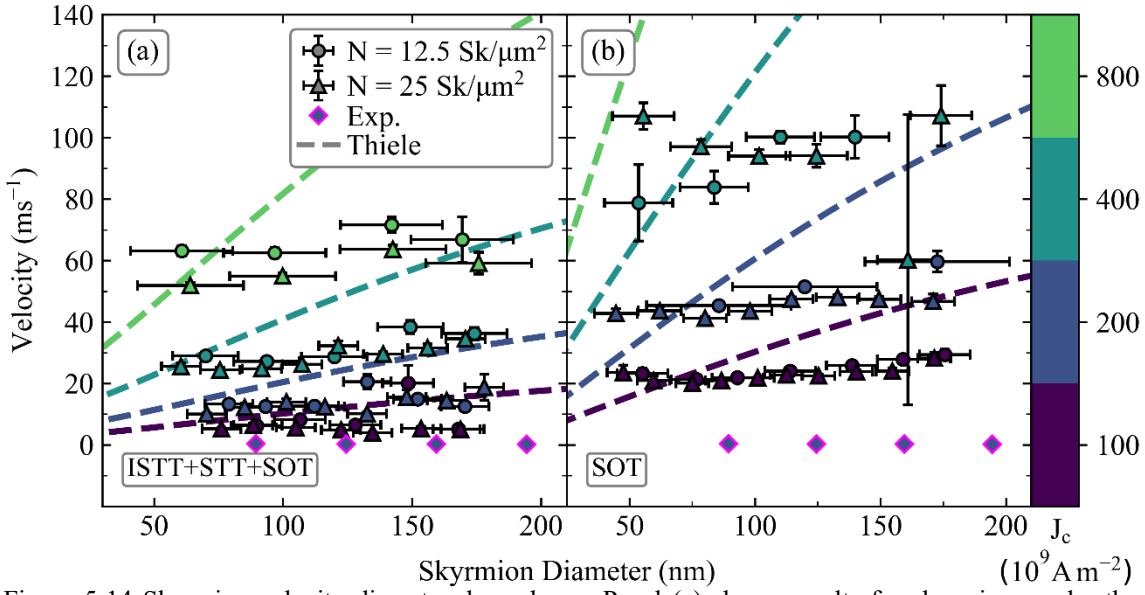

Figure 5-14 Skyrmion velocity diameter dependence. Panel (a) shows results for skyrmions under the influence of ISTT+STT+SOT and (b) shows the influence of SOT alone. The solid disks and triangles represent $N = 12.5$ and $N = 25$ Sk/μm^2 respectively, each corresponding to an applied current density shown by the colour bar. The Magenta-outlined diamonds with blue centre represent the experimental results. The coloured dashed lines show the solutions obtained from the Thiele model with $\alpha = 0.1$, for an isolated skyrmion at the respective current density, using the same colour coding.

This holds both for the SOT-only case, as well as the full spin torque case. Experimental skyrmion velocities recorded reach up to ~ 2.5 ms^{-1} with a mean of ~ 0.5 ms^{-1} which are lower than the values obtained in simulations. This is possibly due to the multilayer composition, interface quality and multilayer stack repetition. However, with the inclusion of the ISTT and STT (noting again that the Thiele model predicted a much larger ISTT effect compared to the STT), the skyrmion velocities align closer to those found experimentally, compared to the SOT-only case, as may be seen in Figure 5-14. Thus, for the full spin torque case at $J_c = 2\times10^{11}$ Am^{-2}, the average velocity obtained from modelling is ~ 10 ms^{-1}. On the other hand, for the SOT-only case, the average velocity at this current density is > 40 ms^{-1}. Also, Tan *et al.* (2021) reported average collective skyrmion velocities ranging up to ~ 10 ms^{-1} (for J_c up to ~ 5.5×10^{11} Am^{-2}), which is again close to the values obtained here using the full spin torque but is in disagreement with the SOT-only model. Moreover, Legrand *et al.* (2017) reported on stacks based on Pt(3 nm)/Co(0.6 nm – 1 nm)/Ir(1 nm), also containing skyrmion collections with sub-100 nm diameter skyrmions, with velocities of less than 0.5 ms^{-1} observed for J_c up to 3.0×10^{11} Am^{-2}. Once again, this is in disagreement with the SOT-only model, even when the disorder is taken into account, but the values obtained here by including ISTT are closer

to the experimental values. These results, put together with the SkHA values in Figure 5-12(c), show the SOT-only model does not adequately account for the experimental data. Moreover, these results also highlight the importance of the ISTT, which helps to account for the discrepancy between the experimental results and the SOT-only model, particularly for SkHA values, but also helps to explain the small experimental skyrmion velocity values.

Finally, it must be noted that ISTT should also be present for domain walls in multilayers since any magnetisation gradients in FM layers will result in diffusive vertical spin currents towards adjacent metallic layers. Furthermore, experimental evidence for a huge negative STT was obtained for ultra-thin Co layers interfaced with Pt[37]. This torque was found to be much larger than the bulk STT, act in the opposite direction to the bulk STT (thus with a negative spin polarisation), and scale inversely with the Co layer thickness. These features are remarkably similar to those discussed here in relation to ISTT for skyrmions, and the origin of such a huge negative STT could be the ISTT arising from diffusive vertical spin currents. Investigation of ISTT for domain walls in multilayers, however, is left for future work. Finally, evidence for an STT with effective negative spin polarisation was found by Ummelen *et al.* (2018), for skyrmion bubble motion. As remarked by the authors, this is not compatible with SOT, but with a negative STT. Again, the observed negative STT could be the interfacial contribution to the total STT, which indeed acts with an effective negative spin polarisation. A possible further experiment to directly demonstrate the presence of ISTT is to investigate a stack with broken inversion symmetry, e.g. Pt/Co/Cu/Pt, but with Pt layers of equal thickness. Such a structure may allow cancellation of the SOT from the Pt layers, due to the long spin-flip length in Cu, whilst maintaining the inversion asymmetry, and hence non-zero DMI, required to stabilise Néel-skyrmions. In such a structure, any skyrmion movement cannot arise from SOT, allowing for a direct comparison of skyrmion movement and ISTT modelling. This is discussed and implemented in Chapter 7.

5.7 Conclusion

In this chapter, the motion of skyrmion collections in ultra-thin HM/FM multilayers with landscape disorder, utilising micromagnetic simulations, has been studied with spin torques computed with a self-consistent spin transport solver and compared to experimental results and numerical modelling using the Thiele equation. The SOT, ISTT

and STT have been considered, and for ultra-thin films, the bulk STT effect on skyrmion motion is negligible compared to the SOT and ISTT. The SkHA is strongly dependent on the effect of the combined torques, and the small SkHA values observed in experiments are in good agreement with modelling, which includes the ISTT, also explaining the observed diameter-independent SkHA and spread of experimental SkHA values at the same current density. This is in contrast to the model which considers the SOT as the only driving torque, where large discrepancies in SkHA of 50° are observed. The collective skyrmion motion is found to be described by an average group velocity over the diameter range, which stands in marked contrast to the velocities obtained from isolated skyrmion motion. Furthermore, the group velocities obtained with the inclusion of ISTT are comparable to those found in experiments. This is not the case for the SOT-only model, which again shows large discrepancies of over 40 ms^{-1} with the experimental data. Our results shed further light on collective current-induced skyrmion motion, and highlight the significance of the ISTT in understanding current-induced skyrmion motion in magnetic multilayers.

Chapter References

1. Reichhardt, C., Reichhardt, C. J. O. & Milosevic, M. V. Statics and Dynamics of Skyrmions Interacting with Pinning: A Review. *ArXiv* (2021) doi:10.1103/RevModPhys.94.035005.

2. Iwasaki, J., Mochizuki, M. & Nagaosa, N. Current-induced skyrmion dynamics in constricted geometries. *Nat Nanotechnol* **8**, 742–747 (2013).

3. Capic, D., Garanin, D. A. & Chudnovsky, E. M. Skyrmion – skyrmion interaction in a magnetic film. *Journal of Physics: Condensed Matter* **32**, 415803 (2020).

4. Reichhardt, C. & Reichhardt, C. J. O. Nonlinear transport, dynamic ordering, and clustering for driven skyrmions on random pinning. *Phys Rev B* **99**, 104418 (2019).

5. Siemens, A., Zhang, Y., Hagemeister, J., Vedmedenko, E. Y. & Wiesendanger, R. Minimal radius of magnetic skyrmions: Statics and dynamics. *New J Phys* **18**, 045021 (2016).

6. Tan, A. K. C. *et al.* Visualizing the strongly reshaped skyrmion Hall effect in multilayer wire devices. *Nat Commun* **12**, 4252 (2021).

7. Kim, J.-V. & Yoo, M.-W. Current-driven skyrmion dynamics in disordered films. *Appl Phys Lett* **110**, 132404 (2017).

8. Woo, S. *et al.* Current-driven dynamics and inhibition of the skyrmion Hall effect of ferrimagnetic skyrmions in GdFeCo films. *Nat Commun* **9**, 959 (2018).

9. Feilhauer, J. *et al.* Controlled motion of skyrmions in a magnetic antidot lattice. *Phys Rev B* **102**, 184425 (2020).

10. Lepadatu, S. Effect of inter-layer spin diffusion on skyrmion motion in magnetic multilayers. *Sci Rep* **9**, 9592 (2019).

11. MacKinnon, C. R., Lepadatu, S., Mercer, T. & Bissell, P. R. Role of an additional interfacial spin-transfer torque for current-driven skyrmion dynamics in chiral magnetic layers. *Phys Rev B* **102**, 214408 (2020).

12. Song, K. M. *et al.* Skyrmion-based artificial synapses for neuromorphic computing. *Nat Electron* **3**, 148–155 (2020).

13. Lin, S.-Z., Reichhardt, C., Batista, C. D. & Saxena, A. Particle model for skyrmions in metallic chiral magnets: Dynamics, pinning, and creep. *Phys Rev B* **87**, 214419 (2013).

14. Bogdanov, A. New localized solution to the nonlinear field equation. *JETP Lett* **62**, 231 (1995).

15. Lin, S.-Z. & Hayami, S. Ginzburg-Landau theory for skyrmions in inversion-symmetric magnets with competing interactions. *Phys Rev B* **93**, 064430 (2016).

16. Raabe, J. *et al.* PolLux: A new facility for soft X-ray spectromicroscopy at the Swiss Light Source. *Review of Scientific Instruments* **79**, 113704 (2008).

17. Schütz, G. *et al.* Absorption of circularly polarized X-rays in iron. *Phys Rev Lett* **58**, 737 (1987).

18. Hrabec, A. *et al.* Current-induced skyrmion generation and dynamics in symmetric bilayers. *Nat Commun* **8**, 15765 (2017).

19. Zeissler, K. *et al.* Discrete Hall resistivity contribution from Néel skyrmions in multilayer nanodiscs. *Nat Nanotechnol* **13**, 1161–1166 (2018).

20. Tinevez, J. Y. *et al.* TrackMate: An open and extensible platform for single-particle tracking. *Methods* **115**, 80–90 (2017).

21. Zeissler, K. *et al.* Diameter-independent skyrmion Hall angle observed in chiral magnetic multilayers. *Nat Commun* **11**, 428 (2020).

22. Legrand, W. *et al.* Hybrid chiral domain walls and skyrmions in magnetic multilayers. *Sci Adv* **4**, eaat0415 (2018).

23. Lepadatu, S. Efficient computation of demagnetizing fields for magnetic multilayers using multilayered convolution. *J Appl Phys* **126**, 103903 (2019).

24. Woo, S. *et al.* Observation of room-temperature magnetic skyrmions and their current-driven dynamics in ultrathin metallic ferromagnets. *Nat Mater* **15**, 501–506 (2016).

25. Bass, J. & Pratt, W. P. Spin-diffusion lengths in metals and alloys, and spin-flipping at metal/metal interfaces: An experimentalist's critical review. *Journal of Physics Condensed Matter* **19**, 183201 (2007).

26. Halas, S. & Durakiewicz, T. Work functions of elements expressed in terms of the Fermi energy and the density of free electrons. *Journal of Physics Condensed Matter* **10**, 10815 (1998).

27. Zhang, S., Levy, P. M. & Fert, A. Mechanisms of spin-polarized current-driven magnetization switching. *Phys Rev Lett* **88**, 236601 (2002).

28. Petitjean, C., Luc, D. & Waintal, X. Unified drift-diffusion theory for transverse spin currents in spin valves, domain walls, and other textured magnets. *Phys Rev Lett* **109**, 117204 (2012).

29. Zhang, W., Han, W., Jiang, X., Yang, S. H. & Parkin, S. S. P. Role of transparency of platinum-ferromagnet interfaces in determining the intrinsic magnitude of the spin Hall effect. *Nat Phys* **11**, 496–502 (2015).

30. Juge, R. *et al.* Current-Driven Skyrmion Dynamics and Drive-Dependent Skyrmion Hall Effect in an Ultrathin Film. *Phys Rev Appl* **12**, 044007 (2019).

31. Reeves, G. K., Lawn, M. W. & Elliman, R. G. Resistivity measurements of thin film iridium on silicon. *Journal of Vacuum Science & Technology A: Vacuum, Surfaces, and Films* **10**, 3203 (1998).

32. Zhang, W. *et al.* Spin pumping and inverse spin Hall effects - Insights for future spin-orbitronics (invited). *J Appl Phys* **117**, 172610 (2015).

33. Tokaç, M. *et al.* Interfacial Structure Dependent Spin Mixing Conductance in Cobalt Thin Films. *Phys Rev Lett* **115**, 056601 (2015).

34. Jiang, W. *et al.* Direct observation of the skyrmion Hall effect. *Nat Phys* **13**, 162–169 (2017).

35. Reichhardt, C., Ray, D. & Reichhardt, C. J. Collective transport properties of driven skyrmions with random disorder. *Phys Rev Lett* **114**, 217202 (2015).

36. Litzius, K. *et al.* The role of temperature and drive current in skyrmion dynamics. *Nat Electron* **3**, 30–36 (2020).

37. Azzawi, S., Hindmarch, A. T. & Atkinson, D. Magnetic damping phenomena in ferromagnetic thin-films and multilayers. *J Phys D Appl Phys* **50**, 473001 (2017).

6 Driving Skyrmion in the Presence of Stochastic Thermal Fields

In the previous chapter, a skyrmion collection was driven by a current in a multilayer system experimentally, which was then replicated using *Boris*. The interfacial spin-transfer torque (ISTT), alongside the spin-orbit torque (SOT) and bulk spin-transfer torque (STT), was shown to have a significant reduction in the skyrmion Hall angle (SkHA) and velocity, aligning computational results much closer to experimental results. Whereas, when the SOT was the only torque considered in driving the skyrmions, large discrepancies were observed, highlighting the significance of the ISTT.

Presented in this chapter is the study of the effect of a finite temperature when driving skyrmions in ultra-thin magnetic multilayers, in which the Monte Carlo algorithm is applied to obtain the Curie temperature of multilayers, and then a skyrmion is driven with a finite temperature set. Due to temperature effects, Eq. 3-13 can no longer be used as there are multiple magnetisation switching points, meaning the skyrmion information cannot be deduced, therefore a new method for tracking skyrmions is developed and implemented, which works even when stochasticity is present. The SOT and ISTT are simulated and discussed as one and not individually from this point on, as the previous chapters have thoroughly discussed the spin torques independently.

6.1 Introduction

Micromagnetic modelling is excellent for understanding the dynamics of a spectrum of magnetic systems due to the ability to probe certain parameters to gain a vast amount of information, and this extends when including temperature as well. However, when temperature is included in simulations it becomes much more difficult to model thermal effects as the parameter dependence needs to be known for the specific sample – for example, the Landau-Lifshitz-Bloch (LLB) equation used in micromagnetic temperature modelling[1,2] assumes the temperature dependence of magnetic parameters, unless the temperature dependences are numerically known or imported from atomistic modelling. In atomistic modelling, the LLB is not needed as the stochastic Landau-Lifshitz-Gilbert (LLG) can be used directly. Therefore, atomistic modelling is used in which each individual atomic spin can be modelled with temperature dependencies determined self-consistently over every iteration.

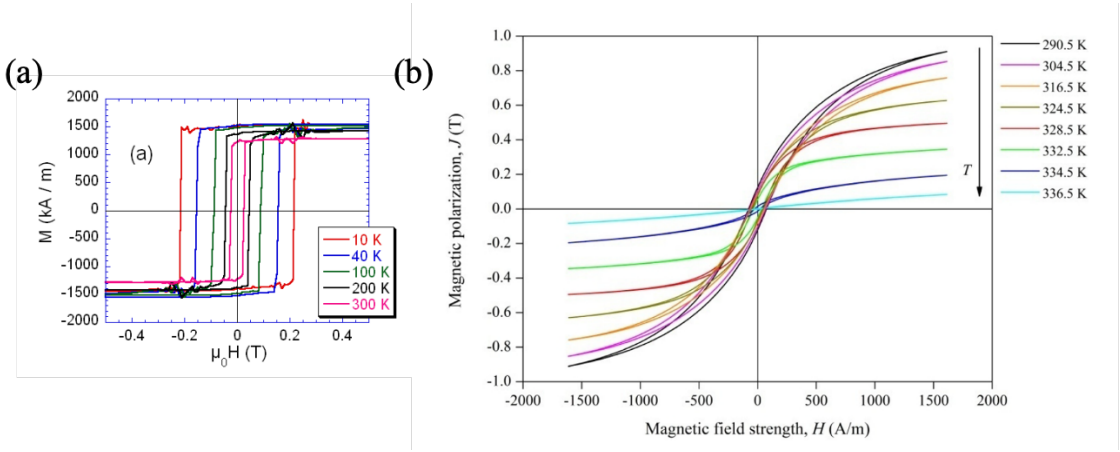

Figure 6-1 (a) Hysteresis loop for a Co/Pt ferromagnetic contact at different temperatures. Image is taken from Ref.[7]. (b) Hysteresis loop for La ($Fe_{10.5}Co_{1.4}Si_{1.1}$) for increasing temperatures close to T_c. Image is taken from Ref.[8]

The magnetisation of a ferromagnet has long been known to be strongly dependent on temperature, as with increasing temperature the thermal energy overcomes the exchange interactions between neighbouring spins, with an increasing effect, to a critical point at which the permanent magnetic properties are lost, namely the Curie temperature. The magnetisation of a material arises due to the thermodynamic average of atomic spins, thus with increasing temperature, the average value of the magnetisation decreases. The effect of temperature on the saturation magnetisation can also be shown via a hysteresis loop, for which, as the temperature of a magnetic body increases towards the Curie temperature, the maximum magnetisation decreases. This is shown by Grenet *et al*. (2009) in Figure 6-1(a), in which hysteresis loops are obtained for a Co(1.6 nm)/Pt(3 nm) contact at different temperatures. The saturation magnetisation is shown to decrease by 30.5% and the coercive field decreases by 88.3% when increasing the temperature from $T = 5$ K to $T = 300$ K. It should be noted here that the predicted Curie temperature of the Co(1.6 nm)/Pt(3 nm) is $T_c = 900$ K, therefore, given a larger temperature range, thus approaching T_c, the expected decrease in the saturation magnetisation will be larger. This is shown in Figure 6-1(b) for La ($Fe_{10.5}Co_{1.4}Si_{1.1}$), with $T_c = 330$ K, whereas T approaches T_c the saturation magnetisation vanishes to near negligible value as expected; other works have also shown this trend[3–5]. Furthermore, the temperature dependence of the magnetisation can be obtained directly from the magnetisation-temperature curve, which can be modelled using Eq. 6-1 below[6].

$$M(T) = \left(1 - \frac{T}{T_c}\right)^{\chi} \qquad \text{Eq. 6-1}$$

Here, T is the variable temperature, T_c is the Curie temperature and χ is the Bloch constant. Eq. 6-1 can be fit to an $M - T$ curve using T_c and χ as fitting constants, and thus the full temperature dependence can be used in simulations.

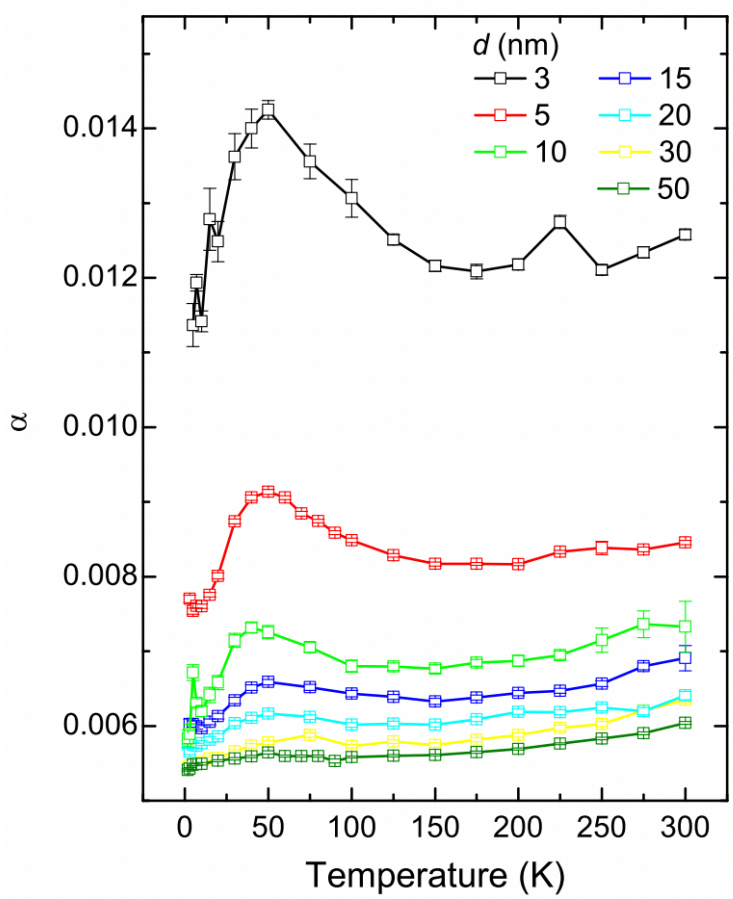

Figure 6-2 Temperature dependence on the Gilbert damping of permalloy thin films with TaN capping. The temperature dependence on the Gilbert damping is shown for permalloy film thicknesses of 3, 5, 10, 15, 20, 30 and 50 nm. Image is taken from Ref.[17].

Another important parameter that is strongly dependent on temperature is the Gilbert damping, α, which is a crucial factor in magnetisation dynamics and has many applications in spintronics devices, such as magnetic random-access memory and high-frequency microwave devices[9–13]. The Gilbert damping can be understood to be the relaxation of spin processional motion towards equilibrium and is used in the LLG equation to describe spin dynamics[14,15]. Verhagen *et al.* (2016)[16] show for a Co(10

nm)/Pt(10 nm) the Gilbert damping at $T = 30$ K, $\alpha = 0.0123$ and at $T = 300$ K, $\alpha = 0.0062$. Zhao *et al.* (2016)[17] experimentally show the damping is temperature dependent, as displayed in Figure 6-2, furthermore, the damping is revealed to be strongly dependent on thickness as well, as discussed earlier.

The Gilbert damping temperature dependence can also be obtained using

$$\alpha = \alpha_0 \left(1 - \frac{T}{3T_c}\right) \qquad \text{Eq. 6-2}$$

Where α_0 is the damping at absolute zero (0 K), temperature is the variable temperature and T_c is the Curie temperature. Similar to the magnetisation dependence, Eq. 6-1, T_c is used as a fitting parameter but α_0 is used as well in Eq. 6-2. The equation above encompasses multiple contributions to damping such as spin pumping[18–20] when heavy metals are adjacent, magnon damping and two-magnon damping[21–24].

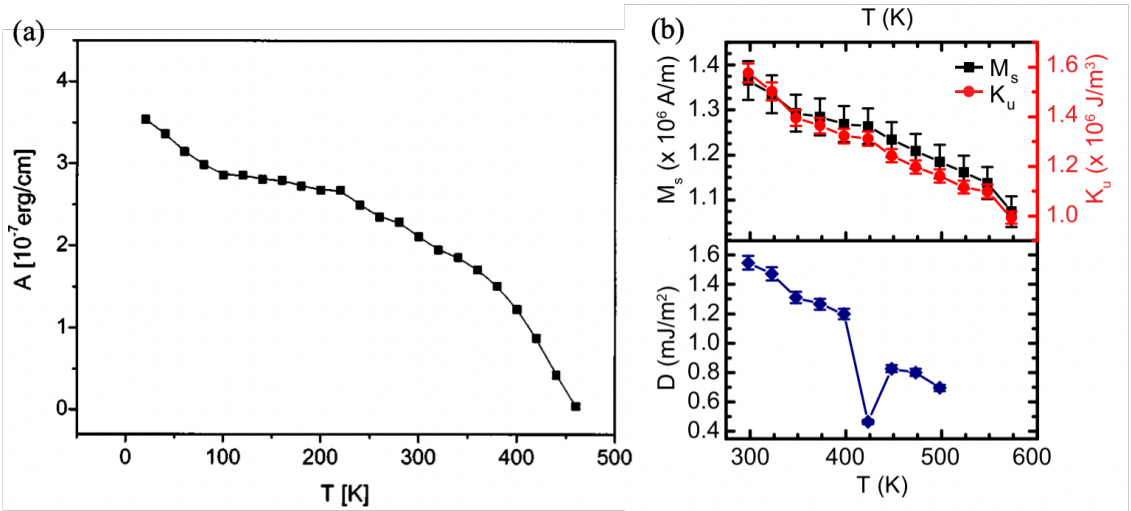

Figure 6-3 (a) Temperature dependence of the exchange stiffness coefficient. Image accreditation Ref.[27]. (b) Magnetocrystalline anisotropy, K_u, overlayed on M_s data and the Dzyaloshinskii-Moriya interaction strength D_{DMI}. Image accreditation Ref.[28].

The exchange interaction is a fundamental mechanism in ferromagnetic (FM) materials as it aligns neighbouring spins. The strength of the exchange stiffness is represented by the exchange stiffness coefficient, A_{ex}, which has been shown to be temperature dependent[25–27]. As temperature increases, so do thermal fluctuations, which reduces the

degree of ordering of neighbouring spins, lowering the effective value of A_{ex}. This is shown by Vértesy and Tomáš (2003)[27] in which the exchange parameter and its temperature dependence were determined for epitaxially grown magnetic thin garnet films which is shown in Figure 6-3(a). As the temperature increases there is a nearly linear decrease in A_{ex}, a trend which is also shown by Moreno *et al.* (2016)[25].

The Dzyaloshinskii-Moriya interaction (DMI), as already discussed, is akin to the exchange interaction, however, instead of aligning neighbouring atoms parallel, the DMI tends to align neighbouring spins perpendicular. The strength of the DMI mechanism is represented by the DMI coefficient D_{DMI} and is crucial for stabilising skyrmions in a magnetic system. Schlotter *et al.* (2018) studied a Ta(3 nm)[Pt(2 nm)/Co(1.1 nm)/Cu(1 nm)]$_{15}$/Pt(2 nm) structure finding that the interfacial DMI is dependent on temperature but varies more strongly with temperature than M_s and the bulk DMI, indicating a higher sensitivity to temperature and thermal fluctuations. This is shown in Figure 6-3(b), in which D_{DMI} decreases almost linearly with increasing temperature. Furthermore, Rózsa *et al.* (2017)[29] derived a temperature dependence of DMI and found that the dependence scales with the exchange interaction strength. Zhang *et al.* (2022)[30] also conducted an in-depth investigation on Co(1.5 nm)/Pt(1.5 nm) structures for T = 293 K up to T = 393 K, finding also a strong linear D_{DMI} dependence as well as for M_s and K_u.

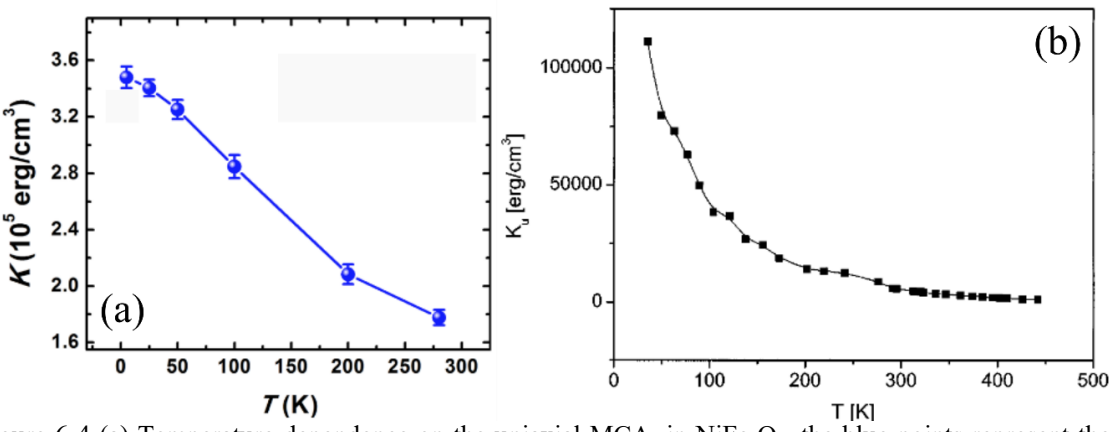

Figure 6-4 (a) Temperature dependence on the uniaxial MCA, in $NiFe_2O_4$, the blue points represent the experimental observations. Image adapted from Ref.[31]. (b) Temperature dependence of the uniaxial anisotropy for a thin magnetic garnet film. Image adapted from Ref.[27].

Lastly, magnetocrystalline anisotropy (MCA) is discussed. In essence, the MCA gives rise to a preferred orientation of the magnetic moments in a magnetic body and the term, K_u, is known as the MCA energy. There are various forms of anisotropy, depending on

the crystal structure, the most common of which are the uniaxial and cubic anisotropy, however, more complex anisotropies exist such as tetragonal, hexagonal and rhombohedral anisotropy. MCA arises due to electron spins coupling to the periodic potential of well-defined magnetic crystal structures through the spin-orbit interaction leading to an additional energy term which varies locally with the orientation of the magnetic moments. The MCA is strongly dependent on temperature, reducing quickly as temperature increases towards the Curie temperature. The dependence is evident in heat-assisted magnetic recording[32,33] in which the magnetic media writing is achieved by heating the material, such that the MCA decreases, leaving set information as the media cools[34–37]. The theoretical description of the temperature-dependent MCA was developed by Callen and Callen (1966)[38] which yields a power law scaling correlating $K_u(T)$ and $M_s(T)$ at low temperatures ($T << T_c$) as

$$\frac{K_u(T)}{K_u(0)} = \left[\frac{M_s(T)}{M_s(0)}\right]^n \qquad \text{Eq. 6-3}$$

Where $M_s(T)$ is the temperature-dependent saturation magnetisation, $n = \frac{l(l+1)}{2}$ is the exponent depending on the crystal symmetry and degree of correlation between the direction of adjacent spins[31] and l is the order of the anisotropy. Therefore, for uniaxial anisotropy with order l = 2[39,40], then the ideal scaling of K_u is M^3 where $M(T)$ is the magnetisation temperature dependence. Experimental evidence of the decrease of K_u with temperature is shown in Figure 6-3(b) for Ta(3 nm)/[Pt(2 nm)/Co(1.1 nm)/Cu(1 nm)]$_{15}$/Pt(2 nm) which is also evident in Figure 6-4(a).

6.1.1 The Curie temperature

As is well-known, magnetic materials only possess their permanent magnetic properties when below the Curie temperature, also known as the Curie point. In a FM material, the magnetic moments align parallel to their neighbouring moments, due to the exchange interaction causing spontaneous magnetisation, however, this is only when the temperature of said material is below the Curie temperature. When the temperature of a FM material becomes larger than the Curie temperature, thermal disorder overcomes the weak exchange interaction, resulting in a breakdown of alignment between neighbouring moments, causing a phase transition of the material to a paramagnetic state. In the paramagnetic state, the material does not have a net magnetic moment compared to the FM order phase.

Table 6-1 Micromagnetic material parameters for Co

Parameter	Value
Exchange stiffness, A	10 pJ/m
DMI exchange constant, A_{DMI}	-1.5 mJ/m^2
Magnetisation, M_s	600 kAm^{-1}
Uniaxial anisotropy, K_1	380 kJ/m^3
Damping, α	0.1
Relative gyroscopic ratio	1.3
Lattice constant, a	0.25 nm

To determine the Curie temperature of a magnetic body for use in micromagnetic simulations, multiple methods can be used, however, requiring significant computational resources and time. Spin dynamics use the LLG equation supplemented with a stochastic field. It is possible to obtain the magnetic parameters' temperature dependences by bringing the magnetic body in thermodynamic equilibrium and then obtaining the required information from many stochastically generated spin collections, but this is very inefficient when using large systems with very small time steps. A better method of obtaining the temperature dependences is using the parallel Monte Carlo algorithm to

generate spin collections that follow an expected Boltzmann distribution[41]. This method consists of randomly probing atomistic spins and rotating the spin in a small cone about its original positions, called a Monte Carlo move, and a new orientation of the spin is accepted given by the Boltzmann distribution below. The Monte Carlo move is accepted with a probability based on the Boltzmann distribution, otherwise, the move is rejected, and the spin orientation is not changed, which is attempted for all spins in the mesh such that once all spins have been trailed one Monte Carlo iteration is completed.

$$P_i = \exp\left(-\frac{\Delta E_i}{k_B T}\right) \qquad \text{Eq. 6-4}$$

The energy between the original spin and new spin orientation – the Monte Carlo move – is given by ΔE_i which is obtained from a spin Hamiltonian including numerous interactions, given below for E_i for spin i moment μ_S and direction $\widehat{\boldsymbol{S}}_i$

$$E_i = \sum_{j \epsilon N_i} J_{ij} \widehat{\boldsymbol{S}}_i \cdot \widehat{\boldsymbol{S}}_j - K_{u,i}\left(\widehat{\boldsymbol{S}}_i \cdot \hat{\boldsymbol{e}}_i\right)^2 + K_{c,i}\left(\hat{S}_{x,i}^2 \hat{S}_{y,i}^2 + \hat{S}_{x,i}^2 \hat{S}_{z,i}^2 + \hat{S}_{y,i}^2 \hat{S}_{z,i}^2\right) - \mu_0 \mu_{S,i} \widehat{\boldsymbol{S}}_i^2 \cdot \boldsymbol{H}_a \qquad \text{Eq. 6-5}$$

The energy change between the original spin orientation and the Monte Carlo move is obtained from a spin Hamiltonian, which includes four terms. The first is the isotropic exchange interaction, the second and third terms are the uniaxial and cubic anisotropy with energies $K_{u,i}$ and $K_{c,i}$, respectively, and the fourth is the external field contributions. It should be noted that uniaxial and cubic contributions are not present together.

Parallelisation of the Monte Carlo algorithm can be easily and efficiently achieved using the standard red-black checkerboard ordering approach method[41–44], which separates non-interacting spins into two sets: red and black. This eliminates data race conditions in which multiple threads in a single process access the same memory locations and at least one thread is accessing for a write operation, however, this is only the case in this situation if only the near neighbour spins are included in the exchange interaction for a simple

cubic structure. Furthermore, a realistic body-centred cubic (bcc) structure can be considered as two interpenetrating simple primitive lattices[45] and thus the red-black checkerboard ordering method can be applied to each sub-lattice in turn which allows consideration of exchange interactions between any number of spins in different sub-lattices[41]. Thus, for bcc, there are four sets of non-interacting spins, each containing one-quarter of the total of atomistic spins, i.e. from the initial separation of non-interacting spins, then the splitting into two sub-lattices. For a face-centre cubic (fcc) structure, as for Co, four interpolating simple primitive lattices can be used, leading to eight sets of non-interacting spins, each containing one-eighth the total atomic spins. It must be noted that this is a very efficient parallelisation if there is a large enough number of spins in each subset. Lepadatu *et al.* (2021) show that introducing the red-black checkerboard scheme into GPU computations is significantly faster than standard CPU computations. Furthermore, for systems with 1 million spins and above, the parallel Monte Carlo algorithm is over 200 times faster compared to the serial version, and scales linearly with increasing problem size [41].

To determine the magnetisation temperature scaling the parallel Monte Carlo algorithm is used in a Co fcc mesh. The material parameters for Co are shown in Table 6-1. It should be noted that temperature dependences are determined atomistically, therefore certain material parameters must be converted from energy density to energy units, as the former is no longer applicable for atomistic modelling. These are given below.

$$\mu_s = \frac{M_s a^3}{\mu_B} \quad \text{Eq. 6-6}$$

$$K = K_1 a^3 \quad \text{Eq. 6-7}$$

$$D = A_{DMI} a^3 \quad \text{Eq. 6-8}$$

$$J = 2A \quad \text{Eq. 6-9}$$

Here, a is the lattice constant of a = 2.5 Å, therefore the following conversions can be made: the magnetic moment using Eq. 6-6, atomistic anisotropy using Eq. 6-7, atomistic DMI using Eq. 6-8 and atomistic exchange with Eq. 6-9. To obtain a temperature

dependence for the magnetisation of Co, a temperature sweep from 0 and beyond T_c is completed such that each temperature has a normalised to zero temperature value, as shown in Figure 6-5 for smooth Co surface and a roughened Co surface. To obtain T_c from Figure 6-5, Eq. 6-1 is fit to the magnetisation profile using χ and T_c. The Curie temperature with no roughness is T_c = 423.7 K, χ = 0.57. When a surface roughness is applied, with a depth of d_{rough} = 5 Å and a roughness spacing $S_{rough} = 20a$, the Curie temperature is reduced T_c = 345.67 K, χ = 0.44. Roughness has been shown to decrease the Curie temperature of a material as shown by Zhao *et al.* (2000) and Zeng *et al.* (2011)[46,47] with layer thickness also having a significant effect [48].

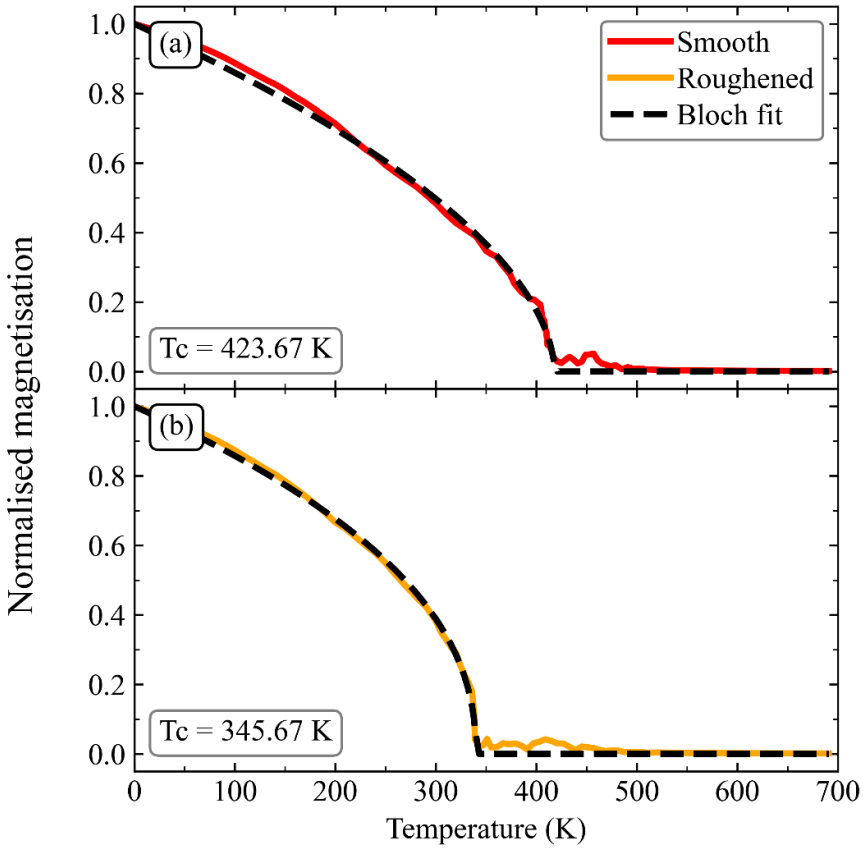

Figure 6-5 The relationship between normalised magnetisation and temperature for a Co(200 x 200 x 1) (nm) layer, obtained using the parallel Monte Carlo algorithm. The magnetisation scaling is fitted using the Bloch law resulting in (a) T_c = 423.67 K with no roughness and (b) T_c = 345.67 K with roughness (depth = 5 Å, and spacing = 50 Å).

6.2 Results and discussion

To begin, the geometrical constraints on an isolated skyrmion, whilst relaxing the system to an equilibrium state, are discussed. As the simulations in this chapter are being completed using atomistic modelling, the dimensions of the system now become limited due to the computational resources required. The systems dimension used are 50 nm x 50 nm x 1nm with periodic boundary conditions in the *xy* plane allowing the simulation over a much larger effective area which is very useful in the case of a much smaller mesh area. Due to the smaller mesh dimensions, smaller skyrmions are simulated in the range of ~ 15 nm up to ~ 30 nm. A skyrmion is then placed in the centre of the mesh and relaxed in three stages: (i) the initial relaxation phase with no roughness, (ii) the second phase with an applied roughness and (iii) the final stage with all the previous stages and a set temperature, all relaxed using the steepest descent method. Note that when the temperature is included in the final stage reaching a predetermined minimum $|\boldsymbol{m} \times \boldsymbol{H}|$ is difficult due to the thermal fluctuations resulting in large fluctuations in the normalised maximum torque, given as $|\boldsymbol{m} \times \boldsymbol{H}|/M_s^2$, so a time-step-iteration constraint is also included as a timeout so the simulation does not run indefinitely. The skyrmion size, controlled via an out-of-plane magnetic field and mesh size were tuned such that the skyrmion has limited interactions with its projection, a consequence of the Dirichlet *xy* boundary conditions. The landscape disorder, in the form of surface roughness, used in this simulation has a maximum roughness depth of 0.375 Å and 5 Å coherence length.

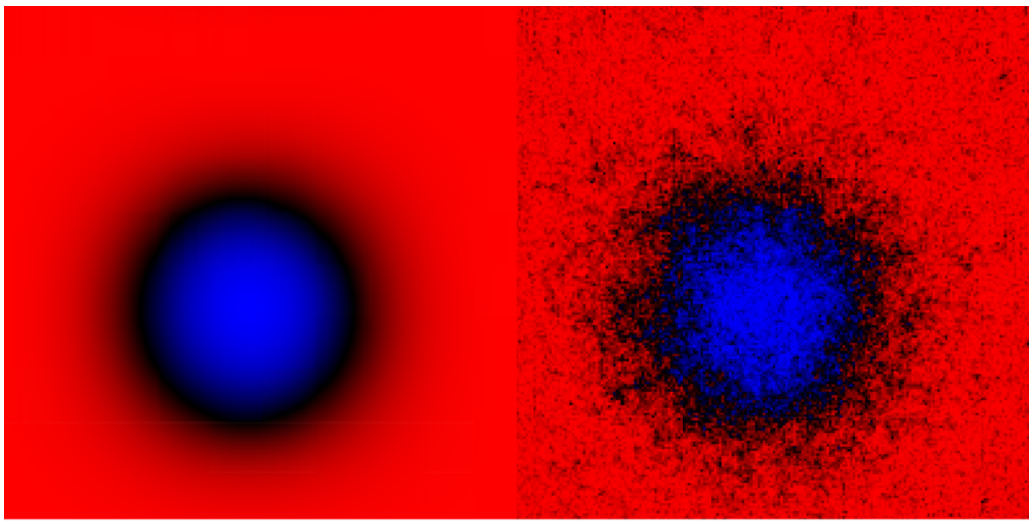

(a) (b)

Figure 6-6 A simulation view of a skyrmion at rest after the three relaxation stages at (a) T = 0 K and (b) T = 100 K.

As the temperature is now included in the modelling process, thermal fluctuations are an obvious occurrence, even more so when nearing the Curie temperature. This can be seen in Figure 6-6 in which a skyrmion has been placed in the centre of the magnetic body for T = 0 K and T = 100 K, then relaxed through the three stages as detailed above. Furthermore, from Figure 6-6, the skyrmion has moved during the relaxation phase evident as the skyrmion centre is no longer centred in the square mesh (where it was created during the simulation design) due to the effects of the thermal fields and local energy landscape, suggesting an equilibrium state has been achieved.

In the previous chapter, the skyrmions were modelled micromagnetically with the skyrmion information gathered using the *skypos* algorithm (see chapter 3.3.2), however, now that temperature stochasticity is included and modelling is carried out atomistically, the *skypos* algorithm cannot be used. The *skypos* algorithm is not valid in this case as it relies on the crossing points – regions of magnetic moment reversal – of the z-component of the magnetisation to obtain the diameter and position (see moment reversal in Figure 6-11(b)). Typically, there are multiple sites of magnetic reversal when stochasticity is included. The skyrmion information must then be gathered manually which alongside atomistic modelling increases the computational demand. To determine the skyrmion information the diameter and centre position in the x and y directions are required. This can be achieved by taking magnetisation profiles through both directions, however, due to thermal fluctuations these profiles become more distorted with larger temperatures making the centre point and diameter very difficult to accurately determine. The solution to this is simply to average a number of line profiles with the aim to reduce the noise which can be achieved by taking a line profile at regular time steps over a reasonably short time period. For a full simulation period of 3 ns and a timestep of 2 fs, there are 1,500,000 iterations – here a line profile is taken every iteration for 10,000 iterations (20 ps), thus 10,000-line profiles for x and y directions, independently of each other, which are then averaged. Figure 6-7(a) shows one set of line profiles for T = 100 K which is then averaged to one line profile shown in Figure 6-7(b). An ideal skyrmion typically has a much more defined magnetisation profile akin to a step function, as shown by Wang *et al.* (2018)[49], which is not clear in Figure 6-7(b). Thus, the diameter is taken as the difference in averaged magnetisation profile length between the two-moment reversal points, and the centre point of the skyrmion is taken as the centre point between the reversal points, illustrated by the red and blue lines in Figure 6-7(b), respectively.

With this information, a pseudo-tracker for the skyrmions has been created akin to the *skypos* algorithm, however, the method described above is not dynamic as it will not track a moving skyrmion. The tracker can be made to track a skyrmion in *Python* using a current x and y position variable, that can be updated with every averaging step. Note the averaging step size is large enough to eliminate noise but small enough as to not lose resolution in the skyrmion path. The position of the skyrmion is incremental with each profile average such that the difference between the known starting point and the new centre point can be used to update the current position variables. On the next iteration, the magnetisation profile position is adjusted according to the current position variables and repeated until the end of the simulation.

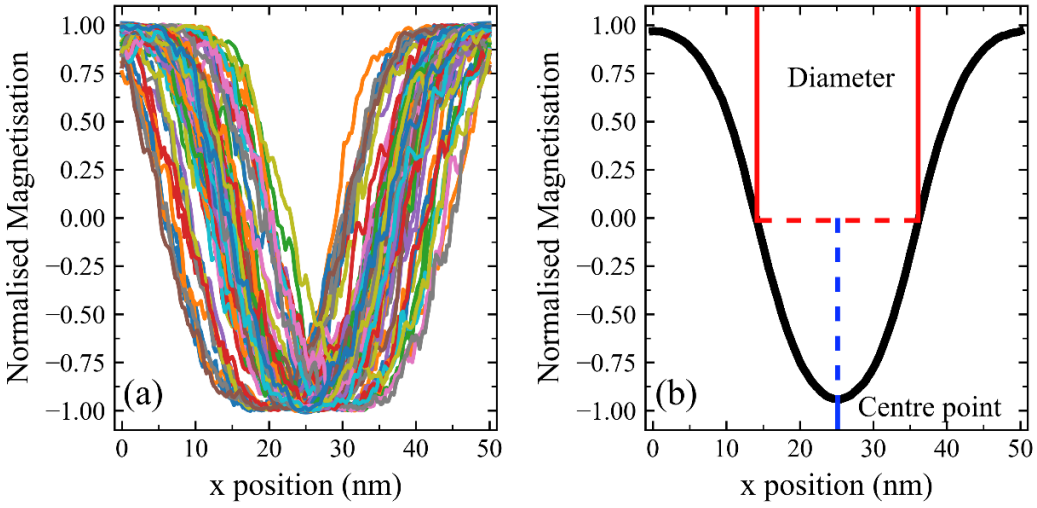

Figure 6-7 (a) Multiple magnetisation line profiles (in the x direction in this case) as shown by the solid lines in a spectrum of colours taken each time step. (b) Shows the average of all the line profiles in (a) which can be used to determine the skyrmion's centre point, in blue, and diameter, in red.

The diameter effect will now be discussed. The skyrmion diameter as a function of the applied magnetic field is shown in Figure 6-8. The method for determining the average diameter was discussed above. Furthermore, the average in Figure 6-8 is determined over all applied current densities such that each point contains a range of current density J_c = 100 GAm^{-2} to 800 GAm^{-2}. Note that this may seem conflicting as there is evidence of skyrmion inflation with increasing current density. However, Figure 6-9 shows for a large and small applied fields the difference in diameter at each temperature is minimal for both smaller and larger diameters. Thus, taking averages of the diameters across all current densities is valid in this case.

As expected, Figure 6-8 displays a decreasing trend, where with a larger applied magnetic field there is a decrease in the skyrmion diameters; this is also displayed in Figure 4-4. Interestingly, the trend shown in Figure 4-4 does not exist here as it now becomes a linear relationship. Furthermore, there is clear evidence that with an increased temperature the diameter increases which is displayed in Figure 6-8 where for H = 7 kAm^{-1} the average diameters for T = 0 and 150 K are ~ 22 nm and ~ 26 nm, respectively. The rate of change of diameter also decreases with larger temperatures where for T = 0 and 150 K the rate of changes is ~ -0.106 and ~ -0.080 m2/A, respectively.

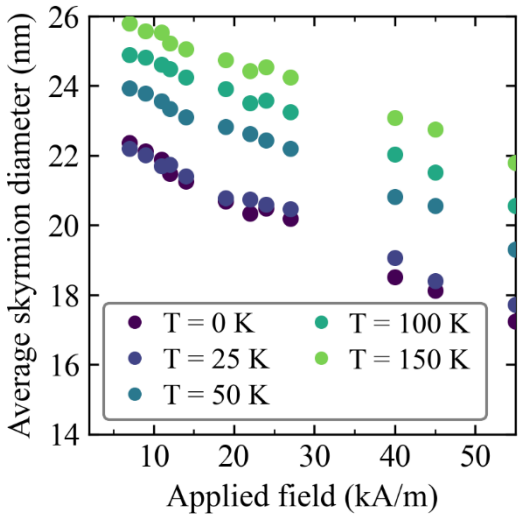

Figure 6-8 Average skyrmion diameter as a function of applied out-of-plane magnetic field for T = 0, 25, 50, 100, 150 K. Error bars have been omitted as to keep the figure understandable and readable.

Figure 6-9 shows the averaged diameter for H = 7 and H = 45 kAm^{-1} as a function of temperature. Again, it is clear, as stated above, there is a diameter-temperature dependence such that with increasing temperature the diameter also increases with the trend almost linear. However, the key point apparent in Figure 6-9(a,b) is that the diameter averages of J_c = 200 and 800 GAm^{-2} are very similar and overlap strongly with error analysis suggesting little to no change in the skyrmion diameter across different flow regimes. The diameter can also be analysed over the simulation, as shown in Figure 6-10 which shows the change in skyrmion diameter over a 3 ns simulation time. Comparing Figure 6-10(a) and Figure 6-10(e) for T = 0 and 150 K, respectively, it is clear there is a significant difference in the spread of diameter. For T = 0 K the diameters over time are much more defined than larger temperatures, as with increasing temperature the spread in diameter increases in noise due to the increased thermal fluctuations.

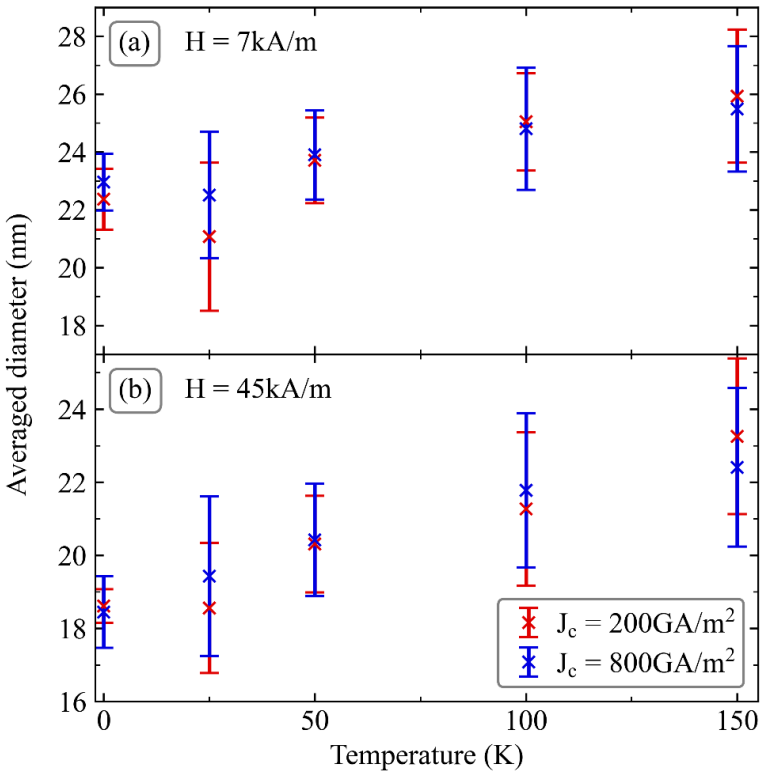

Figure 6-9 Relationship between the average diameter and temperature for (a) H = 7 kAm^{-1} and (b) H = 45 kAm^{-1}. The red and blue points indicate an applied current of J_c = 200 and 800 GAm^{-2}, respectively.

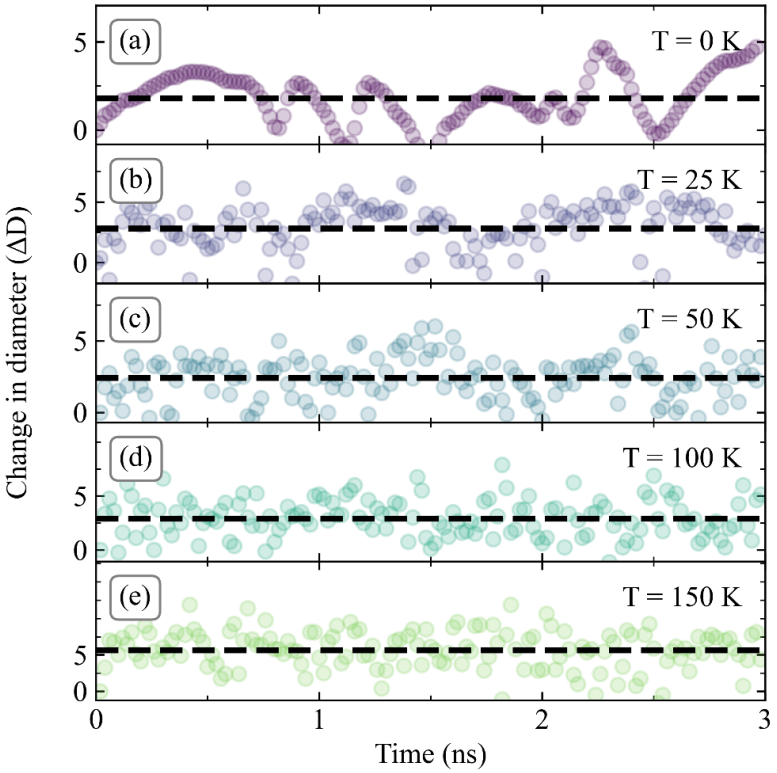

Figure 6-10 Change in diameter as a function of time for temperatures (a) T = 0 K, (b) T = 25 K, (c) T = 50 K, (d) T =100 K and (e) T =150 K. All temperatures have an applied field H = 45 kAm^{-1} and applied current J_c = 800 GAm^{-2}.

Examples of skyrmion paths extracted using the stochastic *skypos* algorithm (the newly created method) are now discussed. There are three skyrmion motion regimes, as discussed in earlier chapters, namely, the pinned, creep and flow regimes, for an isolated skyrmion. It is also well established that the local energy landscape of a magnetic body heavily influences the threshold current densities, thus the three regimes, however, this is even more so when the temperature is modelled. The effect of temperature on skyrmion motion regimes is shown in Figure 6-11. Note in Figure 6-11, each regime is shown for the largest driving current at which the regime is clearly displayed. In the pinned regime panel, the skyrmion at lower temperatures is immediately pinned, whereas the larger temperature is eventually pinned after falling from the creep regime into the pinned regime. Interestingly, the applied current density here is not the same for both skyrmions as they are driven using a 200 GAm^{-2} and 100 GAm^{-2} driving current for T = 25 K and T= 100 K, respectively. For the creep regime, the driving currents are 400 GAm^{-2} and 300 GAm^{-2} for T = 25 K and T = 100 K, respectively. Finally, in the flow regime, the driving currents are 650 GAm^{-2} and 500 GAm^{-2} for T = 25 K and T = 100 K, respectively. It is clear that when a larger temperature is applied to the magnetic system, not only the threshold current is reduced but also the threshold for the remaining regimes. Reduced threshold currents are expected for larger temperature as the thermal fluctuations have adverse effects on skyrmion stability[50], as shown in Figure 6-6. Furthermore, it is well established that skyrmion threshold currents, and thus velocity, are strongly dependent on the local energy landscape with heavily roughened surfaces requiring larger driving current to unpin a skyrmion. Litzius *et al.* (2020)[51] show driving skyrmions becomes more efficient for higher temperatures and thus yields faster skyrmion motion, further suggesting larger temperatures reduce regime threshold currents as shown in Figure 6-11.

Figure 6-12 shows the velocity dependence on the applied current density similar to that of Figure 4-10 in which a linear dependence is displayed, however, included is the temperature dependence at different applied field strengths. It is clear that for all applied field strengths, i.e. the skyrmion diameter, there is a strong dependence on temperature with larger temperatures yielding faster skyrmions as shown by Litzius *et al.* (2020)[51]. Larger temperature result in larger skyrmions due to the stability of the skyrmions and the increased energy of the system. Figure 6-12 shows a marked difference between T = 0 and T = 150 K for larger applied current densities. For H = 7 kAm^{-1} there is little difference in velocity for J_c = 100 GAm^{-2} between T = 0 and 150 K, however, when J_c =

800 GAm^{-2} there is a difference of ~ 46 ms^{-1}. Furthermore, when a larger out-of-plane field is applied, such that a smaller skyrmion is created, there is a slight reduction in the change of velocity between the smallest and largest temperature ~ 40 ms^{-1}.

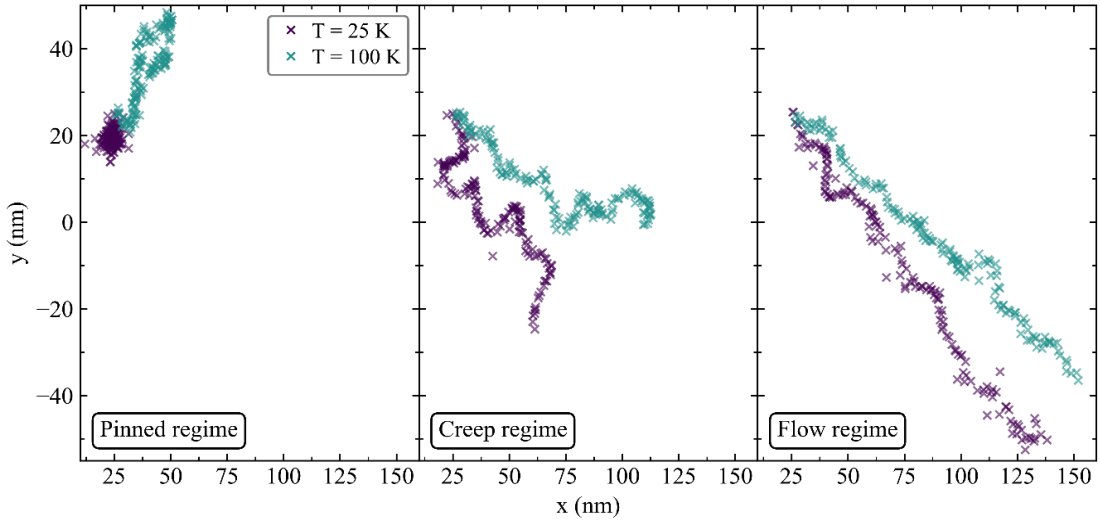

Figure 6-11 Simulated skyrmion paths illustrating the pinned, creep and flow regimes for (navy blue) T = 25 K and (cyan) T = 100 K. From left to right, for T = 25 K the corresponding current densities are 200, 400 and 650 GAm^{-2}, and for T = 100 K the corresponding current densities are 100, 300 and 500 GAm^{-2}, respectively.

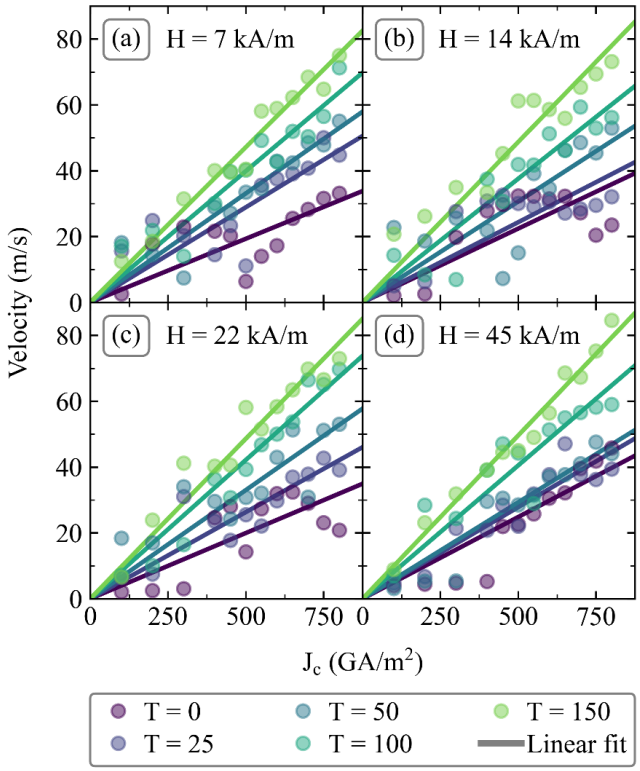

Figure 6-12 Relationship between skyrmion velocity and applied current density for (a) H = 7 kAm^{-1}, (b) 14 kAm^{-1}, (c) 22 kAm^{-1} and (d) 45 kAm^{-1}. The coloured points correspond to temperatures T = 0 K, 25 K, 50 K, 100 K and 150 K.

The SkHA is also strongly affected by the applied current density, as already discussed in previous chapters, as with an increasing driving current the skyrmion velocity also increases, as also shown in Figure 6-12, thus flow regimes and hence skyrmion paths have decreased variability with larger driving currents. Figure 6-13 shows the relationship not only between the skyrmion Hall and the applied current density but also the temperature and diameter dependence. As for Figure 6-12, the out-of-plane fields are H = 7, 14, 22 and 45 kAm^{-1} with T = 0, 25, 50, 100 and 150 K. Again, it is clear that temperature has a strong effect, however, unlike skyrmion velocity, there is a large difference between small driving currents. For example, in Figure 6-13(d) at J_c = 300 GAm^{-2} the change in the SkHA between T = 25 and T = 150 K is ~ 17°. This is mainly due to the skyrmion flowing in the creep regime where it sporadically jumps between weak pinning sites, therefore making the determination of the SkHA difficult.

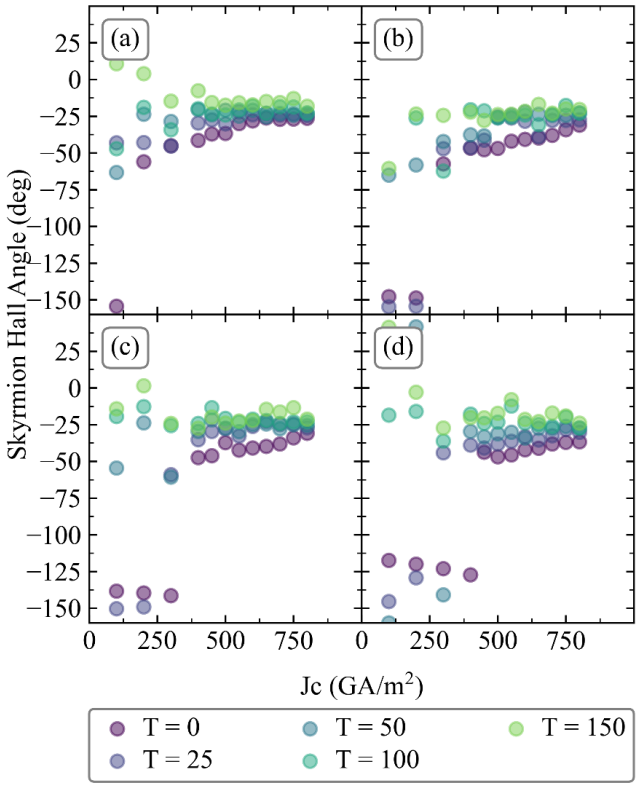

Figure 6-13 Relationship between skyrmion Hall angle and applied current density for (a) H = 7 kAm^{-1}, (b) 14 kAm^{-1}, (c) 22 kAm^{-1} and (d) 45 kAm^{-1}. The coloured points correspond to temperatures T = 0 K, 25 K, 50 K, 100 K and 150 K.

The most effective method of determining the SkHA is a linear fit to the path, between the initial and final points. On the other hand, as the driving current increases to J_c = 800 GAm^{-2}, the SkHA tends towards a single value which is clearly evident in Figure 6-13(a)

and (c) as the skyrmion traverses in the flow regimes and is minimally affected by surface roughness. Interestingly, skyrmions in Figure 6-13 show a similar trend to that shown by Jiang *et al.* (2017)[52] in which the skyrmion has an initial flat SkHA dependence due to pinned skyrmions followed by a steep linear increase in the SkHA as the skyrmion passes the pinning threshold current and velocity increases. Finally, the skyrmion reaches a point at which its SkHA flattens to a nearly constant value as it has a strong flow motion. These characteristics are clearly shown in Figure 6-13(c,d) for all temperatures, however, the characteristics become more difficult to visualise with increasing diameters, Figure 6-13(a,b), where at the largest diameter the trend becomes a more gradual change – the convergence of the SkHA occurs over a much larger J_c range than smaller diameters.

Figure 6-14 shows the relationship between the SkHA and velocity with both temperature and diameter displayed. Figure 6-14 confirms the above-mentioned effects in Figure 6-12 and Figure 6-13 in which at small driving currents, thus small velocities, the skyrmions experience high deflection due to the local energy landscape, which is typical of the creep regime, after which the SkHA flattens to an almost constant value which has been shown experimentally[51,53,54]. Interestingly, the flattening of this trend is apparent for all temperatures. There are two distinct velocity behaviours here: (i) the creep regime up to ~ 12 ms^{-1} and (ii) the flow regime above 12 ms^{-1}. The results for a range of temperatures suggest a collapse on to a universal trend for temperature-dependent SkHA-velocity relationship, which is nearly independent of surface roughness, corresponding well qualitatively with Litzius *et al.* (2020)[51]. Interestingly, these results show characteristics of an independent SkHA-velocity relationship on diameter as all diameters shown have very similar initial sharp increases which then flatten at approximately equal SkHAs, further suggesting a collapse into a universal trend, similar to experimental results in similar systems[51–54]. Furthermore, it can be deduced from Figure 6-14 that larger temperatures require a smaller velocity to enter the flow regimes as discussed earlier, evident when comparing T = 0 and T = 150 K. In all cases, in Figure 6-14, for T = 150 K, nearly no skyrmions appear in the initial sharp increase but reside in the second phase when the trend flattens and all points for T = 150 K appear to exhibit a linear trend, due to the increased thermal fluctuations, unlike T = 0 K where skyrmions regularly appear in the initial sharp increase.

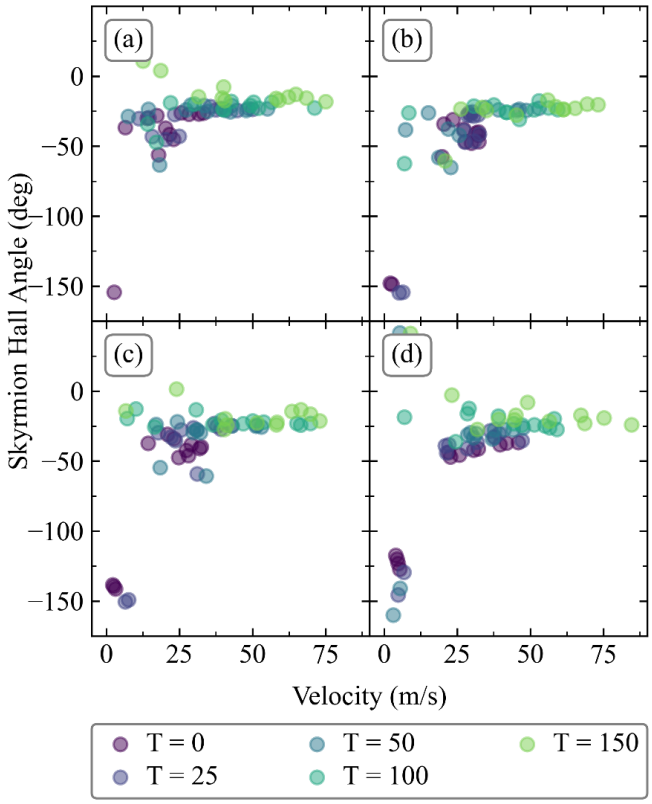

Figure 6-14 The skyrmion Hall angle dependence on the skyrmion velocity for (a) H = 7 kAm^{-1}, (b) 14 kAm^{-1}, (c) 22 kAm^{-1} and (d) 45 kAm^{-1}. The coloured points correspond to temperatures T = 0 K, 25 K, 50 K, 100 K and 150 K.

Ideally, the Thiele equation would be used to verify these results, however, an in-depth derivation of a stochastic field Thiele equation is beyond the scope of this work and is proposed work for the future. However, in the meantime, some simple changes can be made to the Thiele equation to incorporate some temperature terms, namely the magnetisation and the damping terms, both of which are well established to be temperature dependent. The magnetisation and damping temperature dependence[55] can be modelled using Eq. 6-1 and Eq. 6-2, respectively. Ideally, the incorporation of these dependences will align the Thiele model better to simulated results. Therefore, a simplistic temperature-dependent Thiele equation from Eq. 2-29 with Eq. 6-1 and Eq. 6-2 becomes

$$v(T) = \sqrt{\frac{(u_{SOT} - \beta_{STT} D u_{STT})^2 + u_{STT}^2}{1 + \left(\alpha_0 \left(1 - \frac{T}{3T_c}\right) D\right)^2}} \qquad \text{Eq. 6-10}$$

$$\tan(\theta_{SkHA}) = \frac{u_{SOT} + (\alpha - \beta_{STT})Du_{STT}}{\alpha D u_{SOT} - (1 + \alpha\beta_{STT}D^2)u_{STT}}$$

where $u_{sot}\ (T) = \frac{\mu_B \theta_{SHAeff} \pi R J_{HM}}{4e(1-T/T_c)\chi\ d_F}$ and $u_{stt}\ (T) = \frac{P_{STT} g \mu_B J_{FM}}{\left(3e(1-T/T_c)\chi(1+\beta_{STT}^2)\right)}$. However, these inclusions into the temperature dependence parameters of the Thiele equation do not align with the simulated results for the velocity. This is highly likely as only α and M_s have temperature dependent models implemented into the Thiele model in this instance. Thus, it is suggested that a stricter model be fully explored from first principles. Weißenhofer et al. (2021)[56] demonstrated a temperature-dependent model using a skyrmion couple to a magnonic heat bath which led to an additional dissipative friction term, however, even though the model aligns with simulated results there is a large diameter discrepancy between the two methods. Albeit this work provides a strong framework for future development.

6.3 Conclusion

In this chapter, the temperature dependence of skyrmion motion has been studied in ultra-thin Pt(3 nm)/Co(1 nm) magnetic bodies with landscape disorder, utilising atomistic modelling to self-consistently determine temperature dependences or magnetic parameters.

To begin, a new tracking method was devised and implemented as the *skypos* algorithm was no longer applicable for modelling thermal fluctuations due to temperatures as it requires two magnetisation reversal points. The new method averaged line profiles in the *x* and *y* directions over multiple time steps, thus eliminating thermal noise. This then allowed critical points of a magnetisation profile to be determined, such as the central point, for calculation of the new centre point and the diameters.

The Curie temperature for the bilayer structure was then determined for a smooth and roughened surface using the Monte Carlo algorithm, resulting in a decrease of ~ 78 K for the roughened surface. Skyrmions were then driven under various driven currents, temperatures and out-of-plane applied magnetic fields. The diameter increased nearly linearly with temperature but did not change between different current densities. Furthermore, the diameter fluctuations were relatively small but did increase with

temperature as expected. The SkHA was shown to have a markedly similar result to the literature with skyrmions having an initial flat trend which then passes the pinning threshold and jumps linearly and rapidly to a maximum SkHA with a near-constant trend. There was a slight dependence of the skyrmion size where at the largest diameters the trend became a more gradual change – the convergence of the SkHA occurs over a much larger J_c range than smaller diameters. This chapter was further able to shed light on the ISTT but under the influence of thermal fluctuations. Results compared well to experimentally obtained results in the literature and this shows the significance of the ISTT.

Chapter References

1. Garanin, D. A. Uniform and non-uniform thermal switching of magnetic particles. *Phys Rev B* **98**, 144425 (2018).

2. Garanin, D. A. Fokker-Planck and Landau-Lifshitz-Bloch equations for classical ferromagnets. *Phys Rev B* **55**, 3050 (1997).

3. Wurmehl, S. *et al.* Half-metallic ferromagnetism with high magnetic moment and high Curie temperature in Co2FeSi. *J Appl Phys* **99**, 08J103 (2006).

4. van Kesteren, H. W. & Zeper, W. B. Controlling the Curie temperature of Co/Pt multilayer magneto-optical recording media. *J Magn Magn Mater* **120**, 271–273 (1993).

5. Evans, R. *et al.* The influence of shape and structure on the Curie temperature of Fe and Co nanoparticles. *J Appl Phys* **99**, 08G703 (2006).

6. Posth, O. *et al.* Influence of growth parameters on the perpendicular magnetic anisotropy of [Co/Ni] multilayers and its temperature dependence. *J App Phys* **106**, 023919 (2009).

7. Grenet, L. *et al.* Spin injection in silicon at zero magnetic field. *Appl Phys Lett* **94**, 032502 (2009).

8. Gozdur, R. & Najgebauer, M. Scaling analysis of phase transitions in magnetocaloric alloys. *J Magn Magn Mater* **499**, 166239 (2020).

9. Lourembam, J. *et al.* Thickness-Dependent Perpendicular Magnetic Anisotropy and Gilbert Damping in Hf/Co20Fe60B20/MgO Heterostructures. *Phys Rev Appl* **10**, 044057 (2018).

10. Lee, A. J. *et al.* Metallic ferromagnetic films with magnetic damping under 1.4 × 10−3. *Nat Commun* **8**, 234 (2017).

11. Rana, B. *et al.* Nonlinear Control of Damping Constant by Electric Field in Ultrathin Ferromagnetic Films. *Phys Rev Appl* **14**, 014037 (2020).

12. Chumak, A. V., Vasyuchka, V. I., Serga, A. A. & Hillebrands, B. Magnon spintronics. *Nat Phys* **11**, 453–461 (2015).

13. Demidov, V. E. *et al.* Magnetic nano-oscillator driven by pure spin current. *Nat Mater* **11**, 1028–1031 (2012).

14. Landau, L. D. & Lifshitz, E. M. *Statistical Physics*. (Pergamon Press Ltd, 1980).

15. Landau, L. & Lifshitz, E. On The Theory Of The Dispersion Of Magnetic Permeability In Ferromagnetic Bodies. *Phys. Zeitsch. der Sow* **8**, 153–169 (1935).

16. Verhagen, T. G. A. *et al.* Temperature dependence of spin pumping and Gilbert damping in thin Co/Pt bilayers. *Journal of Physics Condensed Matter* **28**, 056004 (2016).

17. Zhao, Y. *et al.* Experimental Investigation of Temperature-Dependent Gilbert Damping in Permalloy Thin Films. *Sci Rep* **6**, 22890 (2016).

18. Verhagen, T. G. A. *et al.* Temperature dependence of spin pumping and Gilbert damping in thin Co/Pt bilayers. *Journal of Physics: Condensed Matter* **28**, 056004 (2016).

19. Rojas-Sánchez, J.-C. *et al.* Spin Pumping and Inverse Spin Hall Effect in Platinum: The Essential Role of Spin-Memory Loss at Metallic Interfaces. *Phys Rev Lett* **112**, 106602 (2014).

20. Avilés-Félix, L., Butera, A. & Gómez, J. E. Spin pumping and inverse spin Hall effect in antiferromagnetic exchange coupled [Co/Ru/Co]/Pt heterostructures. *Appl Phys Lett* **110**, 052402 (2017).

21. Fletcher, R. C., Lecraw, R. C. & Spencer, E. G. Electron Spin Relaxation in Ferromagnetic Insulators. *Physical Review* **117**, 995 (1960).

22. Sparks, M., Loudon, R. & Kittel, C. Ferromagnetic Relaxation. I. Theory of the Relaxation of the Uniform Precession and the Degenerate Spectrum in Insulators at Low Temperatures. *Physical Review* **112**, 791 (1961).

23. Yuan, S. J., Sun, L., Sang, H., Du, J. & Zhou, S. M. Interfacial effects on magnetic relaxation in Co/Pt multilayers. *Phys Rev B* **68**, 134443 (2003).

24. Sakoguchi, A., Oshima, D., Iwata, S. & Kato, T. Electric-Field Modulation of Perpendicular Magnetic Anisotropy and Damping Constant in MgO/Co/Pt Trilayers. *IEEE Trans Magn* **58**, 1–5 (2022).

25. Moreno, R. *et al.* Temperature-dependent exchange stiffness and domain wall width in Co. *Phys Rev B* **94**, 104433 (2016).

26. Atxitia, U. *et al.* Multiscale modeling of magnetic materials: Temperature dependence of the exchange stiffness. *Phys Rev B* **82**, 134440 (2010).

27. Vértesy, G. & Tomáš, I. Temperature dependence of the exchange parameter and domain-wall properties. *J Appl Phys* **93**, 4040 (2003).

28. Schlotter, S., Agrawal, P. & Beach, G. S. D. Temperature dependence of the Dzyaloshinskii-Moriya interaction in Pt/Co/Cu thin film heterostructures. *Appl Phys Lett* **113**, 092402 (2018).

29. Rózsa, L., Atxitia, U. & Nowak, U. Temperature scaling of the Dzyaloshinskii-Moriya interaction in the spin wave spectrum. *Phys Rev B* **96**, 094436 (2017).

30. Zhang, Y. *et al.* Direct observation of the temperature dependence of the Dzyaloshinskii–Moriya interaction. *J Phys D Appl Phys* **55**, 195304 (2022).

31. Chatterjee, B. K., Ghosh, C. K. & Chattopadhyay, K. K. Temperature dependence of magnetization and anisotropy in uniaxial NiFe2O4 nanomagnets: Deviation from the Callen-Callen power law. *J Appl Phys* **116**, (2014).

32. Thiele, J. U., Maat, S. & Fullerton, E. E. FeRh/FePt exchange spring films for thermally assisted magnetic recording media. *Appl Phys Lett* **82**, 2859 (2003).

33. Challener, W. A. *et al.* Heat-assisted magnetic recording by a near-field transducer with efficient optical energy transfer. *Nat Photonics* **3**, 220–224 (2009).

34. Alex, M. *et al.* Characteristics of thermally assisted magnetic recording. *IEEE Trans Magn* **37**, 1244–1249 (2001).

35. Lyberatos, A. & Guslienko, K. Y. Thermal stability of the magnetization following thermomagnetic writing in perpendicular media. *J Appl Phys* **94**, 1119 (2003).

36. Saga, H., Nemoto, H., Sukeda, H. & Takahashi, M. New recording method combining thermo-magnetic writing and flux detection. *Jpn J Appl Phys* **38**, (1999).

37. Thiele, J. U., Coffey, K. R., Toney, M. F., Hedstrom, J. A. & Kellock, A. J. Temperature dependent magnetic properties of highly chemically ordered Fe55−xNixPt45L10 films. *J Appl Phys* **91**, 6595 (2002).

38. Callen, H. B. & Callen, E. The present status of the temperature dependence of magnetocrystalline anisotropy, and the l(l+1)2 power law. *Journal of Physics and Chemistry of Solids* **27**, 1271–1285 (1966).

39. Long, G. *et al.* Magnetic anisotropy and coercivity of Fe3Se4 nanostructures. *Appl Phys Lett* **99**, 202103 (2011).

40. Wang, J., Zhao, F., Wu, W. & Zhao, G. M. Unusual temperature dependence of the magnetic anisotropy constant in barium ferrite BaFe12O19. *J Appl Phys* **110**, 096107 (2011).

41. Lepadatu, S., Mckenzie, G., Mercer, T., MacKinnon, C. R. & Bissell, P. R. Computation of magnetization, exchange stiffness, anisotropy, and susceptibilities in large-scale systems using GPU-accelerated atomistic parallel Monte Carlo algorithms. *J Magn Magn Mater* **540**, 168460 (2021).

42. Block, B., Virnau, P. & Preis, T. Multi-GPU accelerated multi-spin Monte Carlo simulations of the 2D Ising model. *Comput Phys Commun* **181**, 1549–1556 (2010).

43. Weigel, M. & Yavors'kii, T. GPU accelerated Monte Carlo simulations of lattice spin models. *Phys Procedia* **15**, 92–96 (2011).

44. Block, B., Virnau, P. & Preis, T. Multi-GPU accelerated multi-spin Monte Carlo simulations of the 2D Ising model. *Comput Phys Commun* **181**, 1549–1556 (2010).

45. Misra, Prasanta. *Physics of Condensed Matter*. (Elsevier Science, 2010).

46. Zhao, D., Liu, F., Huber, D. L. & Lagally, M. G. Magnetization on rough ferromagnetic surfaces. *Phys Rev B* **62**, 11316 (2000).

47. Zeng, L. *et al.* The growth, surface topography and Curie temperature in Ni thin films: Kinetic lattice Monte Carlo simulation. *Adv Mat Res* **150–151**, 493–498 (2011).

48. Koyama, T. *et al.* Dependence of Curie temperature on Pt layer thickness in Co/Pt system. *Appl Phys Lett* **106**, 132409 (2015).

49. Wang, X. S., Yuan, H. Y. & Wang, X. R. A theory on skyrmion size. *Communications Physics* **1**, 31 (2018).

50. Tang, C. *et al.* Effects of temperature and structural geometries on a skyrmion logic gate.

51. Litzius, K. *et al.* The role of temperature and drive current in skyrmion dynamics. *Nat Electron* **3**, 30–36 (2020).

52. Jiang, W. *et al.* Direct observation of the skyrmion Hall effect. *Nat Phys* **13**, 162–169 (2017).

53. Zeissler, K. *et al.* Diameter-independent skyrmion Hall angle observed in chiral magnetic multilayers. *Nat Commun* **11**, 428 (2020).

54. Juge, R. *et al.* Current-Driven Skyrmion Dynamics and Drive-Dependent Skyrmion Hall Effect in an Ultrathin Film. *Phys Rev Appl* **12**, 044007 (2019).

55. Lepadatu, S. Interaction of magnetization and heat dynamics for pulsed domain wall movement with Joule heating. *J Appl Phys* **120**, 163908 (2016).

56. Weißenhofer, M., Rózsa, L. & Nowak, U. Skyrmion Dynamics at Finite Temperatures: Beyond Thiele's Equation. *Phys Rev Lett* **127**, 047203 (2021).

7 Synthetic Antiferromagnetic Skyrmions: Initial Work and Analysis

In this chapter, an initial investigation into skyrmion motion in synthetic antiferromagnetic (SAF) and ferrimagnetic structures (SYF) is presented. SAFs and SYFs are very exciting prospects when considering skyrmion motions because the transverse motion to the applied current direction can be almost eliminated, making them very promising for future skyrmionics devices. Much more work needs to be completed on this work as it is a new field, however, the result shown in this chapter is still useful.

7.1 Introduction

It is well-known by now that magnetic skyrmions are localised 2D spin textures that exist in magnetic systems due to the Dzyaloshinskii-Moriya interaction (DMI)[1], and interfacial DMI in ultra-thin multilayer systems, produced from a broken inversion symmetry. As shown in previous chapters and other works, isolated skyrmions can be created, stabilised and manipulated in ferromagnets due to the DMI [2–7] and, crucially, an externally applied field perpendicular to the plane of the skyrmion. Detectable skyrmions are also becoming much smaller and more work is being conducted, which is very promising for skyrmionics devices, however, further decreasing skyrmion size reduces stability due to thermal fluctuations[8] in ferromagnetic (FM) structures.

Remembering one of the most important difficulties of skyrmions is the transverse motion with respect to the current direction, the skyrmion Hall effect leading to the skyrmion Hall angle (SkHA), it may be suggested that a progression from FM structures should be made. For one interesting alternative to FM, see Figure 7-1(a), structures are antiferromagnetic (AFM) structures as shown in Figure 7-1(b) – systems of alternating orientations of magnetic moments which can be considered two coupled subsystems of anti-aligned magnetic moments. AFMs not only compensate for the skyrmion Hall effect and thus the SkHA, but also nearly eliminate the dipolar fields allowing for smaller skyrmions to be created, stabilise and manipulate AFM skyrmions[9,10]. AFM skyrmions are then very exciting prospects as they eliminate the major issues highlighted above, however, due to the nature of AFMs having no net magnetic moments it becomes difficult to control and detect skyrmions in these structures.

True AFM skyrmions have been difficult to realise due to the arrangement of magnetic moments but have been recently observed[11], however, SAFs, as seen in Figure 7-1(d), the structure can be used as a substitute that can be composed by a typical heavy metal (HM)/FM bilayer with strong interfacial DMI coupled to another antiferromagnetically through a non-magnetic spacer layer, via the Ruderman-Kittel-Kasuya-Yoshida (RKKY) interaction[12]. Legrand *et al*. (2019)[13] showed the stabilisation of AFM skyrmions in SAF structures at room temperature. Also, spin states existed in a SAF with vanishing perpendicular magnetic anisotropy which was turned into AFM skyrmions utilising the interlayer electronic coupling. Furthermore, Juge *et al.* (2022)[14] report on the observation of isolated skyrmions in compensated synthetic antiferromagnets at zero field and room temperature using X-ray magnetic microscopy using micromagnetic modelling to confirm this[15].

Like AFMs, SAFs also produce near to no dipolar interactions. Another structure is a SYF, as seen in Figure 7-1(d), which is akin to the SAF, however, a typical ferrimagnet has similar magnetic arrangements to an AFM but there is a magnetic bias in the structure in a preferred direction and thus a net magnetic moment exists.

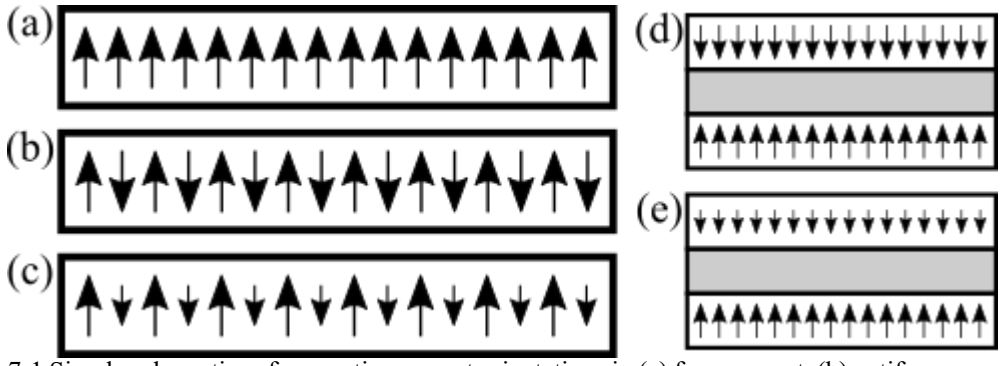

Figure 7-1 Simple schematics of magnetic moment orientations in (a) ferromagnet, (b) antiferromagnet, (c) ferrimagnet, (d) synthetic antiferromagnet with non-magnetic spacer layer, (e) synthetic ferrimagnet with non-magnetic spacer layer.

7.2 Method

To begin, a method of procedurally generating SAF/SYF structures is created so that the thickness of an individual layer in a SAF/SYF stack could be easily changed. This is required as *Boris* uses spatial coordinates to define the bounds of multiple layers, but also allows a singular *Python* script to create and drive a skyrmion system. The structure created is a Pt(3 nm)/Co(1 nm)/Ir(1 nm)/Co(x)/Pt(3 nm) where x is the varying thickness

of the upper Co2 layer – an illustration is shown in Figure 7-2. From this point on, the lower Co layer and upper Co layer will be referenced as Co1 and Co2 as shown in Figure 7-2, respectively. Due to the increase in net thickness of the magnetic body compared to previous structures used, the in-plane *xy* dimensions were set to 400 x 400 nm with non- and magnetic cell size (1 nm, 1 nm, 0.2 nm). For both FM layers the interfacial DMI, uniaxial anisotropy and surface exchange interactions were enabled and all layers had the transport module enabled. The alignment of the magnetic moments is set out-of-plane in the $+z$ direction for Co1 and the $-z$ direction for Co2, thus replicating Figure 7-1(d). Periodic boundary conditions are set in the *xy* directions to provide a wraparound effect for the stray field. The material parameters for this system are shown in Table 7-1. A skyrmion is placed in the centre of both Co layers with opposite core and chirality directions, and the system is set to relax using the *LLGStatic* with the steepest descent (*SDesc*) solving method.

The spin torques of the system can now be determined, however, unlike with a Co/Pt bilayer system, for SAF/SYF the procedure is much more involved due to the increased number of FM layers. This is accomplished by first condensing each FM layer independently such that the system is effectively composed of two subsystems: a Pt/Co1(1 nm)/Ir and an Ir/Co2(*x*)/Pt system. Furthermore, to simplify this system and calculations further, the spin Hall angle for Ir is set to zero as the true value is near negligible. As in previous chapters, a small potential must be applied so spin accumulation is generated in the system which is used to determine the fitting parameters.

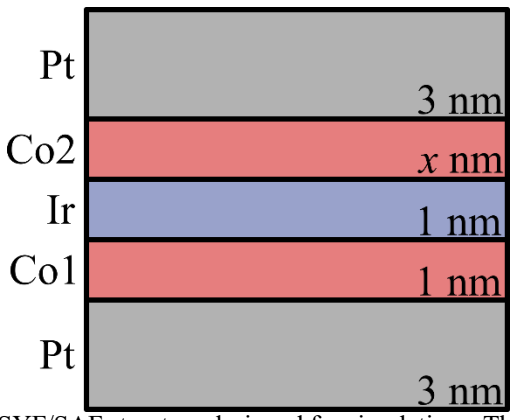

Figure 7-2 Illustration of the SYF/SAF structure designed for simulations. The system is considered a SYF when unbalanced (Co1≠Co2) and SAF when balanced (Co1=Co2). *x* is the thickness of Co2 measured in nm.

For the spin torques obtained with the self-consistent spin transport solver, the contributions observed are the spin-orbit torque (SOT) due to the spin Hall effect (SHE), as well as the interfacial spin-transfer torque (ISTT) due to interlayer spin diffusion. To obtain solutions for these contributions, P, β, r_G and $\theta_{SHA,eff}$ are obtained numerically. Thus, the spin accumulation is computed using the spin transport solver and the total spin torque is obtained – Eq. 2-28. Then, Eq. 2-51 and Eq. 2-54, for the SOT and ISTT respectively, are used to obtain the above constants as fitting parameters to the total spin torque. Whilst $\theta_{SHA,eff}$ and r_G do not depend on the skyrmion diameter, P and β are not constant and show a small dependence on skyrmion diameter due to spin diffusion, similar to the enhancement of Zhang-Li non-adiabaticity obtained for vortex cores[16,17]. The ISTT can be simply determined by setting θ_{SHA} in both Pt layers equal to 0, thus eliminating any SOT contribution, then using Eq. 2-54 to obtain P and β for each Co layer separately. The system is then set back to its original state with intrinsic material parameters so that the determining r_G and $\theta_{SHA,eff}$ can be determined. As θ_{SHA} in Ir is equal to zero, only the Pt/Co interfaces need to be considered, thus for the Co1/Pt interface P, β, $\theta_{SHA,eff}$ and r_G in the upper Co2(x)/Pt are set to 0, respectively, then Eq. 2-53 can be used to determine r_G and $\theta_{SHA,eff}$. This *vice-versa* process can then be carried out to determine the fitting parameters for the upper Co2(x)/Pt. The process is then repeated for varying layer thickness for the up Co2(x) layer.

Table 7-1 Material parameters used to model the Pt/Co/Ir/Co/Pt bilayer. (a) Value is obtained using Ref.[18] in conjunction with Eq. 4-1 for Im($G^{\uparrow\downarrow}$)

Parameter	Value	References
$\lvert D \rvert$ (Co)	1.5 mJm^{-2}	[19]
M_s (Co)	600 kAm^{-1}	[19]
A (Co)	10 pJm^{-1}	[19]
K_u (Co)	380 kJm^{-3}	[19]
α (Co)	0.03, 0.1	[20–26]
g_r (Co)	1.3	[27]
σ (Co)	5 MSm^{-1}	[28]
D_e (Co)	0.0012 m^{2}s^{-1}	[29]
D_e (Pt)	0.004 m^{2}s^{-1}	[30]
λ_{sf} (Co)	42 nm	[27–29,31]
λ_J (Co)	2 nm	[32]
λ_φ (Co)	3.2 nm	[33]
λ_{sf}(Pt)	1.4 nm	[34]
σ (Pt)	7 MSm^{-1}	[34]
$Re\left(G^{\uparrow\downarrow}\right)$ (Pt/Co)	1.5+i0.45 PSm^{-2}	[18,34,35]
$Im(G^{\uparrow\downarrow})$ (Pt/Co)	0.45 PSm^{-2}	(a)
θ_{SHA} (Pt)	0.19	[34]

7.3 Smooth structures

In this section, preliminary results are shown for a skyrmion in SAF/SYF systems. As there are now two skyrmions in the system, both skyrmions are tracked and recorded. Figure 7-3 shows the relationship between the SkHA and the skyrmion diameter for varying Co thickness as shown by the colour bar. The spots, crosses and triangles are the full torque, SOT-only and ISTT-only contribution, respectively. The diameter is determined as an average of both Co1 and Co2 skyrmions, i.e. each skyrmion's x and y diameter is averaged, and the total mean is determined from this. As might be apparent, Figure 7-3 is remarkably similar qualitatively to Figure 4-6(a) for all torques. The SkHA increases rapidly for the full torque with a skyrmion diameter up to 100 nm, after which a flattening of the trend occurs which is more apparent for thinner Co thicknesses. This behaviour is largely due to the thickness of the upper Co2 layer such that with a Co1 > Co2 the net magnetic moment is much stronger in the $+z$ direction which alongside the out-of-plane magnetic field there is a much larger control of the diameter, thus a larger range of skyrmion diameters is achievable.

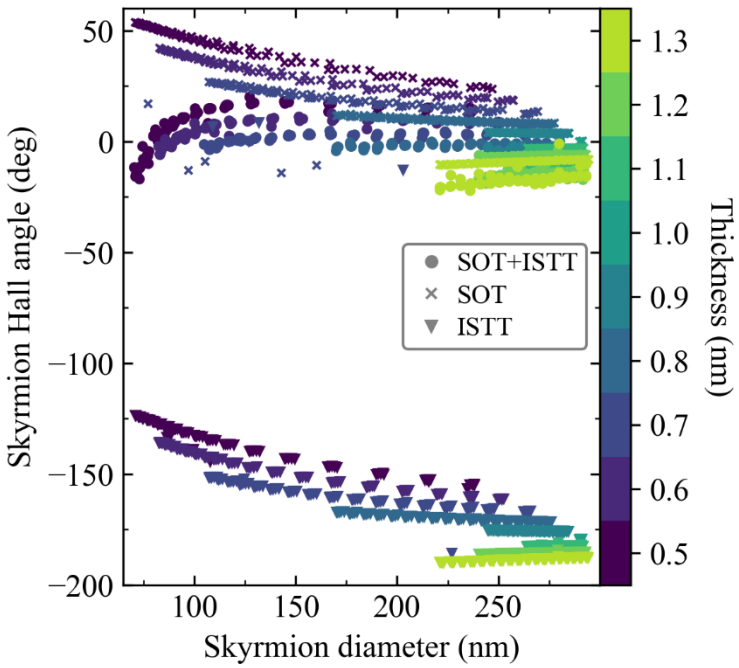

Figure 7-3 Effect of skyrmion diameter on the skyrmion Hall angle for a SAF structure (t_{Co2} = 1 nm) and multiple SYF structures ($t_{Co2} \neq 1$ nm). The colour bar represents the thickness of the top Co layer thickness in an ideal Pt/Co/Ir/Co(t_{Co2})/Ta. The spots, crosses and triangles represent the SOT+ISTT, SOT and ISTT, respectively.

As in previous results, there are three distinct curves: (i) the full torque, (ii) the SOT only and (iii) the ISTT alone, suggesting that in SYF/SAF systems there is a significant contribution to the skyrmion motion from the ISTT. Furthermore, the ISTT has a significant effect on small skyrmions, especially less than 100 nm even in this new system. The thickness also has a marked effect on the SkHA with the SkHA reducing ~ 3° with increasing Co2 thickness – the reason for this is not fully understood at this point in the analysis, however, as the Co2 layer thickness increases to the point at which Co2 = Co1, the system becomes balanced. The Co2 begins to have a larger effect on the transverse skyrmion motion as the effects of the SOT and ISTT begin to cancel. This is evident when Co2 = Co1 at which the system is considered a SAF and the system is fully balanced resulting in a SkHA ~ 0°. Figure 7-4 shows the SkHA as a function of Co2 thickness when skyrmions are in the flow regime driven by an applied current density of J_c = 500 GAm^{-2}. The spots and crosses represent the SOT+ISTT and SOT only, respectively. Interestingly, as thickness increases for H = 1 kAm^{-1} and H = 4 kAm^{-1} for both the SOT+ISTT and SOT alone, there is a linear decrease in the SkHA with increasing Co2 thickness, with a nearly linear increase in skyrmion diameter. When increasing the out-of-plane applied field to H = 6.5 kAm^{-1} and H = 9.8 kAm^{-1}, the SOT remains stagnant in its trend with only a slight change in the gradient, however, when the ISTT is included the trend remains similar to the SOT at larger thickness but deviated rapidly below Co2 = 0.7 nm.

The SOT as expected yields the largest velocity compared to the ISTT, however, when combined, the resulting velocities are significantly reduced to almost stationary due to the corresponding torques acting in near opposite directions. Interestingly, there is near to no change in the velocity with increasing thickness for the full torque unlike for the individual torque, suggesting thickness has little effect on skyrmion motion for the ISTT and SOT, however, this is likely to be different when the bulk STT is included and other forms of damping such as spin pumping and magnon damping.

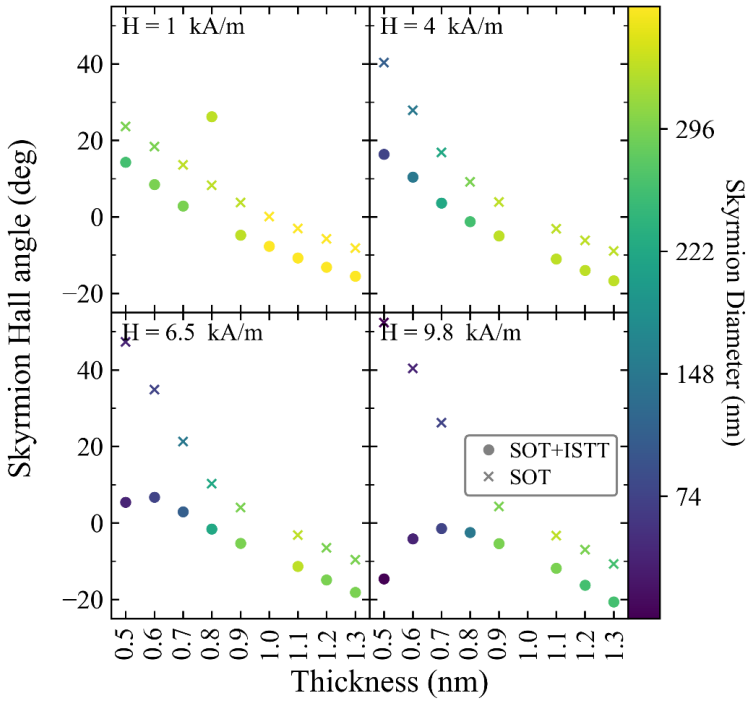

Figure 7-4 The skyrmion Hall angle as a function of thickness on a smooth surface. Skyrmions are driven at J_c = 500 GAm^{-2}, thus in the flow regime. Each panel corresponds to a different out-of-plane applied magnetic field. The colour bar on the right-hand side represents the average skyrmion diameter which is taken as an average of the x and y diameters.

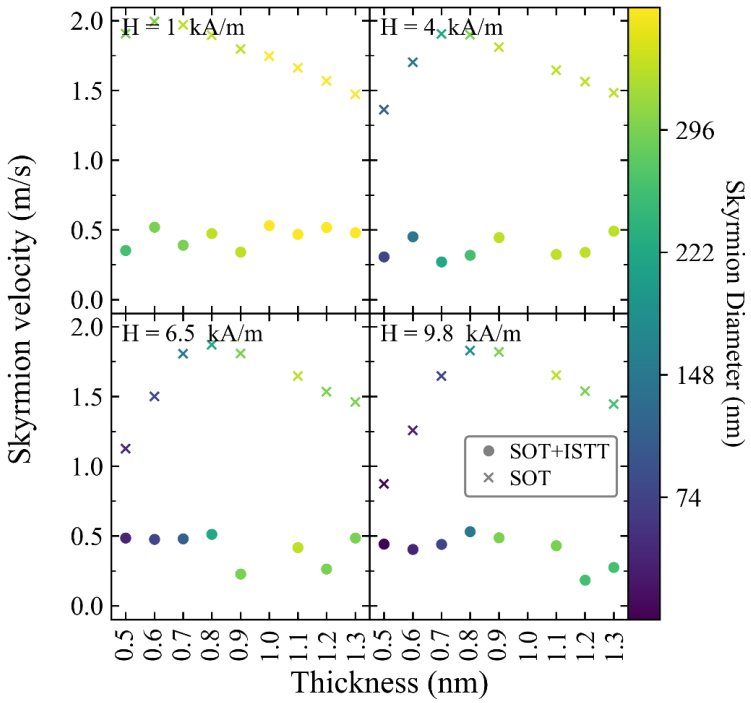

Figure 7-5 The skyrmion velocity as a function of Co2 thickness on a smooth surface. Skyrmions are driven at J_c = 500 GAm^{-2}, thus in the flow regime. Each panel corresponds to a different out-of-plane applied magnetic field. The colour bar on the right-hand side represents the average skyrmion diameter which is taken as an average of the x and y diameters.

7.4 Roughened structures

Following skyrmions in SYF/SAF structures with no roughness, the next step is to compare these findings with roughness included, therefore, in this section roughness is included between both Co/Pt interfaces. Note that the spin torques had to be redetermined with this in mind.

In nearly all cases, both skyrmions are pinned to each other due to the stray field produced by each skyrmion. In the cases the skyrmion pair disassociated the simulation is disregarded; the cause of this was due to either one or both of the skyrmions annihilating due to the presence of significant applied current density and/or a pinning site.

Figure 7-6 shows the relationship between the SkHA and the skyrmion diameter with included roughness at the Co/Pt interfaces. The maximum roughness depth is 1 Å with a coherence length of 40 nm. Each panel represents the applied current density increasing from J_c = 50 GAm^{-2} up to J_c = 500 GAm^{-2} with the colour bar representing the Co2 thickness. In Figure 7-6(a), J_c = 50 GAm^{-2}, the SkHAs appear chaotic besides a slight grouping between like thicknesses. This, however, is not the case for all applied currents, as with increasing applied current density the skyrmion behaviour becomes more defined, as shown in Figure 7-6(c) for J_c = 500 GAm^{-2}, and is similar both qualitatively and quantitatively to that of Figure 7-3. This is as expected due to the increased applied current density which leads to different flow regimes as discussed in previous chapters, namely the pinned, creep and flow regimes.

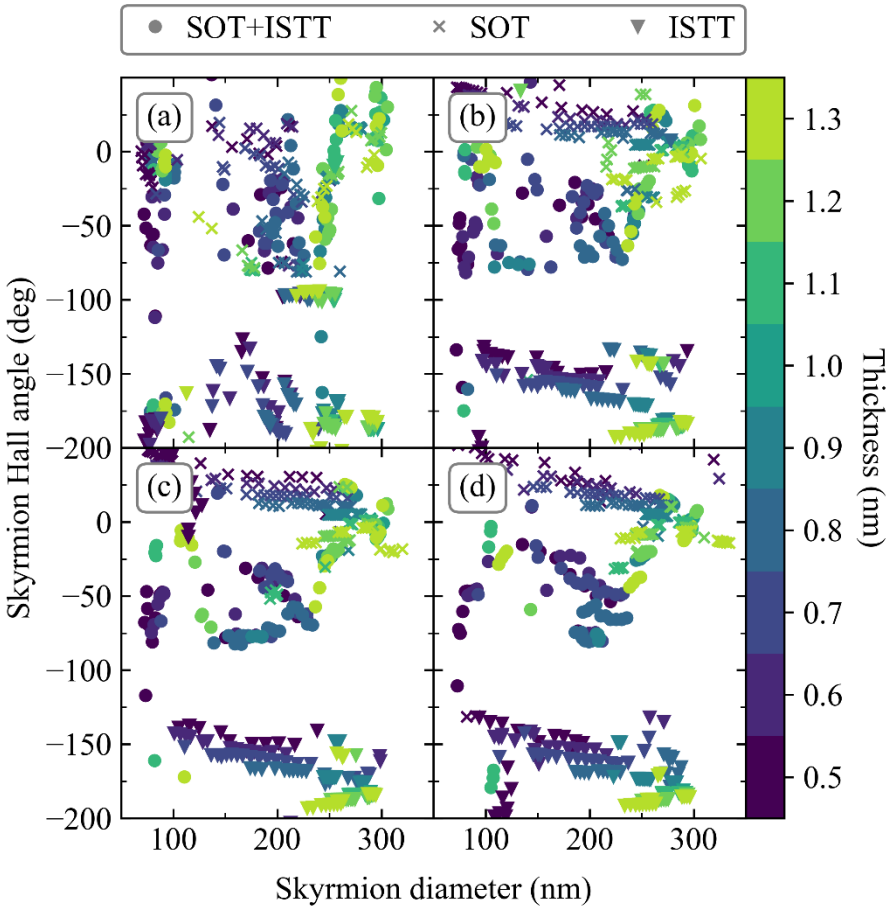

Figure 7-6 The relationship between the skyrmion Hall angle and the skyrmion diameter for SAF/SYF Pt/Co/Ir/Co/Ta structures. Each panel represents an applied current density of (a) $J_c = 50$ GAm^{-2}(b) $J_c = 200$ GAm^{-2} (a) $J_c = 300$ GAm^{-2} and (a) $J_c = 500$ GAm^{-2}. The colour bar shows the thickness of the upper Co layer.

To further observe the dependences on thickness, the average SkHA and skyrmion velocity for each thickness are shown in Figure 7-8 and Figure 7-7, respectively. Figure 7-7 shows the effect of thickness on the velocity of the skyrmion. The SOT and SOT+ISTT show markedly similar velocities, with SOT typically slightly larger. Unlike the ideal case, there is no discernible gradient to the linear trend, however, the full torque-driven skyrmions have very similar velocities to the ideal case, in the same order, albeit slightly lower.

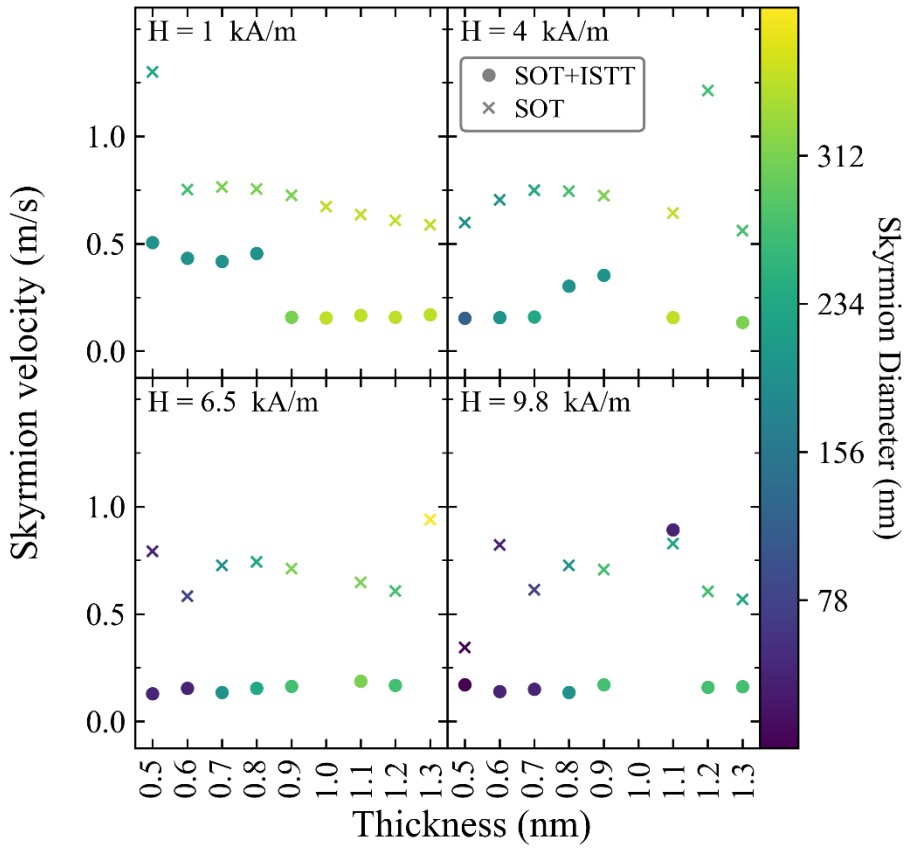

Figure 7-7 The skyrmion velocity as a function of Co2 thickness with surface roughness applied. Skyrmions are driven at J_c = 500 GAm^{-2}, thus in the flow regime. Each panel corresponds to a different out-of-plane applied magnetic field. The colour bar on the right-hand side represents the average skyrmion diameter which is taken as an average of the x and y diameters.

Finally, the SkHA thickness dependence shown in Figure 7-8 shows similar trends to that of Figure 7-4 with similar SkHAs and decreasing almost linear trends. More importantly, the SkHA at Co2 = 1 nm, a balanced system with the SkHA ~ 0° which is a crucial result as this is ideal for industrial applications such as skyrmionics storage devices. For lower applied out-of-plane magnetic fields (large diameters) such as H = 1 kAm^{-1}, there is little gradient compared to Figure 7-4 with the SkHA ~ 0°, however, with an increasing field strength a sharper gradient occurs for the SOT and SOT+ISTT.

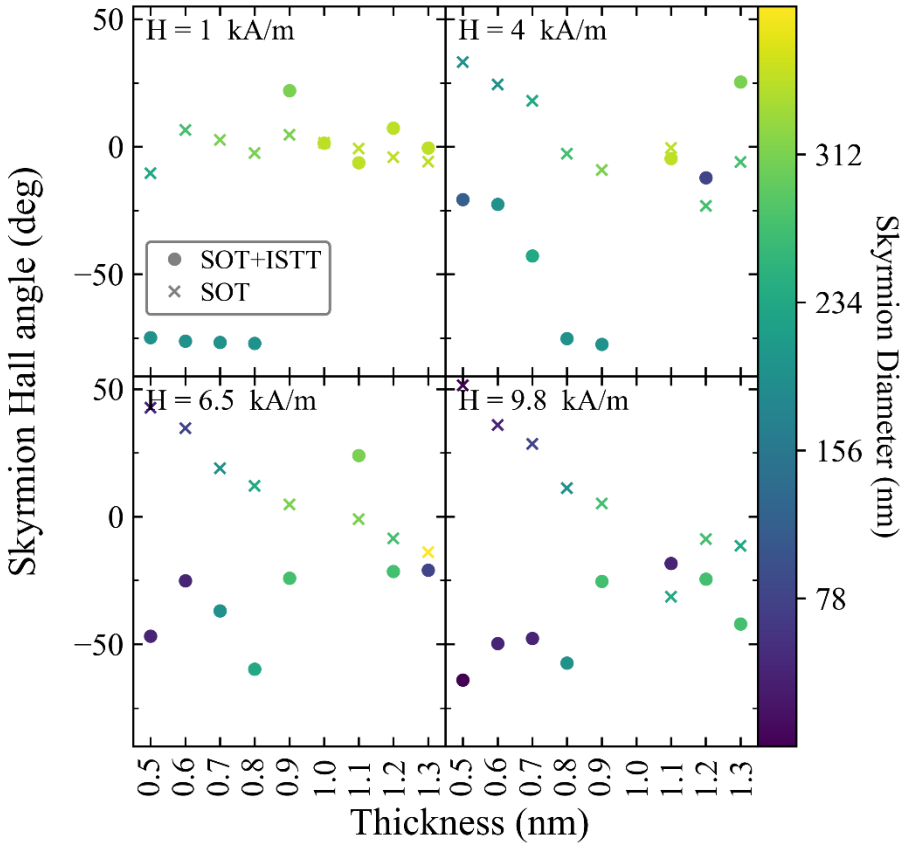

Figure 7-8 The skyrmion Hall angle as a function of Co2 thickness with surface roughness applied. Skyrmions are driven at J_c = 500 GAm^{-2}, thus in the flow regime. Each panel corresponds to a different out-of-plane applied magnetic field. The colour bar on the right-hand side represents the average skyrmion diameter which is taken as an average of the x and y diameters.

7.5 Verification of ISTT

To further explore the ISTT in SYF and SAF structures, a Cu layer was inserted into the above stack so it becomes a Pt/Co1/Ir/Co2/Cu/Pt. The hypothesis of including the Cu layer is to preserve the interfacial DMI, thus allowing stabilising of the skyrmion, but more importantly, due to the large spin-flip length of Cu ~ 170 nm, the SOT generated in the upper Pt layer is preserved through the Cu layer which is then absorbed at the Co2/Cu interface. The skyrmions in both Co layers are equally manipulated but in opposite directions and thus cancel out, resulting in a zero in-plane velocity. Also, due to the nature of SAF structures, the Magnus-like force cancels, resulting in a zero transverse velocity. The net velocity is thus zero for the SOT contribution. Figure 7-9 shows the results following the same simulations as in the previous sections but with the inclusions of the Cu layer. Figure 7-9(a) shows the SkHA as a function of the skyrmion diameters. It is clear to see that for all thicknesses of Co2, the SOT-only contribution results in a SkHA

of 0° across the board. Furthermore, the ISTT and ISTT+SOT are completely overlapping, further confirming the negligible contribution due to the SOT. This is further confirmed by Figure 7-9(b), which shows the skyrmion velocity dependence on diameter. The contribution due to SOT-only results in a net skyrmion velocity of ~ 0 ms^{-1} for Co2 thickness, confirming the negligible action of the SOT. Again, as for the SkHA, the ISTT and ISTT+SOT results overlap almost perfectly.

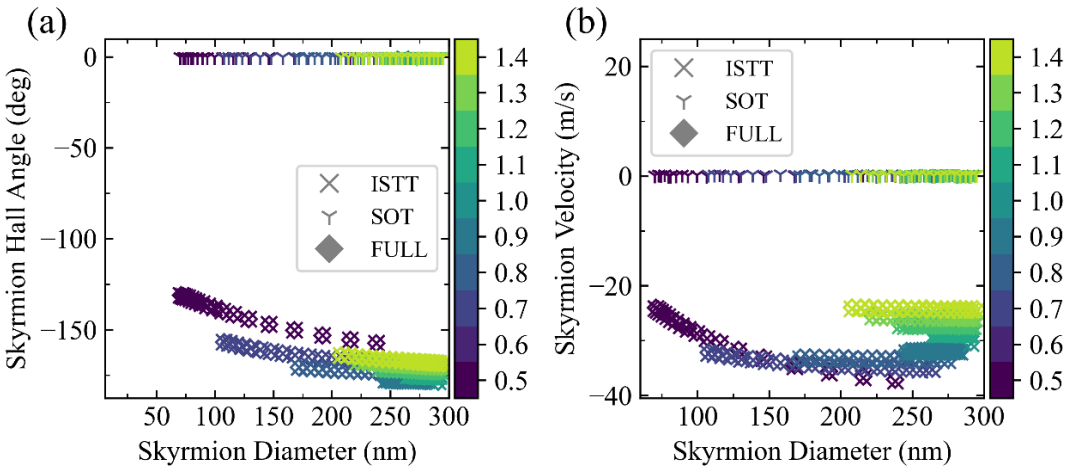

Figure 7-9 Results for SYF and SAF structures with an included Cu layer. (a) SkHA relationship on diameters and (b) the skyrmion velocity dependence on diameter. The crosses, diamonds and down triangle represent the ISTT, SOT+ISTT and SOT only. The colour bar represents the thickness of the Co2 layer.

7.6 Conclusion

In this short chapter the initial simulations, analysis and results for a system of Pt/Co/Ir/Co(x)/Pt synthetic antiferromagnets and ferrimagnets are shown with and without the disorder. As well as the SOT, the ISTT is used to drive skyrmions with the ISTT showing a significant contribution, especially for smaller skyrmion diameters less than 100 nm which is similar to previous results on a Co/Pt bilayer for isolated and collective skyrmion motion. Interestingly, when the balanced system was created, Co1 = Co2, the skyrmion velocities were ~ 0.15 ms^{-1} with SkHAs ~ 0°.

The initial results from this chapter are very promising, however, more work is needed to fully understand this system and the behaviours of skyrmions, including but not limited to the thickness dependence when Co2 > Co1. Furthermore, there is not a fully developed set Thiele equation to describe the skyrmion velocity and SkHA for SAF and SYF structures which would be very useful for comparisons between simulations and

experimental observations. A development such as this would have benefits across multiple systems as the Thiele model would have to be adapted for a multilayer system. It would also be beneficial to understand the skyrmion dynamics in SAF and SYF structures with the added effect of stochasticity in the form of finite temperature. As discussed throughout this thesis, knowing the effect on skyrmions is vitally important for the progression into applications, such as memory devices, especially given the exciting prospects of SYF/SAF skyrmions negating the SkHA.

Chapter References

1. Tonomura, A. *et al.* Real-Space Observation of Skyrmion Lattice in Helimagnet MnSi Thin Samples. *Nano Lett* **12**, 1673–1677 (2012).

2. Garanin, D. A., Chudnovsky, E. M., Zhang, S. & Zhang, X. Thermal creation of skyrmions in ferromagnetic films with perpendicular anisotropy and Dzyaloshinskii-Moriya interaction. *J Magn Magn Mater* **493**, 165724 (2020).

3. Park, J. *et al.* Compositional gradient induced enhancement of Dzyaloshinskii–Moriya interaction in Pt/Co/Ta heterostructures modulated by Pt–Co alloy intralayers. *Acta Mater* **241**, 118383 (2022).

4. Lu, J., Li, M. & Wang, X. R. Quantifying the bulk and interfacial Dzyaloshinskii-Moriya interactions. *Phys Rev B* **101**, (2020).

5. Dijk, B. Van. Skyrmions and the Dzyaloshinskii-Moriya Interaction. *Thesis* 75 (2014).

6. Yang, H., Thiaville, A., Rohart, S., Fert, A. & Chshiev, M. Anatomy of Dzyaloshinskii-Moriya Interaction at Co/Pt Interfaces. *Phys Rev Lett* **115**, 267210 (2015).

7. Kim, K.-W., Moon, K.-W., Kerber, N., Nothhelfer, J. & Everschor-Sitte, K. Asymmetric skyrmion Hall effect in systems with a hybrid Dzyaloshinskii-Moriya interaction. *Phys Rev B* **97**, 224427 (2018).

8. Varentcova, A. S. *et al.* Toward room-temperature nanoscale skyrmions in ultrathin films. *npj Computational Materials 2020 6:1* **6**, 1–11 (2020).

9. Barker, J. & Tretiakov, O. A. Static and Dynamical Properties of Antiferromagnetic Skyrmions in the Presence of Applied Current and Temperature. *Phys Rev Lett* **116**, 147203 (2016).

10. Zhang, X., Zhou, Y. & Ezawa, M. Magnetic bilayer-skyrmions without skyrmion Hall effect. *Nat Commun* **7**, 1–7 (2016).

11. Aldarawsheh, A. *et al.* Emergence of zero-field non-synthetic single and interchained antiferromagnetic skyrmions in thin films. *Nat Commun* **13**, 7369 (2022).

12. Parkin, S. S. P., Bhadra, R. & Roche, K. P. Oscillatory magnetic exchange coupling through thin copper layers. *Phys Rev Lett* **66**, 2152 (1991).

13. Legrand, W. *et al.* Room-temperature stabilization of antiferromagnetic skyrmions in synthetic antiferromagnets. *Nat Mater* **19**, 34–42 (2020).

14. Juge, R. *et al.* Skyrmions in synthetic antiferromagnets and their nucleation via electrical current and ultra-fast laser illumination. *Nat Commun* **13**, 4807 (2022).

15. Dohi, T., DuttaGupta, S., Fukami, S. & Ohno, H. Formation and current-induced motion of synthetic antiferromagnetic skyrmion bubbles. *Nat Commun* **10**, 5153 (2019).

16. Claudio-Gonzalez, D., Thiaville, A. & Miltat, J. Domain wall dynamics under nonlocal spin-transfer torque. *Phys Rev Lett* **108**, 227208 (2012).

17. Bisig, A. *et al.* Enhanced Nonadiabaticity in Vortex Cores due to the Emergent Hall Effect. *Phys Rev Lett* **117**, 277203 (2016).

18. Juge, R. *et al.* Current-Driven Skyrmion Dynamics and Drive-Dependent Skyrmion Hall Effect in an Ultrathin Film. *Phys Rev Appl* **12**, 044007 (2019).

19. Woo, S. *et al.* Observation of room-temperature magnetic skyrmions and their current-driven dynamics in ultrathin metallic ferromagnets. *Nat Mater* **15**, 501–506 (2016).

20. Yuan, J., Sun, L., Sang, H., Du, J. & Zhou, M. Interfacial effects on magnetic relaxation in Co/Pt multilayers. *Phys Rev B* **68**, 134443 (2003).

21. Benguettat-El Mokhtari, I. *et al.* Interfacial Dzyaloshinskii-Moriya interaction, interface-induced damping and perpendicular magnetic anisotropy in Pt/Co/W based multilayers. *J Appl Phys* **126**, 133902 (2019).

22. Beaujour, J. M. L. *et al.* Ferromagnetic resonance study of sputtered Co|Ni multilayers. *European Physical Journal B* **59**, 475–483 (2007).

23. Barati, E., Cinal, M., Edwards, D. M. & Umerski, A. Gilbert damping in magnetic layered systems. *Phys Rev B* **90**, 014420 (2014).

24. Schellekens, A. J. *et al.* Determining the Gilbert damping in perpendicularly magnetized Pt/Co/AlOx films. *Appl Phys Lett* **102**, 082405 (2013).

25. Barman, A. *et al.* Ultrafast magnetization dynamics in high perpendicular anisotropy [CoPt]n multilayers. *J Appl Phys* **101**, 09D102 (2007).

26. Mizukami, S. *et al.* Gilbert damping in perpendicularly magnetized Pt/Co/Pt films investigated by all-optical pump-probe technique. *Appl Phys Lett* **96**, 152502 (2010).

27. Beaujour, J. M. L., Lee, J. H., Kent, A. D., Krycka, K. & Kao, C.-C. Magnetization damping in ultrathin polycrystalline Co films: Evidence for nonlocal effects. *Phys Rev B* **74**, 214405 (2006).

28. Bass, J. & Pratt, W. P. Spin-diffusion lengths in metals and alloys, and spin-flipping at metal/metal interfaces: An experimentalist's critical review. *Journal of Physics Condensed Matter* **19**, 183201 (2007).

29. Lepadatu, S. Boris computational spintronics - High performance multi-mesh magnetic and spin transport modeling software. *J Appl Phys* **128**, 243902 (2020).

30. Halas, S. & Durakiewicz, T. Work functions of elements expressed in terms of the Fermi energy and the density of free electrons. *Journal of Physics Condensed Matter* **10**, 10815 (1998).

31. Piraux, L., Dubois, S., Fert, A. & Belliard, L. The temperature dependence of the perpendicular giant magnetoresistance in Co/Cu multilayered nanowires. *European Physical Journal B* **4**, 413–420 (1998).

32. Zhang, S., Levy, P. M. & Fert, A. Mechanisms of spin-polarized current-driven magnetization switching. *Phys Rev Lett* **88**, 236601 (2002).

33. Petitjean, C., Luc, D. & Waintal, X. Unified drift-diffusion theory for transverse spin currents in spin valves, domain walls, and other textured magnets. *Phys Rev Lett* **109**, 117204 (2012).

34. Zhang, W., Han, W., Jiang, X., Yang, S. H. & Parkin, S. S. P. Role of transparency of platinum-ferromagnet interfaces in determining the intrinsic magnitude of the spin Hall effect. *Nat Phys* **11**, 496–502 (2015).

35. MacKinnon, C. R., Lepadatu, S., Mercer, T. & Bissell, P. R. Role of an additional interfacial spin-transfer torque for current-driven skyrmion dynamics in chiral magnetic layers. *Phys Rev B* **102**, 214408 (2020).

8 Conclusions and Further Work

8.1 Conclusions

Presented in this thesis is the investigation into the role of the significant interfacial spin-transfer torque (ISTT) in current-driven skyrmion dynamics alongside the well-documented spin-orbit torque (SOT). The ISTT arises from an accumulation of spin in magnetic layers at magnetisation gradients resulting in a diffusive vertical spin current, whereas the SOT arises in a non-magnetic material with string spin-orbit coupling and is governed by the spin Hall effect. The inclusion of the ISTT in micromagnetic modelling and the Thiele model has reduced the discrepancy between the SOT-only models and experimental observations. The SOT-only model resulted in reasonable agreement at large skyrmion diameters but this was not true at smaller diameters, such that with the inclusion of the ISTT this discrepancy was significantly reduced for both the skyrmion Hall angle (SkHA) and the skyrmion velocity.

In this work, four studies investigated the effect of the ISTT on skyrmion dynamics, each with the view to standardizing the ISTT physically and within micromagnetic modelling.

In Chapter 4, isolated skyrmion motion in Pt/Co bilayers was investigated with and without the inclusion of landscape disorder in the form of surface roughness. Initially, smooth surfaces were considered with the aim to investigate the effect of the ISTT in ideal conditions. The SOT, ISTT and SOT+ISTT were all investigated and it was found, as expected, the SOT has a significant effect on skyrmion dynamics, as well as the ISTT, especially for skyrmion diameters < 100 nm, resulting in drastically different combined torque characteristics. Furthermore, the SOT-only model is shown to agree on large skyrmions, whilst for smaller skyrmions, the inclusion of the ISTT term resulted in decreasing SkHA with decreasing skyrmion diameter. In addition to this, the spin mixing conductance ratio for Co/Pt was determined numerically, using literature-obtained values resulting in G_r= 0.3. It is commonly accepted that the imaginary component of the spin-mixing conduction is negligible and thus disregarded, however non-negligible spin-mixing conductance has been reported. Here, using a non-negligible imaginary component of the complex spin-mixing conductance, the imaginary component was shown to have a significant effect on skyrmion motion. When considering a skyrmion of ~ 65 nm, the ratio of the spin-mixing conductance resulted in SkHAs of ~ 38° and ~ 60°

for G_r= 1 and G_r= 0.125, respectively, when including the ISTT. Disordered systems were then considered in which a surface roughness was applied to the top layer of the Co in the Co/Pt bilayer. As expected, roughness had a significant effect on the skyrmion motion with three well-documented regimes apparent, namely the pinned, creep and flow regimes. It was found that the SkHA approached the ideal results for large driving forces. Furthermore, the ISTT was shown again to have a significant effect on the SkHA and velocity with results markedly similar, qualitatively, to published experimental works. The SOT-only model resulted in a SkHA ~ 88° for a skyrmion diameter of ~ 65 nm, whereas, a SkHA of ~ 60° was observed with the ISTT included. For skyrmion diameters > 65 nm and < 65 nm, the SOT-only and ISTT+SOT model began to converge, and diverge rapidly, respectively. The results obtained for a range of skyrmion diameters were shown to collapse onto a universal SkHA-velocity dependence, nearly independent of the surface roughness characteristics. This initial study displayed the shortfalls of the SOT-only Thiele model but more importantly shed light on the skyrmion mechanics under the influence of the ISTT.

In Chapter 5, a logical progression was taken by increasing from a single skyrmion to an array of skyrmions which was defined as a group of interaction skyrmions. Again, the ISTT and the SOT were considered but now the bulk STT was also considered for completeness. It was initially predicted, using the Thiele model with individual spin torques considered, that the ISTT and SOT would have almost equal strengths at smaller skyrmion diameters but in the opposite directions, with the bulk STT having a negligible effect due to the thickness dependence.

This chapter is unique compared to other results chapters as the results obtained via modelling are directly compared to experimental results obtained. It was shown that the SkHA is strongly dependent on the effect of the combination of all torques and the small SkHA values observed in experiments are in good agreement with modelling which included the ISTT, also explaining the observed diameter-independent SkHA, and spread of experimental SkHA values at the same current density. This was in contrast to the SOT-only model where SkHA discrepancies as large as 50° were apparent. When ISTT was included ~ 83 % of modelled results aligned within the standard error on the mean of experimental observation, whereas when the SOT-only model is considered, there was zero overlap for both the standard error on the mean as well as the spread. The collective skyrmion motion was found to be described by an average group velocity over the

diameter range, which stands in marked contrast to the velocities obtained from isolated skyrmion motion. Furthermore, the group velocities obtained with the inclusion of ISTT are comparable to those found in experiments. This is not the case for the SOT-only model, which again shows large discrepancies of over 40 ms^{-1} with the experimental data. The results from this chapter again shed light on the collective skyrmion motion and highlights the significance of the ISTT in micromagnetic modelling, to reduce discrepancies between experimental and modelled results.

In Chapter 6, atomistic modelling was used to model the effect of stochasticity in the form of a finite temperature. With the foundation for ISTT complete, the investigation into the effect of temperature in conjunction with the ISTT was paramount. To begin, as the *skypos* algorithm was no longer applicable for tracking skyrmion motion, a new method was devised and implemented by taking an average of the skyrmion profile over many time steps and then determining the new position and diameters from the averaged profiles. The important Curie temperature for the Co/Pt bilayer structure was determined for smooth and roughened samples using the Monte Carlo algorithm resulting in a difference of $\Delta T_c \sim 78\ K$ with the smooth surface having a larger T_c. Skyrmions were then driven under a spectrum of applied current densities and temperatures with varying out-of-plane magnetic field strengths for skyrmion stability. It was found that the skyrmion diameter increased nearly linearly with temperature but did not change between different current densities. Furthermore, the diameter fluctuations were relatively small but did increase with temperature as expected. Skyrmion velocity was shown again to linearly increase with applied current but also increase with temperature such that for skyrmions driven by J_c = 750 GAm^{-2} there was a difference in velocity for T = 150 K and T = 0 K of ~ 40 ms^{-1} with larger velocities for the former. The SkHA was shown to have a markedly similar result to the literature with skyrmions having an initial flat trend which then passes the pinning threshold and jumps linearly and rapidly to a maximum SkHA with a near-constant trend. There was a slight dependence on the skyrmion size, where at the largest diameters the trend became a more gradual change – the convergence of the SkHA occurred over a much larger J_c range than at smaller diameters. This chapter was further able to shed light on the ISTT under the influence of thermal fluctuations. Results compared well to experimentally obtained results in the literature and this shows the significance of the ISTT.

In the final results chapter, Chapter 7, the initial investigation into skyrmion motion in synthetic antiferromagnetic (SAF) and ferrimagnetic structures (SYF) was presented. A structure of Pt/Co1/Ir/Co2/Pt was devised so the Co2 layer could be adjusted in thickness to unbalance a SAF into an SYF structure. For smooth structures, the SkHA dependence on diameter was shown to be similar to that obtained in Chapter 4, with the ISTT having a significant effect on the skyrmion motion for a diameter < 100nm. The most significant discrepancy between the inclusion of the ISTT and SOT-only results was for small skyrmions (~ 65 nm), with differences of SkHAs ~ 65°, with the ISTT model resulting in much smaller SkHAs. Both models also showed similar trends to isolated skyrmion motion in bilayers, in which the trends rapidly diverged from each other at smaller diameters.

Furthermore, the SkHA and velocity relationship on Co2 thickness was investigated and shown to have a significant effect, such that the SkHA reduces rapidly with increasing thickness as well as velocity remaining almost constant when ISTT is included. For rough surfaces, the SkHA was shown to be significantly more sporadic but showed that increasing driving force tended towards the ideal conditions. Furthermore, there was no discernable change in the velocity trend except for a slight reduction in velocity. For the SkHA, the steep gradient almost vanished for small out-of-plane applied fields. Much more work is needed on this work as it is a new field, however, the results shown in this chapter are still useful. This work was also used to propose a structure that can experimentally verify the ISTT without the SOT contribution with the use of a Cu layer. Introducing the Cu layer into the SAF resulted in a negligible SOT contribution resulting in a zero SkHA and skyrmion velocity.

The results in this thesis shed further light on current-induced skyrmion motion, and highlight the significance of the ISTT in understanding current-induced isolated and collective skyrmion motion in magnetic systems with included surface roughness and stochastic thermal fields.

8.2 Further work

To begin, it would be very interesting to test and model the ISTT in different structures and magnetic systems. Here Pt/Co systems are used exclusively as there has been much work conducted into skyrmion motion and the material properties, however, to further

validate the existence and diversity of work into the ISTT, structures such as Ta/Co[1] and W/Co[2] or even permalloy[3] and Gadolinium compounds[4,5] could be investigated. As an extension of this, simulations on a multi-stack geometry would be crucial, as typically experimental stacks consist of upwards of five repetitions depending on the thicknesses of individual layers. It is expected that the diameter of skyrmions would change with increasing repetition count, as shown in Chapter 7, but it is unknown how the ISTT generated in each layer would affect skyrmion motion.

A large portion of this work is compared to the Thiele model. In Chapter 4, skyrmion motion with the ISTT included is compared to the SOT-only Thiele model and is shown to drastically vary, whereas, in Chapter 5, the Thiele model with ISTT included is shown to correspond well with experimental results and modelled results. However, there is still a large gap in development for the Thiele model which includes taking into account multi-layer compositions and thickness for SYF and SAF structures meaning it cannot be used reliably for these systems. Furthermore, the temperature has not been included in the Thiele model sufficiently, as a result, temperature-dependent parameters such as damping and magnetization saturation are input directly with their dependence into the Thiele model, however, the results obtained do not correspond well with obtained simulations. It should be noted that attempts for a temperature-dependent Thiele model have been performed using a magnonic heat bath[6] which leads to a dissipative term that is linear in temperature, however, this only provides a framework and much work is still needed.

The ISTT is not only present for skyrmions but also for any domain wall structures, given there is a significant magnetisation gradient. This is why the ISTT effect is strong for small skyrmions. Therefore, it would be very interesting to observe the effect of the ISTT in thin-magnetic layers for different magnetic textures such as vortex, Bloch and Néel DWs. Further to this, skyrmions with different winding numbers such as anti-skyrmions, Bloch skyrmions and skyrmionium could also benefit significantly from research into the effect of the ISTT.

Further work into the non-adiabaticity parameter, β, is required both computationally and, more importantly, experimentally, as it is paramount in determining the ISTT and bulk STT. In this work, the ISTT results in a large negative non-adiabaticity parameter when used as a fitting parameter, compared to the much smaller STT value in terms of magnitude. For example, values determined for the former and latter in this work are

$\beta_{ISTT} = -1.13$ and $\beta_{STT} = 0.002$, respectively. Typically, β_{STT} is shown to be negligible in Co thin films[7–9] which is expected due to the thickness dependence, however, it has been shown that a large negative β exists [10] in Co thin films contrary to STT theory. This large negative β results in a torque opposite to the direction of the standard bulk STT and could justify the existence of the ISTT, however, more work is required to understand these large negative values.

The spin-mixing conductance used in the drift-diffusion model can be developed further to include the transmitted spin-mixing conductance[11] alongside the interfacial method used in this work. Currently, the interfacial method involves the absorption of a spin current entirely and instantaneously at the interface between a HM/FM layer. It has been proposed that given thin enough layers, which are comparable to the spin dephasing length, the spin current may not be entirely absorbed across the interface and in the injected layer, thus resulting in non-negligible effects, such as a field-like SOT. This could significantly affect the strength of the ISTT due to the large diffusive spin current generated. This method needs to be fully developed in conjunction with the interfacial method and then implemented into *Boris* so that this can be investigated with the ISTT in mind.

Finally, and most importantly, experimental verification of the ISTT is required in which only the ISTT is affecting skyrmion motion, thus SOT would be eliminated. This may be rather difficult to achieve, however, as discussed in Chapter 7, this may be possible with the use of a balanced SAF system with the inclusion of a Cu layer which is valid computationally. The means of doing this are beyond the scope of this work.

Chapter References

1. Park, J. *et al.* Compositional gradient induced enhancement of Dzyaloshinskii–Moriya interaction in Pt/Co/Ta heterostructures modulated by Pt–Co alloy intralayers. *Acta Mater* **241**, 118383 (2022).

2. Lin, T. *et al.* Observation of room-temperature magnetic skyrmions in Pt/Co/W structures with a large spin-orbit coupling. *Phys Rev B* **98**, 174425 (2018).

3. Berganza, E. *et al.* 3D quasi-skyrmions in thick cylindrical and dome-shape soft nanodots. *Sci Rep* **12**, 3426 (2022).

4. Mokkath, J. H. Magnetic skyrmions in monoatomic-thin Gadolinium square-shaped nanoislands. *Physica E Low Dimens Syst Nanostruct* **136**, 115015 (2022).

5. Tokura, Y. & Kanazawa, N. Magnetic Skyrmion Materials. *Chem Rev* **121**, 2857–2897 (2021).

6. Weißenhofer, M., Rózsa, L. & Nowak, U. Skyrmion Dynamics at Finite Temperatures: Beyond Thiele's Equation. *Phys Rev Lett* **127**, 047203 (2021).

7. Cormier, M. *et al.* Effect of electrical current pulses on domain walls in Pt/Co/Pt nanotracks with out-of-plane anisotropy: Spin transfer torque versus Joule heating. *Phys Rev B* **81**, 024407 (2010).

8. Emori, S. *et al.* Spin Hall torque magnetometry of Dzyaloshinskii domain walls. *Phys Rev B* **90**, 184427 (2014).

9. Franken, J. H., Herps, M., Swagten, H. J. M. & Koopmans, B. Tunable chiral spin texture in magnetic domain-walls. *Sci Rep* **4**, 5248 (2014).

10. Je, S.-G. *et al.* Emergence of Huge Negative Spin-Transfer Torque in Atomically Thin Co layers. *Phys Rev Lett* **118**, 167205 (2017).

11. Kim, K. W. Spin transparency for the interface of an ultrathin magnet within the spin dephasing length. *Phys Rev B* **99**, 224415 (2019).

Appendix A: Skyrmion Motion Script

```
import os
import sys
import numpy as np
from scipy.optimize import curve_fit
import matplotlib.pyplot as plt
import math
from Boris.NetSocks import NSClient

ns = NSClient('localhost', serverport=1001)
directory = os.path.dirname(sys.argv[0]) + "\\"
ns.default()
ns.chdir(directory)

# Constants
xdim = 400e-9
ydim = 400e-9
H = 5000
Jc = 5e12

ns.default()

ns.setmaterial('Pt', [0, 0, 0, xdim, ydim, 3e-9])  # add Pt layer
ns.addmaterial('Co/Pt', [0, 0, 3e-9, xdim, ydim, 4e-9])  # add Co
layer
ns.setangle(0, 0)  # set angle of magnetic moments
ns.setfield(H, 0, 0)  # set angle of magnetic moments

ns.skyrmion('Co/Pt', [-1, -1, 150e-9, xdim/2, ydim/2])  # create
skyrmion in center of mesh

ns.setode('LLGStatic', 'SDesc')  # set ode to relax
ns.editstagestop(0, 'mxh', 1e-4)  # threshold to relax to

ns.cuda(1)  # turn on cuda computations
ns.Run()  # Run sim
ns.reset()  # reset all trackables

# add modules to Co and Pt layers
ns.addmodule('Co/Pt', 'transport')
ns.addmodule('Co/Pt', 'iDMexchange')
ns.addmodule('Co/Pt', 'aniuni')
ns.addmodule('Pt', 'transport')

ns.setstage('Relax')
ns.editstagestop(0, 'time', 10e-9)
ns.setdefaultelectrodes()
ns.setpotential(-40e-3)
ns.setode('LLG-SA', 'RKF45')

ns.pbc('Co/Pt', 'x 5')
ns.pbc('Co/Pt', 'y 5')

# Determine fitting constants here and apply them to the materials

# convert current density to volatge in this setup
elC_Fm1 = ns.setparam('Co/Pt', 'elC')
ns.meshfocus('Co/Pt')
```

```
meshrect = ns.meshrect('Co/Pt')
Area = meshrect[4] * meshrect[5]
R_Co = meshrect[3] / (elC_Fm1 * Area)
voltage = -R_Co * j * Area
ns.setdefaultelectrodes()
ns.setpotential(voltage)

ns.Run()  # run
```

Appendix B: RK4 Simple Python

```
import matplotlib.pyplot as plt
import numpy as np
from matplotlib.ticker import MultipleLocator

def RungeKutta(t, y, dt, dydt):
    # Calculate slopes
    k1 = dt * dydt(t, y)
    k2 = dt * dydt(t + dt / 2., y + k1 / 2.)
    k3 = dt * dydt(t + dt / 2., y + k2 / 2.)
    k4 = dt * dydt(t + dt, y + k3)

    # Calculate new x and y
    y = y + 1. / 6 * (k1 + 2 * k2 + 2 * k3 + k4)
    t = t + dt

    return t, y


def Function(t, y):
    return t ** 2


def Solution(t):
    return t ** 3 / 3. + 2 / 3.


t0 = 1.
y0 = 1.
dt = 0.4
t_end = 2.

t_RK4 = [t0]
y_RK4 = [y0]

y = y0
t = t0

for i in np.arange(t, t_end, dt):
    t, y = RungeKutta(t, y, dt, Function)
    t_RK4.append(t)
    y_RK4.append(y)


def Euler(t, y, dt, dydt):
    return t + dt, y + dt * dydt(t, y)


t_EULER = [t0]
y_EULER = [y0]

y = y0
t = t0

for i in np.arange(t, t_end, dt):
    t, y = Euler(t, y, dt, Function)
    t_EULER.append(t)
    y_EULER.append(y)
```

```
## Plot solution at this point
plt.show()
```